Master of Science Thesis

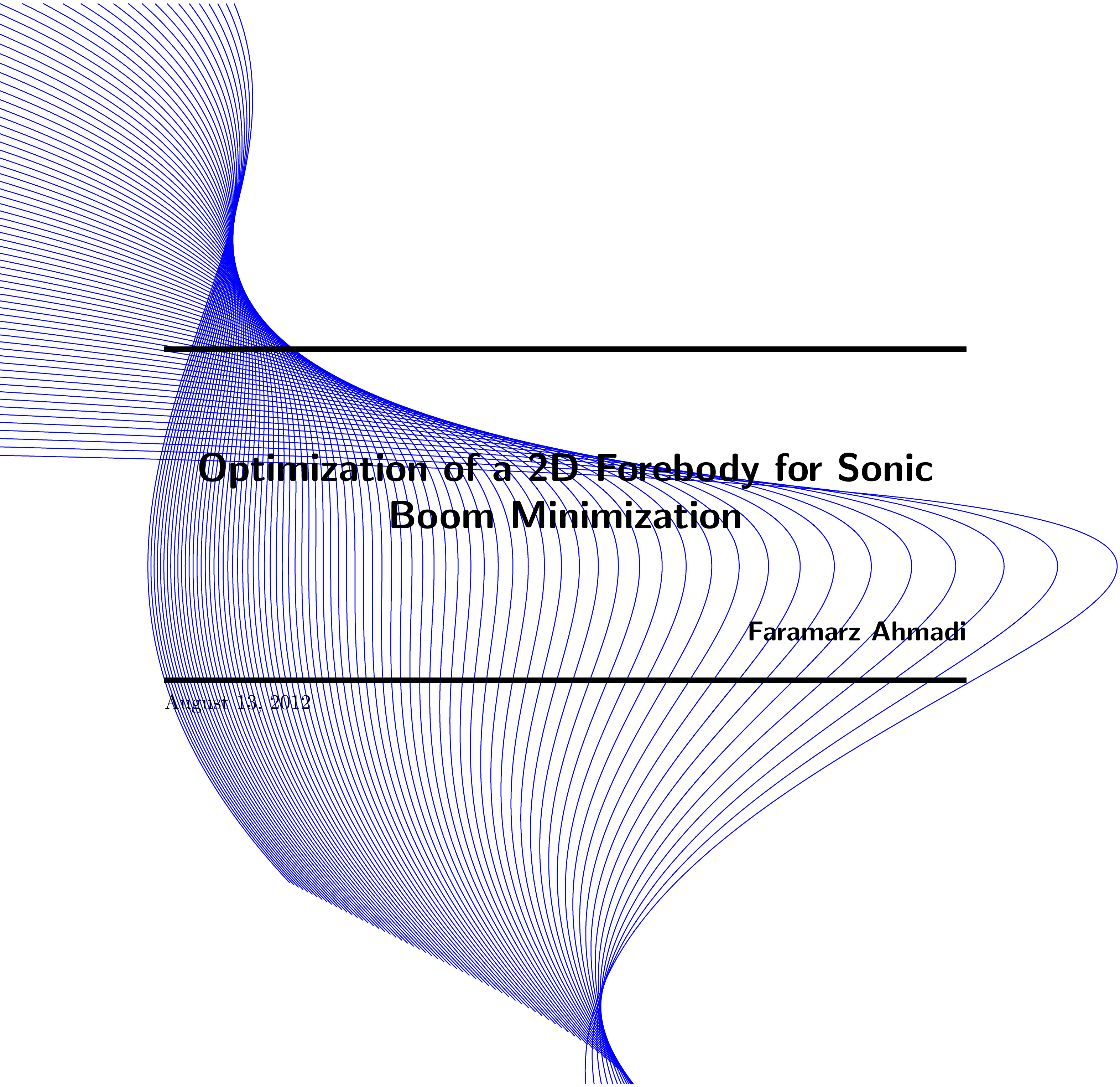

Optimization of a 2D Forebody for Sonic Boom Minimization

Faramarz Ahmadi

August 13, 2012

Faculty of Aerospace Engineering

Delft University of Technology

Optimization of a 2D Forebody for Sonic Boom Minimization

MASTER OF SCIENCE THESIS

For obtaining the degree of Master of Science in Aerospace
Engineering at Delft University of Technology

Faramarz Ahmadi

August 13, 2012

Faculty of Aerospace Engineering · Delft University of Technology

Delft University of Technology

Delft University Of Technology
Department Of
Aerodynamics

The undersigned hereby certify that they have read and recommend to the Faculty of Aerospace Engineering for acceptance the thesis entitled **"Optimization of a 2D Forebody for Sonic Boom Minimization"** by **Faramarz Ahmadi** in partial fulfillment of the requirements for the degree of **Master of Science**.

Dated: August 13, 2012

The theory developer and supervisor: ______________________
Prof.dr.ir.P.G.Bakker

Supervisor: ______________________
Dr.ir.F.F.J.Schrijer

Reader: ______________________
Dr.ir.Wim van Horssen

Reader: ______________________
Dr.Richard P. Dwight

PREFACE

This report is the thesis for the degree of master of science at the chair of Aerodynamics, faculty Aerospace Engineering, at Delft University of Technology. The author tries in his master thesis to obtain a minimized sonic boom for a 2D, non-generating lift body with a defined thickness. In order to reach this goal he analyzes the relation of a 2D contour geometry with the asymptotic shock strength it produces in a steady and inviscid supersonic flow.
There have been done many studies in different fields in order to reduce the sonic boom strength. This thesis is based on the asymptotic shock strength which is derived from 2D inviscid *Burgers equation.* An object moving with a supersonic speed creates shock and expansion waves together corresponding to its detailed geometry. The expansion waves interact with the shock wave and as a result a sound wave will be formed in a large distance which is called sonic boom.

The interaction between these two waves leads to the decreasing of the shock strength. This reducing process has an asymptotic behavior which means the strength of the shock approaches zero when the distance goes to infinity. So it means an earlier merging of the shock wave with expansion waves has a weaker sonic boom as result.

This thesis is a following on another master student's work, *T.Francken* who has worked before on a relation between the shock strength and the geometry of an object with infinitesimally small thickness [Francken [2009]]. This relation which is called the *BASS* measure, has been developed by *Prof.dr.ir.P.G.Bakker.*

ABSTRACT

When an object moves near sonic speed a shock wave will be formed and all disturbances and discontinuities remain localized in an area downstream of the shock wave. The impact of sonic boom is both of psychosomatic and structural damage. The sonic boom is unacceptable to the human ears due to the fact that it appears without warning and it produces structural damage. The sonic boom is unavoidable for an airplane which has lift, so the effort should be made to minimize the unacceptability degree on the part of the people.

A measure for the sonic boom strength is based on the asymptotic behavior of the interaction between the shock and expansion waves caused by a body moving with the speed of sound. The theory used to obtain this measure is based on the method of characteristics for a 2D, steady, inviscid and isentropic supersonic flow. This measure is called *BASS* which stands for *Bakker Asymptotic Shock Strength.* The *BASS* measure represents a relation between the body geometry and the asymptotic shock strength it produces.

The *BASS* measure is applied to a 2D non-lift generating contour with a certain thickness. Subsequently, the achieved measure is optimized by a variational approach which results in two types of contours indicated by the asymptotic shock strength. The volume of these contours is considered as constraint to the variation problem. The influence of thickness and Mach number on contour geometry and asymptotic shock strength will be investigated. In addition, the aerodynamic properties across the shock wave and drag wave caused by these contours will be studied.

Results show that the first variant contours cause a lower magnitude of asymptotic shock compared to the non-optimized contours with similar volumes while another variant contours are not optimum. It seems also when thickness is set to be constant both contour types do not depend upon the Mach number because the achieved contours show similar behavior for the asymptotic shock strength at different Mach numbers. And when the Mach number is set to be constant and the thickness increases, it will result in geometries which generate higher asymptotic shock strength for different Mach numbers.

ACKNOWLEDGEMENTS

Without the enthusiastic personality of Professor Bakker, the author had not been interested in the gasdynamic course which eventually encouraged him to choose this graduation topic. He would like to extend his gratitude to Prof.dr.ir.P.G.Bakker and also dr.ir.F.F.J.Schrijer for providing the overall guidance, feedbacks and their valuable input during the work on this thesis.

CONTENTS

LIST OF FIGURES

LIST OF TABLES

LIST OF ABBREVIATIONS, ACRONYMS AND SYMBOLS

Abbreviations and Acronyms

Short notation	Description
BASS	Bakker Asymptotic Shock Strength
l	Leading edge
s	Shoulder
w	Wedge
2D	Two dimensional
w.r.t.	With respect to

Symbols

Latin Symbols

Symbol	Description	Basic Unit
A_l	The leading asymptotic shock strength	
k_l	The Mach factor dependent on θ_0	
K	The constraint for the variation problem	
$\tilde{l}_0$	The asymptotic shock strength coefficient dependent on θ_0	
$F(x)$	Contour function	
u	Horizontal projected characteristic lines from the x axis	
M	Mach number	

Greek Symbols

Symbol	Description	Basic Unit
α	Angle of attack	
β	Prandtl-Meyer factor, $\sqrt{M^2-1}$	
Γ	Characteristic	
γ	Ratio of specific Heat	
θ	Characteristic angle	
φ	Flow angle w.r.t the surface	
μ	Mach angle	
ν	Prandtl-Meyer angle	
τ	Contour thickness	
Υ	The shock path in x-direction	
υ_0	The free flow characteristic angle	
υ	The characteristic angle	
Σ	The asymptotic shock strength	

CHAPTER 1

INTRODUCTION

When the Bell X-1 airplane exceeded Mach number 1 in 1947 aerodynamicists came to know that sonic boom is a direct consequence of the shock wave pattern establishing around the aircraft when traveling at supersonic speeds. Actually, sonic boom phenomenon was not a new discovery because it was already known within the ballistics community [J.Plotkin & J.Maglieri [2003]]. Until this flight, supersonic speeds were achieved primarily by artillery. There are two significant differences between this kind of waves and that of supersonic aircrafts. The first difference is that aircrafts have lift and so the wave field is not the simple axisymmetric pattern of projectiles and the second one is the flight altitudes, so it means atmospheric variations can not be anymore neglected. In the past decades, theory, flight test and experimental analysis have gone hand in hand to develop an understanding of how sonic boom is generated. By understanding this, scientists have been managed to develop prediction theories for sonic boom propagation and the corresponding reduction methods. In this introduction part, first of all the origin of sonic boom phenomenon will be discussed. Subsequently a short summary will be given of the famous *Whitham* sonic boom theory, its implementations and shortcomings. The idea of asymptotic characteristic of the sonic boom on which almost all of this thesis work is based will be the next topic in this part. Finally the goal and research question together with the outline for this theoretical report will be given.

1.1 The origin of the sonic boom

An airplane that flies at a certain altitude causes pressure wave disturbances which travel in all directions at the local speed of sound a. In figure 1.1 the aircraft is considered to be a point which moves with a velocity of $u \geq a$ from point A to B. The pressure disturbances caused by this aircraft can be observed as circular wave fronts. When the speed of the aircraft increases, these pressure waves will be compressed at the successive positions of the aircraft. This will result in formation of a so called Mach envelope around the aircraft, given by the straight line BC, which is tangent to the family of circles. All the sound is contained in the Mach envelope and so in fact the envelope is the location of the sonic boom [Kaour [2004]]. In a 2D perspective the Mach envelope looks like a wedge, see figure 1.1. The semi-angle of this Mach wedge is known as the Mach angle which has the following relationship with the Mach number:

$$\mu = sin^{-1}\left(\frac{1}{M}\right) \tag{1.1}$$

If the disturbances are stronger than a simple sound wave, then the wave front becomes stronger than a Mach wave, creating an oblique shock wave at an angle β to the free stream, where $\beta > \mu$. In other words, a Mach wave is an infinitely weak oblique shock wave. In a real 3D view the resulting waves seem to form a conical oval, called a Mach cone. The intersection of the Mach cone with the ground is called footprint of pressure disturbances. By knowing this, we can define sonic boom as the noise generated by these shock waves as observed in the footprint at the ground. The sonic boom is in fact a weak shock because the typical overpressure Δp at the ground is up to 100 Pa resulting in a shock strength of order 10^{-3} of the atmospheric pressure.

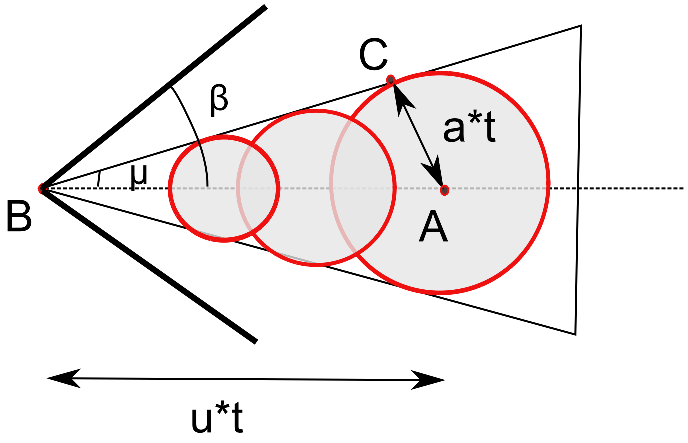

Figure 1.1: A wedge Mach envelope

1.2 The Whitham's theory

After the origin of sonic boom is known men tried to develop theories in order to predict the sonic boom propagation through the atmosphere and to minimize the sonic boom strength. The most applicable theory which is used even today from theoretical parts to wind tunnel tests and CFD approaches is the *Whitham's theory*. According to this theory, the wavefronts from the aircraft to the ground can be divided into three regions; near-field, mid-field and far-field flow, see figure 1.2. Figure 1.2 is a schematic of the coalescence of the near-field shock waves, that leads to a so called N-wave in the far-field. From this figure some important points of attention can be drawn:
The sonic boom defined by the *Whitham's theory* is characterized by a pressure disturbance in the footprint which has an initial quick pressure rise and furthermore a second instantaneous rise back to the local pressure. Between these two abrupt pressure increase there is also a linear decrease in the pressure to below local pressure. In fact, the observer

on the ground perceives the bow shock and the tail shock as consequences of two mentioned abrupt pressure jumps. It is now obvious that the amplitude and length of this sonic boom N-wave shape are related to the geometry of the airplane. The loudness of the booms which will be heard can be determined by the level of the pressure disturbance Δp. Furthermore, when the time between these two shocks is very short then the ground observer will hear only one boom [J.Plotkin [2001]]. As it was mentioned above figure 1.2 shows basically three different wavefronts and the corresponding signatures at three distances from the aircraft away. For an axisymmetric body as a well known airfoil there are generally two waves, the bow shock which is attached to the nose and the tail shock which is attached to the tail. But as we know an aircraft is not a smooth and axisymmetric body, so what happens in the near-field is that the shock wave pattern contains many shock waves, corresponding to the various compressions caused by the geometry of the aircraft. However, away from the aircraft the shock wave patterns will evolve because of nonlinear effects like atmospheric turbulence and air temperature gradients. In the far-field the shock wave patterns merge and form basically two main waves, the bow and tail shock wave [Ferri & Schwartz [n.d.]]. This procedure for determining the shock formation and computing the corresponding distortion was developed by *Whitham* and is known as the *Whitham's theory* for sonic boom. From previous studies [Curry [2008]],

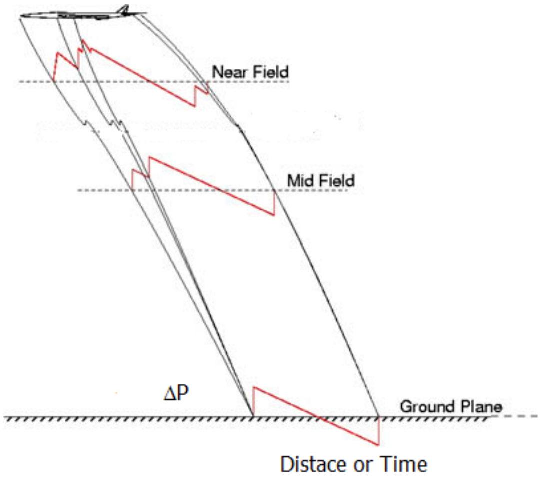

Figure 1.2: Pressure signature diagram—From [Nadarajah [2011]]

it can be concluded that there are many factors which have an influence on the sonic boom strength namely weight, size, and shape of the aircraft, furthermore there is the altitude, attitude and flight path, and weather or atmospheric conditions. A heavier aircraft causes a stronger sonic boom than a light aircraft because the former displaces more air and creates more lift. One of the most effective approaches to reduce the sonic boom intensity is altitude, because it determines distance along which the sonic boom travels before reaching the ground. The direction and strength of shock waves are influenced by wind, aircraft speed and direction, air temperature and pressure. In all these classical studies [Curry [2008]] on the sonic boom the point was reached that any improvement in the parameters that govern the efficiency of the aircraft's performance will result in a reduction of the aircraft's weight. This reduction in weight results in a reduction of the sonic boom as a consequence. Not only weight but also improvements in the (ratio) thrust to weight, the (ratio) lift to drag, the structural efficiency and the specific fuel consumption result in sonic boom minimization [Seebass & Argrow [1998]]. Going to this matter, minimization the sonic boom and obtaining better aerodynamic performance, is beyond the scope of this thesis.

In the following section a brief summary of theoretical part of the *Whitham's theory* will be given and furthermore its implementation and limitations will be discussed. The *Whitham's theory* is chosen to be explained in this thesis for it is an analytical prediction method on which almost all ongoing researches of today are based on it. In addition the *Whitham's theory* can be used to investigate the sonic boom characteristic caused by a simple 2D body with a certain thickness.

1.3 Fundamentals of Whitham's theory

As it was mentioned above, the standard sonic boom theory is based on *Whitham's theory* which describes the axisymmetric wave field caused by an axisymmetric projectile such a bullet. In fact the *Whitham's theory* is nothing more than a modification of the linear supersonic theory of a non-lifting, slender and axisymmetric pointed body. This theory predicts the location and strength of the shock waves emanating from the body. The issue of how the sonic boom can be computed for the mentioned body is tackled by using the linearized supersonic flow theory in combination with the supersonic area rule methods. The linear theory predicts the entire flow field using straight characteristic Mach lines emanating from a point on the body surface [G.B.Whiham [1952]]. As it can be observed from figure 1.2, the wavefronts are curved while linearized flow theory predicts straight characteristic lines, see figure 1.3. There are two reasons for this: First, the supersonic flow is inherently non-linear, while linearized flow theory is just an approximation that assumes weak waves propagate at acoustic velocity. This non-linearity in actual supersonic flow field can be explained by the fact that the amplitude of the waves depends on their corresponding velocities which again depend on the aircraft geometry and the axial location of the waves. Second, the atmosphere is non-uniform and the speed of sound generally decreases with increasing altitude. According to the *Whitham's theory* the near-field is considered to be a small region in which the pressure field directly depends on the geometry and the aerodynamics of the aircraft. It is of high importance to note that the atmospheric gradients do not play an important role in this region. In order to obtain the acoustic signature in the near-field the reference [K.J.Plotkin [1989]] considers a slender axisymmetric body in a uniform supersonic flow, see figure 1.3. Based on linearized supersonic flow theory the near-field overpressure Δp asserted by the *Whitham's theory* can be calculated by using the following two equations (1.2 and) (1.3):

$$\Delta p(x-\beta r, r) = p_0 \frac{\gamma M^2 F(x-\beta r)}{\sqrt{2\beta r}} \tag{1.2}$$

Where:

- Δp is the overpressure related to the cylindrical acoustical wave.

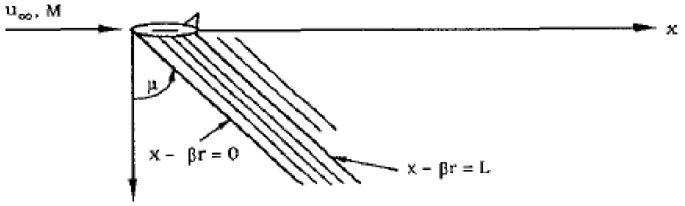

Figure 1.3: Linearized Flow Area Rule Theory—From [K.J.Plotkin [1989]]

- p_0 is the undisturbed ambient pressure.
- x is the axial coordinate (body fixed reference).
- r is the radius.
- γ is the ratio of specific heats.
- M is the Mach number.
- β is the Prandtl-Glauert factor.

$$F(x) = \frac{1}{2\pi} \int_0^x \frac{A''(\xi)}{\sqrt{x-\xi}} d\xi \tag{1.3}$$

In equation (1.3) A is the cross sectional area of the vehicle along cuts aligned with the Mach angle (i.e. cuts along the x-βr lines) shown in figure 1.3.
Equation (1.2) represents the cylindrical spreading of the acoustic disturbance in a uniform atmosphere and equation 1.3 is known as *Whitham*'s F-function that represents the acoustic source strength which is based on linearized supersonic flow area rule theory. The F-function has an implicit dependence on Mach number due to A being defined by Mach tangent cutting planes. These two equations refer to the near-field flow because the wave signature shapes change with distance due to non-linear effects [K.J.Plotkin [1989]][J.Plotkin [2001]] .
In fact, these two equations are derived for axisymmetric bodies in steady level flight. It should not be forgotten to say that figure 1.2 and these two equations are presented from an aerodynamic perspective, in body-fixed coordinates. Later on *Lomax* and *Walkden* showed that the axisymmetric body area rule could be generalized to asymmetric bodies [K.J.Plotkin [1989]]. The idea was motivated by lift generating bodies and validated by generalizing *A(x)* to an equivalent area $A_e(x,\varphi)$ which is a function of azimuthal angle φ about an axis through the body and defined by the flight direction. The equivalent area consists of two components: a volume component and a lift component. The volume component is calculated in the same way as for an axisymmetric body, except for that the cutting plane must be aligned with the azimuth, such that it is tangent to that azimuth on the corresponding Mach cone. The lift component for the equivalent area can

be calculated by:

$$A_L(x, \varphi) = \frac{\beta}{\rho u_\infty^2} \int_0^x L(x, \varphi) dx \tag{1.4}$$

Where $L(x,\varphi)$ is the component of lift per unit length in the φ direction, and ρ is the ambient density.

In order to analyze the sonic boom propagation in a real and non-uniform atmosphere it was needed to define a new approach to sound tracing. Therefore the *Whitham*'s sonic boom theory was shifted from an aerodynamic perspective to an acoustic perspective in which the reference frame was changed to atmosphere-fixed coordinates and the method of geometrical acoustics was applied. Figure 1.4 shows an equivalent sketch as it is given in figure 1.2, but in atmosphere-fixed coordinates. The aircraft is flying from left to right, and boom propagation and evolution is shown along rays. The rays are orthogonal to the wavefronts and represent the paths along which the acoustic disturbances propagate. In fact the rays represent the space which will be traced out by the boom while the waves represent the boom as it exists at a given instant [K.J.Plotkin [1989]]. In other words, although the wavefronts shown in figure 1.2 exist at a given time, each point on the wave was generated by the aircraft at some earlier time. And the rays indicate the trajectories the disturbance will follow as it propagates to the ground. A bundle of these rays is called a ray tube along which the acoustic energy is conserved, see equation (1.5).

$$P(\frac{S}{\rho_0 a_0})^{\frac{1}{2}} = \text{constant} \tag{1.5}$$

- P refers to the acoustic overpressure.
- ρ_0 and a_0 is the variable density and ambient sound speed.
- S is the ray tube area.

This equation shows the propagation of the geometric acoustic rays through the non-uniform atmosphere which at the same time shows the conservation energy along the rays. So, now we know in order to perform the geometrical acoustic ray tracing we need two inputs namely; the airplane trajectory and the structure of the atmosphere [K.J.Plotkin [1989]] [Seebass & Argrow [1998]][J.Plotkin [2001]]. Once the geometrical acoustic ray tracing is performed which is a major task in sonic boom computer programs it is now possible to obtain an analytic solution for the shock strength and duration of N-waves far from the vehicle. This is namely a far-field result which is valid at large distance where the local cross-flow effects are negligible and linear flow theory can be applied. The acoustic overpressure Δp in a ray-fixed coordinates can be written as follows [K.J.Plotkin [1989]]:

$$\Delta p = p - p_0 = p_0 * \frac{F(\tau)}{\sqrt{B}} \tag{1.6}$$

with:

- $\tau = t - \int_0^s ds/a_0$.
- t is time.
- s is the distance along a ray.

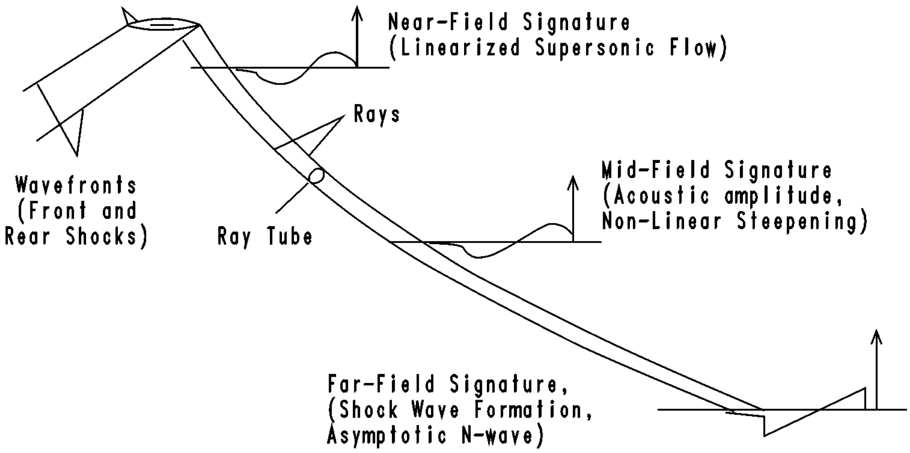

Figure 1.4: Comparison between wave (body-fixed) and ray (atmosphere-fixed) perspectives—[From K.J.Plotkin [1989]]

- a_0 is the undisturbed ambient sound speed.
- B is the amplitude expression based on the Blokhintzev invariant.

τ indicates an arbitrary point on the acoustic wave and t is its arrival time at location s. *Whitham* replaces a_0 by the term $a+u$ in the equation 1.6. The terms a and u are the perturbed sound speed and the velocity respectively. For an isentropic acoustic wave the propagation speed is the following:

$$a + u = a_0 \left(1 + \frac{\gamma + 1}{2\gamma} \frac{p - p_0}{p_0} \right) \tag{1.7}$$

Using this equation gives us the new definition for the arrival time t:

$$t = \tau + \int_0^s \frac{ds}{a_0} - \frac{\gamma + 1}{2\gamma a_h} F(\tau) \int_0^s \frac{ds}{\sqrt{B}} \tag{1.8}$$

The last term of this equation indicates the advance of each signature point and is proportional to its F-function value and a quadrature term, $\sqrt{B}$, which is independent of F. This quadrature term is part of the ray geometry solution and is called the age factor. This factor measures in fact how long the signal has undergone the distortion process [D.Hayes [1971]].

An example of development of an acoustic wave computed using equation 1.8 is shown in figures 1.5a to 1.5c,[K.J.Plotkin [1989]]. Figure 1.5a shows the overpressure Δp in the near-field, figure 1.5b indicates the effect of acoustic propagation where the amplitude changes but the shape remains unchanged. Figure 1.5c shows non-linear steepening proportional to the age parameter and the amplitude of each element of the original F-function. Parts of the aged signature showed in figure 1.5c are triple valued. This is physically not possible. It seems as at some earlier time the aging process would cause the signature slope to be vertical. It looks as a discontinuous pressure jump is taken place. The propagation of this pressure jump must be handled as a shock wave, rather than an isentropic wave. The speed of a weak shock of strength Δp can be calculated by the linearizing the *Rankine-Hugoniot* relations which is:

$$u_s = a_0 \left(1 + \frac{\gamma + 1}{4\gamma} \frac{\Delta p}{p_0} \right) \tag{1.9}$$

This speed is slower than the isentropic wave speed behind it, so this is the reason why the original signature is absorbed into the shock. In general the linearized shock speed is equal to the average of the isentropic wave speeds ahead of and behind it. This leads to the *area balancing* rule for fitting shocks. This process will be done as follows that first the steepend isentropic signature should be constructed , then the triple valued areas must be eliminated by fitting shocks such that total area is conserved. So, these three-valued regions in figure 1.5c are in fact the locations where the shock waves have been formed, and the shocks are fitted by an area balancing. This is shown in this figure by the equal shaded areas ahead of and behind shock. As we have observed the signature aging leads to an N-wave. Two characteristic elements for this type of wave are the shock overpressure Δp and the total duration t. If we now only concentrate on the positive portion of the N-wave, the corresponding overpressure can be obtained by determining the value of τ corresponding to the wave just behind the shock. The value of τ will increase with distance from the aircraft, as earlier phases of the wave are absorbed into the shock. From equation (1.8) the arrival time of the shock can be written in another form with denoting the value of τ as *T(s).*

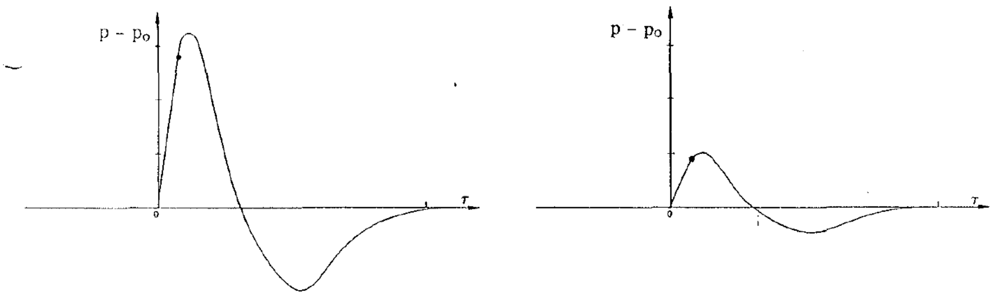

(a) Signature Near Aircraft (F-function Shape).

(b) Far Field, Acoustic Amplitude Change, Same Shape.

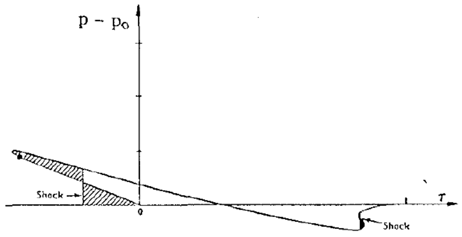

(c) Far-Field Steepened (Aged) Signature.

Figure 1.5: Evolution and Steepening of Sonic Boom Signatures—From [K.J.Plotkin [1989]]

$$t_{shock} = T(s) + \int_0^s \frac{ds}{a_0} - \frac{\gamma + 1}{2\gamma a_h} F(T(s)) \int_0^s \frac{ds}{\sqrt{B}} \tag{1.10}$$

Differentiating the equation (1.10) with respect to s gives us the expression $\frac{dt_{shock}}{ds}$ which is in fact the inverse of the shock speed u_{shock} given in equation (1.9). Combining these two equations results a differential equation for *T(s)*.

$$F(T(s)) = \left[2\int_0^{T(s)} F(\tau)d\tau\right]^{1/2} \left[\frac{\gamma+1}{2\gamma a_h}\int_0^s \frac{ds}{\sqrt{B}}\right]^{-1/2} \tag{1.11}$$

As we observe from this equation *T(s)* appears as a limit in one integral on the right hand side. It means at very large distances, most of the original *Whitham*'s F- function will be immersed in the shock. and *T(s)* will be sufficiently close to the first zero of F at τ_0 that the integral will asymptote $\int_0^{\tau_0} F(\tau)d\tau$. The final shock strength is the following expression:

$$\Delta p_{shock} \approx \frac{p_0}{\sqrt{B}} \left[2\int_0^{\tau_0} F(\tau)d(\tau)\right]^{\frac{1}{2}} \left[\frac{\gamma+1}{2\gamma a_h}\int_0^s \frac{ds}{\sqrt{B}}\right]^{\frac{-1}{2}} \tag{1.12}$$

The overpressure for different waves such as plane (B=constant), cylindrical ($B\propto$s) or spherical ($B\propto$s^2) waves in a uniform atmosphere can vary asymptotically as follows:

$$\Delta p_{shock} \propto \begin{cases} s^{-1/2} & \text{plane} \\ s^{-3/4} & \text{cylindrical} \\ s^{-1}(logs)^{-1/2} & \text{spherical} \end{cases} \tag{1.13}$$

1.3.1 The implementation and limitations of Whitham's theory

A complete implementation of standard sonic boom theory is very complex so that evaluation by a computer program is preferred. Up to now there are a couple of computer programs developed to implement the *Whitham's theory.* All these programs treat the F-function as an input and perform the ray tracing and signature aging calculation. The F-function input can be obtained from a separate linearized flow calculation which is achieved from wind tunnel or from computational schemes, [K.J.Plotkin [1989]]. Between the years 1969 and 1972 there were two computer programs developed from which both of them are used today or at least they have made the central part of all other programs up to our time, [J.Plotkin [2001]].
The first program was *ARAP* model made by Hayes [K.J.Plotkin [1989]] which considered all details from standard theory for a general maneuvering aircraft in a horizontal, non-uniform and windy atmosphere. The second program was developed by *Thomas* [K.J.Plotkin [1989]] which was made in a way that one could directly input Δp from wind tunnel tests. It is of high importance to note that each of these programs has its own capabilities and limitations.
The experimental research on sonic boom by NASA has lead to build models from flat plate and bodies of revolution to complex aircraft models at Mach numbers up to about 2. Wind tunnel tests have validated the pressure disturbances in the near-field and extrapolated these measurement data to the required distances by means of the ray tracing method. At Mach numbers above 2.0 the measured overpressure in the near-field is different from that calculated by the analytical method and so the provided results are not sufficiently reliable [K.J.Plotkin [1989]].
More recently, CFD methods have come to be regarded as an alternative to wind tunnel testing. These CFD schemes have been required to calculate the F-function in the near-field. But, obtaining a complete near-field signature from CFD requires a very large

spatial grid than ever have been used for aerodynamic design purposes. Men hopes with the increase of computational power in the future time the entire flow field of any aircraft can be computed even to very large distance [K.J.Plotkin [1989]][Kaour [2004]].

While the *Whitham's theory* is the most applicable theory for 3D flow, it can not be used yet for the purpose of finding an accurate relation between the geometry of the aircraft to the signature produced in the near-field. That is because the pressure disturbances produced in the near-field are strongly non-linear which are neglected by the theory. So, in order to take these non-linear effects into account scientists have recently developed higher order solutions of the governing differential equations by retaining higher order terms in the equations. But, these methods are not yet used sufficiently advanced to allow the use of such methods for the prediction of practical problems. And also these higher order approximation methods like the *Whitham's theory* can not be used at higher Mach numbers because their results are based on improved linearized theory [Ferri & Schwartz [n.d.]].
In addition, there are phenomena like hypersonic flight speeds, focused booms, shock wave rise times and atmospheric turbulence effects which are beyond the capabilities of the *Whitham's theory*. These phenomena will be described in short respectively below,[K.J.Plotkin [1989]][J.Plotkin [2001]][Kaour [2004]]:
As it mentioned above, the *Whitham's theory* neglects the non-linear effects in the near-field because they decrease rapidly moving away from the aircraft, so that in the far-field the linearized flow area rule theory can be applied. The *Whitham*'s prediction has been validated for slender bodies at moderate supersonic Mach numbers. It means the flow field for the hypersonic speed vehicle must be analyzed in one or other ways.
When an aircraft accelerates, turns or does other maneuvers, it seems that the shock waves focus which lead to the amplification of sonic boom intensity. When boom focusing occurs the observed overpressure at the ground is about 2 to 5 times larger than those in a typical N-wave. This phenomenon let the ray tube area vanish in some points so that the ray tracing method used by the *Whitham's theory* can not be applied anymore.
In addition the *Whitham's theory* does not take the structure of the shock waves into account and therefore uses the weak shock theory which in fact implies thin waves. But recently flight tests show that sonic boom shocks are substantially thicker than what has been expected.
Some questions regarding propagation through turbulence in the lower atmosphere, absorption and dispersion due to non-equilibrium and viscosity effects remain open. The effects of atmospheric turbulence are also beyond the capability of ray tracing method used by *Whitham's theory* because the *Whitham's theory* neglects the presence of turbulence in the atmosphere .

1.4 The asymptotic shock strength

As it can be noticed from above, there are a lot of studies from theoretical fields to wind tunnel tests and CFD approaches performed in order to minimize the sonic boom. But almost all of these methods have one common point which is using the basic sonic boom theory, *Whitham's theory*. Being precisely, all of these studies in one or other ways have validated the *Whitham's theory*. But, as it was mentioned in the previous section, there

are also deficiencies and unknown fields within the accepted sonic boom theory.
However, considering the basic sonic boom theory the central point of this thesis will be the studying of the asymptotic characteristic of the shock wave. From linearized supersonic flow theory it is known when an object with a finite length moves with a supersonic speed there will occur both shock waves as well as expansion waves. As it was already shown in figure 1.2 the expansion waves together with shock waves are the results of the body geometry. The expansion waves will intersect with the shock waves as they travel into the space and merge with the shock. The interaction between these two waves will result in weakening of the shock and causes its angle to approach the Mach angle. In fact, the asymptotic shock strength is an indication for the sonic boom produced by the body geometry which can be observed in a large distance. In other words, the shock wave has an asymptotic characteristic for which the strength goes to zero when the shock moves to the infinity. For this reason, the sonic boom strength can be studied asymptotically in terms of the shock strength. The asymptotic shock strength is not only dependent on the flight height but also on the Mach number. It is also worthy to note that the most desirable asymptotic shock strength is the one which is as low as possible. In order to have such a low strength we can change the behavior of the asymptotic shock by changing the body geometry in such a way that it goes faster to zero.
In *Whitham's theory* men also try to change the geometry in such a way that the lowest possible near-field overpressure arises. Subsequently, the near-field overpressure is extrapolated by the ray tracing method to the far-field on the ground and the known N-wave signature being obtained. This N-wave signature on the ground is the indicator for the sonic boom strength and does not have the same asymptotic behavior as we have for the asymptotic shock strength theory. In other words, although in *Whitham's theory* the results for the far-field are not a direct consequence of the body geometry but they represent the sonic boom strength observed on the ground. On the other hand, the results obtained on the basis of the asymptotic shock strength theory indicates the relation between the body geometry and its influence on the sonic boom strength.
This thesis is in fact a following work of *T. Francken* who has investigated into the *BASS*-measure which is derived by *prof.dr.ir.P.G Bakker*. *BASS* stands for *Bakker Asymptotic Shock Strength* and can be used as a measure for the asymptotic shock strength. *T.Francken* has tried in his thesis work to achieve an understanding of the influence of the shape of a 2D lift-generating object on the *BASS* magnitude. The *BASS*-measure in his work has been investigated coupled with requirements for the angle of attack and lift coefficient. For more information about his research work see [Francken [2009]].
In the current thesis, special attention will be drawn to focus on minimization of the asymptotic shock strength by finding a 2D optimum contour geometry which has a certain thickness. The influence of lift will be neglected for this thesis since the body is assumed being in a non-lift configuration. The main question in this thesis can be formulated as follows:

What is the most optimum 2D and non-lift generating contour with a certain thickness to have the minimum asymptotic shock strength for different Mach numbers?

1.4.1 Thesis outline

The supersonic flow which is considered to be 2D, steady and inviscid can be modeled with the *Euler* equations. Based on these equations, the characteristic equations can be derived. This basic theory will be discussed in chapter 2. Using the characteristic method and the *BASS* measure from [Francken [2009]] enables us to find an expression for the asymptotic shock strength for a 2D body with a certain thickness. These all will be discussed in chapter 3. The expression which is determined for the asymptotic shock strength will be analyzed as a variation problem in chapter 4. The solution to this variation problem leads to a very complex first order differential equation for which the characteristics will be discussed in chapter 5. In chapters 6 and 7 the attention will be drawn to the properties of the optimized contours which are obtained based on the variation problem. In chapter 8, the *Whitham's theory* will be applied to the achieved 2D optimal contours and the overpressure results based on this theory will be compared with results achieved by the asymptotic shock strength theory. The results of different parts will be evaluated in the last chapter and the research question will be answered. Moreover, there will be some recommendations formulated for further studies.

CHAPTER 2

STEADY 2D FLOW

In this chapter, the characteristic equations will be derived to describe a 2D, steady and inviscid supersonic flow. Subsequently, The development of the inviscid *Burgers equation* will be explained which is needed to define a simple wave flow domain. For a more in depth discussion of the fundamental theory used in this section the reader is referred to [P.G.Bakker & Leer [2005]].

2.1 Fundamental gasdynamics for 2D steady, inviscid, isentropic supersonic flow

The theory of characteristics evaluates the development of the shock wave in a supersonic flow which can be build up from the characteristic Mach lines. The characteristic equations can be defined by ordinary differential equations, the compatibility relations. A 2D, steady, inviscid supersonic flow in a *(x,y)* domain can be modeled by the *Euler* equations. These equations neglect the effects of viscosity, heat conduction and external forces. It is also assumed that the flow is adiabatic which means the total enthalpy is constant. Furthermore, the flow is assumed being steady and isentropic for which the entropy remains constant along a streamline [P.G.Bakker & Leer [2005]].

$$u\frac{\partial \rho}{\partial x} + v\frac{\partial \rho}{\partial y} + \rho\frac{\partial u}{\partial x} + \rho\frac{\partial v}{\partial y} = 0 \tag{2.1}$$

$$\rho u\frac{\partial u}{\partial x} + \rho v\frac{\partial u}{\partial y} + \frac{\partial p}{\partial x} = 0 \tag{2.2}$$

$$\rho u\frac{\partial v}{\partial x} + \rho v\frac{\partial v}{\partial y} + \frac{\partial p}{\partial y} = 0 \tag{2.3}$$

$$u\frac{\partial H}{\partial x} + v\frac{\partial H}{\partial y} = 0 \tag{2.4}$$

After expressing everything in entropy and total enthalpy instead of pressure and density the whole system of *Euler* equations can be summarized in the following form:

$$\mathbf{A}W_x + \mathbf{B}W_y = 0 \tag{2.5}$$

In this expression $\mathbf{A}$ and $\mathbf{B}$ are two Flux Jacobians in x and y directions respectively and W is a vector consisting of the following terms $W{=}(u,\ v,\ \mathrm{d}\bar{s}, H)^T$. In order to diagnolize the system stated by equation (2.5) we need to transform the variables using $dV{=}\mathbf{L}dW$ such that:

$$V_x + \Lambda V_y = 0 \tag{2.6}$$

Now, the eigenvalues of $\mathbf{A}^{-1}\mathbf{B}$ is needed to help us to find out the transformation. The eigenvalues are dimensionless and represent a direction.

$$\lambda_{1,4} = tan(\varphi \mp \mu) \tag{2.7}$$

$$\lambda_{2,3} = tan(\varphi) \tag{2.8}$$

The eigenvalue $\lambda_{2,3}$ is the local flow direction and the eigenvalue $\lambda_{1,4}$ indicate the two directions of steady acoustic waves or the characteristic directions of the supersonic flow and are referred to as Γ^- and Γ^+ respectively. To be sure the domain of influence is downstream of a certain point in the flow, the characteristics also must be directed downstream. From now on, there will be only worked on a flow aligned system, so the coordinate system will be changed from *(x,y)* to *(s,n)*. After writing the expression (2.5) in the new coordinate system aligned variables this equation becomes the following:

$$\tilde{\mathbf{A}}Z_s + \tilde{\mathbf{B}}Z_n \tag{2.9}$$

With the Flux Jacobian A and B in *(s,n)* domain:

$$\tilde{\mathbf{A}} = \begin{bmatrix} 1-M^2 & 0 & 0 & 0 \\ 0 & -q^2 & 0 & 0 \\ 0 & 0 & 1 & 0 \\ 0 & 0 & 0 & 1 \end{bmatrix} \tag{2.10}$$

$$\tilde{\mathbf{B}} = \begin{bmatrix} 0 & q & 0 & 0 \\ q & 0 & \frac{a^2}{\gamma(\gamma-1)} & -1 \\ 0 & 0 & 0 & 0 \\ 0 & 0 & 0 & 0 \end{bmatrix} \tag{2.11}$$

The eigenvalues of equation (2.9) are the following:

$$\lambda_{1,4} = \mp tan\mu \tag{2.12}$$

$$\lambda_{2,3} = 0 \tag{2.13}$$

Where μ is the Mach angle calculated by equation (1.1) and also knowing tan $\mu{=}\frac{1}{\sqrt{M^2-1}}$. These eigenvalues result in matrix L, which consists of the corresponding eigenvectors:

$$\begin{bmatrix} \sqrt{M^2-1} & q & \frac{q\sqrt{M^2-1}}{\gamma(\gamma-1)M^2} & -\frac{\sqrt{M^2-1}}{q} \\ 0 & 0 & 1 & 0 \\ 0 & 0 & 0 & 1 \\ -\sqrt{M^2-1} & q & -\frac{q\sqrt{M^2-1}}{\gamma(\gamma-1)M^2} & \frac{\sqrt{M^2-1}}{q} \end{bmatrix} \tag{2.14}$$

So, now the left row eigenvector method can be used to find out the new state quantities from:

$$dV = \mathbf{L}dZ \tag{2.15}$$

This results in the following expressions:

$$dV_1 = \sqrt{M^2-1}dq + qd\varphi + \frac{q\sqrt{M^2-1}}{\gamma(\gamma-1)M^2}d\bar{s} - \frac{\sqrt{M^2-1}}{q}dH \tag{2.16}$$

$$dV_2 = d\bar{s} \tag{2.17}$$

$$dV_3 = dH \tag{2.18}$$

$$dV_1 = -\sqrt{M^2-1}dq + qd\varphi - \frac{q\sqrt{M^2-1}}{\gamma(\gamma-1)M^2}d\bar{s} + \frac{\sqrt{M^2-1}}{q}dH \tag{2.19}$$

Now, the characteristic equations can be written in the following form:

$$\frac{\partial V_i}{\partial s} + \lambda_i \frac{\partial V_i}{\partial n} = 0 \tag{2.20}$$

Using the notion V^- instead of V_1 and V^+ instead of V_4 gives us:

$$\text{along } \Gamma^{\mp}, \text{with } \frac{dn}{ds} = \mp tan\mu \Rightarrow dV^{\mp} = 0 \tag{2.21}$$

$$\text{along } \Gamma^{0}, \text{with } \frac{dn}{ds} = 0 \Rightarrow dV_2 = dV_3 = 0 \tag{2.22}$$

The compatibility equations for an adiabatic non-isentropic flow can be obtained after rewriting of dV^- and dV^+ with variables q, φ, ρ and p:

$$dV^- = (d\varphi - \frac{\sqrt{M^2-1}}{\gamma M^2}\frac{dp}{p})q \tag{2.23}$$

$$dV^+ = (d\varphi + \frac{\sqrt{M^2-1}}{\gamma M^2}\frac{dp}{p})q \tag{2.24}$$

As it was assumed that flow is an isentropic flow i.e d$\bar{s}$=0 and dH=0, so, the compatibility equations can be formulated in an integral form and after a renormalization of the eigenvectors they will be:

$$dV^{\mp} = \frac{\sqrt{M^2-1}}{q}dq \pm d\varphi \tag{2.25}$$

The first part of the equation (2.25) is the differential form for the *Prandtl-Meyer* function $\nu(M)$:

$$d\nu = \frac{\sqrt{M^2-1}}{q}dq \tag{2.26}$$

So, the compatibility relations for isentropic flow are the following:

$$dV^{\mp} = d\nu \pm d\varphi \tag{2.27}$$

After integration, it can be concluded that the invariants for the isentropic flow $V^{\mp}$ are:

$$\text{along } \Gamma^{-}, \text{slope}: \frac{dy}{dx} = \upsilon^{-} = tan(\varphi - \mu) = tan(\theta^{-}) \Rightarrow V^{-} = \nu + \varphi \tag{2.28}$$

$$\text{along } \Gamma^{+}, \text{slope}: \frac{dy}{dx} = \upsilon^{+} = tan(\varphi + \mu) = tan(\theta^{+}) \Rightarrow V^{+} = \nu - \varphi \tag{2.29}$$

2.1.1 Simple Waves

Figure 2.1 shows the expansion fan due to a pressure decrease in a supersonic flow initially having a free flow Mach number M_0 in the undisturbed flow domain 0. The thick line in this figure depicts a wall which consists of an horizontal and a curved line. The undisturbed flow on the horizontal wall is deflected over a certain angle through the curved wall. In addition, the thin lines represent the straight characteristic Mach lines Γ^{+} and the dashed lines represent the curved characteristic Mach lines Γ^{-} which are originating from domain 0. So, due to the undisturbed flow domain there is one thing clear that along the curved Γ^{-} characteristic lines the corresponding compatibility equation remains constant, $V^{-} = \nu + \varphi$=constant. Furthermore in figure 2.1 the points A and B are two arbitrary points in the expansion wave. These two points are laying on two Γ^{-} characteristic lines but on the same Γ^{+} characteristic. This condition can be expressed as follows:

$$\text{along } \Gamma^{-}: \ \nu_B + \varphi_B = \nu_A + \varphi_A = \nu_\infty + \varphi_\infty = \text{constant} \tag{2.30}$$

$$\text{along } \Gamma^{+}: \ \nu_B - \varphi_B = \nu_A - \varphi_A \tag{2.31}$$

Equations (2.30) and (2.31) seem to be true only if:

$$\nu_B = \nu_A \ and \ \varphi_B = \varphi_A \tag{2.32}$$

From this we can conclude that along a certain Γ^{+} characteristic in the expansion wave both ν and φ are constant. This condition also makes the angle of the characteristic line θ being constant which implies that the Γ^{+} characteristics are straight lines in the expansion fan. Figure 2.1 represents in fact a very special case of the expansion wave in which one of the invariants (in this example V^{-}) is uniform. This type of expansion wave is called the simple wave which is governed by the characteristic equation conforming the equation (2.20):

$$\frac{\partial}{\partial x}(\nu - \varphi) + tan(\varphi + \mu)\frac{\partial}{\partial y}(\nu - \varphi) = 0 \tag{2.33}$$

This equation can be used to derive the inviscid *Burgers equation* for the simple waves in a 2D steady and inviscid supersonic flow, see equation (2.34).

$$\frac{\partial \upsilon}{\partial x} + \upsilon\frac{\partial \upsilon}{\partial y} = 0 \tag{2.34}$$

So, the *Burgers equation* is now expressed in the slope of the local characteristics, $\upsilon = tan(\varphi + \mu)$. For a full discussion of how this equation is derived the reader is referred to the document [P.G.Bakker & Leer [2005]].

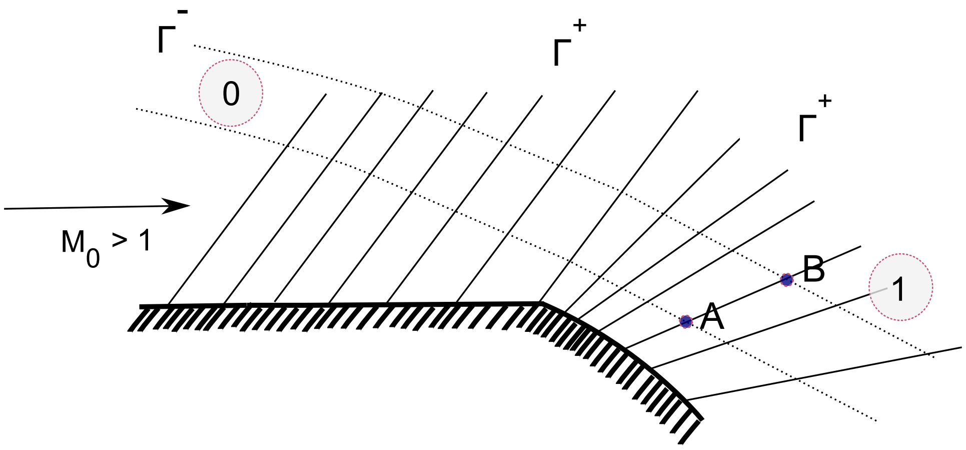

Figure 2.1: Simple wave flow in a supersonic flow field

CHAPTER 3

ASYMPTOTIC SHOCK STRENGTH

In the previous chapter the theory of characteristics was used to define a 2D steady and inviscid supersonic flow field. At the end of this chapter it was also shown how we can apply the characteristic equations and their compatibility relations to a simple wave flow. In the present chapter first a summary will be given for the *BASS* theory which is a measure of the asymptotic shock strength for an object having a very small thickness in a supersonic flow field. A full description of this theory can be found in [Francken [2009]]. Subsequently, the geometry of a 2D body with a certain thickness will be introduced for which the asymptotic shock strength will be determined in this report.

3.1 Bakker asymptotic shock strength (BASS)

According to theory of characteristics, in a compression flow field, the characteristic lines show a convergent trend. And when the characteristics tend to cross each other a shock wave will be formed. In order to model this shock wave we need to solve the *Burgers'* equation (2.34) explained in the previous chapter. The solution for the *Burgers'* equation is a non-rotational jump equation as follows:

$$\left(\frac{dy}{dx}\right)_{shock} = \frac{1}{2}(\upsilon_0 + \upsilon_1) \tag{3.1}$$

This equation represents the slope of a shock wave as the average of the slopes of the characteristic lines υ_0 and υ_1 merging into the shock. The practical problem with this equation is when the orientation is rotated the characteristic slopes will be changed w.r.t each other. So, in order to analyze the asymptotic shock strength later on in this report a rotational invariant jump equation is required as follows:

$$\left(\frac{dy}{dx}\right)_{shock} = tan\left(\frac{\theta_0 + \theta_1}{2}\right) \tag{3.2}$$

This equation shows that the angle of the shock path equals the bisector of the characteristic angles before and behind the shock. Using the trigonometric relations, this equation can be written in terms of υ as follows:

$$\left(\frac{dy}{dx}\right)_{shock} = \frac{\sqrt{1+\upsilon_0^2}\sqrt{1+\upsilon_1^2}+\upsilon_0\upsilon_1-1}{\upsilon_0+\upsilon_1} \tag{3.3}$$

Once the shock path can be modeled by the invariant jump equation (3.2), the strength of such a shock wave can be determined by the following expression:

$$\Sigma = tan\theta_1 - tan\theta_0 = \upsilon_1 - \upsilon_0 \tag{3.4}$$

As it was mentioned, θ_1 and θ_0 are the characteristic angles behind and before the shock wave respectively. This expression will be used throughout this thesis to measure the asymptotic strength of the shock.

An object which moves with a supersonic speed causes the occurrence of the shock wave as well as the expansion waves. The expansion waves interact with the shock wave as they move into the space. Due to this interaction, the shock strength will be decreased and eventually becomes zero when the distance goes to infinity. A measure for the decay of the shock strength to zero when the distance goes to infinity is described by an expression derived by P.G.Bakker and is referred to *BASS*. BASS stands for the Bakker asymptotic shock strength and represents the asymptotic decay behavior of the shock strength for a body with infinitesimally small thickness. A short description of the BASS theory is given below:

According to [P.G.Bakker & Leer [2005]] and [Francken [2009]] the error in the solution will be very small because for the weak shocks the pressure jump is of the order $(\Delta p)^3$. It means that the assumption the flow is isentropic for the Mach range $1.3 < M_0 < 3.5$ makes sense. The isentropic assumption for the weak shocks was in fact necessary to apply the simple wave theory.

In order to achieve the *BASS* measure we must project the characteristics onto the x-axis and this is only possible when we know the υ-distribution along the x-axis. Figure 3.1 illustrates the details of an object with geometry *y=f(x)* in a supersonic flow field with the assumptions which have been already mentioned. According to the simple wave theory all curved Γ^- characteristics originate from the undisturbed flow field and therefore the invariant of the isentropic flow V_0^- remains constant everywhere in the flow domain. The Γ^+ characteristics are straight lines and have a slope of $\upsilon = tan\theta = tan(\mu+\varphi)$. As it can be observed in figure 3.1, *P(x,y)* is an arbitrary point in the upper domain of the profile and the value υ for this point is the following:

$$\upsilon_P(x,y) = \frac{y-f(\zeta)}{x-\zeta} \tag{3.5}$$

Where ζ is the x-coordinate of point *Q(x,y)* which itself is the intersection point of the Γ^+ characteristic with the object surface. This equation indicates in fact the gradient of the line PQ which equals to υ_P. The task is now to express ζ as function of x and y. According to the simple wave theory we know already $\nu_P = \nu_Q$ and $\nu_Q + \varphi_Q = V_0^-$. This gives us ν_Q as follows:

$$\nu_Q = V_0^- - tan^{-1}(f^-(\zeta)) \tag{3.6}$$

In this equation $f^-(\zeta)$ is the gradient of the object in point Q which also indicates the flow direction. We can express υ as follows:

$$\upsilon = \left(\frac{dy}{dx}\right)_{\Gamma^+} = tan\theta = tan(\varphi+\mu) = \frac{tan\varphi + tan\mu}{1-tan\varphi tan\mu} \tag{3.7}$$

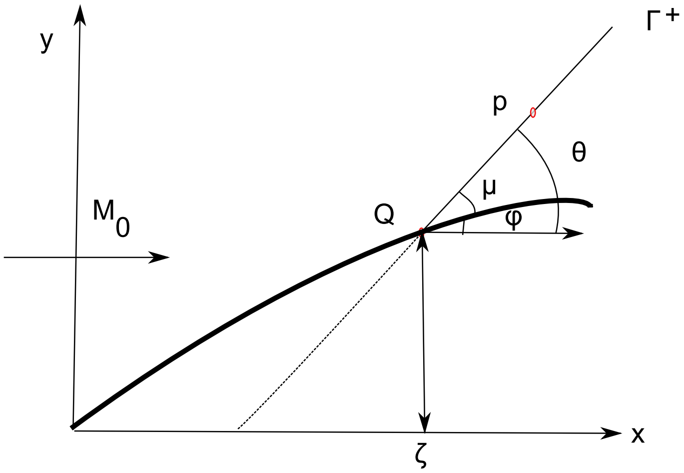

Figure 3.1: An object in a supersonic flow field

Using this equation and knowing the slope of characteristic Mach lines along the x-axis $tan\mu = \frac{1}{\beta}$ we can express the flow direction as follows:

$$tan\varphi = \frac{\beta\upsilon - 1}{\beta + \upsilon} \tag{3.8}$$

This equation shows the flow direction φ as a function of υ along the x-axis with the known *Prandtl-Glauert* factor β which can be defined as follows:

$$\beta = \sqrt{\frac{\gamma+1}{\gamma-1}}tan\left(\frac{\nu_0 + \pi/2 - \theta}{\sqrt{\frac{\gamma+1}{\gamma-1}}}\right) \tag{3.9}$$

With knowing the following expression for *Prandtl-Meyer* angle;

$$\nu = \sqrt{\frac{\gamma+1}{\gamma-1}}tan^{-1}\sqrt{\frac{\beta}{\sqrt{\frac{\gamma+1}{\gamma-1}}}} - tan^{-1}\beta \tag{3.10}$$

It is impossible to express υ in terms of x so we do other way around namely x=$x(\upsilon)$. This means we can express x coordinates as a function of the local flow direction x=*x(tanφ)*. So equation 3.8 becomes:

$$x = x\left(\frac{\beta\upsilon - 1}{\beta + \upsilon}\right) \tag{3.11}$$

This equation is called $F(\upsilon)$ function which indicates the x-coordinates in terms of υ along the surface. The x-coordinate of point Q can be defined with $\zeta = F(\upsilon_Q)$ which gives $\upsilon_Q = F^{-1}(\zeta)$. So, there are now two expressions for $\upsilon(x, y)$ at point Q as follows:

$$\upsilon(x, y) = \frac{y - f(\zeta)}{x - \zeta} \tag{3.12}$$

$$\upsilon(x, y) = F^{-1}(\zeta) \tag{3.13}$$

From these two expressions we are able to write ζ as a function of x and y, $\zeta = \zeta(x, y)$. This result together with equations (3.12) and (3.13) enable us to describe the location of $\upsilon(x, y)$ along the surface. For the analytical simplicity, the υ-distribution will be projected into the x-axis which means the characteristic lines will continue until they intersect the x-axis. This means that y-coordinate of point Q becomes zero for which the corresponding υ becomes:

$$\upsilon(x, y) = \frac{y}{x - \zeta} = F^{-1}(\zeta) \tag{3.14}$$

From this we know that $\zeta = x - \frac{y}{\upsilon}$ which results in $F(\upsilon) = x - \frac{y}{\upsilon}$. And this gives us the corresponding y-coordinates of the characteristic lines as follows:

$$y = \upsilon(x, y)\left[x - F(\upsilon(x, y))\right] \tag{3.15}$$

Once the υ-distribution is known along the surface, the next step to make the *BASS theory* complete is to define an expression for the shock path. Equations (3.3) and (3.15) together will result in a new form of the jump equation as follows:

$$\frac{dy}{dx} = \frac{d\upsilon}{dx}\left(x - F(\upsilon)\right) + \upsilon - \upsilon\frac{d\upsilon}{dx}F' \tag{3.16}$$

It should be noted that υ in this equation indicates υ_1. And the differential equation $\frac{d\upsilon}{dx}$ represents the υ-distribution along the shock wave. Integration of $\frac{d\upsilon}{dx}$ with the known boundary conditions at the leading edge x=$F(\upsilon_l)$=0 results in desired coordinates for the shock path as follows:

$$x = \Upsilon(\theta) = \frac{cos\theta}{1 - cos(\theta - \theta_0)}\int_{\theta_L}^{\theta}(sin\theta - sin\theta_0)d(F(\upsilon)) \tag{3.17}$$

$$y = tan\theta(\Upsilon(\theta) - F(tan\theta)) \tag{3.18}$$

The parameter x given in expression (3.17) represents the shock path location which can be determined by integration of the characteristics along the shock wave. For more details in derivation of theses parameters the reader is referred to [Francken [2009]]. As it was earlier explained, the asymptotic shock strength can be defined as a measure that the shock strength decays to zero when the shock wave goes to infinity. This definition is obviously to observe from equation (3.17) which shows when $\theta \to \theta_o$, the shock wave goes to an infinite distance from the object, $\Upsilon(\theta) \to \infty$.

Earlier it was mentioned the asymptotic shock strength can be determined by equation (3.4). And we know that substitution of equation (3.17) in (3.18) gives us the behavior of the shock strength when $y \to \infty$. So, in order to calculate the asymptotic shock strength we must express $\Sigma(y)$ explicitly. For this reason, firstly $\Upsilon(\theta)$ must be developed in terms of $(tan\theta - tan\theta_0)$ by using Taylor series expansions. Putting the new $\Upsilon(\theta)$ into eqation (3.18) gives us a new definition of the vertical path of the shock as follows:

$$y = \frac{\tilde{l_0}tan\theta_0 + O(\Sigma)}{\frac{1}{2}cos^4\theta_0\Sigma^2 + O(\Sigma^3)} \tag{3.19}$$

This result gives us the following expression for Σ.

$$\Sigma = tan\theta - tan\theta_0 = \sqrt{\frac{2\tilde{l_0}tan\theta_0}{cos^4\theta_0}}\frac{1}{\sqrt{y}} = k_l\frac{1}{\sqrt{y}} + \text{Higher Order Terms} \tag{3.20}$$

As it can be observed, the asymptotic shock strength will decay to zero with the factor k_l, where the simplified form of the dominant coefficient $\tilde{l_0}$ is the following:

$$\tilde{l_0} = cos\theta_0 \int_{\theta_0}^{\theta_l} F sin\theta d\theta \tag{3.21}$$

The influence of higher order terms is very small, therefore it is decided to neglect the effect of these higher order terms in the asymptotic shock strength Σ. It means the dominant term for the asymptotic shock strength when $y \rightarrow \infty$ becomes:

$$k_l = \sqrt{\frac{2sin\theta_0 A_l}{cos^4\theta_0}} \tag{3.22}$$

The term $\frac{\sqrt{2sin\theta_0}}{cos^2\theta_0}$ is constant and does not depend on body geometry. As it only gives the Mach number of the undisturbed flow, it is considered as the M_{factor}. We already know the characteristic angle of the undisturbed flow θ_0 is the sum of the undisturbed Mach angle and undisturbed flow angle θ_0=μ_0+φ_0. So, this help us to express M_{factor} only in free flow Mach number as follows:

$$M_{factor} = \frac{\sqrt{2} M_0^{\frac{3}{2}}}{M_0^2 - 1} \tag{3.23}$$

Thus, A_l can be addressed as the only measure for the asymptotic shock strength of the leading edge shock which depends on the shock wave-expansion interaction:

$$A_l = \int_0^{x_0} (cos\theta_0 - cos\theta) dx \tag{3.24}$$

According to the *BASS* theory this integral indicates the asymptotic shock strength for an object in a steady and inviscid supersonic flow. A_l is an integration of the cosθ-distribution along the body surface in a domain which is defined from 0 at the nose to x_0 at the shoulder point of the body where the θ_0 characteristic intersects. At the shoulder point a *Prandtl-Meyer* expansion wave will occur where the flow expands to the free flow condition. And x_0 is in fact the x-coordinate of the intersection of the Γ_0-characteristic through the shoulder point for which the slope is zero with the x-axis. So, in this way the x-coordinates which are involved in this integral are actually the x-locations of the projected characteristic lines onto the x-axis.

3.2 Application of the BASS theory to a 2D forebody

In [Francken [2009]] the *BASS theory* has been applied to lifting bodies namely: a flat plate, a plate with a kink, a multiple kinked plate, a smoothly curved plate and curved profile with thickness. But, in this thesis we will apply the *BASS* measure to a 2D body with a small thickness. Furthermore, the body is in a non-lift generating condition. This body has a (thickness/chord)-ratio of τ. And because the length of the span is assumed to be constant so we work only on a 2D contour, see figure 3.2 . The 2D forebody consists of two surface segments namely a convex surface with a declined slope and a horizontal

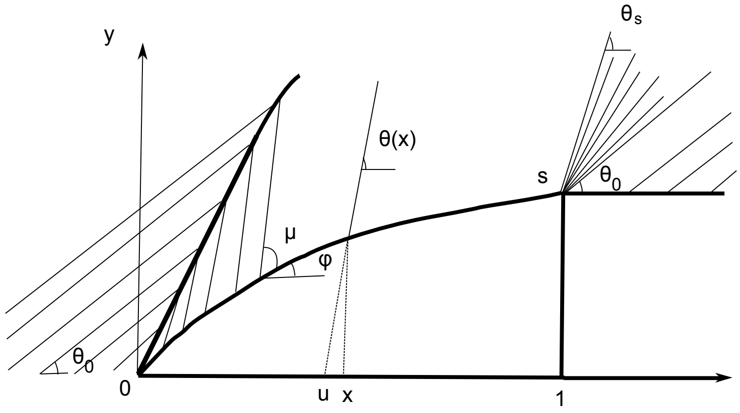

Figure 3.2: The distribution of characteristic lines along the contour surface

surface parallel to the undisturbed flow direction. This body with a zero angle of attack in figure 3.2 can be defined in a (x,y)-coordinate by the following expression:

$$y = \tau F(x) \text{ with } 0 \leq x \leq 1 \tag{3.25}$$

In combination with the following boundary conditions:

$$F(0) = 0 \text{ and } F(1) = 1 \tag{3.26}$$

If the length of the chord c, the span b are supposed to be 1 and the maximum thickness equals to τ, so it means that the contour shown in figure 3.2 will have a volume of y=τF. When this body moves with a supersonic speed a shock wave will be formed, starting at the leading edge. The shock is formed due to the sudden compression at the leading edge of the contour. This shock wave is called the leading edge shock and will be attached to the nose because it is assumed that body being pointed at the leading edge. In front of the shock the flow is uniform with the free flow Mach number M_0 in which the characteristic lines are parallel to each other. After this compression because the first surface segment of the body which is illustrated in figure 3.2 shows a slope decreasing from the nose to the shoulder point s, so we expect that the characteristic lines right after the nose will be expanded until the shoulder point. At the shoulder point, there occurs a *Prandtl-Meyer* expansion fan. This type of expansion wave is because the flow is deflected over a very small turning angle between the first and second wall. After the expansion fan the flow is back in its original condition. And since there is no surface deflection on the second surface part so the characteristic lines remain parallel to the undisturbed flow characteristics. In the previous section, it was shown that υ-distribution is known along the x-axis. So this makes the projection of the characteristics onto the x-axis possible. In order to express the characteristic angles θ corresponding to the forebody shown in figure 3.2 as a function of x first we write the local characteristic slope by using equation (3.7). Considering that flow at the surface is parallel to the both segments, so the flow direction is a function of x.

$$tan\varphi = \left(\frac{dy}{dx}\right)_{contour} = \tau F^{'}(x) \tag{3.27}$$

We know also the slope of the characteristic Mach lines which are also known along the x-axis by $\tan\mu = \frac{1}{\beta}$. So, now the expression for μ and equation (3.27) can be inserted into the equation (3.7) which gives us the following expression:

$$tan\theta = \frac{\beta\tau F^{'}(x) - 1}{\beta - \tau F^{'}(x)} \tag{3.28}$$

Equation (3.28) represents the characteristic angles θ as a function of x with the known *Prandtl-Glauert* factor β and *Prandtl-Meyer* angle μ which are given by equations (3.9) and (3.10) respectively. As it was mentioned above, since the local slope of the characteristics are known along the x-axis, so the projection of these characteristics onto the horizontal x-axis is possible. This projection is needed to visualize the integral (3.24) which gives a cosθ-distribution along the x-axis. And this projection can be done by simply letting the characteristics cross the upper surface without changing their θ's. As we have mentioned the first part of the body which is illustrated in figure 3.2 has a convex geometry. So, this requires the projection of the x-coordinates to a new horizontal line, the u-axis. This is needed to find the horizontal coordinates of the local characteristics. Figure 3.3 illustrates the location of one characteristic line which is zoomed in one point at the convex surface. Using this figure enables us to find a relation between the u- and x-coordinates with the characteristic angles. This relation is expressed in the following equation:

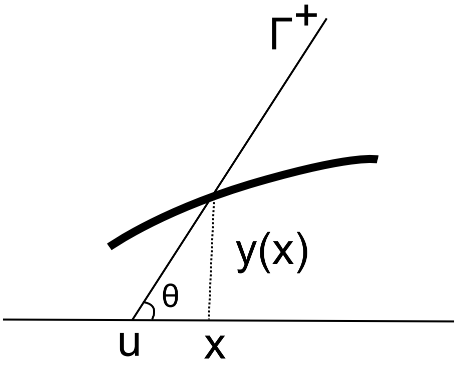

Figure 3.3: The relation between x and u-coordinates with θ

$$\upsilon = tan\theta = \frac{y(x)}{x-u} = \frac{\tau F(x)}{x-u} \rightarrow u = x - \frac{\tau F(x)}{tan\theta} \tag{3.29}$$

From theory we know already that the last characteristic of the expansion wave has the same angle as the undisturbed characteristic θ_0, and its first characteristic line is considered to have an angle of θ_s. This makes the point s very important because both of these characteristics originate here at this point, see upper figure 3.4. As it can be observed from figure 3.4 these two characteristics are extrapolated to the horizontal x-axis. By using equation (3.29) the intersection points of these two characteristics with the x-axis can be again projected into the horizontal u-axis, see figure 3.4 below. This will result in cos θ-graph which in fact is constructed by projecting the Γ^+ characteristics on the horizontal line through the shoulder point. In other words, the area indicated by the red line achieved in this figure shows the cos θ-distribution of the characteristics along the contour surface and its area represents the asymptotic shock strength for the body. The red area of the cos θ-graph in figure 3.4 which is a sum of the area I and II represents the asymptotic shock strength for the body. This area is called the shock strength area

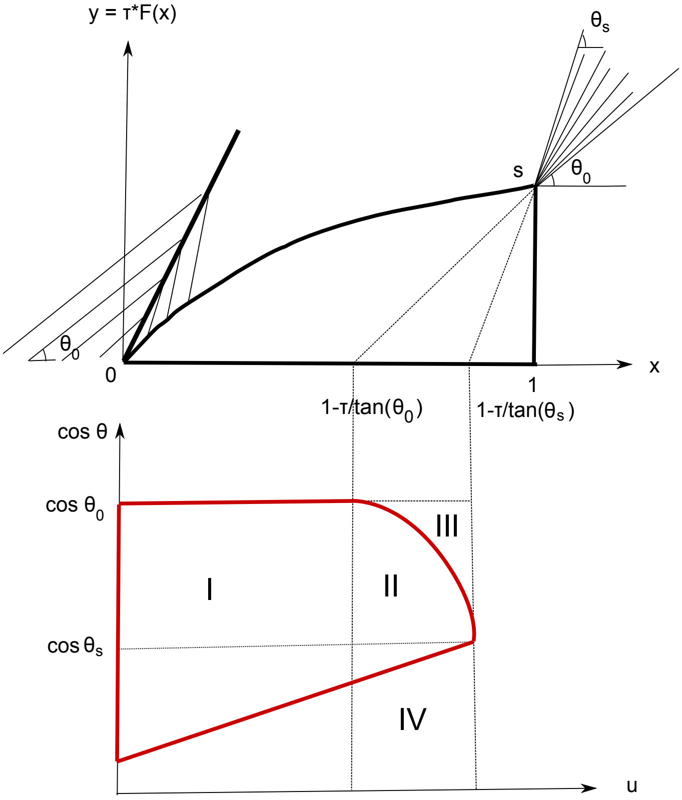

Figure 3.4: A 2D body in supersonic flow with the corresponding cos $\theta-$ graph

and can be determined in the following way:

$$A_l = I + II = I + II + III - III = I + II + III - (III + II + IV) + II + IV \quad (3.30)$$

As we can observe from figure 3.4, the sum of the area's *I+II+III* is equal to the integral A_l given in (3.24). This integral is defined in a range of $[0,u_s]$, see below:

$$I + II + III = \int_0^{1-\tau/tan\theta_s} (cos\theta_0 - cos\theta)du \quad (3.31)$$

The sum of the area's *II+III+IV* is give as follows:

$$II + III + IV = \tau cos\theta_0 \left(\frac{1}{tan\theta_0} - \frac{1}{tan\theta_s} \right) \quad (3.32)$$

Due to the fact that we have two values for the cosθ at the shoulder point, so we will get a curved line in the cos θ-graph for this region. The area *II+IV* equals to the area under this curved path.

$$II + IV = \tau \left(\frac{1}{sin\theta_0} - \frac{1}{sin\theta_s} \right) \quad (3.33)$$

Inserting all these expressions into the equation (3.30) gives us the following:

$$A_l = \int_0^{1-\tau/tan\theta_s} (cos\theta_0 - cos\theta)du - \tau cos\theta_0 \left(\frac{1}{tan\theta_0} - \frac{1}{tan\theta_s} \right) + \tau \left(\frac{1}{sin\theta_0} - \frac{1}{sin\theta_s} \right) \quad (3.34)$$

After simplifying we obtain the required equation for the asymptotic shock strength of the mentioned body:

$$A_l = \int_0^{1-\tau/tan\theta_s} (cos\theta_0 - cos\theta)du + \tau \left(sin\theta_0 - \frac{1 - cos\theta_0 cos\theta_s}{sin\theta_s} \right) \tag{3.35}$$

Considering the following abbreviations:
c=cos θ , s=sin θ , c_0=cos θ_0 , c_s=cos θ_s , s_0=sin θ_0 , s_s=sin θ_s
So, we can write equation (3.35) in a simple way.

$$A_l = \int_0^{1-\tau/tan\theta_s} (c_0 - c)du + \tau \left(s_0 - \frac{1 - c_0 c_s}{s_s} \right) \tag{3.36}$$

Using equation (3.22) gives us the general integral for the asymptotic shock strength for a 2D body with a maximum thickness τ shown in figure 3.4 as follows:

$$k_l = \sqrt{\frac{2sin\theta_0}{cos^4\theta_0} * \int_0^{1-\tau/tan\theta_s} (cos\theta_0 - cos\theta)du + \tau \left(sin\theta_0 - \frac{1 - cos\theta_0 cos\theta_s}{sin\theta_s} \right)} \tag{3.37}$$

CHAPTER 4

OPTIMIZATION PROBLEM

In the previous chapter the *BASS* theory was applied to a 2D body with a defined thickness in a non-lift generating condition, see figure 3.4. This application resulted in the expression (3.36) which indicates a measure for the asymptotic shock strength and depends on the body geometry and Mach number M_0. In this chapter we try to find an optimized contour function by using equation (3.36).

4.1 Variation problem

The goal of optimization is to find an optimized contour function $F(x)$ with the corresponding boundary conditions $F(0)$=0 and $F(1)$=1 in such a way that the solution for the expression (3.36) becomes an extreme. In order to achieve this goal first we write equation (3.36) by using the short notations in the following way:

$$A_l = \int_0^{1-\tau/tan\theta_s} (c_0 - c)du + \tau \left(\frac{s_0^2}{s_0} - \frac{1 - c_0 c_s}{s_s} \right) \tag{4.1}$$

For this integral there are many constraints possible to be involved such as area, a certain geometry shape, volume, etc. But as we are concerned in this thesis with the optimization problem for a 2D body with a certain thickness, so the volume can be chosen as constraint. As it is assumed that the span- and chord-length equal to 1 and the (thickness/chord)-ratio is τ so the volume constraint can be expressed as follows:

$$K = \int_0^1 F(x)dx = \frac{V}{\tau} \tag{4.2}$$

This expression shows that the optimized contours have a volume V which must be smaller than τ. But before the optimization analysis, there are two points which must be taken into account:

- The angle of the characteristic line at the shoulder point θ_s varies with the body geometry. It means the upper boundary of the integral A_l is not a known value.

For this reason, this boundary must be considered as a part of the optimization problem.

- The independent variables in expressions A_l and K are not synchronized because A_l is defined in a (u-cos θ)-coordinate system with a limit of $[0,u_s]$ while K represents the volume of the body which is defined in the (x,y)-coordinate system with a range of [0,1].

In order to operate the expressions A_l and K simultaneously we need to synchronize A_l and K. For this reason, these two parameters must be defined in a similar coordinate system with the same limit. So, the first step for doing synchronization is to transform the integral (4.1) which is defined in a u-axis to the x-domain. As it was also mentioned before the characteristics are projected into the x-axis and then to the second horizontal axis u in cos (θ)-graph. It means that the characteristics are also a function of x, see equation (3.29). So, the integral (4.1) can be written in the x-domain as follows:

$$I = \int_0^{u_s = 1 - \tau / tan\theta_s} (c_0 - c)\frac{du}{dx}dx \tag{4.3}$$

The differentiating of equation (3.29) gives us:

$$\frac{du}{dx} = 1 - \frac{\tau F^{'}(x)}{tan\theta} + \frac{\tau F(x)}{sin^2\theta}\frac{d\theta}{dx} \tag{4.4}$$

In order to find $\frac{d\theta}{dx}$ we need to differentiate equation (3.28) w.r.t. x which results in the following:

$$\left\{\frac{d\beta}{d\theta}tan\theta + \beta(1 + tan^2\theta))\right\}\frac{d\theta}{dx} = \tau F^{''}(\beta + tan\theta) + \tau F^{'}\left(\frac{d\beta}{d\theta} + 1 + tan^2\theta\right)\frac{d\theta}{dx} \tag{4.5}$$

Since $\frac{d\beta}{d\theta}$ is unknown in this expression, so we can determine it just by differentiating equation (3.9) w.r.t. θ:

$$\frac{d\beta}{d\theta} = -\left(1 + \frac{\beta^2}{6}\right) \tag{4.6}$$

Inserting this result into equation (4.5) gives us the following:

$$\frac{d\theta}{dx} = \frac{\tau F^{''}(\beta + tan\theta)}{N} \tag{4.7}$$

The term N in this expression is a short notation for the following expression:

$$N = \beta(1 + tan^2\theta) - \left(1 + \frac{\beta^2}{6}\right)tan\theta + \tau F^{'}\left(\frac{\beta^2}{6} - tan^2\theta\right) \tag{4.8}$$

With all these known terms, the integral (4.1) is now transformed to the x-domain. So the optimization problem with the corresponding constraint (4.2) becomes the following:

$$A_l = \int_0^1 (c_0 - c)\left\{1 - \frac{\tau F^{'}(x)}{tan\theta} + \frac{\tau^2 F(x)}{sin^2\theta}F^{''}\frac{(\beta + tan\theta)}{N(F^{'})}\right\}dx + \tau\left(s_0 - \frac{1 - c_0 c_s}{s_s}\right) \tag{4.9}$$

In order to bring the second term inside the integral of A_l we need to write it in the following way:

$$\tau\left(s_0-\frac{1-c_sc_0}{s_s}\right)=\tau\int_0^1\left\{s_0-\frac{d}{dx}\left(\frac{x}{sin\theta}\right)+\frac{d}{dx}\left(\frac{c_0x}{tan\theta}\right)\right\}dx \tag{4.10}$$

By solving the following differential equations we obtain a new formulation of the second term for the integral A_l.

$$\frac{d}{dx}\frac{x}{sin\theta}=\frac{1}{sin\theta}-\frac{xcos\theta}{sin^2\theta}\frac{d\theta}{dx}=\frac{1}{sin\theta}-\frac{xcos\theta}{sin^2\theta}\frac{\tau F^{''}(\beta+tan\theta)}{N(F^{'})} \tag{4.11}$$

$$\frac{d}{dx}\frac{c_0x}{tan\theta}=\frac{c_0}{tan\theta}-\frac{c_0x}{sin^2\theta}\frac{d\theta}{dx}=\frac{c_0}{tan\theta}-\frac{c_0x}{sin^2\theta}\frac{\tau F^{''}(\beta+tan\theta)}{N(F^{'})} \tag{4.12}$$

Inserting these terms in equation (4.10) results in the following:

$$\tau\left(s_0-\frac{1-c_sc_0}{s_s}\right)=\tau\int_0^1\left\{s_0-\frac{1}{s}+\frac{cc_0}{s}+\frac{x}{s^2}\frac{\tau F^{''}}{N(F^{'})}(\beta+tan\theta)(c-c_0)\right\}dx \tag{4.13}$$

Putting this into the integral (4.9) gives us the following expression:

$$A_l=\int_0^1\left\{(c_0-c)\left(1-\frac{\tau(F^{'})}{tan\theta}+\frac{\tau^2FF^{''}}{sin^2\theta}\frac{(\beta+tan\theta)}{N(F^{'})}-\frac{x}{s^2}\frac{\tau^2F^{''}}{N(F^{'})}(\beta+tan\theta)\right)+\tau(s_0-\frac{1}{s}+\frac{cc_0}{s})\right\}dx \tag{4.14}$$

As it can be observed, this integral contains the unknown functions, F, $F^{'}(x)$, $F^{''}(x)$ and x. In order to solve this integral we must formulate it as a variation problem which does not depend explicitly on x. This can be done by removing x in this integral. So, in order to get rid of x we define a new function namely G=F-x. So, it means consequently $F^{'}$=$G^{'}$+1 and $F^{''}$=$G^{''}$. The new function G gives a new expression for the integral (4.14) as follows:

$$A_l=\int_0^1\left\{(c_0-c)\left(1-\frac{\tau(G^{'}+1)}{tan\theta}+\frac{\tau^2GG^{''}}{sin^2\theta}\frac{(\beta+tan\theta)}{N(G^{'})}\right)+\tau(s_0-\frac{1}{s}+\frac{cc_0}{s})\right\}dx \tag{4.15}$$

And the constraint (4.2) also can be expressed in terms of G:

$$K_G=\int_0^1 G(x)dx=\frac{S}{\tau}-\frac{1}{2}=S_G \tag{4.16}$$

In order to find the extreme value for the integral (4.15) we just need to determine the function *G(x)* in such a way that A_l becomes an extreme and it also conforms the constraint (4.16). The integral (4.15) can be defined as a variation problem as follows:

$$A_l=\int_0^1 F(G,G^{'},G^{''})dx:\ \text{The extreme function} \tag{4.17}$$

Where F is a given function:

$$F=F_0(G^{'})+F_1(G^{'})GG^{''} \tag{4.18}$$

And G is a function of x with the corresponding boundary condition *G(0)=G(1)=*0, see below:

$$F_0(G^{'}) = (c_0 - c)\left\{1 - \tau\frac{(G^{'}+1)}{tan\theta} + \tau(s_0 - \frac{1}{s} + \frac{cc_0}{s})\right\} \tag{4.19}$$

$$F_1(G^{'}) = (c_0 - c)\frac{\tau^2}{sin^2\theta}\frac{(\beta + tan\theta)}{N(G')} \tag{4.20}$$

Furthermore, the corresponding constraint also can be defined as a variation problem as follows:

$$K_G = \int_0^1 u(G)dx = S_G : \text{ The related condition} \tag{4.21}$$

Since u is just a function of G, therefore u can be considered as G. As we already know when F does not depend explicitly on x, for the first order *Euler* differential equation $F_G - \frac{d}{dx}F_{G'}$=0 there exists the first integral $F - G^{'}F_{G'}$=constant. This result stimulates us to investigate whether for the second order *Euler* differential equation the first integral exists or not. In order to incorporate the condition 4.21 in this variation problem we add λu to the function F in (4.18). This results in the second order *Euler* equation:

$$(F + \lambda u)_G - \frac{d}{dx}(F + \lambda u)_{G'} + \frac{d^2}{dx^2}(F + \lambda u)_{G''} = 0 \tag{4.22}$$

We can write equation (4.22) as follows:

$$(F + \lambda u)_G - \frac{d}{dx}\left((F + \lambda u)_{G'} + \frac{d}{dx}(F + \lambda u)_{G''}\right) = 0 \tag{4.23}$$

And in order to prove that $(F + \lambda u) - G^{'}(F + \lambda u)_{G'} + G^{'}\frac{d(F+\lambda u)_{G''}}{dx}$=constant is the first integral for the second order case we should differentiate it as follows:

$$\begin{aligned}\frac{d}{dx}\left((F + \lambda u) - p(F + \lambda u)_p + p\frac{d(F + \lambda u)_q}{dx}\right) &= \frac{d(F + \lambda u)}{dx} - \frac{dp}{dx}(F + \lambda u)_p - p\frac{d(F + \lambda u)_p}{dx} \\ &\quad + \frac{dp}{dx}\frac{d(F + \lambda u)_q}{dx} + p\frac{d^2(F + \lambda u)_q}{dx^2}\end{aligned} \tag{4.24}$$

With notations p=$G^{'}$ and q=$G^{''}$. The first term can be written as follows:

$$\frac{d(F + \lambda u)}{dx} = (F + \lambda u)_x + p(F + \lambda u)_G + q(F + \lambda u)_p + \frac{dq}{dx}(F + \lambda u)_q \tag{4.25}$$

Since the term $(F + \lambda u)$ does not depend explicitly on x, so it means that $(F + \lambda u)_x$=0. Now, inserting the result for $\frac{d(F+\lambda u)}{dx}$ into the relation (4.24) gives us the following:

$$\begin{aligned}\frac{d}{dx}\left((F + \lambda u) - p(F + \lambda u)_p + p\frac{d(F + \lambda u)_q}{dx}\right) &= p(F + \lambda u)_G - p\frac{d(F + \lambda u)_p}{dx} + p\frac{d^2(F + \lambda u)_q}{dx^2} \\ &\quad + \frac{dq}{dx}(F + \lambda u)_q + q\frac{d(F + \lambda u)_q}{dx}\end{aligned} \tag{4.26}$$

The first three terms together in this equation equals to zero according to (4.22). So, now there remain only the following:

$$\begin{aligned}\frac{d}{dx}\left((F+\lambda u)-p(F+\lambda u)_p+p\frac{d(F+\lambda u)_q}{dx}\right) &= \frac{dq}{dx}(F+\lambda u)_q+q\frac{d(F+\lambda u)_q}{dx}\\ &= \frac{d}{dx}q(F+\lambda u)_q \qquad (4.27)\end{aligned}$$

Or:

$$\frac{d}{dx}\left((F+\lambda u)-p(F+\lambda u)_p-q(F+\lambda u)_q+p\frac{d(F+\lambda u)_q}{dx}\right)=0 \qquad (4.28)$$

The result for differential equation (4.24) which is the first integral for the *Euler* equation (4.22) becomes the following.

$$F+\lambda u-p(F+\lambda u)_p-q(F+\lambda u)_q+p\frac{d}{dx}(F+\lambda u)_q=\text{constant} \qquad (4.29)$$

So it means that relation $F+\lambda u$=$F_0(p)+F_1(p)GG^{''}+\lambda G$ is not an explicit function of x. Finding the terms $(F+\lambda u)_p$, $(F+\lambda u)_q$ and $\frac{d}{dx}(F+\lambda u)_q$ and inserting them into the first integral (4.29) gives us the following *H(p)*-function:

$$H(p)=F_0(p)+\lambda G-pF_0^{'}(p)+p^2F_1(p)=\text{constant} \qquad (4.30)$$

We can rewrite equation (4.19) and determine its derivative as follows:

$$F_0(p)=c_0-c-\tau p(c_0-c)\frac{c}{s}+\tau(s_0-s) \qquad (4.31)$$

$$F_0^{'}(p)=-\tau(c_0-c)\frac{c}{s}+\frac{d\theta}{dp}\left\{s-\tau c+\tau p\left(\frac{c_0-c}{s^2}-c\right)\right\} \qquad (4.32)$$

Inserting these results and F_1 given in (4.20) into (4.30) gives us the *H(p)*-function which is a first order nonlinear differential equation with dependent variable G, see equation (4.33). This is a first order differential equation because the unknown function G is a first order derivative w.r.t the independent variable x, with the known p=$\frac{dG}{dx}$. In addition, *H(p)* is a nonlinear function because the derivative of the unknown function G appears to the power 2, see the term p^2 in equation (4.33). There are two constant parameters M_0 and τ which can be used as initial values for the *H(p)*-function. And furthermore, this function depends on a given variable θ-range.

$$H(p)=c_0-c+\tau(s_0-s)-\frac{d\theta}{dp}\left\{ps-\tau pc-\tau p^2c\right\}=c_{cst}-\lambda G \qquad (4.33)$$

With:

$$\frac{d\theta}{dp}=\frac{\tau(\beta+\frac{s}{c})}{N} \qquad (4.34)$$

From equation (4.33) we know that *H(p)*-function equals to the expression $c_{cst}-\lambda G$. In order to solve the *H(p)*-function for G we need to determine two constants, c_{cst} and λ. And the only way to approach these two constants is solving them numerically which will be explained in the next chapters.

CHAPTER 5

THE CHARACTERISTICS OF *H(P)*-FUNCTION

In chapters 3 it was shown that a 2D contour causes a combination of shock and expansion waves, the intersection of these waves leads to the shock strength which can be determined by equation (3.36). This strength can be visualized by projecting the characteristics into the x-axis. This projection creates a cos θ-distribution of the characteristics along the x-axis. Computing this cos θ-distribution and including Mach number into equation (3.36) gives us a measure for the asymptotic shock strength, see equation (3.37). What we could think of is to design a 2D contour which causes the lowest possible shock strength. In order to find such a optimum contour we needed to optimize the integral (4.1), see section 4.1. The optimization process required for this integral with the corresponding constraint have been formulated as a variation problem, see equation (4.17). Furthermore, it was shown that this problem does not depend explicitly on x which means that we can find the function G in such a way that the variation problem (4.17) gets an extreme value. This all resulted in a new differential equation (4.33) that depends on two constants τ and M_0. In this chapter we will analyze further this equation and investigate its characteristics that define the optimize contours.

5.1 Influence of M_0

In the last chapter, we have developed a general formulation for the asymptotic shock strength for a 2D body with a (thickness/chord)-ratio of τ. Using a variational approach it is possible now to obtain the optimum contours in terms of the asymptotic shock strength. But first of all the characteristics of differential equation (4.33) needs more investigation. The *H(p)*-function with the corresponding terms (4.31), (4.32) and (4.20) can be defined as follows:

$$H(p) = c - \lambda G = F_0(p) - pF_0^{'}(p) + p^2 F_1(p) \tag{5.1}$$

This function can be analyzed as a variable of p which itself can be determined from $F{=}G{+}x$ and the expression for β given by (3.28), see the following:

$$p = \left(\frac{\beta tan\theta - 1}{\tau\left(\beta + tan\theta\right)} \right) - 1. \tag{5.2}$$

Because M_0 and τ are two initial inputs in this function so it means that p is only a function of one unknown variable which is the angle of the characteristics, θ's. By knowing $\beta_0 = \sqrt{M_0^2 - 1}$ we can use equation (3.10) to find the *Prandtl-Meyer* function for the undisturbed flow ν_0 which subsequently determines the value of β for the characteristics behind the shock by using equation (3.9). For the flow direction in the undisturbed flow field is zero φ_0=0, therefore the angle of the characteristics in this region equals to the Mach angle of these characteristics, $\theta_0 = \mu_0$. And μ_0 can be determined by the known relation (1.1). From this we can conclude that terms (4.31), (4.32) and (4.20) are also a function of the only unknown θ's. Figure 5.1 illustrates the (H-p)-curves for τ=0.10 and a range of free flow Mach number $1.5 \leq M_0 \leq 3$. In other words, every curve is achieved at a certain Mach number. The curve at the most right side is obtained at M_0=1.5 while the curve at the most left side indicates the one achieved at M_0=3.0. It means with increasing the Mach number, the (H-p)-curves move from right to the left. The red curve indicates the (H-p)-curve at M_0=2.0. Furthermore, the blue marker symbols represent the (H,p)-values that are achieved for the undisturbed characteristic angles θ_0's. All these points are on the horizontal line p=-1. This is because as it was mentioned above, the flow direction in the undisturbed flow field is zero φ_0=0 and knowing also the relation F=G+x will result in p=-1. Further, the green marker symbols represent the extreme H-values for different curves when p=0. It shows that gradient of the curves at these points (i.e. the tip of the nose) becomes zero, $\frac{dH}{dp}$=0. So, in order to determine these

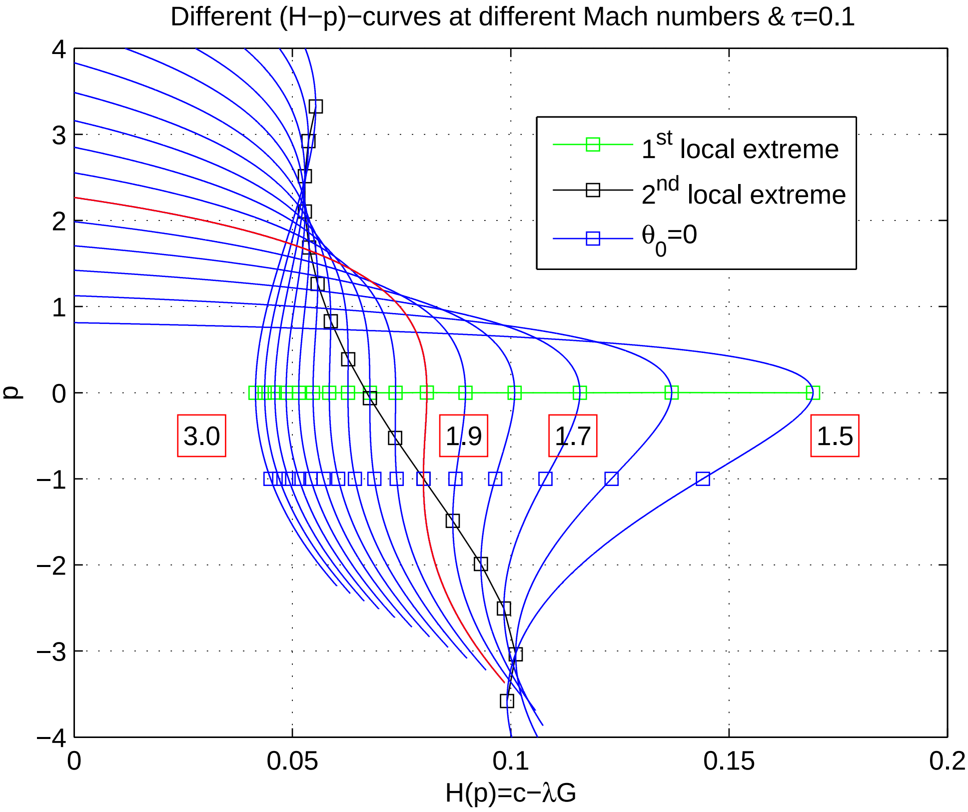

Figure 5.1: (H-p)-plots for $\tau = 0.10$ and $1.5 \leq M_0 \leq 3$

extreme points we need to differentiate expression 5.1 w.r.t p as follows:

$$\frac{dH}{dp} = -F_0^{''} + 2F_1 + pF_1^{'} = 0 \text{ with the condition } p = 0 \tag{5.3}$$

Differentiating $F_0^{'}$ from (4.31) gives us:

$$\begin{aligned} F_0^{''}(p) \quad &= \quad 2\left(-\tau c + \tau\frac{(c_0 - c)}{s^2}\right)\frac{d\theta}{dp} + \\ & (c + \tau s)\left(\frac{d\theta}{dp}\right)^2 + (s - \tau s)\left(\frac{d^2\theta}{dp^2}\right) + \\ & \tau p\left\{s - \frac{2c(c_0 - c)}{s^3} + \frac{1}{s}\right\}\left(\frac{d\theta}{dp}\right)^2 + \\ & \tau p\left\{\frac{c_0 - c}{s^2} - c\right\}\left(\frac{d^2\theta}{dp^2}\right) \end{aligned} \tag{5.4}$$

And also doing differentiating for equation (4.20) results in the folowing:

$$F_1^{'} = \tau\left\{\frac{1}{s}\left(\frac{d\theta}{dp}\right)^2 - 2\frac{c(c_0 - c)}{s^3}\left(\frac{d\theta}{dp}\right)^2 + \frac{(c_0 - c)}{s^2}\frac{d^2\theta}{dp^2}\right\} \tag{5.5}$$

In addition, there are also dark marker symbols present in this figure which indicate the second extreme values for the second nose points of these curves. These points can be determined using expression (5.3) but now with the condition that $p \neq 0$, see the following equation:

$$-F_0^{''} + 2F_1 + pF_1^{'} = 2\tau c\frac{d\theta}{dp} - (c + \tau s)\left(\frac{d\theta}{dp}\right)^2 - (s - \tau c)\frac{d^2\theta}{dp^2} - \tau ps\left(\frac{d\theta}{dp}\right)^2 + \tau pc\frac{d^2\theta}{dp^2} = 0 \tag{5.6}$$

It is of high significant to note that at the intersection point of dark and green line the curves change in shape. This intersection between the first and second extreme points seems to be happened nearly at M_0=2.2. The nose of the curves at the right side of this intersection point is placed also on the right. This kind of curves is called the first variant curve throughout this thesis. The curve that can be obtained at the intersection point (nearly M_0=2.2) shows the coincidence of its first and second local extreme values. This curve will be called the second variant. In contrast to the first variant, there are also curves at the left side of this intersection which have a nose on the left and will be called the third variant curves. As it already mentioned, *H(p)* is in reality a function of θ. So, another interesting figure that can displays the characteristics of *H(p)*-function is the (H-θ)-plot for different curves, see figure 5.2. The upper curve indicates the one correspondent to M_0=1.5 and the lowest placed curve is related to M_0=3.0. So, in this figure, the curves move downwards with increasing M_0. The blue marker signs in this figure indicate the θ_0's for these curves which are placed on the line p=-1 in figure 5.1. And the green and dark signs represent respectively the first and second local extreme values of *H(p)* for which $\frac{dH}{dp}$=0. These are the same points shown in figure 5.1.

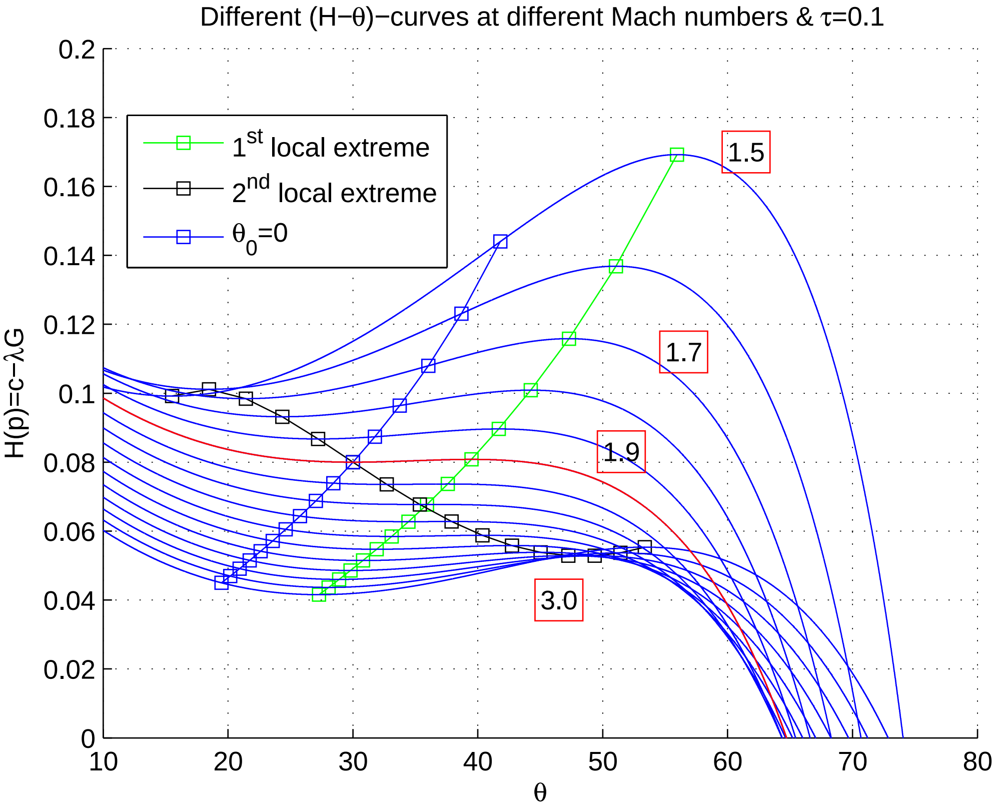

Figure 5.2: (H-θ)-plots for $\tau = 0.10$ and $1.5 \leq M_0 \leq 3$

As we have observed from figure 5.1, when the Mach number increases, the tip of the nose of these curves at p=0 moves to the left. In other words the first variant curves transform gradually to the third variant curves with increasing Mach number. It is very interesting to note that this transformation in shape takes place right after M_0=2.0. In order to know more about this transformation, the (H-p)-curves are illustrated in a smaller domain, $2.0 \leq M_0 \leq 2.4$, see figure 5.3. From right to the left the Mach number is increased from M_0=2.0 up to M_0=2.4 with a step size of 0.02. First of all, it is of high important to observe the overlapping of the blue and dark signs for the curve of M_0=2.0. It means that the θ_0 at M_0=2.0 represents at the same time the second extreme tip of this curve. This is a very special curve characteristic related to M_0=2.0. Further, it is obvious from this figure that transformation of the first variant to the third variant curves occurs gradually in this range of Mach number, ($2.0 \leq M_0 \leq 2.4$). It seems as this transformation takes place for the curves for which the first and second extreme values is similar. From figure 5.3 it is clear to see that curve which shows this property is in the Mach limit of $2.2 \leq M_0 \leq 2.22$. Furthermore, figure 5.4 visualizes *H(p)* as a function of θ for this M_0-domain. The upper line in this figure corresponds to M_0=2.0 for which the angle of the free flow characteristics coincides with the second extreme value of θ ($\theta_0 = \theta_{extreme,2}$). The variant transformation also can be observed from this figure by the intersection of dark with green line. This intersection takes place in the Mach range $2.2 \leq M_0 \leq 2.22$ for which the curve has the same value for the first and second extreme θ.

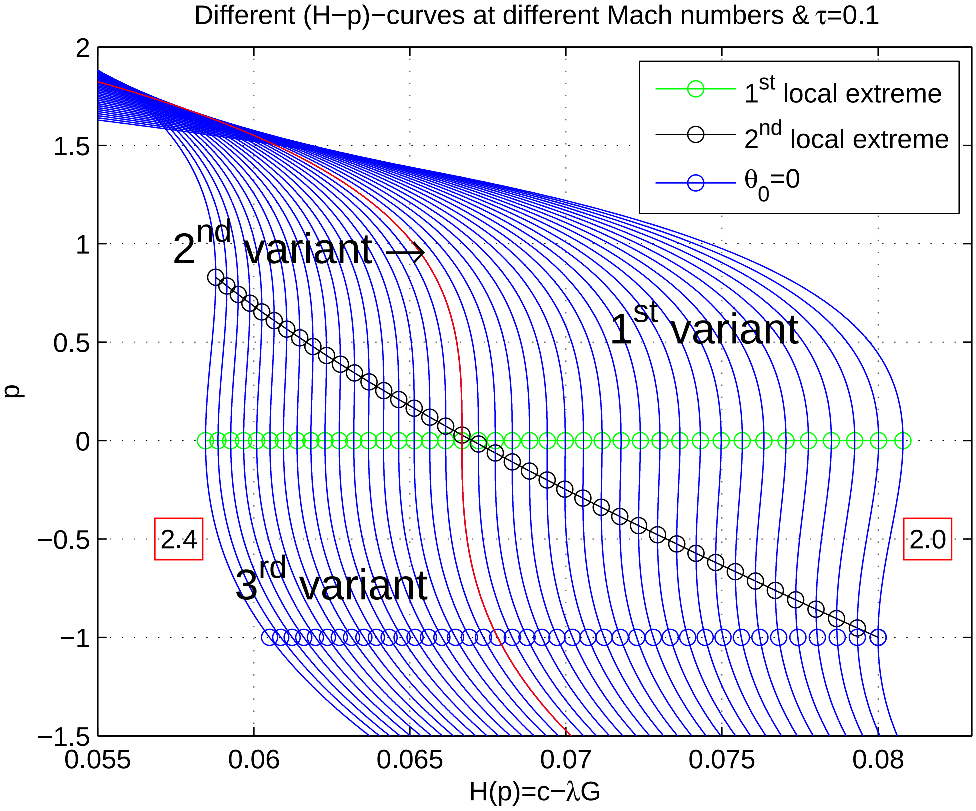

Figure 5.3: (H-p)-plots for $\tau = 0.10$ and $2.0 \leq M_0 \leq 2.4$

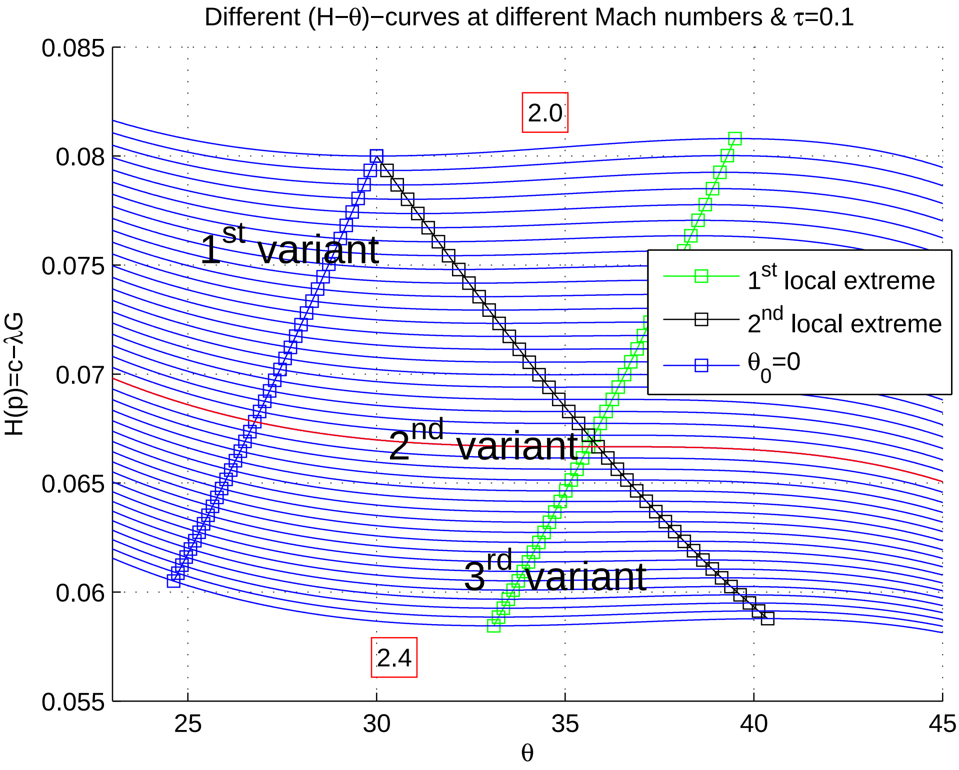

Figure 5.4: (H-θ)-plots for $\tau = 0.10$ and $2.0 \leq M_0 \leq 2.4$

5.2 Influence of τ

In the previous section, different curves correspondent to different Mach numbers have been presented. And it was shown when M_0 increases, the curves transform from first to the third variant. In all these curves τ was assumed to be constant, τ=0.10. But now we are going to change τ for a constant Mach number M_0=2.0. Figure 5.5 shows the (H-p)- and (H-θ)-curves which are achieved for a τ-limit of $0.05 \leq \tau \leq 0.15$. In (H-p)-plot τ is increased from left to the right and in (H-θ)-plot the increasing in τ goes from below to the top. The red curve in both figures indicates the related curve to τ=0.10. In both figures, it is clear that θ_0 coincides with the second extreme θ which was already shown in figures 5.1 and 5.2 for M_0=2.0. It means that even the τ variation does not change this property for the curve at M_0=2.0. The τ-variation can be now applied to the third variant curves. Figure 5.6 illustrates different curves which are obtained at M_0=2.6 and a τ-domain of $0.05 \leq \tau \leq 0.15$. In (H-p)-plot for this Mach number, τ is increased from left to the right and in (H-θ)-plot the τ-increasing goes from down to the top. The red curve in both figures indicates the related curve to τ=0.10. As it can be observed, varying the constant τ will have influence on the (H-p)-plot and this again will result in different

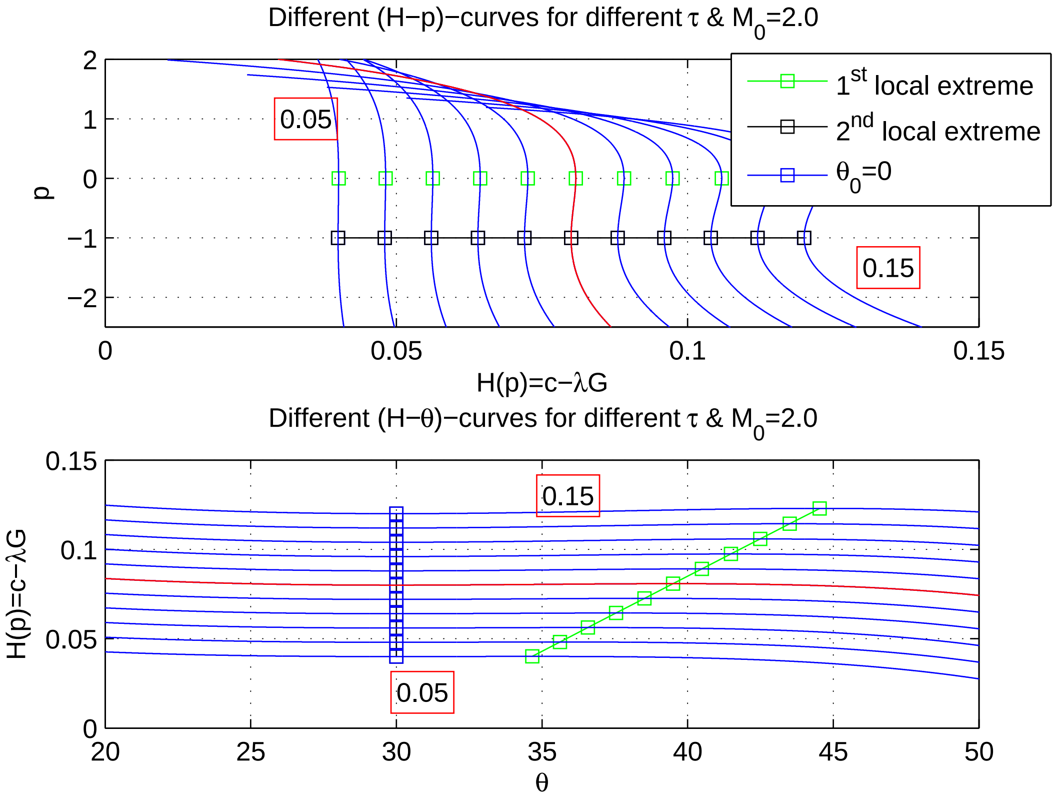
Different (H−p)−curves for different τ & M$_0$=2.0

Different (H−θ)−curves for different τ & M$_0$=2.0

Figure 5.5: Different curves obtained at different τ

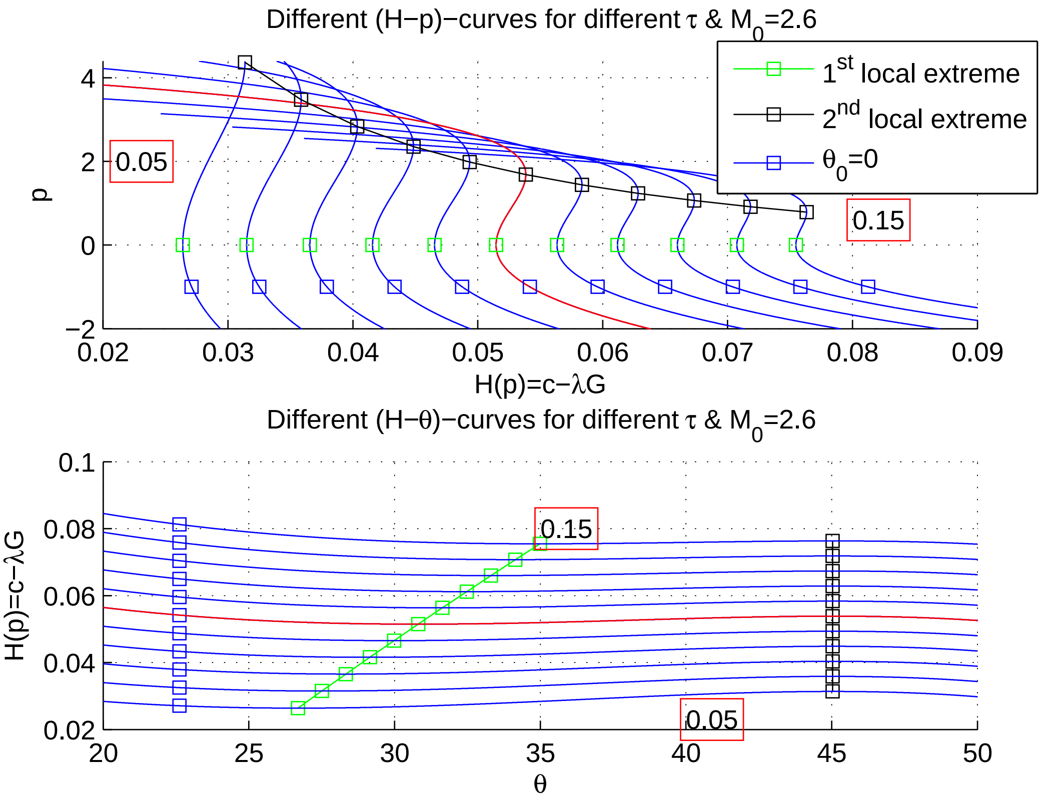

Figure 5.6: Different curves obtained at different τ

contour's geometry. This influence will be discussed in the following chapters.

5.3 Mathematical analysis

In the previous section, on the basis of the Mach number we have developed three different (H-p)-curves. For the first and third variant, the (H-p)-curves near p=0 can be approximated by a parabola. So, this stimulates us to analyze the curves characteristics further for both the first and as well as the third variant. In order to investigate the relation between the (H-p)-curves and the otimum contours geometry we need to analyze mathematically these curves. Because we expect that using the variational approach, the optimum contours are defined in terms of the extreme values for the asymptotic shock strength. And these optimum contours can be derived from these (H-p)-curves. Further we have observed from previous section that there are three different types of curves, so this means that we can derive possibly three different contour's geometry.

5.3.1 First variant curve

The (H-p)-curve near p=0 will be approximated by the following relation:

$$c - \lambda G = b - \alpha p^2, \text{ for } \alpha \ > \ 0 \tag{5.7}$$

Where b and α are considered to be constant. Since p=$\frac{dG}{dx}$ so then we get the following relation:

$$\frac{dG}{dx} = \pm\sqrt{\frac{c - \lambda G - b}{-\alpha}} \tag{5.8}$$

The first variant curve is shown in figure 5.7. We choose on the (c-λG)-axis a certain point and assume for this point G=0. This will define a value for c. Further, we assume this is the point which indicates the contour's leading edge, see the symbol l in figure 5.7. For this point there are two different solutions possible for $\frac{dG}{dx}$. So the solution is both positive as well as negative. First, we start integrating from the point l where G=0 to the point b on the (c-λG)-axis where $\frac{dG}{dx}$=0. This is in fact the integration along the positive section of the curve. The integration process through the positive branch gives us the following solution:

$$\int_l^b dx = \int_l^b \frac{+dG}{\sqrt{\frac{c-\lambda G-b}{-\alpha}}} \ \Rightarrow \ [x]_l^b = 2\left[\frac{\alpha}{\lambda}\sqrt{\frac{c - \lambda G - b}{-\alpha}}\right]_l^b \tag{5.9}$$

- l stands for the contour's leading edge where x_l=0 and G=0. So, it means the first boundary condition is satisfied namely; $G(0)$=0.
- x=x_b with $\frac{dG}{dx}$=0 leads to c-λG=b. It is worth noting to say that this point is the point for which the slope is the same as the slope for a wedge body.

The result of this integration is the following:

$$x_b = -\frac{2\alpha}{\lambda}\sqrt{\frac{c - b}{-\alpha}} \tag{5.10}$$

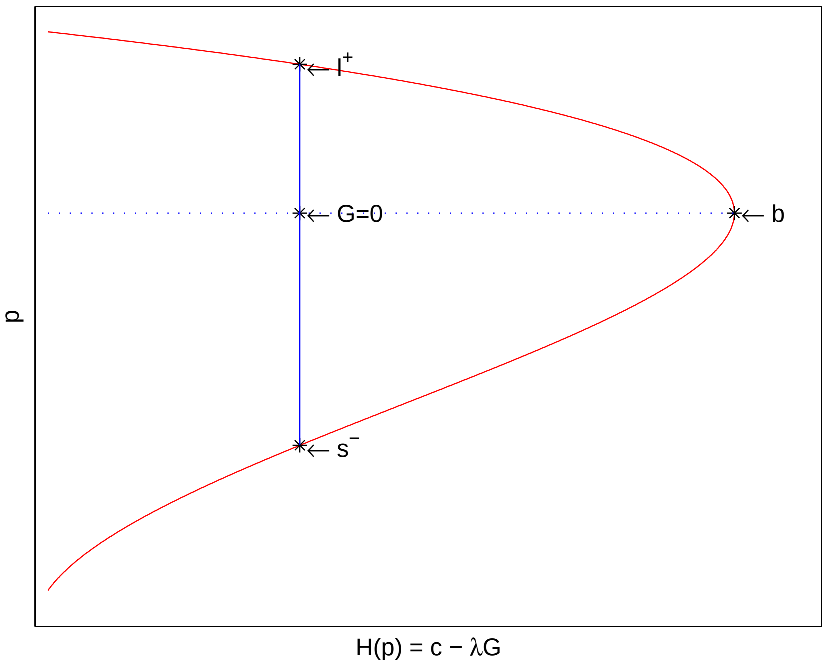

Figure 5.7: First variant curve

So, in order to complete the integration we need to continue along the negative section. The integration process through the negative branch is performed as follows:

$$\int_s^b dx = \int_s^b \frac{-dG}{\sqrt{\frac{c-\lambda G-b}{-\alpha}}} \Rightarrow [x]_s^b = -2\left[\frac{\alpha}{\lambda}\sqrt{\frac{c-\lambda G-b}{-\alpha}}\right]_s^b \tag{5.11}$$

- s stands for the contour' s shoulder point where x_s=1 and G=0.
- x=x_b is the point where $\frac{dG}{dx}$=0 and which leads to c-λG=b as mentioned above.

So, the integration along the negative branch will be the following:

$$x_b - 1 = -\frac{2\alpha}{\lambda}\sqrt{\frac{c-b}{-\alpha}} \tag{5.12}$$

Combining equations (5.10) and (5.12) results in a relation for the multiplier λ as a function of x, b and c:

$$\lambda = -4\sqrt{\alpha}\sqrt{b-c} \tag{5.13}$$

Finally, function *G(x)* can be determined by the integration along the positive branch:

$$\int_l^x dx = \frac{\alpha}{\lambda}\int_{l:G=0}^{x:G} \frac{d\frac{\lambda}{\alpha}G}{\sqrt{\frac{c-\lambda G-b}{-\alpha}}} \tag{5.14}$$

The solution is:

$$x = \frac{2\alpha}{\lambda}\left(\sqrt{\frac{c-\lambda G-b}{-\alpha}} - \sqrt{\frac{c-b}{-\alpha}}\right) \tag{5.15}$$

After inserting λ into this equation we obtain the value for *G(x)* on the interval $0 < x < 0.5$:

$$G(x) = \sqrt{\frac{b-c}{\alpha}}x(1-x) \tag{5.16}$$

The same result is obtained when the integration is performed along the negative branch. Using equations (4.16) and (5.16) we can express the coefficient c in terms of contour volume as follows:

$$K_G = \int_0^1 G(x)dx = \frac{S}{\tau} - \frac{1}{2} = \frac{1}{6}\sqrt{\frac{b-c}{\alpha}} \tag{5.17}$$

From equation (3.2) for the contour geometry and figure 5.8 the function F can be defined as follows:

$$y = \tau F(x) = \tau(x + G(x)) = \tau\left(x + \sqrt{\frac{b-c}{\alpha}}x(x-1)\right) \tag{5.18}$$

It is clear from equation (5.18) if we choose the value of c as near as possible to the value of b then *G(x)*-function approaches zero, So, it means the wedge contour with a volume of 0.5τ will be the most optimum contour, see the red line in figure 5.8. And if the difference between the values b and c increases, so it means that the contour's geometry will also be increased. The geometry illustrated by a blue line in figure 5.8 shows the largest optimum contour for a maximum value of *G(x)*-function. All other optimum contours with different geometries can be found between these two extreme contours.

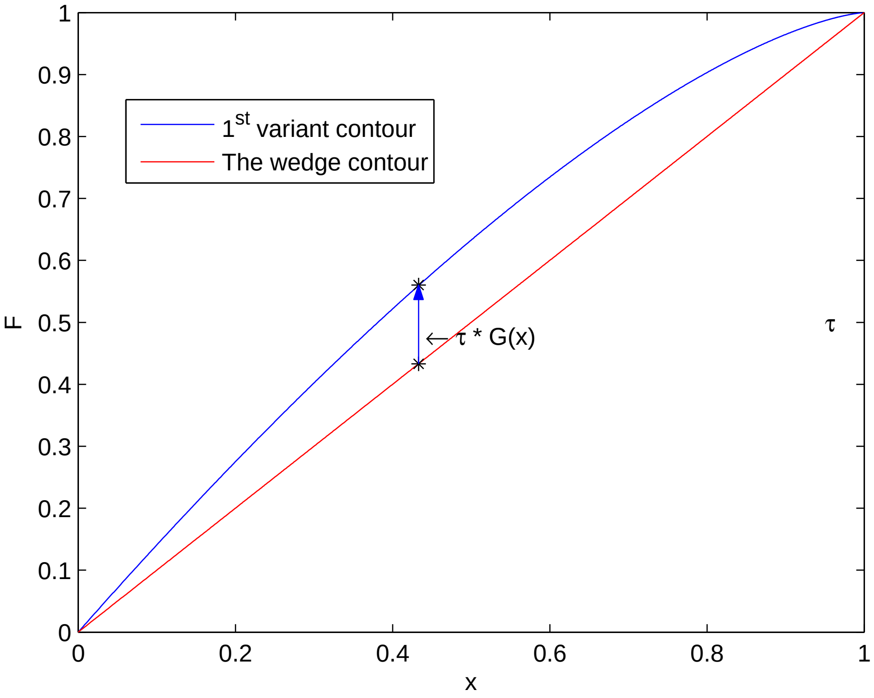

Figure 5.8: First variant contour

5.3.2 Variant III

As it was mentioned before, based on the Mach number there are three different curves possible. Between the first and third variant curves there is a transform variant possible for which further will be explained in the next section. In order to analyze the characteristics of *H(p)*-function for third variant curve we use the curve with the nose towards the left, see figure 5.9. *H(p)*-function is indicated by the following equivalent equation for a parabola

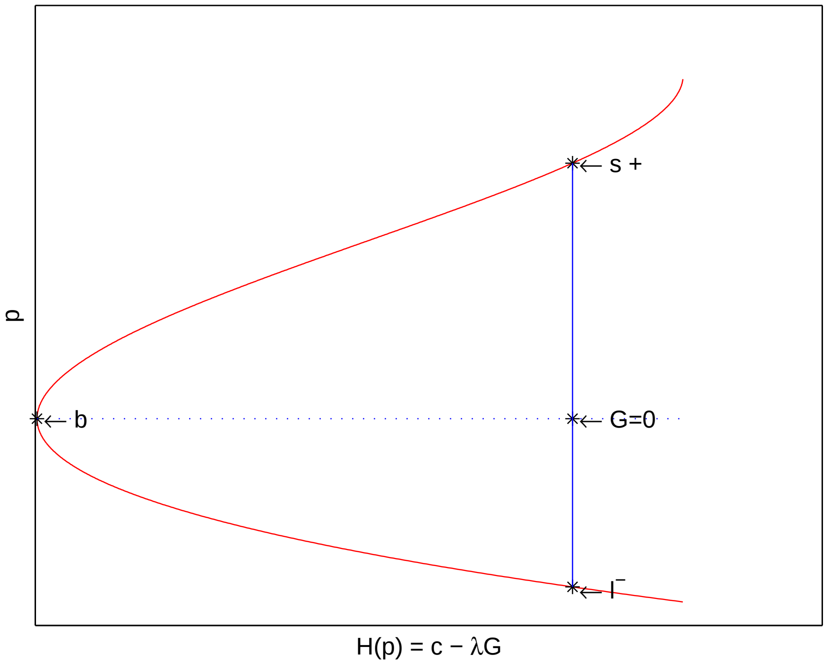

Figure 5.9: Third variant curve

near to the point p=0:

$$H(p) = c - \lambda G = b + \alpha p^2, \text{ for } \alpha > 0 \tag{5.19}$$

By knowing $p=\frac{dG}{dx}$ we have the following expression:

$$\frac{dG}{dx} = \pm\sqrt{\frac{c - \lambda G - b}{\alpha}} \tag{5.20}$$

The analyzing process for this variant is the same as the first variant. Again we choose a point on the *H(p)*-axis where G=0, (*H(p)*=c and $c > b$). For this point there are two values of $\frac{dG}{dx}$ possible namely a positive (on the positive branch) and a negative (on the negative branch). We assume the point on the negative branch is the leading edge where x=0 and the point on the positive branch being the body shoulder where x=1. The integration process will be done one time through the positive branch and one time through the negative branch. The integration through the negative part gives us the following:

$$\int_l^b dx = -\int_l^b \frac{-dG}{\sqrt{\frac{c-\lambda G-b}{-\alpha}}} \tag{5.21}$$

- l is the point of the contour's leading edge where x_l=0 and G=0. So, the first boundary condition is satisfied, $G(0)$=0.
- x=x_b is the point on the *H(p)*-axis where $\frac{dG}{dx}$=0 and this leads to c-λG=b

Now, we get the following equation for x:

$$x_b = -\frac{2\alpha}{\lambda}\sqrt{\frac{c-b}{\alpha}} \tag{5.22}$$

Integration through the positive branch gives us:

$$\int_b^s dx = \int_w^s \frac{dG}{\sqrt{\frac{c-\lambda G-b}{\alpha}}} \tag{5.23}$$

- The symbol s stands for contour's shoulder point where x_s=1 and G=0. So, the second boundary condition is satisfied $G(1)$=1.
- x=x_b with $G^{'}$=0 leads to c-λG=b.

The expression for x can be defined as follows:

$$1 - x_b = -\frac{2\alpha}{\lambda}\sqrt{\frac{c-b}{\alpha}} \tag{5.24}$$

Combining equations 5.22 and 5.24 gives us the value for λ:

$$\lambda = -4\sqrt{\alpha}\sqrt{c-b} \tag{5.25}$$

From $\alpha > 0$ and $c > 0$ we conclude that λ is real and positive. It means we are now able to calculate *G(x)* function in the same way as we have done for the first variant. So, we do the integration process now along the negative branch.

$$\int_l^x dx = \frac{\alpha}{\lambda}\int_{l:G=0}^{x:G} \frac{-d\frac{\lambda}{\alpha}G}{\sqrt{\frac{c-\lambda G-b}{\alpha}}} \tag{5.26}$$

The result of this integration process is the following:

$$x = \frac{2\alpha}{\lambda}\left(\sqrt{\frac{c-\lambda G-b}{\alpha}} - \sqrt{\frac{c-b}{\alpha}}\right) \tag{5.27}$$

After inserting λ into this equation we obtain the value for *G(x)* for the interval $0 < x < 0.5$ as follows:

$$G(x) = -\sqrt{\frac{c-b}{\alpha}}x(1-x)) \tag{5.28}$$

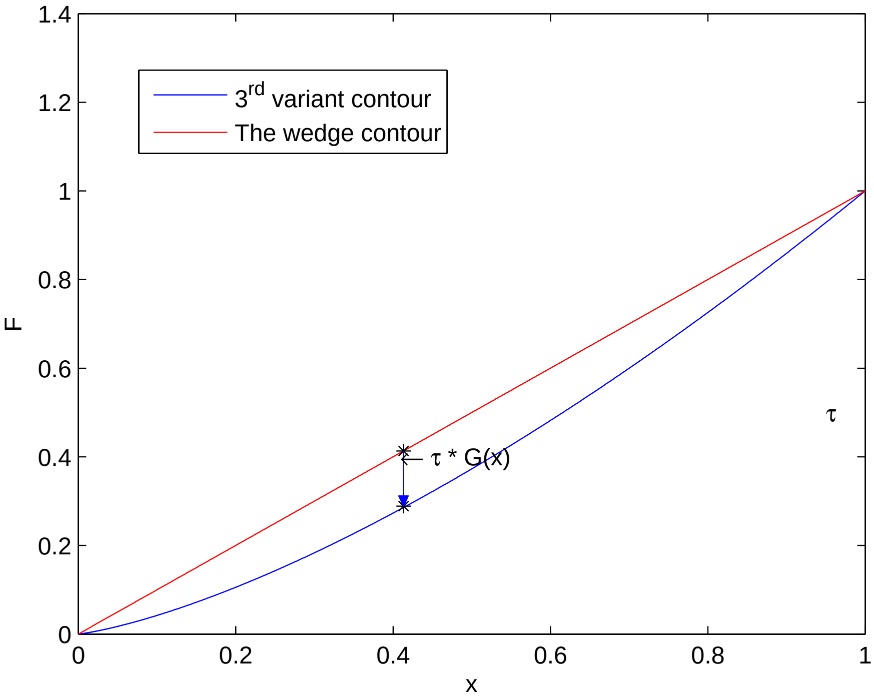

Figure 5.10: Third variant contour

The function *G(x)* is just valid for the interval where x=0 to the point with $\frac{dG}{dx}$=0 and the minus sign indicates the contour is slimmer than a wedge contour, see figure 5.10 . The same result will be achieved for the positive branch. It is obvious from equation (5.28) if we choose the value of c as near as possible to the value of b then *G(x)*-function approaches zero, So, it means the wedge contour with a volume of 0.5τ will be the most optimum contour for the third variant, see the red line in figure 5.10. And if the difference between the values b and c in equation (5.28) increases, so it means that the contour's geometry will be decreased. The geometry shown by a blue line in figure 5.10 indicates the smallest optimum contour for a minimum value of *G(x)*-function. All other optimum contours can be derived for different *G(x)*-function and expected to be found between these two extreme contours.

These two variants show that they both depend on two variable constants; the Mach number M_0 and thickness τ. Further we have observed the integration process applied to the first variant curve will result in a contour which has a convex surface while applying the same integration process to the third variant will lead to a slender contour with a concave surface. From above the specified characteristics of *H(p)*-function in both variants the first as well as the third variant give the possibilities to achieve the optimum contours with the boundary conditions $F(0)$=0 and $F(1)$=1. In other words, the variational approach resulted in *H(p)*-function enables us to obtain the optimum contours which are expressed in terms of the asymptotic shock strength. A very special case of *H(p)*-curve is the transitional curve which appears between the first and third variants. This curve type is explained as last one due to its unique characteristics.

5.3.3 Variant II

As we have observed, the second variant is obtained with a certain *H(p)*-function in a Mach number region where the curve has equal first and second local extreme values. The main characteristic of this curve is the cubical characteristic of $\left(\frac{dG}{dx}\right)$-function for which the sign becomes negative at the inflection point where $\frac{dG}{dx}$=0. In other words, this kind of variant can be achieved as a transitional case from variant *I* to *III* for a Mach range of $2.2 \leq M_0 \leq 2.22$ and τ=0.10. In order to find an exact relation between M_0 and τ for other Mach numbers we need to analyze further the second curve variant. First we look for a relation between M_0 and τ when p=$\frac{dG}{dx}$=0 and it also satisfies the conditions $\frac{dH}{dp} = H^{'}(p)$=0 and $H^{''}(p)$=0. A double differentiating of equation (5.1) w.r.t. p gives us the following:

$$H^{''}(p) = -F_0^{''}(p) - pF_0^{''}(p) + 2F_1(p) + 4pF_1^{'}(p) + p^2F_1^{''}(p) = 0 \tag{5.29}$$

Assuming p=0 results in the following:

$$H^{''}(p) = 2F_1(p) - F_0^{''}(p) = 0 \tag{5.30}$$

Inserting p=0 into equation (5.4) give us:

$$F_0^{''} = 2\left(-\tau c + \tau\frac{(c_0 - c)}{s^2}\right)\frac{d\theta}{dp} + (c + \tau s)\left(\frac{d\theta}{dp}\right)^2 + (s - \tau c)\frac{d^2\theta}{dp^2} \tag{5.31}$$

By knowing $\frac{d\beta}{d\theta} = -1 - \frac{\beta^2}{6}$ from equation (4.34) we can have $\frac{d^2\theta}{dp^2}$:

$$\frac{d^2\theta}{dp^2} = \frac{\tau}{N}\frac{d\theta}{dp}\left\{2 + \frac{2tan\theta}{\beta} - \frac{5}{3}\beta tan\theta\right\} \tag{5.32}$$

Assuming $\tau \neq$0 and $N \neq$0 equation (5.30) becomes:

$$2F_1 - F_0^{''} = \frac{10}{6}\beta^2(1+tan^2\theta) - (\beta + tan\theta)(\beta + \beta tan^2\theta) - (1+tan^2\theta)\left\{2 + 2\frac{tan\theta}{\beta} - \frac{5}{3}\beta tan\theta\right\} = 0 \tag{5.33}$$

By using 1+$tan^2\theta \neq$0 we get:

$$(\beta + tan\theta)(5/3\beta - \beta - 2/\beta) = 0 \tag{5.34}$$

This equation has only one solution namely β^2=3 which gives us M_0=2.0. The transition of variant *I* to *III* takes place for a certain combination of M_0 and τ with the condition that the local Mach number becomes 2 at some point on the contour surface which has a slope of τ. But the question is under which combinations of M_0 and τ does it take place for other Mach numbers?

If we use equation (3.9) we get the following relation between θ and ν_0:

$$\theta = \nu_0 + 3.6202 \tag{5.35}$$

By knowing $\tau = \frac{\beta tan\theta - 1}{\beta + tan\theta}$ for the case when p=0 we are able to find the corresponding τ for different Mach numbers as follows:

$$\tau = \frac{\sqrt{3}tan(\nu_0 + 3.6202) - 1}{\sqrt{3} + tan(\nu_0 + 3.6202)} \tag{5.36}$$

In order to visualize the relation between τ and M_0, first we use a couple of characteristic angles θ as inputs in equation (5.35). This results in the corresponding *Prandtl-Meyer* function for the undisturbed flow ν_0. Subsequently, we use the *Hall*-function to convert these *Prandtl-Meyer* function to the Mach number M_0. The description for the *Hall*-function is given in appendix A. Figure 5.11 shows the transition point for different τ and M_0 values, this line can be approximate by the following polynomial function:

$$\tau = p_1 * M_0 + p_2 \tag{5.37}$$

With the corresponding polynomial constants p_1=0.45468 and p_2=-0.90766.

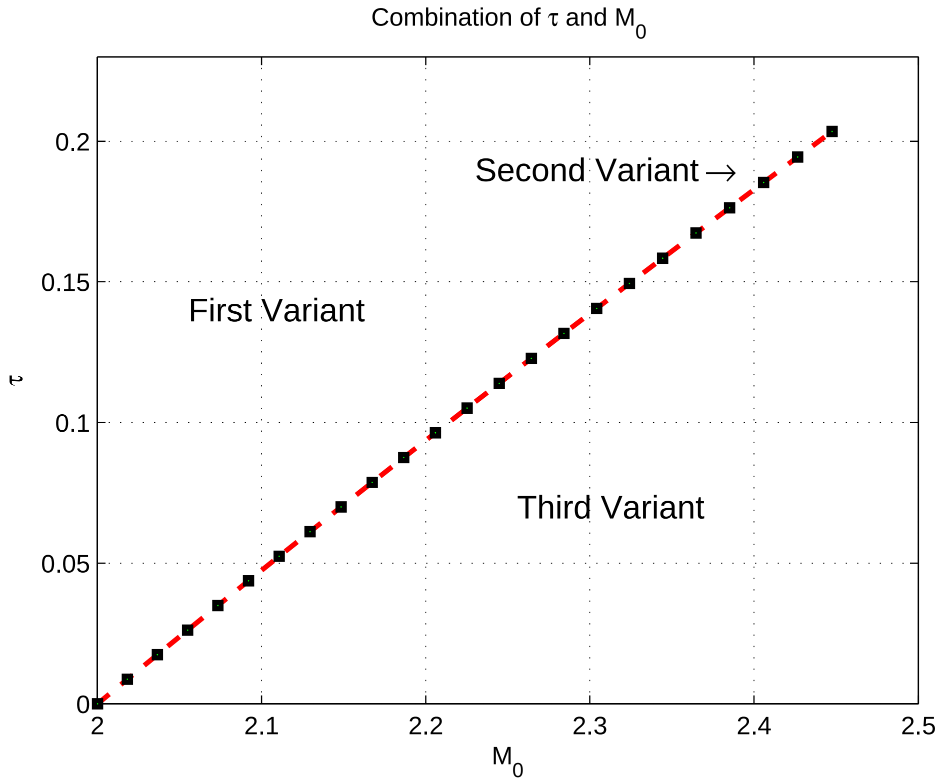

Figure 5.11: The transition points from variant *I* to variant *III*

CHAPTER 6

NUMERICAL ANALYSIS FOR THE FIRST VARIANT

In chapter 5 we have discussed the characteristics of the first order differential equation *H(p)* and then regarding these properties we were able to define three different curves based on the Mach number. The second type curve seemed to be a transitional variant between the first and third variant. The mathematical analysis of this variant was necessary for us to find a relation between two variables M_0 and τ in *H(p)*-function for this transitional variant.

Furthermore, we have noticed that each of the first and third variant curve is supposed to lead to an optimized contour. But it was shown only from a mathematical point of view for a curve close to p=0. So, in this chapter first we will be concerned with the first variant curve by the integration of *H(p)*-function. Further, the asymptotic shock strength caused by the first variant contours will be discussed. The expansion waves which occur together with the shock wave will be the next topic in this chapter. Subsequently, the influence of the variables M_0 and τ on this variant will be investigated. And finally we discuss the aerodynamic properties such as pressure, Mach number and entropy change behind the shock for the optimized contours. The drag force caused by the optimized contours will be another issue to be analyzed in this chapter.

6.1 Integration of *H(p)* curve: first variant

In the previous chapter we have seen that the complicated differential equation (5.1) for a Mach range of $1.5 \leq M_0 \leq 2.0$ and a thickness τ=0.10 has the form of a curve for which the nose is placed to the right, see figure 6.1. It was also developed a method to achieve the corresponding optimized contours with a mathematical analysis by comparing the (H-p)-curve to a parabola near p=0. And this process resulted in an optimum contour which has a convex geometry. But as we see the curve is not defined in a *(x,y)*-coordinate system as the related contour is shown. So, in order to obtain the corresponding optimal contour, we need to integrate the curved line in figure 6.1. As first we take an arbitrary point on the c-λG-axis and assuming there G=0. This gives us the value for *H(p)* which equals to c. Straight above this point is the point n which lies on the positive branch

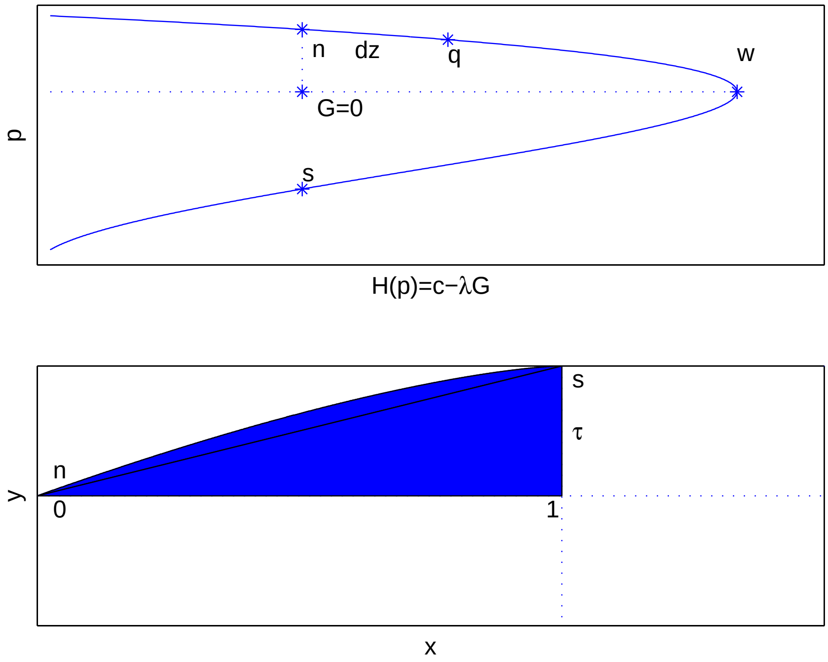

Figure 6.1: Upper plot: First variant curve, Lower plot: First variant contour

of the curve and also indicates G=0. So, it means the location of point n is known, H_n=c. In addition, this point is assumed being the contour's leading edge (nose), see figure 6.1 below. The characteristic angle corresponding to the leading edge is indicated by θ_n. Point n can be connected to the point s on the negative section of the curve. This point assumed to be the contour's shoulder point for which G=0 with the same value of H_n. The characteristic angle correspondent to this point is θ_s which is just before the undisturbed characteristic Mach angle θ_0. Between these two angles there is a small difference because it is needed to have a *Prandtl-Meyer* expansion wave which will be discussed later in this thesis. From point n to the point s we have a certain (H-p)-curve which must be integrated numerically. In order to determine the shape of the curve which starts from point n and ends at point s, we need to compute the slope of the tangent line to the curve at any point on the curve z. The initial value at point n is z=0. Now in order to make a relation between the x-coordinates of contour and the z-values on the curve we multiply the values of x by the constant λ, so, it means that $z = \lambda x$. This enables us to define the values of $p = \frac{dG}{dx}$ on the vertical axis in domain of z. So, there is now a new expression for p as follows:

$$p = \frac{dG}{dx} = \frac{d(\lambda G)}{dz}$$

With the known definition *H(p)*=c-λG, there is also a new relation between p and *H(p)*-function in terms of z as follows:

$$p = \frac{-dH}{dz}$$

All these definitions help us now to define the coordinates of the point n in a z-domain as follows:

$$(H_n, p_n) = \left(c, \frac{-dH_n}{dz}\right) \tag{6.3}$$

The next step is to find the distance dz to the point q on the curved line. So, the most easy way to do that, is to apply the second order numerical integration procedure, the *Heun*'s method, see the following expression:

$$dz = \frac{-(H_q - H_n)}{\frac{1}{2}(\frac{dH_q}{dz} + \frac{dH_n}{dz})} \tag{6.4}$$

This equation with $z_n = 0$ will enable us to have the location of the point q on the curve as follows:

$$z_q = z_n + dz \tag{6.5}$$

This integration method must be applied up to the point s which has the value H_s. As it was mentioned before, this is exactly the same value as H_n. The shoulder point s has been represented on the corresponding contour at x=1, see figure 6.1 below. However, this integration procedure from point n to the point s results in a set of two values namely; the values of z correspondent to the *H(p)*-values. So, with the relation $z = \lambda x$ and also the known location of point s, x_s=1, we notice that the final value of z equals to the constant λ. So, it means $z_{end} = \lambda$. This result will give us the corresponding values for x which are in fact the locations of the characteristic Mach lines along the optimized contour as follows:

$$x = \frac{z}{\lambda} \text{ with } z_{end} = \lambda \tag{6.6}$$

We have now defined the values of two constants, λ and c. This together with equation $H(p) = c - \lambda G$ enables us to get the values of G as follows:

$$G = \frac{c - H(p)}{\lambda} \tag{6.7}$$

Eventually, with F=G+x, the contour can now be defined in a *(x,y)* domain:

$$y = \tau F \tag{6.8}$$

6.2 First variant geometries

In the previous part it was shown that the curve which leads to the optimized contour could be obtained based on an arbitrary point, n. This point could be chosen in many locations on the (H-p)-curve with some limitation that will be explained further. So, this point is very important in the sense that it actually defines the geometry of optimum contours. For this reason we must be aware of, that for the point n there should be a corresponding shoulder point s. These two points must have the same value of *H(p)* on the horizontal axis. The consequences of choosing the location of point n on the curve will be discussed below.

The largest curve

The upper figure 6.2 indicates the location of point n which leads to the largest possible curved line. This figure shows if point n had been chosen a little bit towards the left, so there exists no related shoulder point s for it with the same value of *H(p)*. This is because the curve at point s tends to go backwards. The shoulder point is just located a little bit before the (H,p)- values correspondent to the undisturbed characteristic angle θ_0. This difference is needed as just was mentioned for the forming of the *Prandtl-Meyer* expansion wave. As it is already known the quantity of *H(p)* is a function of the characteristics angle θ. So, in order to match the corresponding points n and s on the (H-p)-curve we need to analyze the distribution of the characteristic angles along the body surface. The Γ^+ characteristics originate from the surface of the optimized contour under a certain angle. As we already know, the slope of these characteristic lines is the sum of Mach angle and the flow direction along the contour surface, $\theta = \mu + \varphi$. Figure 6.2 below shows the variation of the angle of the characteristic lines along the body surface with the corresponding *H(p)*. Figure 6.2 below illustrates that two characteristic lines indicated by n and s are originating with two different angles from the body surface but with the same value for *H(p)*.

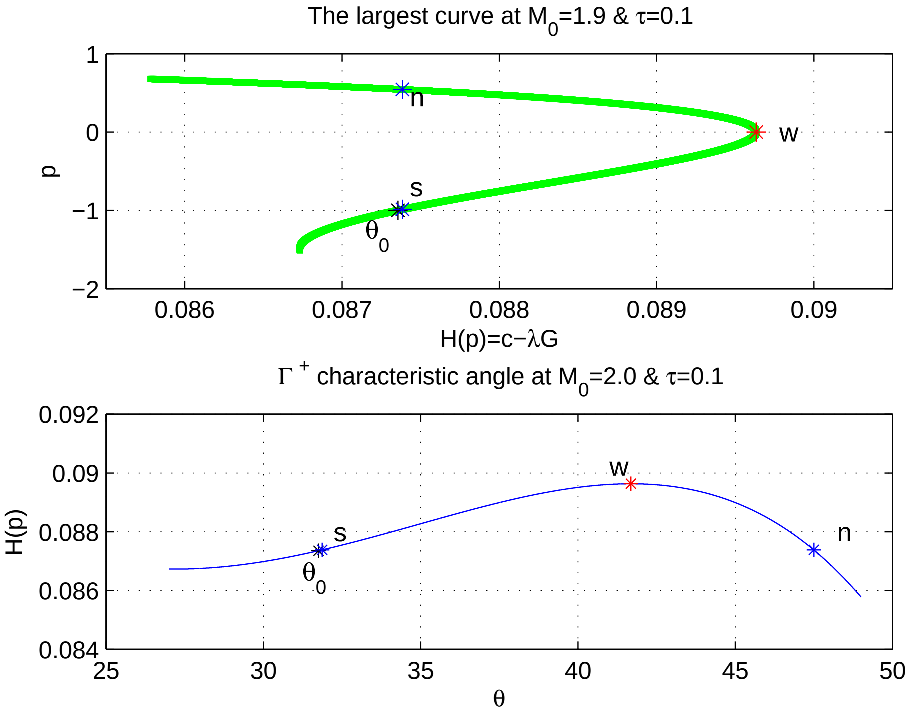
The largest curve at M_0=1.9 & τ=0.1

Γ^+ characteristic angle at M_0=2.0 & τ=0.1

Figure 6.2: Upper plot: (H-p)-curve, Lower plot :(θ-H)-curve

The wedge contour

One of the very important points indicted in the upper figure 6.2 is the point w, which stands for the wedge. This point has the maximum value of *H(p)*. And from equation

(6.7) it is already known that G_w=0 because it was assumed to be the point at the nose of the body and there is no other value of *H(p)* available on the curve. So, this will result in F=x which defines the function for a wedge contour. And from the same figure we observe that $\frac{dG_w}{dx}$=0 which means that the wedge contour has a straight upper surface for which the slope is y=τ. And the corresponding volume for the wedge contour will be 0.5τ. This contour is the smallest contour which is possible for the first variant curves.

6.2.1 The resulting (*H*-*p*)-curves

In the previous part the properties of the largest curve and the wedge point have been investigated for the case $_0$=1.9 and τ=0.10. But, we must aware of the fact that except for this large curved line there are many other curves that can be derived with different lengths. Figure 6.3 illustrates the largest curve for M_0=1.9 and τ=0.10.

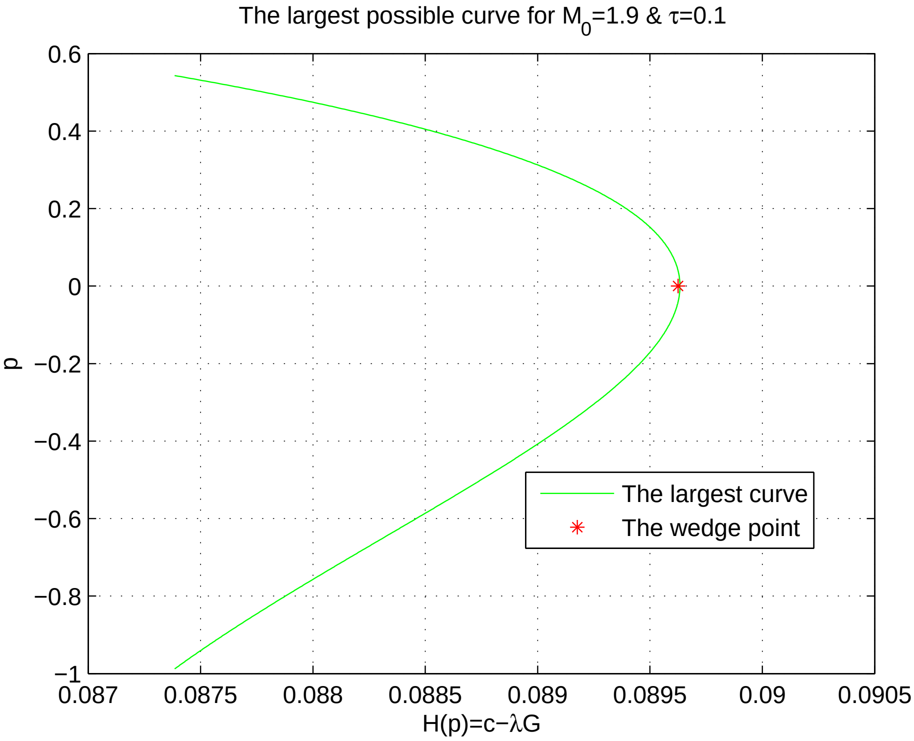

Figure 6.3: Largest possible curve, first variant

6.2.2 The resulting *G*-function

From previous section we can conclude that applying the integration method to the different curves will result in different values of constants c and λ. And by knowing this and equation (6.6) we are able to achieve the x-coordinates of characteristics. After knowing the x location of these characteristics the optimum G-function needs to be determined. Because as we remember from chapter 4 the extreme values for A_l was expressed in terms of optimum contours. And these contours can be defined by the known relation F=G+x.

The function *G(x)* can be determined by using equation (6.7). The results of G-functions corresponding to the largest possible curve is given in figure 6.4. As we can observe from this figure, the *G(x)*-function satisfies the boundary conditions given in chapter 4 for the corresponding variation problem. These boundaries are *G(0)*=*G(1)*=0. Furthermore, it is obvious that the top point of the G-plot is not in the midpoint x=0.5.

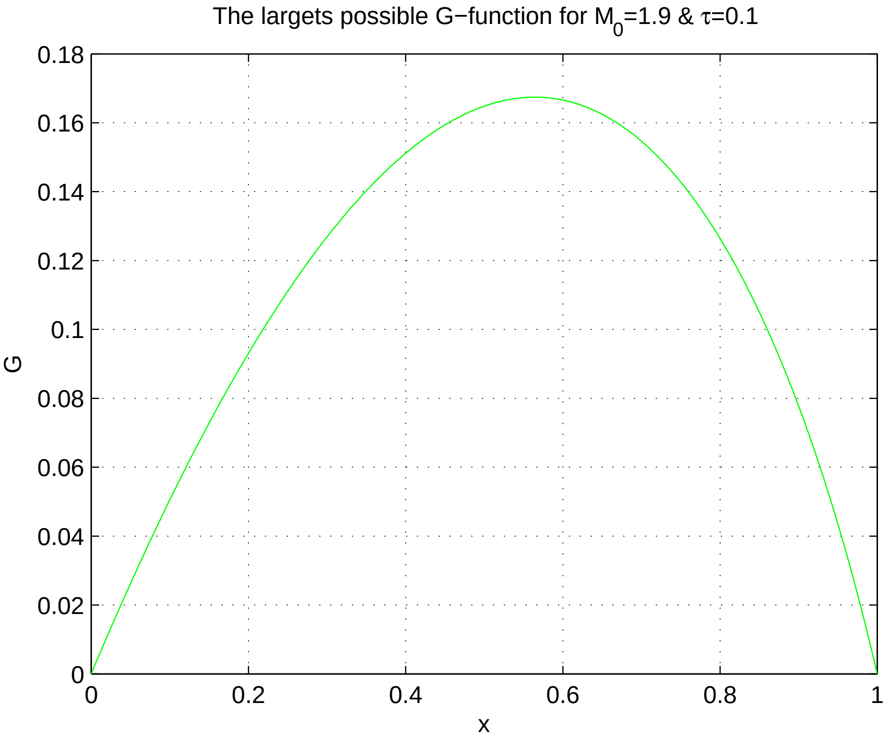

Figure 6.4: The corresponding G-function to the largest curve

6.2.3 The resulting contour function

The integration process was performed to achieve the values of x and G. And these quantities are needed to define the optimized contours. Equation (6.8) gives us an expression for the optimized contours. It is also known that F is the sum of x and G. From this we have the following expression to generate the optimal contours in *(x,y)*-coordinate system.

$$y = \tau(x + G) \tag{6.9}$$

Finally, this expression results in contours illustrated in figure 6.5. Except for the largest, the wedge variant is also included. All other contour variants which can be achieved based on (H-p)-curve in figure 6.3 can be found between the largest and wedge contour shown in figure 6.5. From this figure we can conclude that the size of the curves, shown in figure 6.3 will result in different contour geometries. And these contours have actually different volumes. The largest curve leads to a contour which has a convex surface while the smallest curve results in a straight geometry surface. In order to show the relation between the constant c and volume of different contours see figure 6.6. It is obvious from

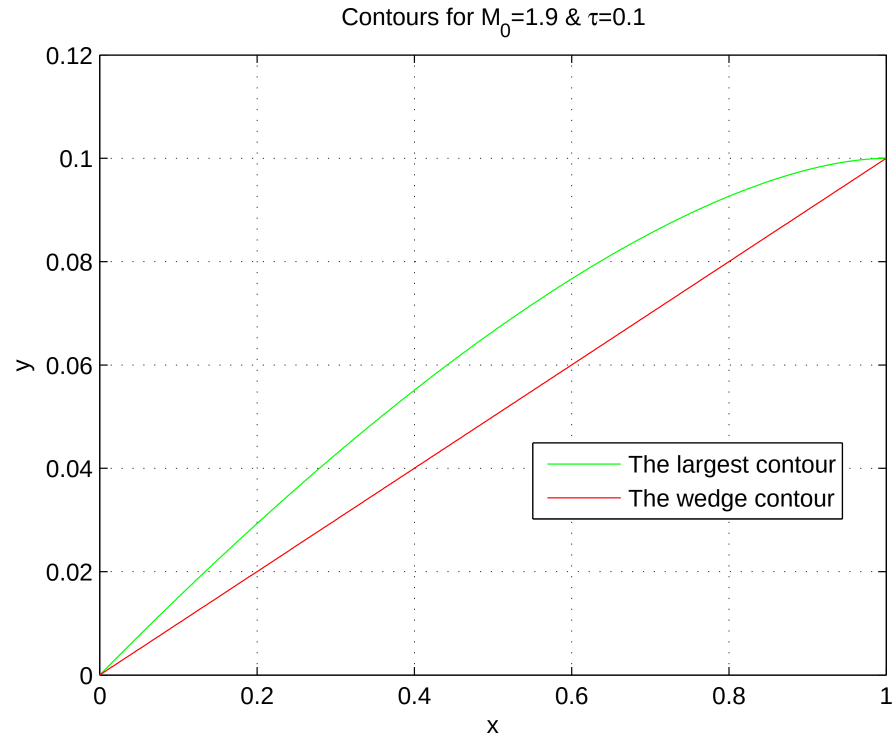

Figure 6.5: The possible contours, first variant

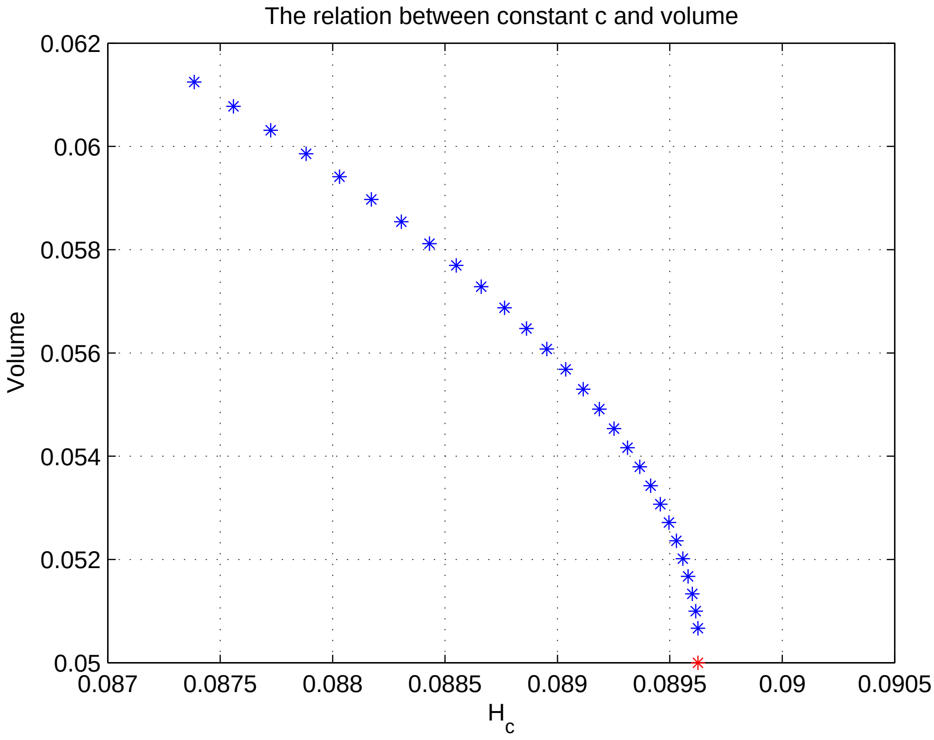

Figure 6.6: The influence of constant c on contour volumes, first variant

this figure if point c is chosen far from the wedge point (when the H_c-value is smaller), then the corresponding curve line becomes larger and this again results in a contour with a larger volume.

6.3 Asymptotic shock strength for the first variant

In the last section 6.2, it has been shown that we could develop many optimized contours with different geometries for M_0=1.9 and τ=0.10. And all these optimal contours have also different volumes. Furthermore, all these contours are able to generate *Prandtl-Meyer* expansion waves which is very important for the asymptotic shock theory. This is because as we remember, the shock which is formed by the optimal contours has an asymptotic characteristic which intersects with the expansion and centered expansion waves issuing from the body surface. This intersection between these waves and shock will result in decreasing the shock strength. And according to the definition of the asymptotic shock strength theory, the most optimum contour is one which causes the intersection between the expansion and shock waves occur earlier so that the strength of the shock faster becomes zero.

The next step is now to investigate the asymptotic shock strength for all different optimum contours in a supersonic flow. In chapter 3 the asymptotic shock strength was already analyzed for a body which has a smooth and continuous upper surface, see figure 3.4. The shock strength area which was the sum of the area's I and II in (cos θ)-graph shown in figure 3.4 was supposed to be the magnitude of the asymptotic shock strength for the corresponding body. Equation (3.36) was developed for this area. The influence of Mach factor M_{factor} is neglected in the term k_l which is in fact a decay factor for the asymptotic shock strength Σ given by (3.20). This is because only the term A_l indicates the relation between the body geometry and the asymptotic shock strength which is caused by it. So, in this part we will be concerned only with applying equation (3.36) to the achieved optimized contours based on the first variant (H-p)-curves. Figure 6.7 illustrates the relation between the asymptotic shock strength and volume for an optimal contour with τ=0.10 and M_0=2.0. In this figure there are two points which are distinguished by color. The green point represents the contour with the largest volume which is the result of the integrated green curve from figure 6.3. It must be noted that this contour is able to generate centered expansion wave because there is a small difference between the first and last characteristic lines at the shoulder point. It appears also that this contour has the largest asymptotic shock strength. The wedge body with a volume of V=0.5τ is marked in this figure with black. So, the conclusion from figure 6.7 is that the asymptotic shock strength increases with volume.

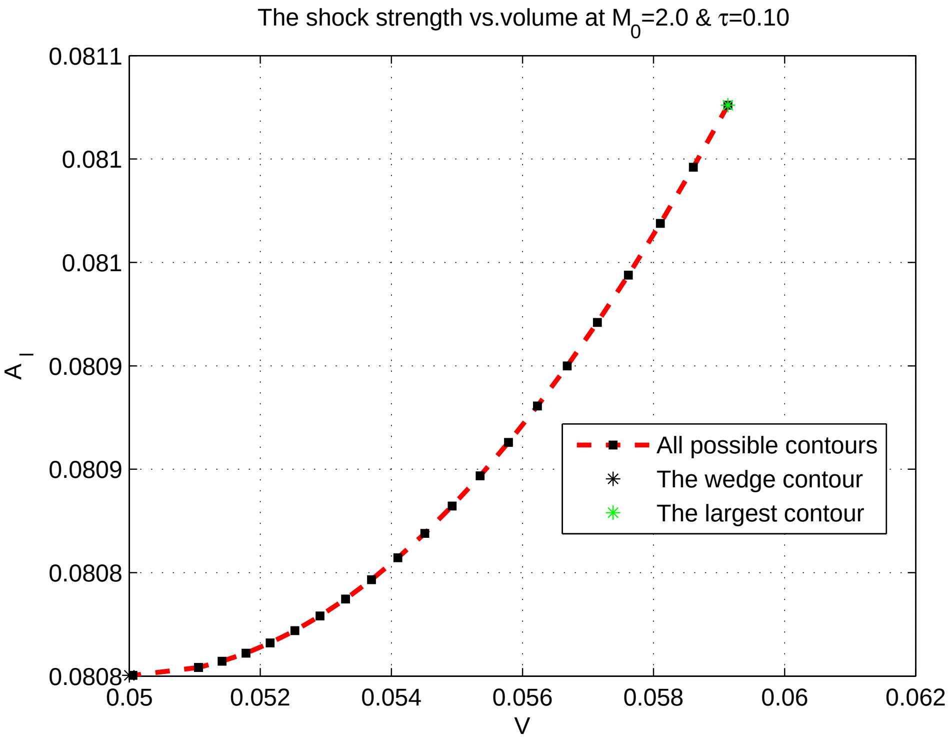

Figure 6.7: The shock strength vs. volume, first variant

It is also of high interest to investigate the asymptotic shock strength for other Mach numbers. Figure 6.8 represents all possible first variant contours with different volumes for the Mach range of $1.5 \leq M_0 \leq 2.0$ with a step size of 0.10. The bottom line in this figure indicates the optimum contours at M_0=2.0. And the uppermost line represents the optimum contours at M_0=1.5. From this figure it is clear to observe that with decreasing Mach number the asymptotic shock strength will be increased for the achieved contours. And also at lower Mach numbers we can have contours with a larger volume. Furthermore, it is obvious from figure 6.8 that the optimal contour in the first variant with a maximum volume can be obtained in a Mach range of $1.7 < M_0 < 1.8$.

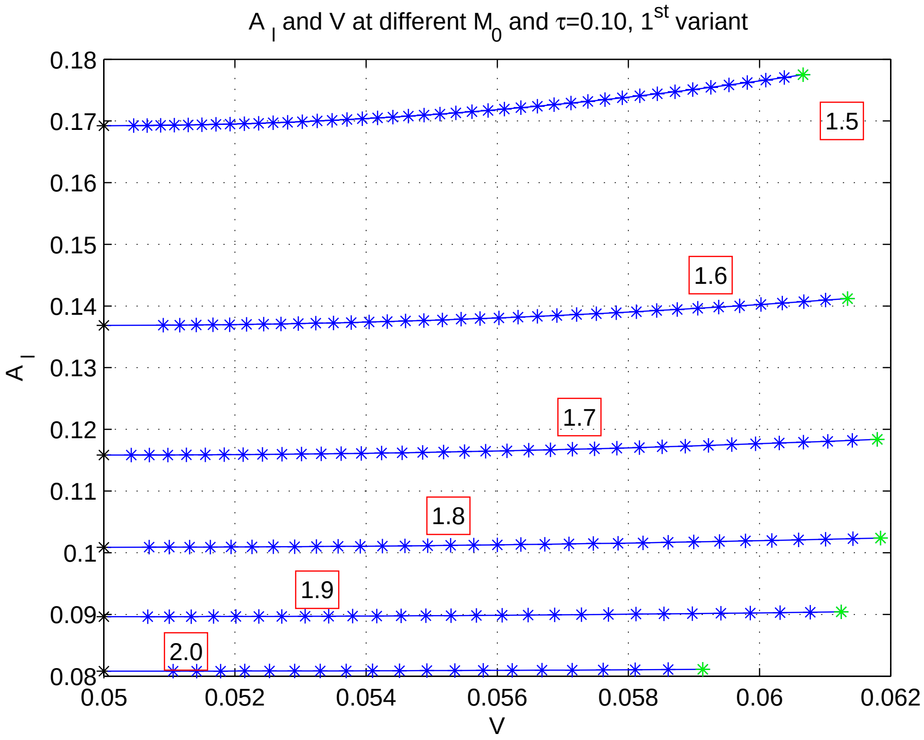

Figure 6.8: The shock strength vs. volume, all possible first variant contours

6.4 Convergence

In order to verify the results of the asymptotic shock strength, it is needed to see if the applied numerical method is convergent. The numerical method used for calculating the asymptotic shock strength is convergent if the solutions are not dependent on the number of points N which define the $(H\text{-}p)$-curve. These are the points from nose to the shoulder which represent the characteristic lines for the optimal contour. The convergence is determined as follows:

$$\text{convergence} = \left(\frac{A_l^N - A_l^{2N}}{A_l^N}\right) \tag{6.10}$$

Where A_l^N is the asymptotic shock strength for the current total number of points and A_l^{2N} indicates the asymptotic shock strength for double of the current number of points. Figure 6.9 illustrates the convergence of the numerical solutions for a large and small contour for the first variant. So, the conclusion which can be derived from this figure is that the numerical methods used for determining the asymptotic shock strength is well convergent because the results are not dependent on amount of number of points.

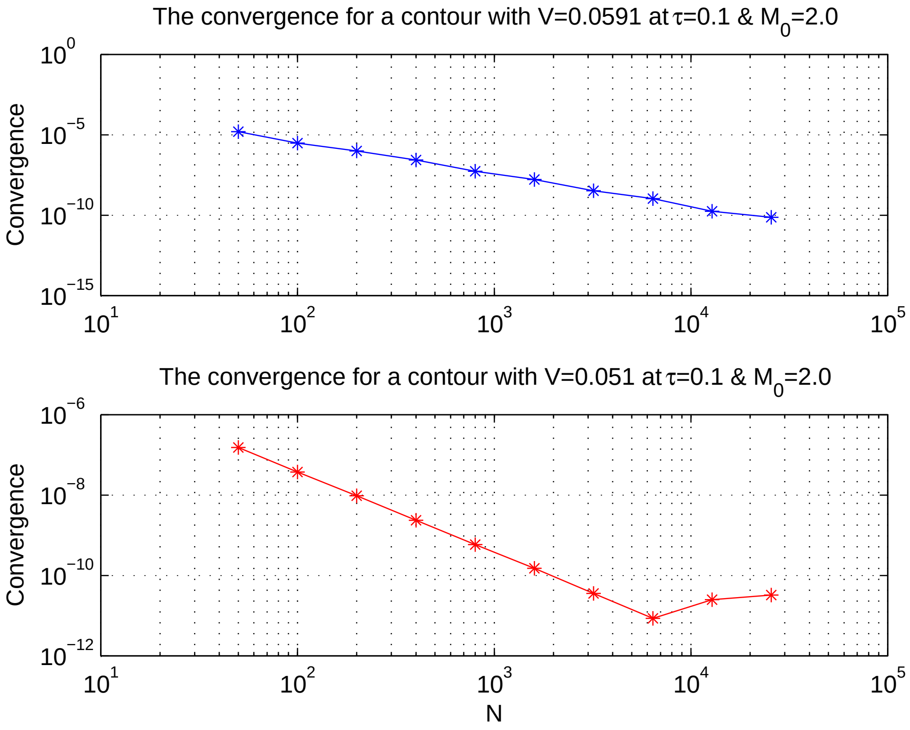

Figure 6.9: The convergence validation

6.5 Validation for the first variant

In order to investigate whether the achieved first variant contours are really optimized or not, the task is now to determine A_l for contours that are not optimized but they have the same volume. In the folowing parts the asymptotic shock strengths of two non-optimized contours will be determined by an analytical approach.

6.5.1 A wedge contour in a steady supersonic flow

A wedge body with a certain thickness τ is considered being in a steady supersonic flow with a Mach number M_0=2.0, see figure 6.10. The wedge body is supposed being in a non-lifting configuration. In chapter 2 we derived the expression (3.36) which expresses the leading shock wave for a 2D body with the same thickness but different upper surface. The upper surface of that body was assumed to decrease continuously instead of a straight line. Therefore in the case of a wedge body we need only the first term of equation (3.36) which is the following:

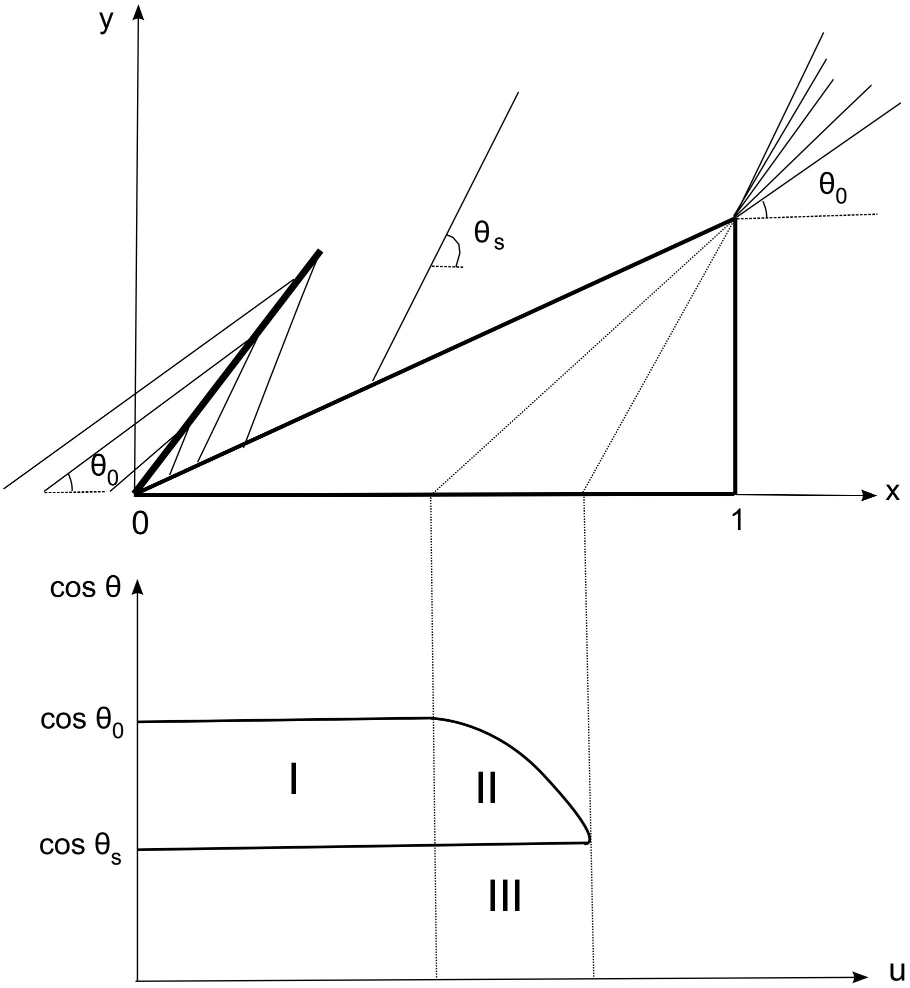

Figure 6.10: A wedge body in steady supersonic flow

$$A_l = \int_0^{1-\tau/tan\theta_s} (cos\theta_0 - cos\theta)du \tag{6.11}$$

As it is already known, the u-coordinates are the locations of the projected characteristic lines onto the x-axis which again being projected vertically onto the u-axis. So, the integration 6.11 is performed in a domain of [0,u_s], with the shoulder point location of $u_s = 1 - \tau/tan\theta_s$. The (cos θ)-graph is an illustration of the integral (6.11). This graph as already known is constructed by projecting the characteristics on the horizontal line through the leading edge. This is simply done by letting the Γ^+ characteristics cross the upper surface without changing their direction. The part that needs more concern is the shoulder point x_s, because at this point we have the θ_s characteristic, the expansion wave characteristics and also the θ_0 characteristic. The asymptotic shock strength area for this wedge contour is the sum of the area's I and II in (cos θ)-graph. The area I is easy to calculate:

$$A_I = (cos\theta_0 - cos\theta_s)(1 - \tau/tan\theta_0) \tag{6.12}$$

At the rear part of the body we get a curved trajectory in the (cos θ)-plot because as it was mentioned there are two values of cos θ present at the shoulder point. So, the area under this curved line can be determined by the following expression:

$$A_{II} + A_{III} = \int_{\tau/tan\theta_s}^{\tau/tan\theta_0} cos\theta(u)du \tag{6.13}$$

The $\theta(u)$ for this curved line is described as follows:

$$\theta(u) = tan^{-1}(\tau/u) \tag{6.14}$$

The equation (6.20) becomes:

$$A_{II} + A_{III} = \int_{\tau/tan\theta_s}^{\tau/tan\theta_0} cos(tan^{-1}(\tau/u))du \tag{6.15}$$

The integration (6.15) gives us the following:

$$A_{II} + A_{III} = \tau(1/sin\theta_0 - 1/sin\theta_s) \tag{6.16}$$

The area A_{III} is simply the following equation:

$$A_{III} = cos\theta_s(tau/tan\theta_0 - tau/tan\theta_s) \tag{6.17}$$

All these area's gives us the total area for $A_I + A_{II}$;

$$\begin{aligned} A_I + A_{II} + A_{III} - A_{III} \quad = \quad & (cos\theta_0 - cos\theta_s)(1 - \tau/tan\theta_0) \\ & +\tau(1/sin\theta_0 - 1/sin\theta_s) \\ & -cos\theta_s(tau/tan\theta_0 - tau/tan\theta_s) \end{aligned} \tag{6.18}$$

This is the measure of the asymptotic shock strength for a 2D wedge body in a steady supersonic flow.

6.5.2 A wedge contour with one kink

In the next step to the optimized contour it is decided to bring a kink in the upper surface of the wedge body from previous section, see point d in figure 6.11. This body is conditioned by a certain thickness τ and a chord line of l_{ac}=1.0. As figure 6.11 illustrates, the expansion process is divided over two angles, which results in two centered expansion waves at points d and f. This special geometry will result in a shock-expansion-expansion interaction situation. In order to find the magnitude of the asymptotic shock we apply again the known integration (6.11) for this case. In the same way as the wedge body, the Γ^+ characteristics are projected on the u-axis to determine the θ distribution along the projected line. In the ($\cos\,\theta$)-graph due to the shock wave there appears a discontinuous jump at the leading edge from $\cos\,\theta_0$ to $\cos\,\theta_1$. Because of the first centered expansion at point d, the graph will follow a curved trajectory from $\cos\,\theta_1$ to $\cos\,\theta_s$. The expansion

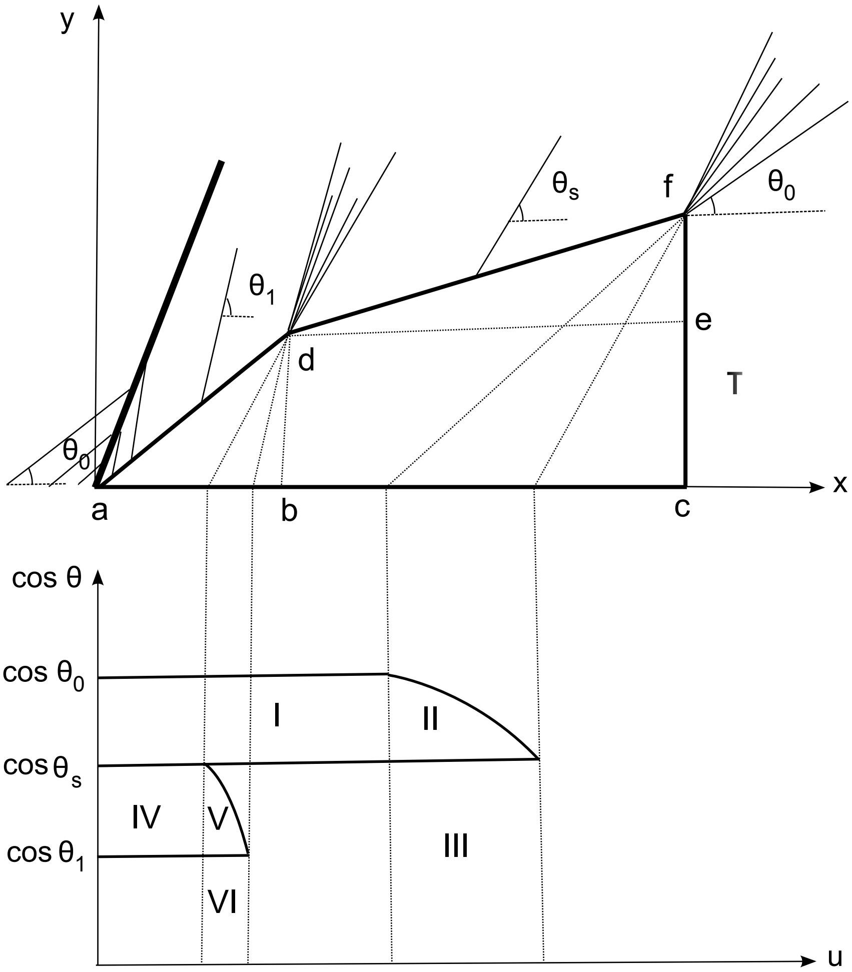

Figure 6.11: A wedge contour with a kink in steady supersonic flow

wave at the shoulder point results also in a curved path from cos θ_s back to the free stream level cos θ_0. In order to obtain the measure for the asymptotic shock strength we repeat again the steps which have been taken in the previous case. It means the sum of the area's *I*, *II*, *IV* and *V* will be the desired measure for this configuration. The area *I* is easy to determine as follows:

$$A_I = (cos\theta_0 - cos\theta_s)(1 - \tau/tan\theta_0) \tag{6.19}$$

The area under the curved line due to the second expansion at the shoulder point will be the following:

$$A_{II} + A_{III} = \int_{\tau/tan\theta_s}^{\tau/tan\theta_0} cos\theta(x)du \tag{6.20}$$

From equation (6.14), the integration of the curved line 6.20 can be expressed as follows:

$$A_{II} + A_{III} = \int_{\tau/tan\theta_s}^{\tau/tan\theta_0} cos(tan^{-1}(\tau/u))du \tag{6.21}$$

This integration will give us the following result:

$$A_{II} + A_{III} = \tau(1/sin\theta_0 - 1/sin\theta_s) \tag{6.22}$$

The area A_{III} is also easy to determine:

$$A_{III} = cos\theta_s(tau/tan\theta_0 - tau/tan\theta_s) \tag{6.23}$$

All these results give the total area for $A_I + A_{II}$;

$$\begin{aligned} A_I + A_{II} + A_{III} - A_{III} \quad = \quad & (cos\theta_0 - cos\theta_s)(1 - \tau/tan\theta_0) \\ & +\tau(1/sin\theta_0 - 1/sin\theta_s) \\ & -cos\theta_s(tau/tan\theta_0 - tau/tan\theta_s) \end{aligned} \tag{6.24}$$

The area formed due to the characteristic lines θ_1 and θ_s is the following:

$$A_{IV} = (cos\theta_s - cos\theta_1)(l_{ab} - \tau l_{ce}/tan\theta_s) \tag{6.25}$$

$$A_V + A_{VI} = \int_{\tau l_{ce}/tan\theta_1}^{\tau l_{ce}/tan\theta_s} cos\theta(u)du \tag{6.26}$$

Again from expression (6.14) the new integration for (6.26) becomes:

$$A_V + A_{VI} = \int_{\tau l_{ce}/tan\theta_1}^{\tau l_{ce}/tan\theta_s} cos(tan^{-1}(\tau l_{ce}/u))du \tag{6.27}$$

This integration results in the following:

$$A_V + A_{VI} = \tau l_{ce}(1/sin\theta_s - 1/sin\theta_1) \tag{6.28}$$

The area A_{VI} is just a rectangular:

$$A_{VI} = cos\theta_1(\tau l_{ce}/tan\theta_s - \tau l_{ce}/tan\theta_1) \tag{6.29}$$

All these results give the total area for $A_{IV} + A_V$ as follows:

$$\begin{aligned} A_{IV} + A_V + A_{VI} - A_{VI} &= (cos\theta_s - cos\theta_1)(l_{ab} - \tau l_{ce}/tan\theta_s) \\ &+\tau l_{ce}(1/sin\theta_s - 1/sin\theta_1) \\ &-cos\theta_1(\tau l_{ce}/tan\theta_s - \tau l_{ce}/tan\theta_1) \end{aligned} \tag{6.30}$$

The sum of equations (6.24) and (6.30) gives the total asymptotic shock strength caused by the wedge contour with one kink at its surface.

$$\begin{aligned} A_I + A_{II} + A_{III} - A_{III} + A_{IV} + A_V + A_{VI} - A_{VI} &= (cos\theta_0 - cos\theta_s)(1 - \tau/tan\theta_0) + \\ &\tau(1/sin\theta_0 - 1/sin\theta_s) - \\ &cos\theta_s(tau/tan\theta_0 - tau/tan\theta_s) + \\ &(cos\theta_s - cos\theta_1)(l_{ab} - \tau l_{ce}/tan\theta_s) + \\ &\tau l_{ce}(1/sin\theta_s - 1/sin\theta_1) - cos\theta_1 \\ &(\tau l_{ce}/tan\theta_s - \tau l_{ce}/tan\theta_1) \end{aligned} \tag{6.31}$$

6.5.3 Comparison between the optimized and non-optimized contour, 1^{st} variant

After we have determined the asymptotic shock strength for the optimized contours, it is now time to check whether the theory behind it is well grounded or not. To do the validation job, we just need to compare the shock magnitude caused by a contour with a kink in its surface to the shock strength of a well optimized contour. But, it should be taken into consideration that these two bodies must have the same volumes because we are only interested to see that the achieved contours are well optimized for the asymptotic shock strength, see figure 6.12. And for this validation analysis we only use the term A_l which is an indication for the asymptotic shock strength. The place of the kink determines the geometry and subsequently the volume of a non-optimized contour. Figure 6.13 depicts the corresponding A_l with volume V for both optimized- and non-optimized contours with a thickness τ=0.10 at M_0=1.9. From this figure it is obvious to see that first variant contours are well optimized.

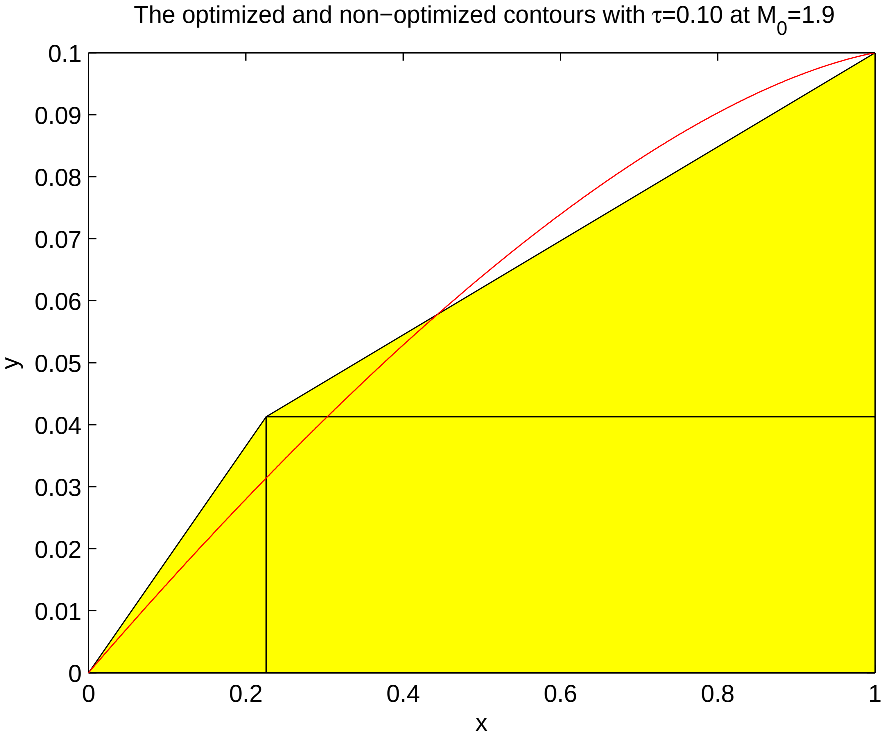

Figure 6.12: The optimized and non-optimized bodies

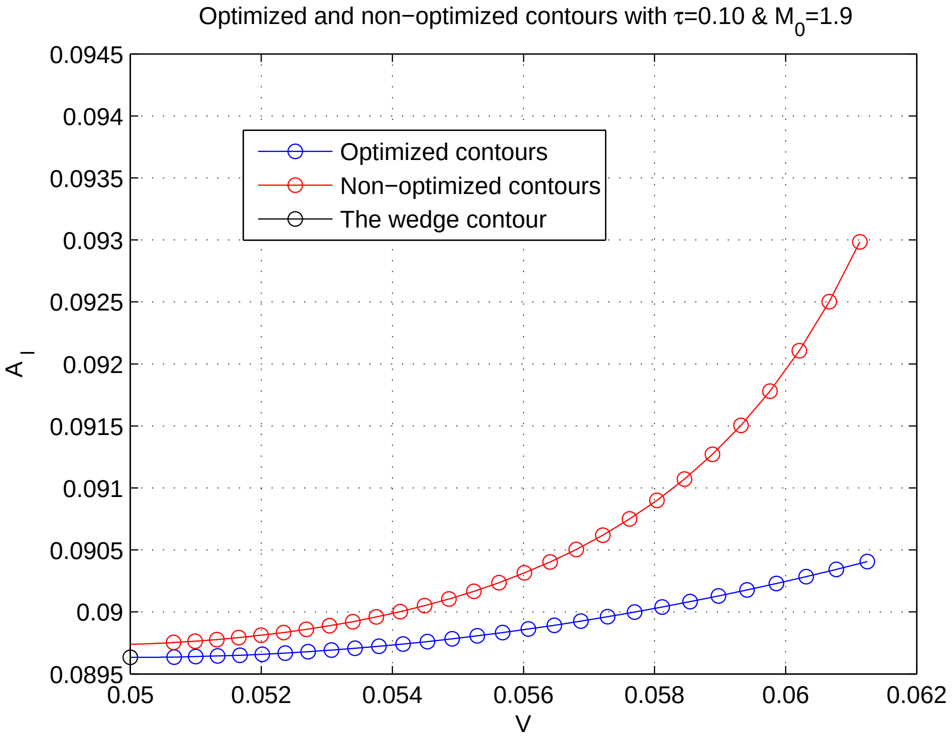

Figure 6.13: Comparison between optimized and non-optimized contours with τ=0.10 and $\mathrm{M}_0 = 1.9$

Figure 6.14 illustrates different contours with the corresponding difference rate η in A_l that can be improved by the optimized contours with the same volume. The difference rate η is defined as follows:

$$\eta = \frac{A_l^{opt} - A_l^{non-opt}}{A_l^{opt}} * 100\% \tag{6.32}$$

The negative sign for η can be explained by using figure 6.13 in which we can observe that the first contour variants are optimum. It means the value of A_l for the optimum contours is smaller than those of the non-optimized contours. In addition it is also to observe from this figure that moving the kink towards right on the horizontal line results in contours with a smaller volume and smaller difference rate η in shock strength. So, we can conclude from this that the first variant contours are well optimized in such a way that they cause the minimum possible asymptotic shock strength.

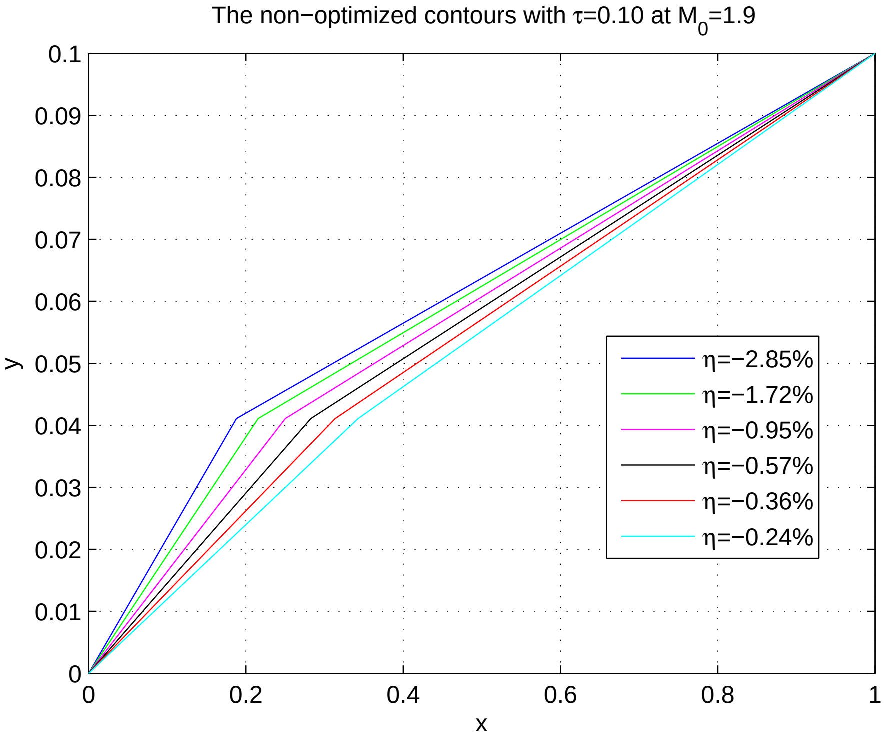

Figure 6.14: The non-optimized bodies

6.5.4 The asymptotic shock strength area, 1^{st} variant

The wedge and a larger contour with τ=0.10 which are optimal at M_0=2.0 have been chosen in order to visualize their corresponding ($\cos\,\theta$)-graph. These plots will illustrate as expected from figure 3.4 the Γ^+ characteristics distribution along the surface and eventually the asymptotic shock strength area. We start first with the wedge body. From figure 6.15, it is easy to notice that there are two important characteristic lines which are needed to construct the ($\cos\,\theta$)-plot. These are the characteristic with angle of θ_w and the

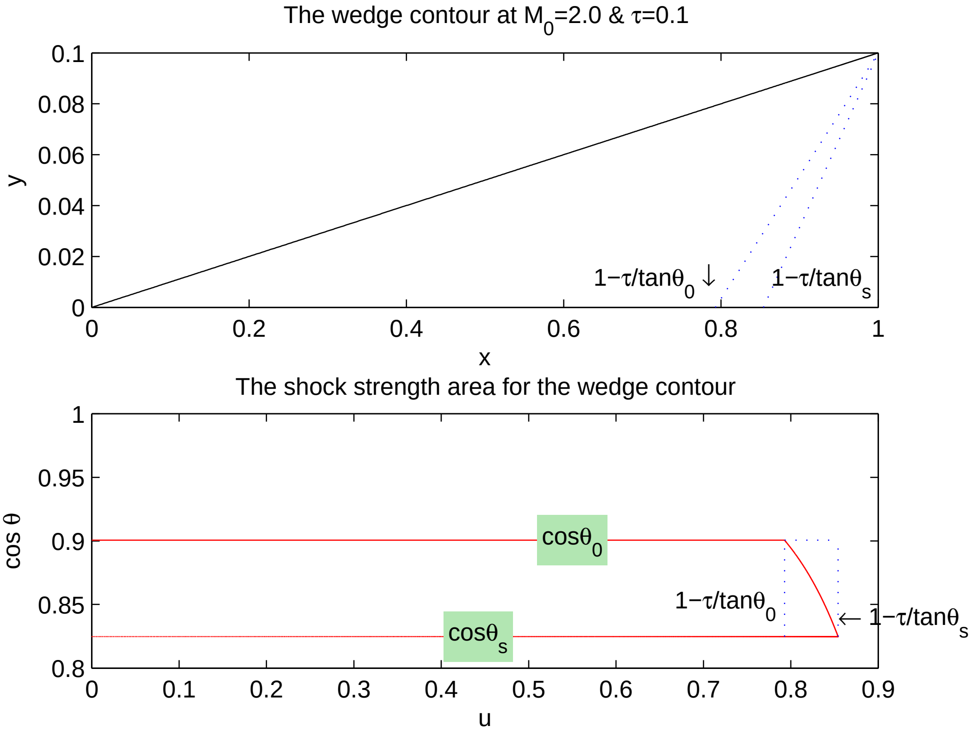

Figure 6.15: The shock strength area for the wedge body

characteristic line with θ_0 at the shoulder point. Because the contour is a wedge body, all of the Γ^+ characteristics directly from the leading edge where the shock wave occurs up to the shoulder point have an angle of θ_s. At the shoulder point there is a small surface deflection where Γ^+ characteristic with the θ_s-angle expands to the uniform flow where the Γ^+ characteristics have an angle of θ_0. So, this effect will cause a *Prandtl-Meyer* expansion wave which is nicely to see as a curved line in the (cos θ)-graph. This is also called the centered expansion fan which consists of infinite number of Mach waves. However, the Γ^+ characteristics distribution from nose to the shoulder point, the location of these characteristics on the u-axis and also the centered expansion wave occurrence at the shoulder point are the necessary elements to construct the corresponding (cos θ)-graph. In fact, the area indicated by the red lines in the (cos θ)-graph is a visualization of the asymptotic shock strength quantity for the wedge body.

We have analyzed the asymptotic shock strength area for a wedge body because of the simple distribution of the characteristics along the contour surface. But for an optimal contour with a larger volume for which the slope of the surface decreases continuously, the shock strength area seems to be different in two points, see figure 6.16. First the distribution of the Γ^+ characteristics along the u-axis. The red line below in figure 6.16 which represents the distribution of the characteristics seem to be increased continuously. Another obvious difference in this figure with the wedge body case is the centered expansion wave which occurs at the shoulder point. The centered expansion wave which is generated for the largest body gives the impression of being smaller than the expansion which is occurred for a wedge body. This small expansion fan is related to the small curved line in the (cos θ)-plot.

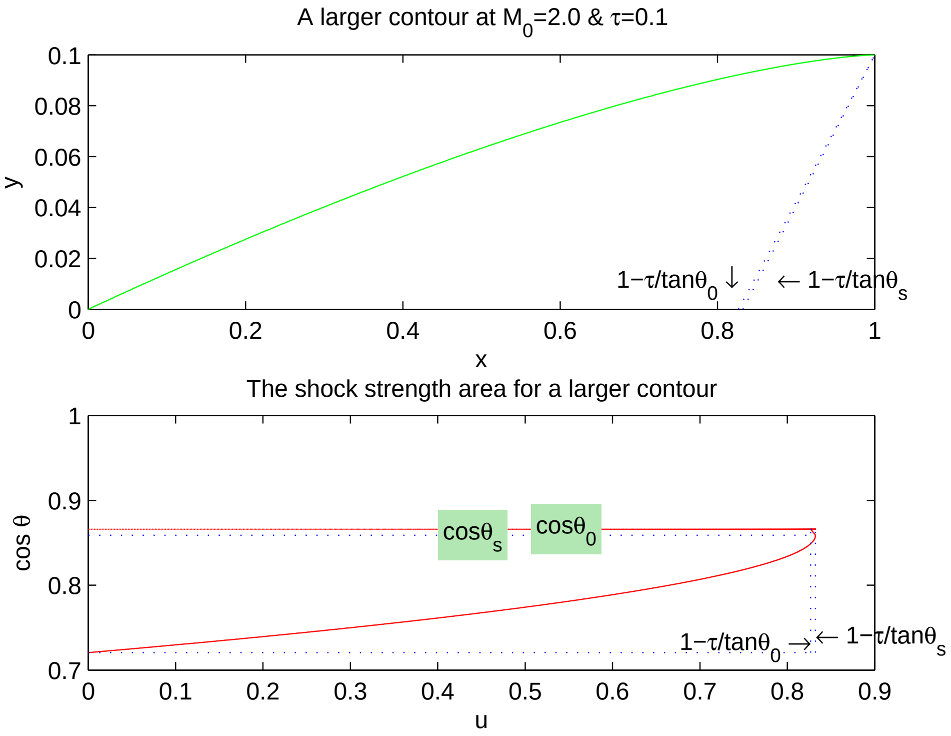

Figure 6.16: The asymptotic shock strength for the largest contour

6.6 Prandtl-Meyer expansion wave, 1th variant

At the end of section 6.5, it was mentioned briefly that there is an inverse relation between the magnitude of the centered expansion wave and the volume of the optimized contours. It means that contours with a larger volume have lower expansion wave at the shoulder point while a wedge body with the lowest volume shows the largest expansion. On the other hand, it is already known there is a proportional relation between the shock strength and the volumes of the optimal contours. So, from this we can conclude that there should be also a relation between the centered expansion wave and shock strength together with the volume of these contours.

As the Mach number of free flow is known, which is M_0=2.0, so the angle of the characteristic line θ_0 corresponding to this Mach number is also known. This characteristic line with angle θ_0 is in fact the last characteristic of the expansion wave. So, in order to analyze the expansion wave at the shoulder point x_s we only need to know the first characteristic of the expansion wave for different contours.

The relation between the shock strength and the expansion wave can be investigated with the interaction between these two waves. From the asymptotic behavior of the shock, we know already that the shock strength starts to become weak due to the merging with the expansion waves. So in order to investigate this matter, we just should know the shock path at the leading edge. The rotational invariant jump equation (3.2) has been developed to model the shock trajectory. As we know in this equation, θ_1 is the angle of the characteristic line directly behind the shock. Figure 6.17 indicates the slope of the shock

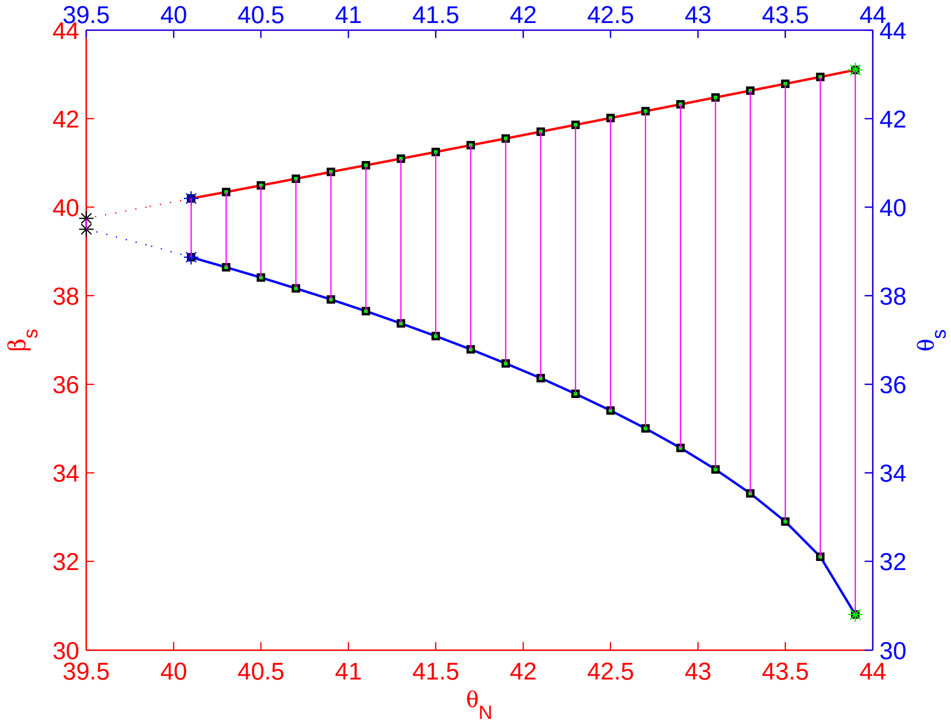

Figure 6.17: The angle of shock and first characteristic of the centered expansion

at the leading edge and the first characteristic line of the expansion wave at the shoulder point for different contours. This figure is based on M_0=2.0 and τ=010. The red line represents the shock angle β_s and belonged to the red axis and the blue line shows the slope of the first characteristic line of the centered expansion θ_s and belonged to the blue axis. And every point on these two lines indicate the optimum contours that can be achieved at this Mach number. Further, the horizontal lines in both axes show the slope of the nose for different bodies. From this figure we know that interaction between the shock and centered expansion wave has an inverse proportional relation with volume. Specifically this figure shows that the interaction between the shock and the first characteristic of the expansion wave for a larger body occurs later than a body with a smaller volume. So, in this case for the wedge body which has the smallest volume, the interaction between these two waves appears faster than any other body in the first variant.

If we take the red line with its red axis from figure 6.17, there remains only the blue line which is of high interest for the magnitude of the expansion waves, see figure 6.18. Figure

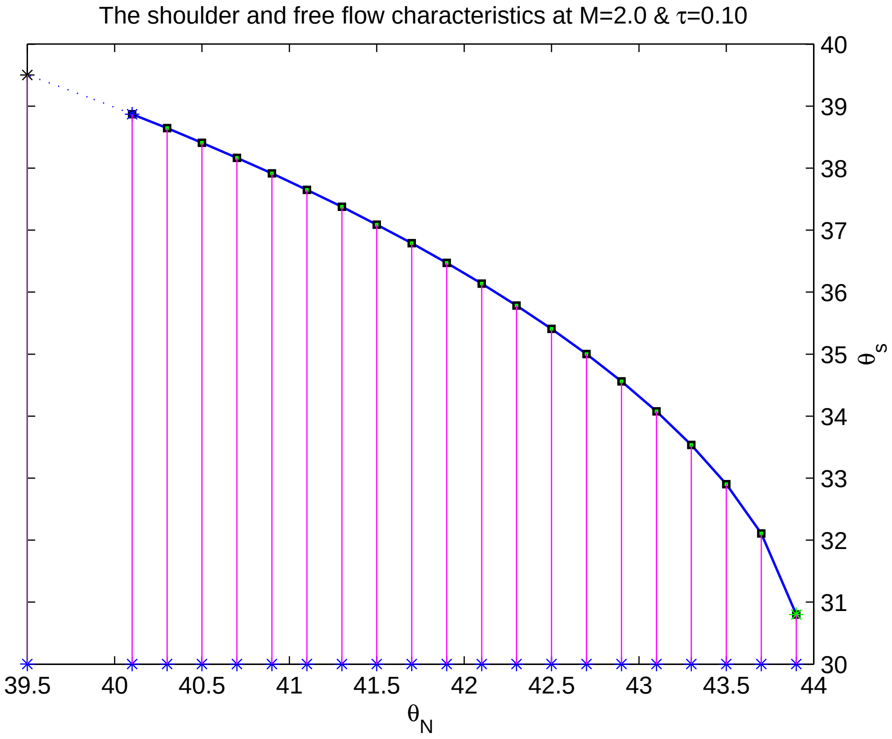

Figure 6.18: The centered expansion magnitude, 1^{st} variant

6.18 is a visualization of the expansion wave magnitude for contours with different volumes. As it can be seen in this figure, the wedge body with the smallest volume indicates the greatest expansion wave.

Figures 6.17 and 6.18 in combination with figure 6.7 gives us now the reason for why the wedge contour with the smallest volume has the lowest asymptotic shock strength. So, this can be now explained with the interaction between the shock wave and centered expansion wave and also the magnitude of the centered expansion wave. From figure 6.17 we observed that interaction between these two waves takes place slower than other larger contours. And from figure 6.18 we notice that the wedge body has also the largest centered expansion wave compared to the larger bodies. Figure 6.19 visualizes the comparison between the wedge and a larger optimum contour.

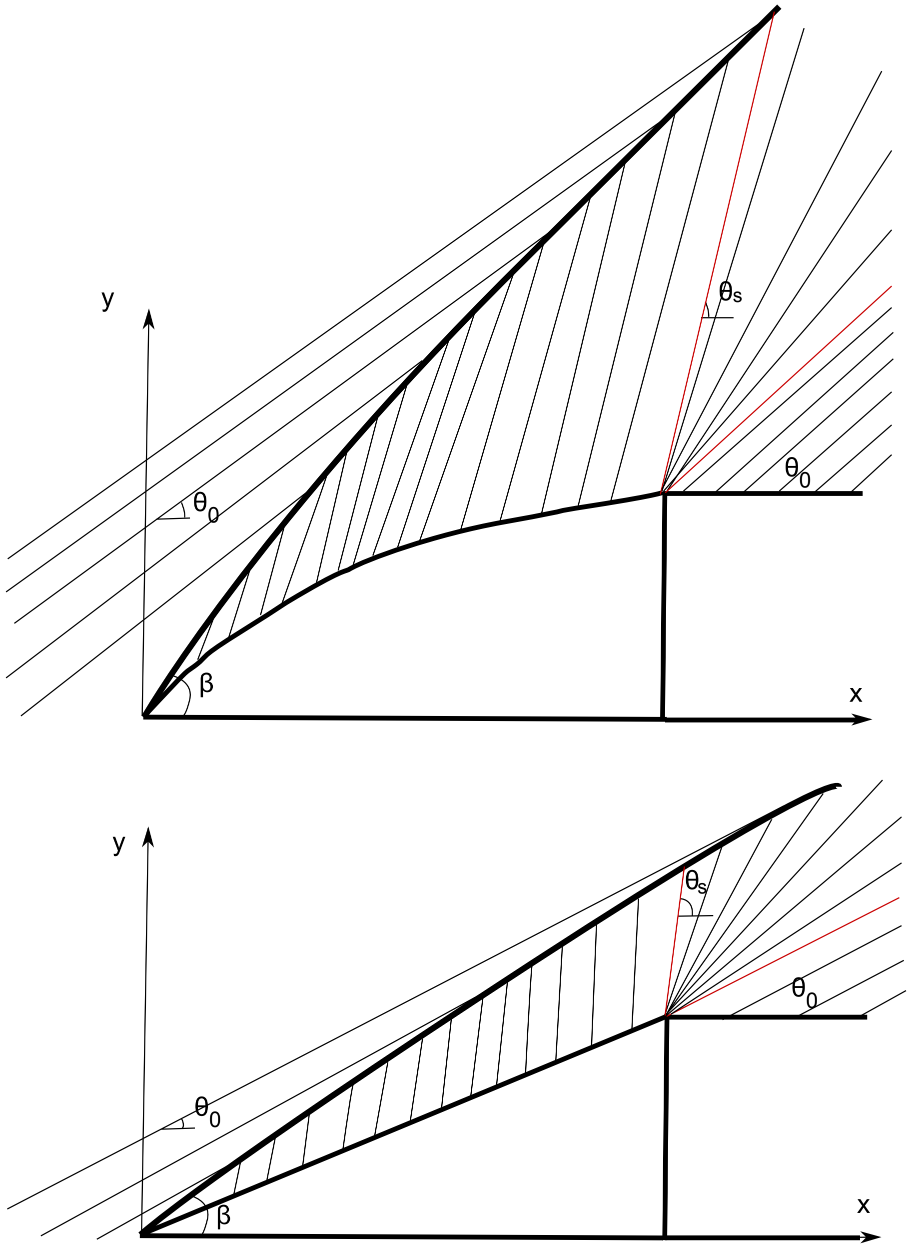

Figure 6.19: The centered expansion wave of a wedge and a larger optimum contour

6.7 Influence of Mach number on k_l, 1^{st} variant

It is of high interest now to know what happens when we put an optimal contour for a given τ, M_0 and volume in a supersonic flow with an Mach number. In order to investigate this, we first must know what happens to the Γ^+ characteristics distribution along the surface. For this reason we write equation (3.28) in the following way and call it function L:

$$\beta tan\theta - 1 - \tau F^{'}(x)(\beta + tan\theta) = 0 \tag{6.33}$$

The quantity of L is a function of the following variables:

$$L = L(F^{'}, \tau, \beta, \theta) \tag{6.34}$$

It is already known that $\tau F^{'}$ is the upper surface inclination. And from equation (3.9), β is a function of ν_0 and θ. The variable ν_0 depends on free flow Mach numbers which can be calculated by using the *Hall* function, see appendix A. The only variable which will be changed in equation (6.34) is the angle of the Γ^+ characteristics θ's along the surface. These new characteristic angles also can be determined from the compatibility relations for the isentropic flows for which the invariant V^- on the curved characteristics is constant. This results in $V^- = \nu_0 + \varphi_0 = \nu + \varphi$. So, it means all the values of ν on the body surface (i.e. behind the shock wave) can be determined by the following relation:

$$\nu = \nu_0 - \varphi \tag{6.35}$$

The variable φ_0=0 in this equation because the flow direction in an undisturbed flow is zero. Figure 6.20 illustrates how the characteristic lines are affected by the Mach number for a contour which is achieved at M_0=2.0 with τ=0.10. Due to simplicity, the first term of equation (3.36), $(cos\theta_0 - cos\theta)$ is used to show the influence of M_0 on Γ^+ characteristics. The first jump at u=0 represents the occurrence of the shock wave at the nose. Further decreasing the angle of the characteristics θ's means increasing the value for cos θ along the surface. And this leads again to an decreasing of the value $(cos\theta_0 - cos\theta)$. This is the reason why the upper line in this figure decreases. Further using the relation (1.1) gives us smaller values for θ_0 at higher Mach numbers. And this again gives higher results for $cos\theta_0$. The blue graph in the middle indicates the area for a contour with a volume of $V\approx$ 0.0571. We observe when we bring this contour in a flow with the Mach number M_0=1.5 the area covered by the characteristics will be increased, see the upper dark graph. And again if we bring the same contour in a flow with higher Mach numbers such as M_0=3.0 the covered area by the characteristic lines will be shrunk, see the green plot in figure 6.20. From this we conclude that the θ's of the characteristics for a certain contour will be increased at lower Mach numbers. This is also to be explained from relation (1.1) which means higher values for μ at lower Mach numbers and this again results in higher characteristic angle, θ.

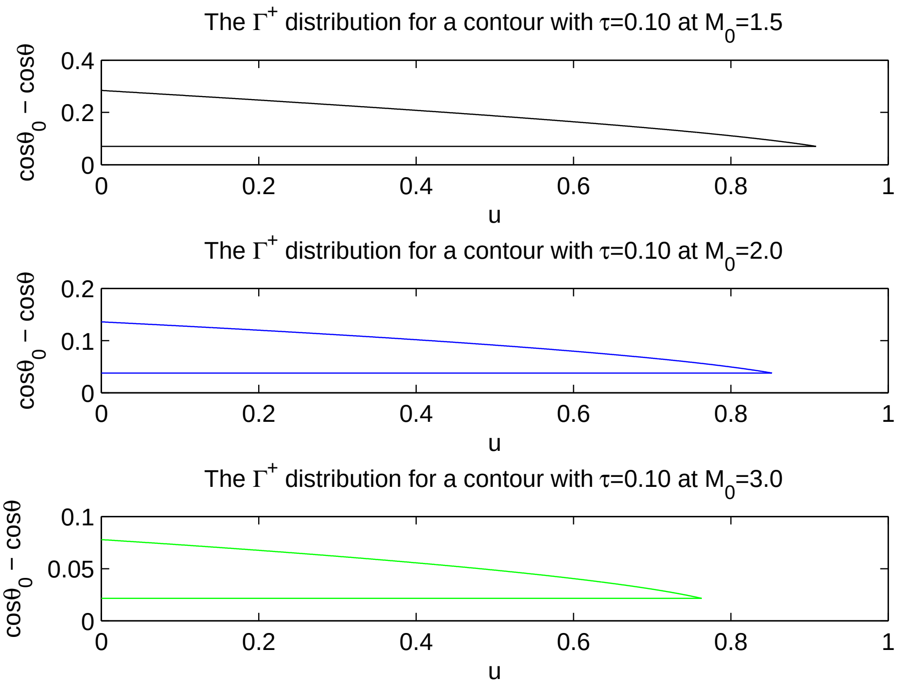

The Γ^+ distribution for a contour with τ=0.10 at M_0=1.5

The Γ^+ distribution for a contour with τ=0.10 at M_0=2.0

The Γ^+ distribution for a contour with τ=0.10 at M_0=3.0

Figure 6.20: The influence of Mach number on the characteristics distribution

In order to quantify the asymptotic shock strength k_l for the same contour at other Mach numbers we use figure 6.21. The red line indicates the k_l variation with M_0 for the optimum contour with a volume of $V\approx$ 0.0571. This contour is achieved at M_0=2.0 and indicated by a red square in figure 6.21. The blue signs in this figure represent the k_l variation for a non-optimized contour which was discussed in the previous part. The non-optimized contour has the same volume as the optimal contour. We observe that blue signs are right above the red line which means that the first variant contour is well optimal even for other Mach numbers. It is also to observe from this figure that k_l values for both optimal and non-optimal contours will be decreased for higher Mach numbers. In order to investigate the k_l-variation for two optimum contours with different volumes

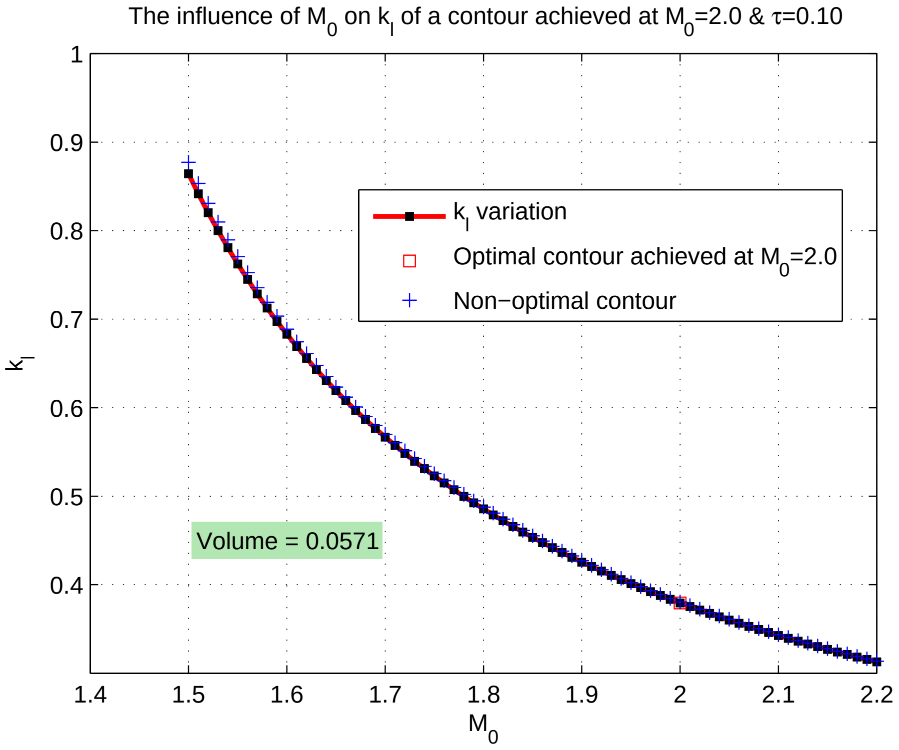

Figure 6.21: The influence of Mach number on the shock strength

we calculate the term $k_l^{wedge} - k_l^{opt}$ for a larger range of Mach number. This term shows the k_l-variation w.r.t the Mach number for a wedge body and an optimum contour with a volume $V\approx$ 0.0571. From figure 6.22, it is obvious that the wedge contour with a volume of V=0.05 shows lower values for k_l at lower Mach numbers, $1.5 \leq M_0 \leq 2.3$, compared to a larger optimum contour with a volume $V\approx$ 0.0571. Subsequently, this difference bacomes higher and goes asymptotically further for higher Mach numbers.

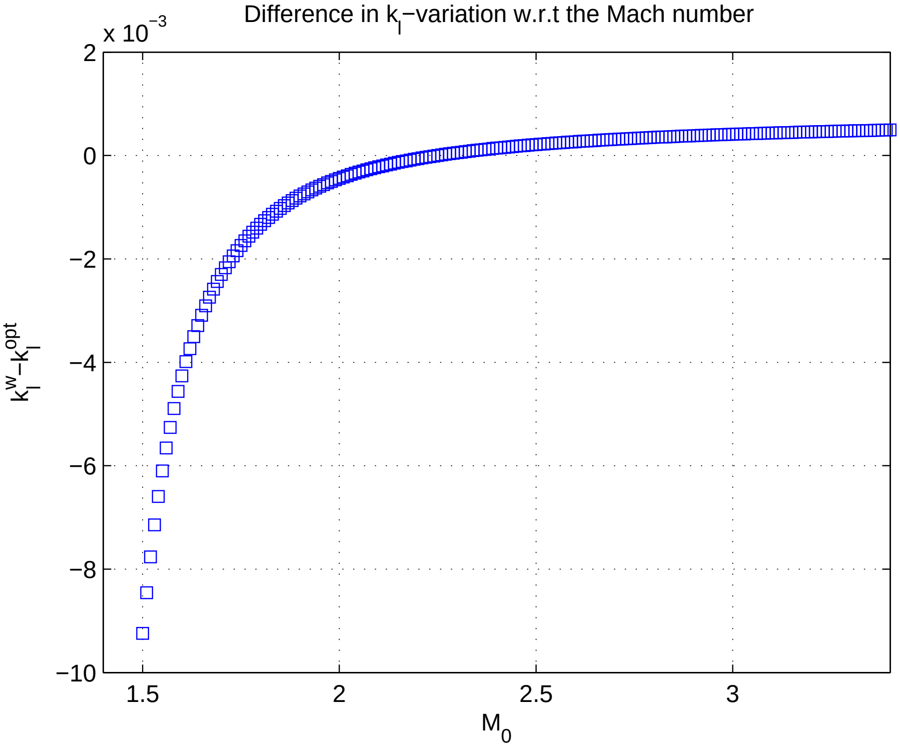

Figure 6.22: Difference in k_l-variation w.r.t Mach number, 1^{st} variant

6.8 M_0 variation for the first variant

In chapter 5 we have discussed different possible (H-p)-curves at different Mach numbers, see figure 5.1. Further, it was shown in order to achieve the first variant contours we can decrease the Mach numbers M_0 with the same constant τ=0.10. For this thesis the domain of Mach number is limited by $1.5 \leq M_0 \leq 2.0$ for the first variant. Due to the simplicity, in this part the two extreme cases at M_0=2.0 and M_0=1.5 will be compared and their properties will be discussed. It is worthy to note that the optimum contour which is obtained here at M_0=2.0 is able to generate centered expansion wave. The results for other cases for the rest of the Mach numbers can be found in appendix B. In figure 5.1 it seems as the (H-p)-curve based on M_0=1.5 being more extended towards right compared to the curve at M_0=2.0. So, it is expected that contours achieved at M_0=1.5 will have a larger volume compared to the contours obtained at M_0=2.0, see figure 6.23. This figure shows the largest possible contours at M_0=2.0 and M_0=1.5. From this we can conclude if in the first variant the Mach number M_0 decreases, it will lead to the contours with a larger volume. But it is of high interest to investigate what will be happened to the shock strength of these larger contours at lower Mach numbers. Figure 6.24 shows a comparison between the shock strength of the bodies which are obtained at M_0=2.0 and M_0=1.5. Figure 6.24 shows when the Mach number decreases, the asymptotic shock strength corresponding to the contours will be increased.

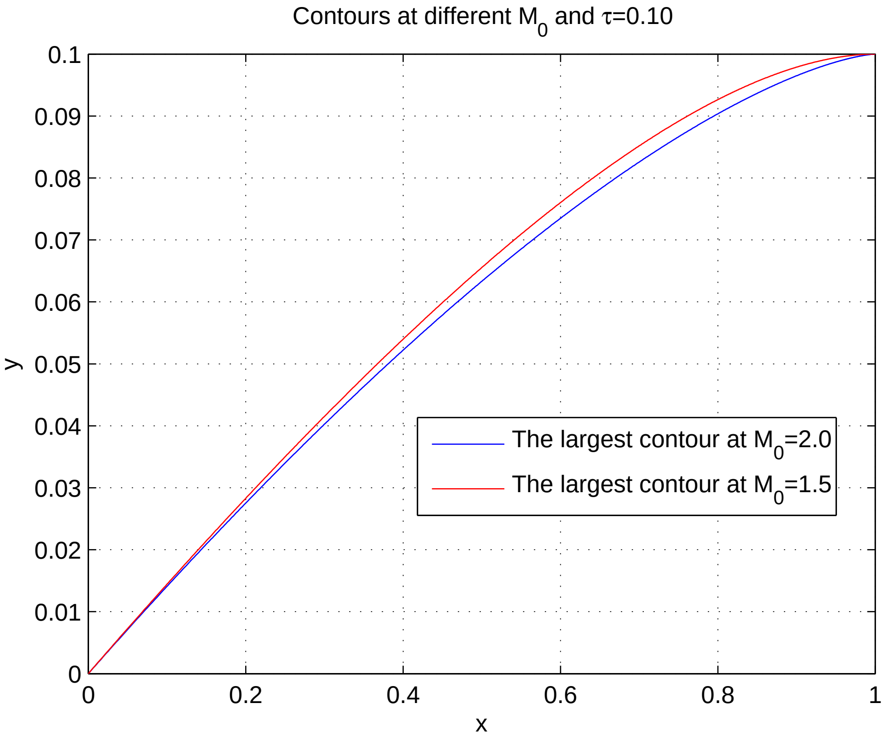

Figure 6.23: Contours at M_0=2.0 and M_0=1.5

It is also of high interest to find the most optimum contour in the first variant. For this purpose, we take the same contour from previous part with a volume of V≈0.0571

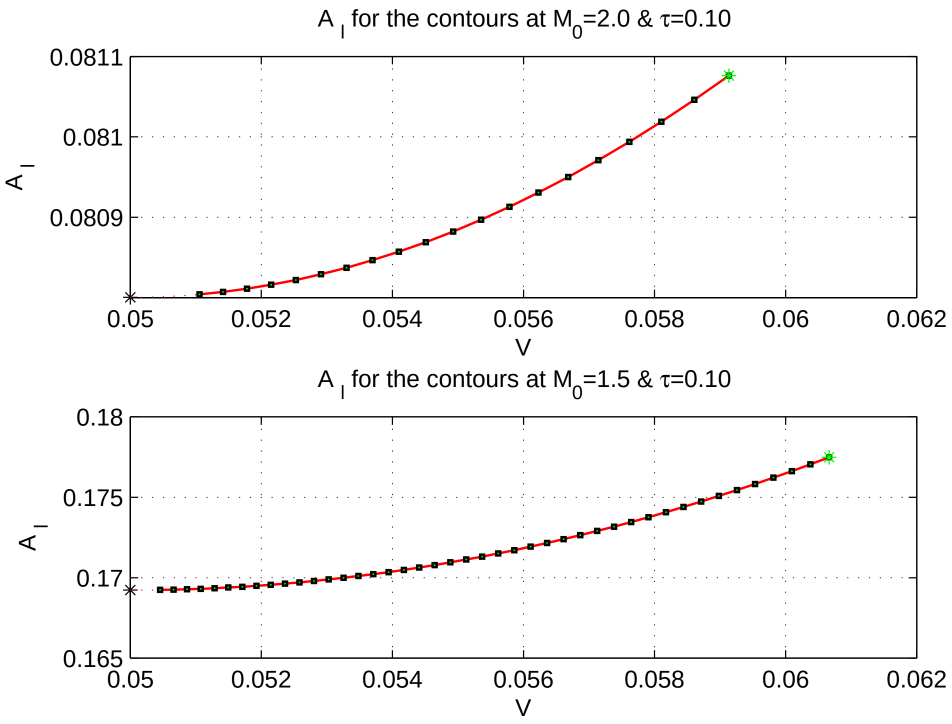

Figure 6.24: The asymptotic shock strength at M_0=2.0 and M_0=1.5

which was obtained at M_0=2.0 and τ=0.10. From figure 6.21 we know also that k_l has an inverse relation with Mach number M_0. So, in order to find the most optimum contour for different Mach numbers we should find the asymptotic shock strength for a contour with a volume of $V \approx 0.0571$ which is achieved in the limit of $1.5 \leq M_0 \leq 2.0$. The result of this investigation can be seen in figure 6.25. In this figure, the red line indicates k_l variation w.r.t the Mach numbers. This line is the same line as it has been shown in figure 6.21 with the non-optimized contour. The blue- and red sign indicate respectively the asymptotic shock strength for the optimized and non-optimized contour. These two points are placed very close to each other because of the small difference. But as we have observed from figure 6.13 the non-optimized contours cause a higher value of A_l. In addition, different points which are marked with different color, placed on the red line, represent the contours with a volume of $V \approx 0.0571$, but they are achieved at different Mach numbers.

The result of figure 6.25 is of high importance because it shows that all these contours which are achieved at different Mach numbers will show the same shock strength behavior for other Mach numbers. In other words, all contours with a certain volume which are obtained at different Mach numbers are also the most optimum contours for the first variant.

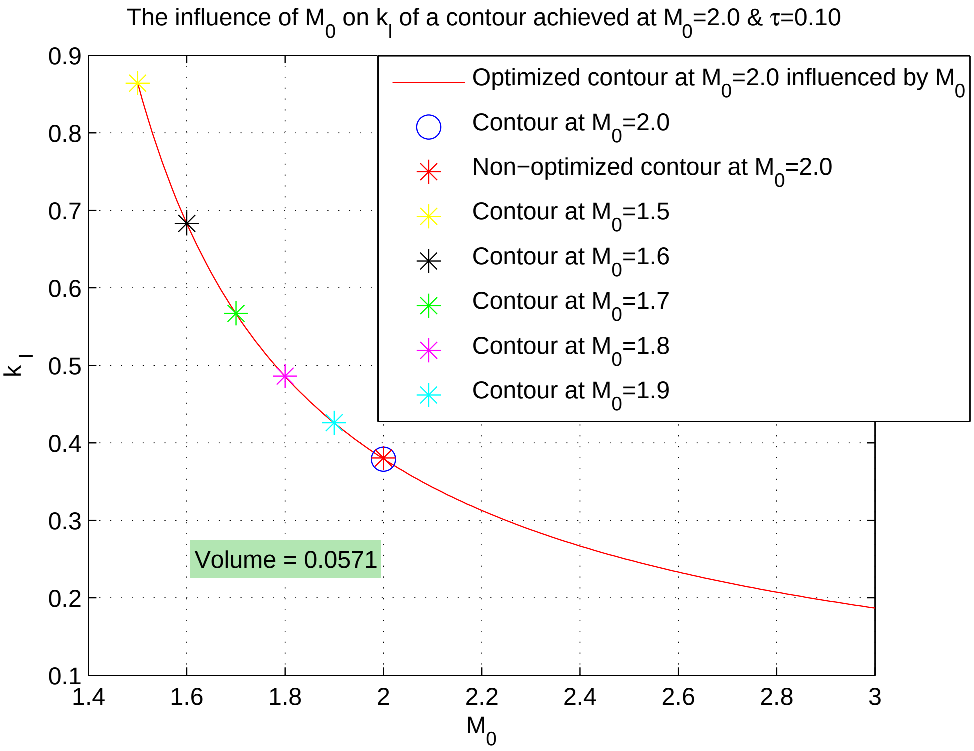

Figure 6.25: The most optimum contour in the first variant, τ=0.10 and different M_0

6.8.1 Same contour at different Mach numbers, 1^{st} variant

In section 6.7 it was chosen for a certain contour with τ=0.10 which was achieved at M_0=2.0. This contour has a certain volume $V\approx$ 0.0571. Further it was shown how the asymptotic shock strength k_l will be changed w.r.t the Mach number. In addition, we have investigated separately the value of k_l for the same contour which has been obtained at different Mach numbers in a range of $1.5 \leq M_0 \leq 1.9$. The results of this investigation have been depicted in figure 6.25. This figure shows that for the first variant an optimum contour can be chosen at any other Mach numbers for $1.5 \leq M_0 \leq 2.0$. This can explained for the asymptotic shock strength behavior remains similar for different Mach numbers. In order to analyze this issue the flow chart 6.26 is illustrated which shows the process that leads to the optimum contours. As we can observe from this diagram, every optimum contour has three input variables, M_0, τ and θ. But before having the optimum contour, these three variables result in a certain (H-p)-curve, see chapter 5. In section 6.7, it was shown that there are two relations available to achieve the new θ's when the Mach number is changed. These two relations have been defined by function L given by (6.34) and the compatibility relations (6.35).

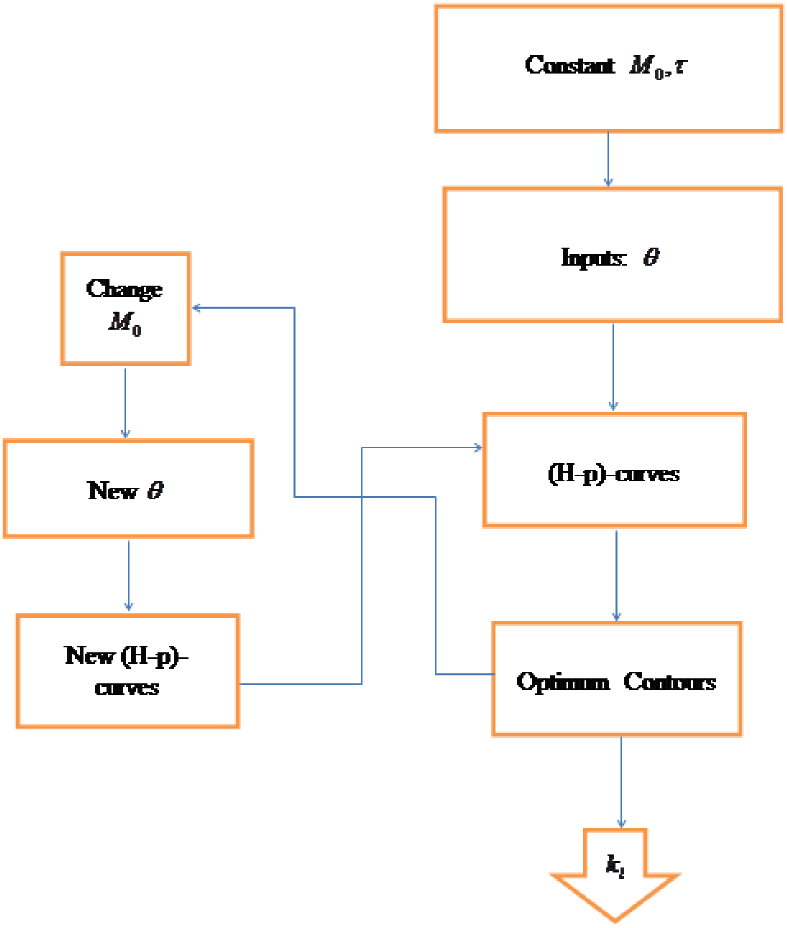

Figure 6.26: The flow diagram for the optimum contours

In order to prove that new θ's are the same θ's which have been used as inputs for the optimum contours at other Mach numbers we just need to compare the corresponding (H-p)-curves. In figure 6.27, the yellow curves are the needed (H-p)-curves for obtaining the optimum contours at different Mach numbers. The red curve at M_0=2.0 indicates the needed (H,p)-values for an optimum contour with a certain volume. And the dark curves at other Mach numbers show the new (H,p)-values as result of changing the Mach number for this contour. So, this proves that the first variant optimum contours are very remarkable in the sense they do not depend upon the Mach number. For this reason, these contours show similar k_l-behavior at different Mach numbers.

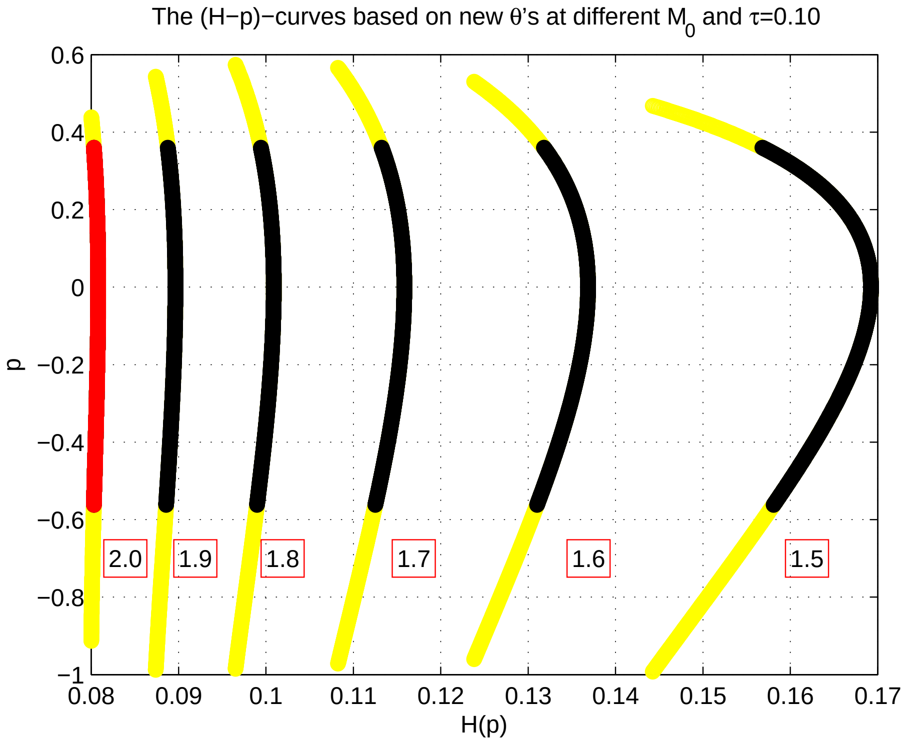

Figure 6.27: Coincidence of (H-p)-curves, 1^{st} variant

6.9 Thickness variation for the first variant

It the previous part 6.8, it was shown when the Mach number decreases and the thickness being constant τ=0.10, it will lead to the contours with larger volumes. But in chapter 5 it was also shown when the Mach number being constant and τ changes, it has effect upon (H-p)-curves, see figure 5.5. The limit for τ variation as it was indicated in chapter 5 is considered to be $0.05 \leq \tau \leq 0.15$. So, changing τ in this domain at M_0=2.0 will still mean the first variant contours. The results of the achieved contours for different τ can be found in appendix C. Figure 6.28 shows that the thickness has a proportional relation with both volume V and the shock strength A_l. With other words, if τ increases, it would be possible to achieve contours with larger volume. And these larger contours will also generate higher asymptotic shock strength.

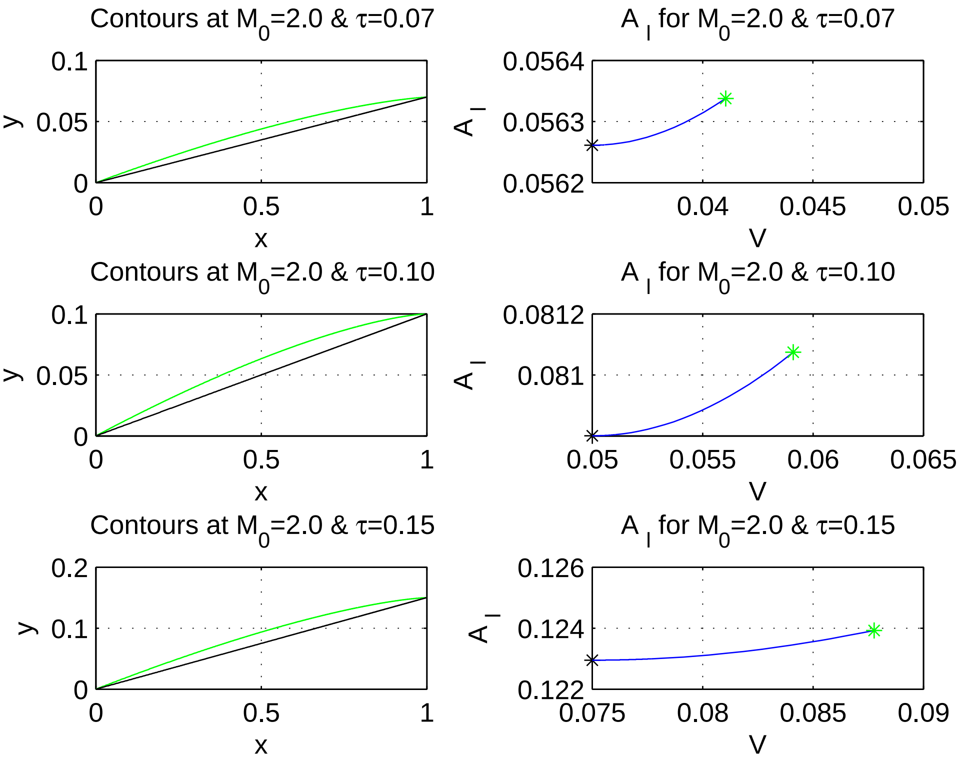

Figure 6.28: The variation of thickness for the first variant

6.9.1 Influence of thickness on k_l, 1^{st} variant

As we observed from section 6.8, figure 6.25 represents the k_l-variation for different Mach numbers. But it also shows that the first variant contours with the same volume which are obtained at different Mach numbers are not dependent on Mach number. Because they show the same asymptotic shock strength characteristic w.r.t other Mach numbers. In other words, every optimum contour with a certain volume can be achieved at different

Mach number. But, as we have mentioned above, we can also achieve optimum contours with different thickness while the Mach number remains constant, see figure 6.28. So, it is now interesting to investigate the relation between thickness and asymptotic shock strength. As we remember L given by (6.34) is also a function of τ. So, we take an optimal contour with a thickness τ=0.12 and M_0=2.0 which has a volume of $V \approx$ 0.071, see the blue mark in figure 6.29. Subsequently we assume that both Mach number M_0 and its geometry remain constant which is not physically possible. This is because changing the thickness let the geometry vary. But the idea is only to study the k_l-characteristic just as a function of τ. So, now by using the L-function, we can determine the new θ's for different τ's. And based on these new θ's we determine the corresponding values of k_l. The red line in figure 6.29 indicates the k_l-variation w.r.t the thickness τ for the mentioned contour. This line shows that the asymptotic shock strength k_l becomes larger with increasing variable thickness τ. It is also to observe from this figure that the optimal contours with a thickness τ=0.13 and τ=0.14 at M_0=2.0 are located on the red line. The reason for this is because as it was mentioned before the geometry of contour is assumed to be constant. So, this gives us now the conclusion that in order to have a contour with a certain volume which causes the minimum possible shock strength, it is better to have a contour with a smaller thickness. Figure 6.30 illustrates different geometries marked in figure 6.29. These contours have different thickness but the same volume. Another interesting point that can be studied is the asymptotic shock strength characteristic w.r.t

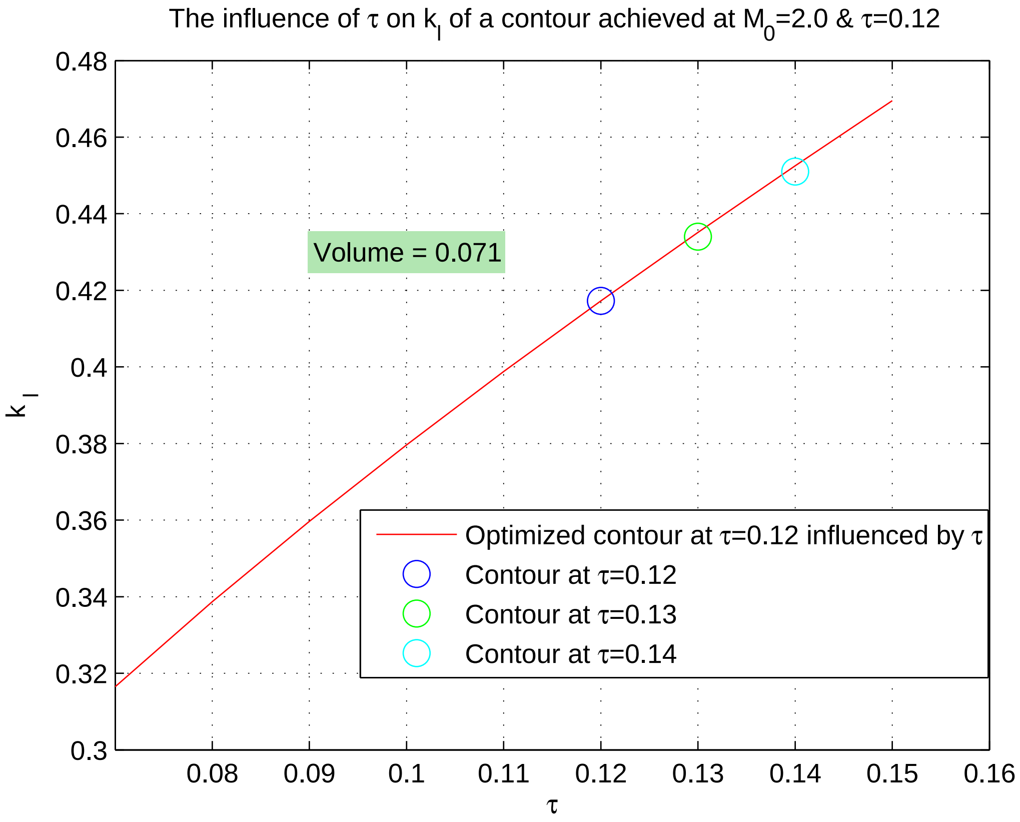

Figure 6.29: The most optimum contour in the first variant, M_0=2.0 and different τ

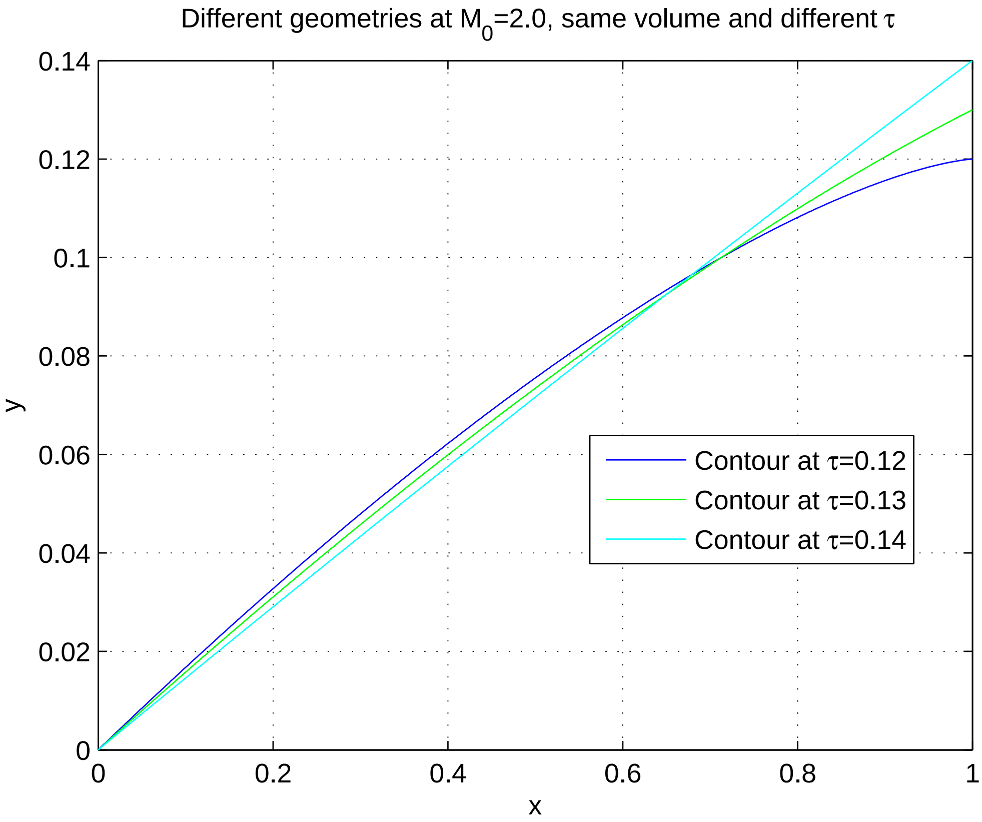

Figure 6.30: Different geometries same volume, different thickness, M_0=2.0

the Mach number for these three different contour geometries with the same volume. Figure 6.31 shows that indeed a contour with a smaller thickness shows lower asymptotic shock strength for different Mach numbers comparing to a contour with a larger thickness and a same volume. In other words, the asymptotic shock strength characteristic of these contours is different for different Mach numbers. So, the conclusion that can be derived from this figure is that the first variant contours are dependent on τ because contours with a certain volume and a smaller thickness generate lower asymptotic shock strength than those with the same volume but a larger thickness.

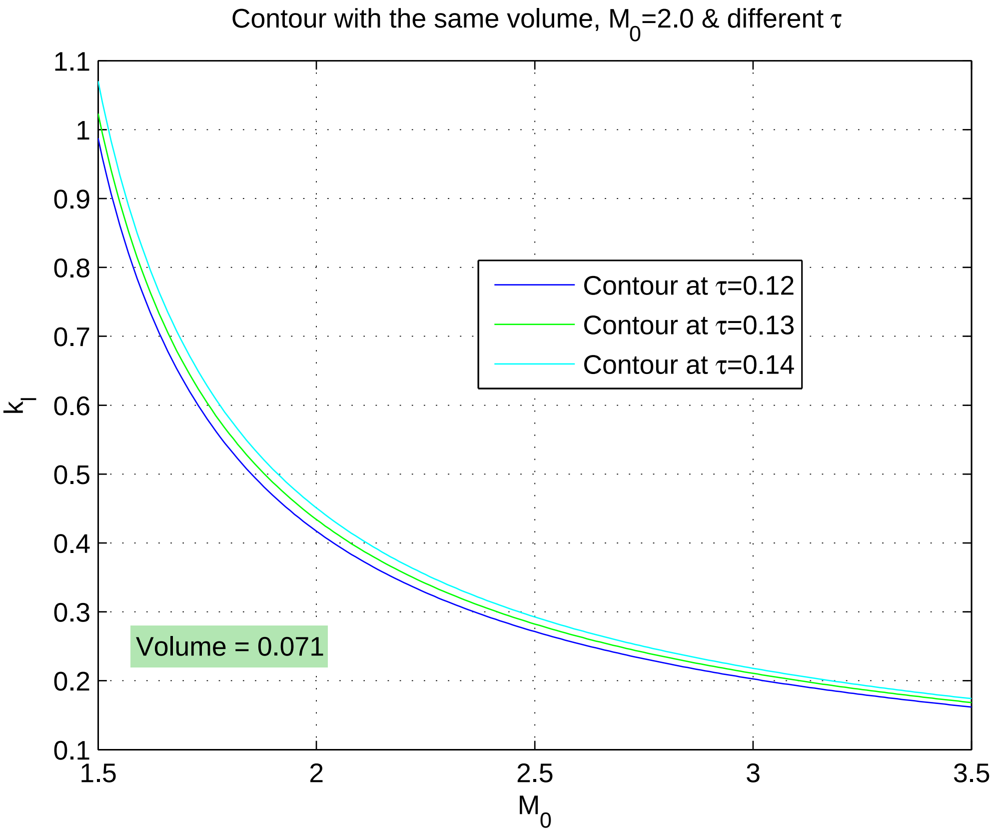

Figure 6.31: The asymptotic shock strength characteristic at different Mach numbers, different thickness

6.10 Aerodynamic properties for 1^{st} variant

As it was mentioned earlier in this report, in order to measure the asymptotic behavior of the sonic boom, the characteristic equations are considered to be used for a 2D, steady, inviscid and isentropic supersonic flow. Considering this assumption, the achieved first variant contours with τ=0.10 at M_0=2.0 can be investigated from an aerodynamic point of view. In this section, the flow properties such as Mach number, pressure, and entropy behind the shock wave will be studied. And finally the drag due to the body geometry and Mach number will be studied. The body which is chosen for this study will be the optimal contour with a volume of $V\approx0.0571$ from previous parts.

Flow velocity and pressure across the shock, 1^{st} variant

Due to the occurrence of the leading shock at the nose of the body, the flow velocities will be changed across the shock. Using equation (6.35) and the *Hall*-function enables us to find the corresponding Mach numbers along the body surface M_c. The Mach variation right behind the shock along the surface is illustrated in figure 6.32. As it can be noticed from this figure, the Mach number will be decreased directly after forming the shock and then will be increased again along the surface towards the shoulder. From relations for the isentropic flow, the static pressure to total pressure ratio is known as follows:

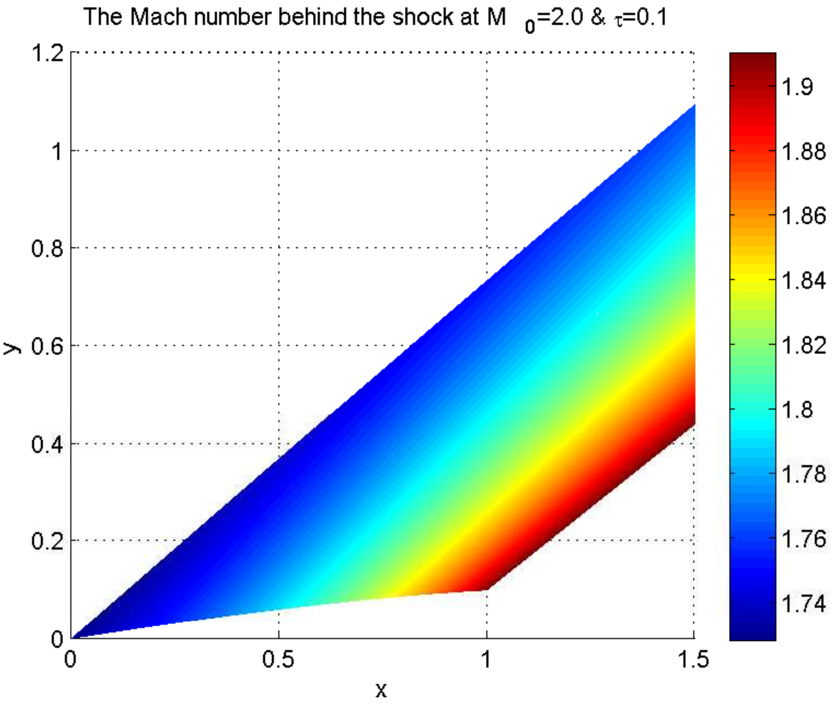

Figure 6.32: The Mach variation for a first variant contour

$$\frac{p_c}{p_t} = \left(1 + \frac{\gamma - 1}{2} M_c^2\right)^{\frac{-\gamma}{\gamma-1}} \tag{6.36}$$

And the same for free flow is the following:

$$\frac{p_0}{p_t} = \left(1 + \frac{\gamma - 1}{2} M_0^2\right)^{\frac{-\gamma}{\gamma-1}} \tag{6.37}$$

Combining equations (6.10) and (6.10) gives us the static pressure as follows:

$$\frac{p_c}{p_0} = \left(\frac{1 + \frac{\gamma-1}{2} M_0^2}{1 + \frac{\gamma-1}{2} M_c^2}\right)^{\frac{\gamma}{\gamma-1}} \tag{6.38}$$

Figure 6.33 represents the static pressure rise immediately after the shock and its decrease along the surface.

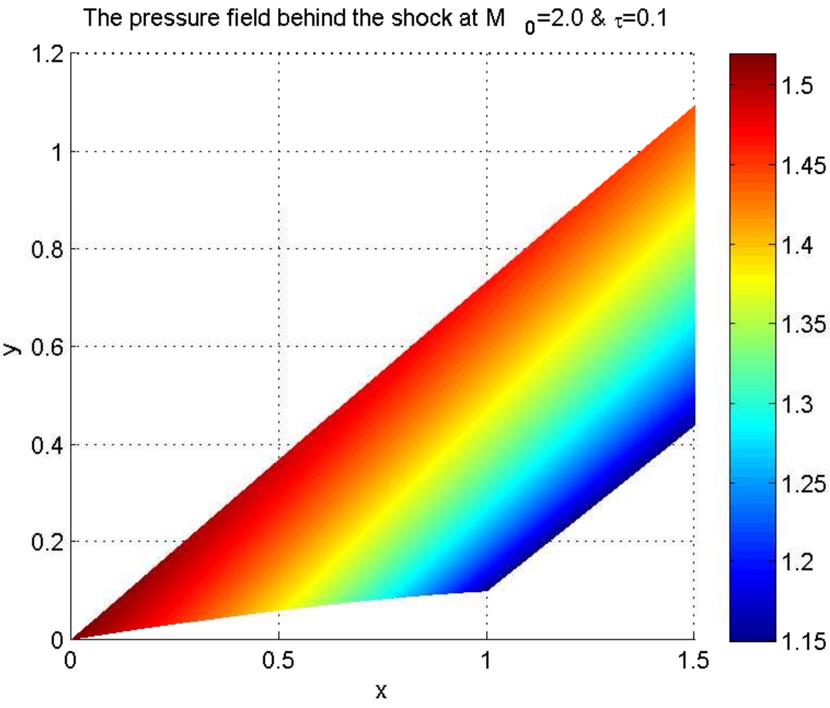

Figure 6.33: Static pressure at M_0=2.0 τ=0.10

And the following expression gives us the pressure coefficient along the body surface.

$$c_{p,c} = \frac{2\left(\frac{p_c}{p_0} - 1\right)}{M_0^2 \gamma} \tag{6.39}$$

Figure 6.34 shows the difference between the linearized supersonic pressure coefficient and the real pressure coefficient for the optimal body. The linearized supersonic pressure coefficient can be determined by the following equation:

$$c_p = \frac{2\varphi}{\sqrt{M_0^2 - 1}} \tag{6.40}$$

This expression indicates a proportional relation between c_p and the local surface incli-

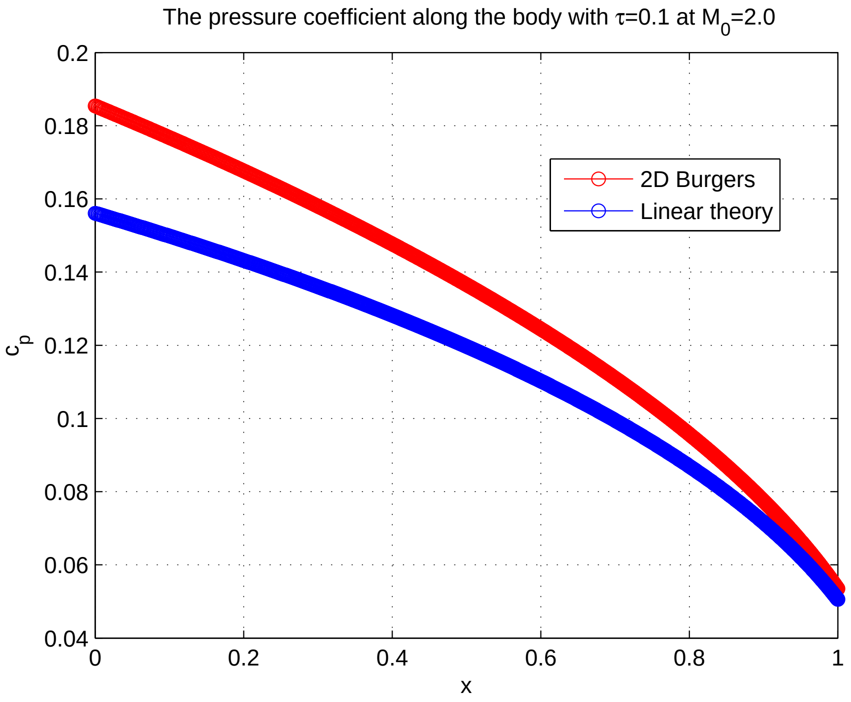

Figure 6.34: Comparison between the supersonic linear theory and 2D Burger

nation φ w.r.t. the free flow and an inverse relation with free flow Mach number M_0. From figure 6.34 it is obvious that c_p coefficient related to the linear theory decrease as the local flow direction decreases along the surface. In addition, from equation (6.39) the c_p coefficient for the first variant contour also decreases because of a decline in local pressure. Before we obtain the flow velocity, we need to determine the local speed of sound a_c. But from the known expression $a_c = \sqrt{\gamma RT}$, we first must determine the static temperature ratio as follows:

$$\frac{T_c}{T_t} = \left(\frac{1 + \frac{\gamma-1}{2} M_0^2}{1 + \frac{\gamma-1}{2} M_c^2} \right) \tag{6.41}$$

From this, the flow velocities along the surface can be determined with the following expressions:

$$\begin{aligned} u_c &= M_c a_c cos\varphi \\ v_c &= M_c a_c sin\varphi \end{aligned} \tag{6.42}$$

φ is the flow direction along the surface. The flow velocities along the body surface in x and y direction are plotted in figure 6.35. In this figure it is obvious that from the nose to the shoulder point the flow velocity in x direction will be increased while in the v direction decreased.

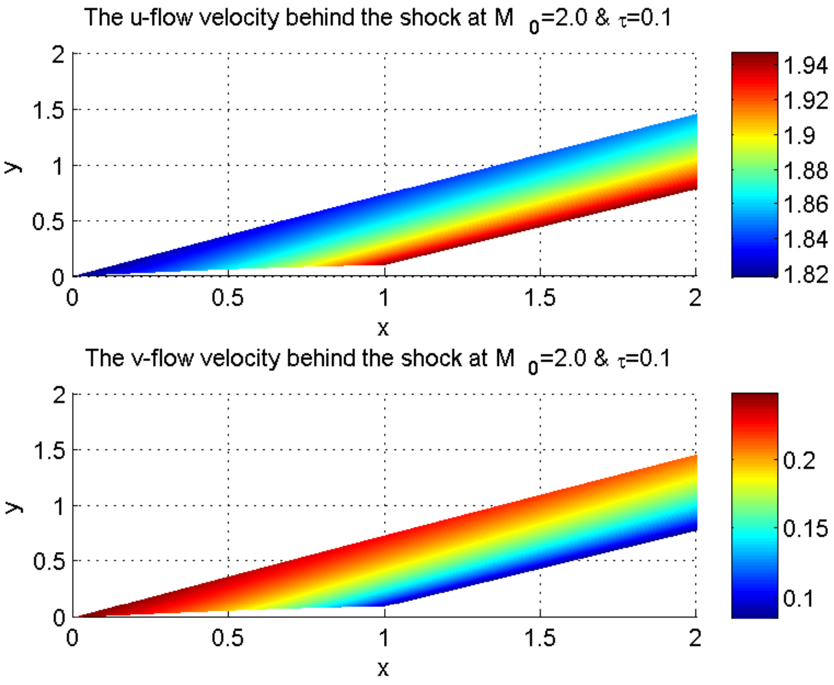

The u-flow velocity behind the shock at M_0=2.0 & τ=0.1

The v-flow velocity behind the shock at M_0=2.0 & τ=0.1

Figure 6.35: The flow velocities, 1^{st} variant

Entropy, 1^{st} variant

As it was mentioned in chapter 2 the characteristic method evaluates the occurrence of the shock wave in a flow which is assumed being isentropic. It means that flow is both adiabatic as well as reversible. But, in reality the shock wave is an irreversible process over which the entropy does not remain constant. In order to investigate the allowable values for free stream Mach number M_0, the second law of thermodynamics must be applied to the flow across a normal shock wave. But as we know, the shock which appears at the nose of the optimal contours is an oblique shock. So, in order to find the corresponding Mach number which is normal to the shock $M_{0,n}$ we use the angle of the shock β_s by using the rotational invariant jump equation (3.2). This results in the following expression for the normal Mach numbers:

$$M_{0,n} = M_0 sin\beta_s \tag{6.43}$$

Where β_s is the angle of the shock through the shock path. Now we can use the ratios of the thermodynamic properties across the normal shock in order to find the entropy change across the shock.

$$\Delta s = c_p ln\left\{\left[1+\frac{2\gamma}{\gamma+1}(M_{0,n}^2-1)\right]\frac{2+(\gamma-1)M_{0,n}^2}{(\gamma+1)M_{0,n}^2}\right\} - Rln\left[1+\frac{2\gamma}{\gamma+1}(M_{0,n}^2-1)\right] \tag{6.44}$$

From equation (6.44) it is obvious that Δs across the shock is only a function of $M_{0,n}$. If $M_{0,n}$=1.0 would be inserted into this equation it results in $s_2 = s_1$ and if $M_{0,n} > 1.0$, then $s_2 - s_1 > 0$. In other words, the second law of thermodynamics means $s_2 - s_1 \geq 0$. The upper figure 6.36 represents the normal upstream Mach numbers along the shock

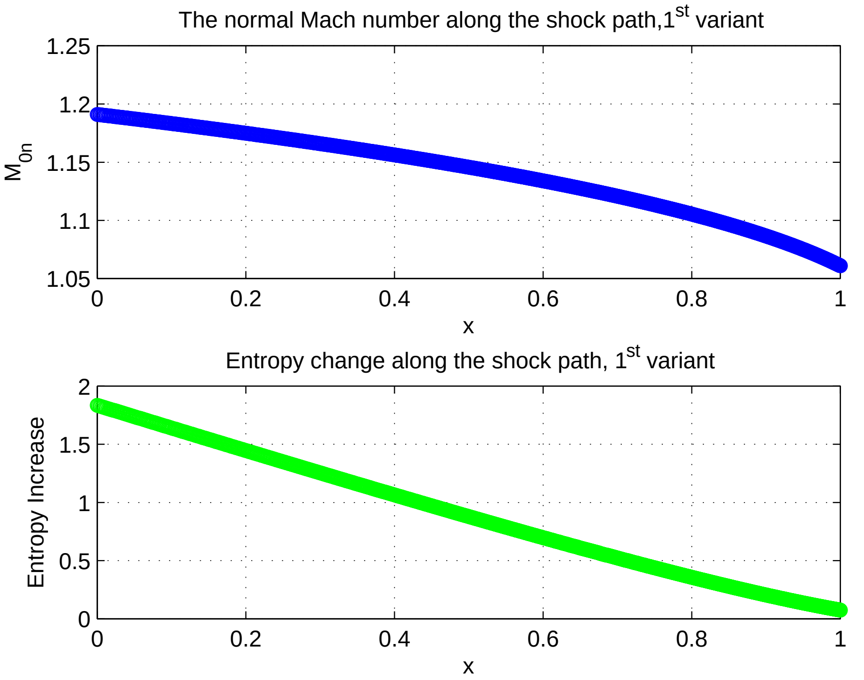

Figure 6.36: Upper plot: the normal Mach number, Lower plot: entropy change, 1^{st} variant

path which decreases from the leading edge to the shoulder point. Figure 6.36 below indicates also the decreasing of entropy change Δs along the shock. At the shoulder point the upstream Mach number becomes very close to 1.0 which also means that Δs approximates 0. Another interesting measurement across the shock wave is the total pressure ratio $\frac{p_{t,2}}{p_{t,1}}$ which is very useful to illustrate the entropy change due to being a dimensionless quantity. Since the total temperature is constant across the normal shock $(T_{t,2} = T_{t,1})$ the relation between the entropy and total pressure can be expressed by the following ratio:

$$\frac{p_{t,2}}{p_{t,1}} = e^{-(s_2 - s_1)}/R \tag{6.45}$$

From this relation we know now that the total pressure change $\frac{p_{t,2}}{p_{t,1}}$ is also a function normal free flow Mach number, $M_{0,n}$. Figure 6.37 shows the total pressure decrease along the shock wave. As it can be observed from this figure, the difference in total pressure between up- and downstream along the shock path is very low. At the shoulder point where the normal Mach number approaches 1, it seems that the total pressure ratio $\frac{p_{t,2}}{p_{t,1}}$ also comes closer to 1. This is because as it was mentioned before the entropy change at this point is approaching zero. So this gives us the conclusion that assuming the flow being isentropic is allowable.

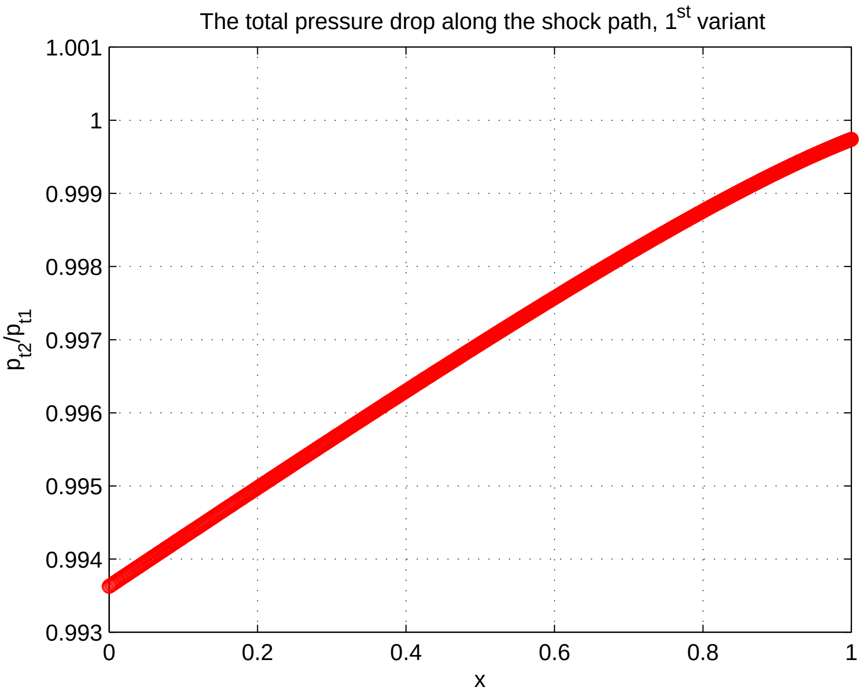

Figure 6.37: The total pressure drop along the shock path

6.11 Drag for the first variant contours

Due to the occurrence of the shock wave at the nose of the body, there will be formed the wave drag which is a characteristic for the supersonic flows. In this section the drag force and its relation with the asymptotic shock strength will be determined. The drag force can be calculated by the following integration:

$$D = \int_0^{\tau} \Delta p dy \tag{6.46}$$

Δp is the difference between pressure behind the shock and the free flow pressure, $p_c - p_0$. And in order to study the drag force in a non-dimensional form we convert the values for drag to the drag coefficient C_D by $C_D{=}D/qS$. In this equation q and S respectively are the dynamic pressure and the frontal body area which equals to τ. Figure 6.38 shows similar behavior as the graph 6.7. It means that contours with larger volumes cause higher drag force. What is also important is to analyze the relation between drag and the asymptotic shock strength for the optimized contours. The results for this study can be found in figure 6.39. This figure indicates a linear relation between these two quantities (i.e. A_l and C_D). The reults for other Mach numbers are illustrated in appendix D. As we can observe from these figures the same relation exists between parameters V and C_D and also between A_l and C_D for the Mach range $1.5 \leq M_0 \leq 1.9$. What is also of high interest is to take an optimum contour with τ=0.10 which is achieved at M_0=2.0 and see how the shock strength and drag force will be influence by the Mach number. Figure 6.40

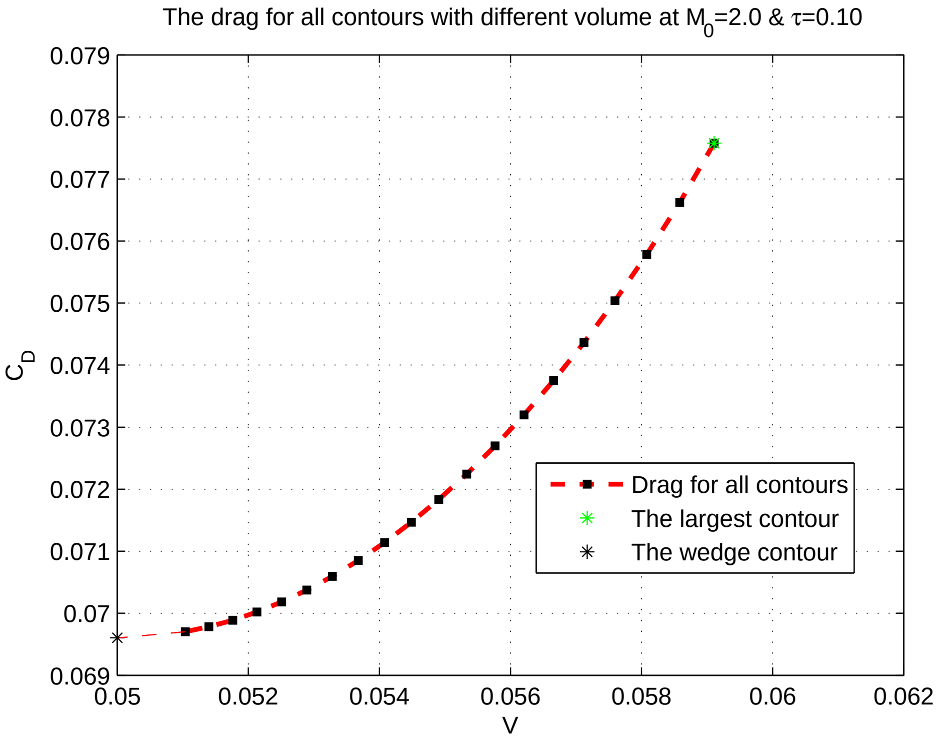

Figure 6.38: The drag coefficient for the optimal contours

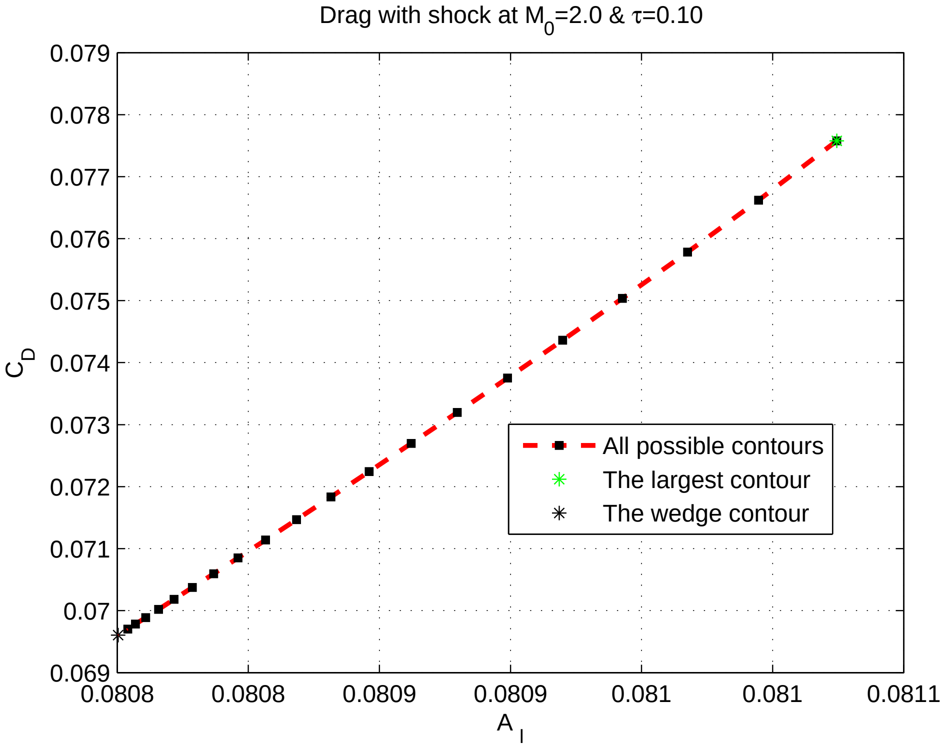

Figure 6.39: Drag with shock strength for the optimum contours

shows this effect on the optimal contour from previous part with a volume of $V \approx 0.0571$. This contour is shown with a blue star. And the dark and green stars indicate the same contour at Mach number M_0=1.5 and M_0=3.0. We notice from this figure that increasing the Mach number ceauses the shock strength and drag being decreased.

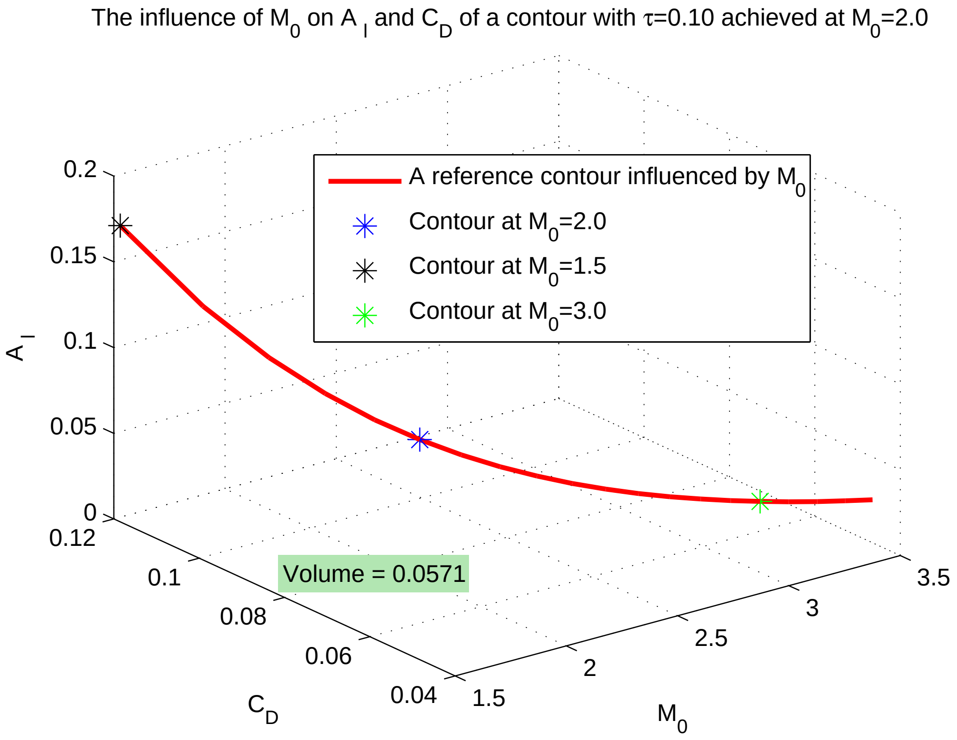

Figure 6.40: The influence of Mach number on shock strength and drag, 1^{st} variant

CHAPTER 7

NUMERICAL ANALYSIS FOR THE THIRD VARIANT

In chapter 6, the characteristics of the first variant contours were investigated to a large extent. In this chapter, the same process will be performed for the third variant. This process consists of the integration of third variant curve and the study on the asymptotic shock strength together with the expansion waves caused by the third variant contours. Furthermore, the influence of the variables M_0 and τ on third variant will be investigated. And finally the aerodynamic characteristics such as pressure, Mach number and entropy behind the shock for the third variant contours will be discussed. The drag force caused by these optimized contours will be another point to be analyzed in this chapter.

7.1 Integration of *H(p)* curve: third variant

In chapter 5 it was shown when τ=0.10, from M_0=2.22 to the higher Mach numbers the (H-p)-curves have a nose towards the left at p=0. Approaching this curve with a parabolic curve at p=0 shows us in this chapter that we can have an optimized contour with a concave surface, see figure 7.1. As we know from the first variant, in order to achieve this kind of contours we must integrate the (H-p)-curves. The integration for this curve will be the same as the first variant with a difference that the leading edge is the point with the negative value for p. So, the coordinates for the point n will be:

$$(H_n, p_n) = \left(c, \frac{dH_n}{dz}\right) \tag{7.1}$$

Again we use the *Heun*'s method to integrate the curved line as follows:

$$dz = \frac{(H_q - H_n)}{\frac{1}{2}(\frac{dH_q}{dz} + \frac{dH_n}{dz})} \tag{7.2}$$

Applying this equation to the whole of the curve results in the following equation for G:

$$G = -\frac{c - H(p)}{\lambda} \tag{7.3}$$

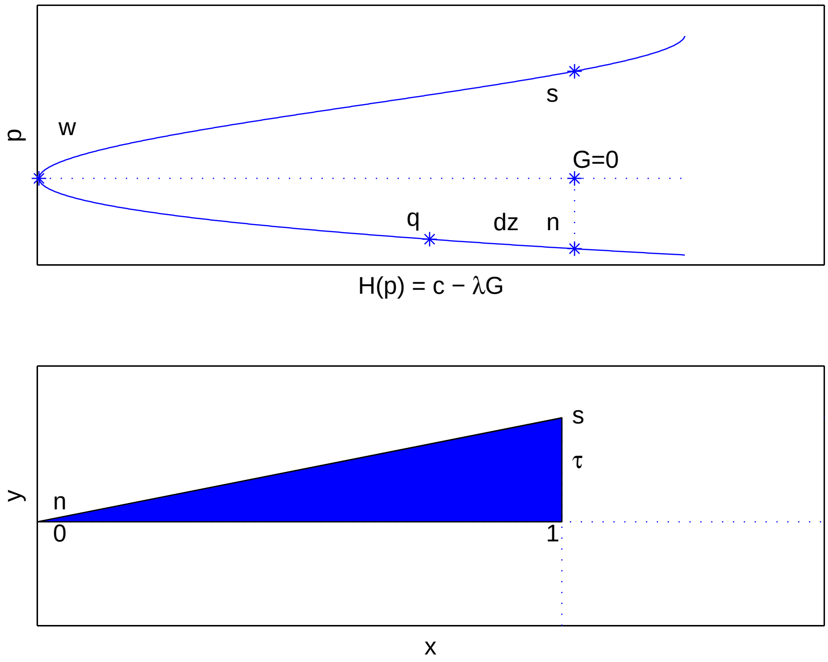

Figure 7.1: Upper plot: Third variant curve, Lower plot: Third variant contour

Knowing $F=G+x$, the third variant contour can be defined in *(x,y)* domain with $y=\tau F$. The third variant contour as it can be seen from figure 7.1 below is slender and has a concave upper surface.

7.2 Third variant geometries

As we have observed from the first variant, point n can be chosen in many places on the curve but with the condition that the corresponding shoulder point s can be found for it. The location of point n determines the length of (H-p)-curve and so the geometry of the contour. This is also the case for the third variant.

The largest curve

As we can obseve, points n and s shown in the upper figure 7.2 represent the most extreme points with the same value for *H(p)*. The angle of the characteristic in the undisturbed flow θ_0, is indicated by a dark sign in both figures. From the lower figure 7.2, we observe easily that the slope of the characteristics will be increased from the nose to the shoulder point. This is the reason why third variant contours have a concave surface.

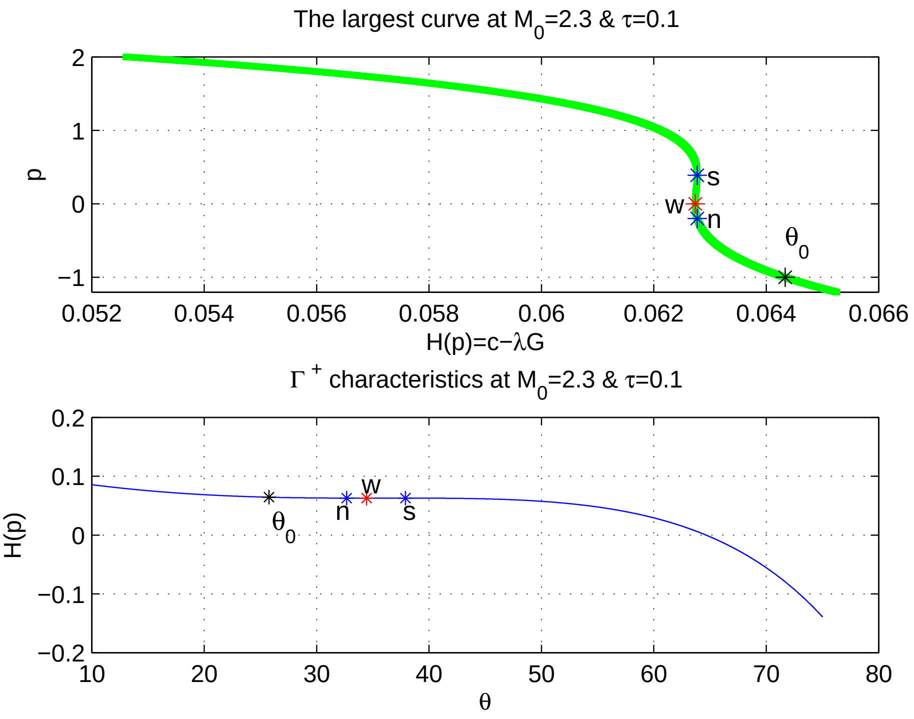

Figure 7.2: The largest curve for the third variant

The wedge contour

How closer we choose the point n to the wedge point w, how larger the contours will be. This is exactly the opposite of what we have observed from the first variant. So, it means that the wedge contour with a volume of 0.5τ becomes the largest possible contour for the third variant.

7.2.1 The resulting (H-p)-curves

As it said before, the upper figure 7.2 represents the largest possible (H-p)-curve for τ=0.10 and M_0=2.3. Figure 7.3 shows again the resulting (H-p)-curve in a smaller region for this Mach number.

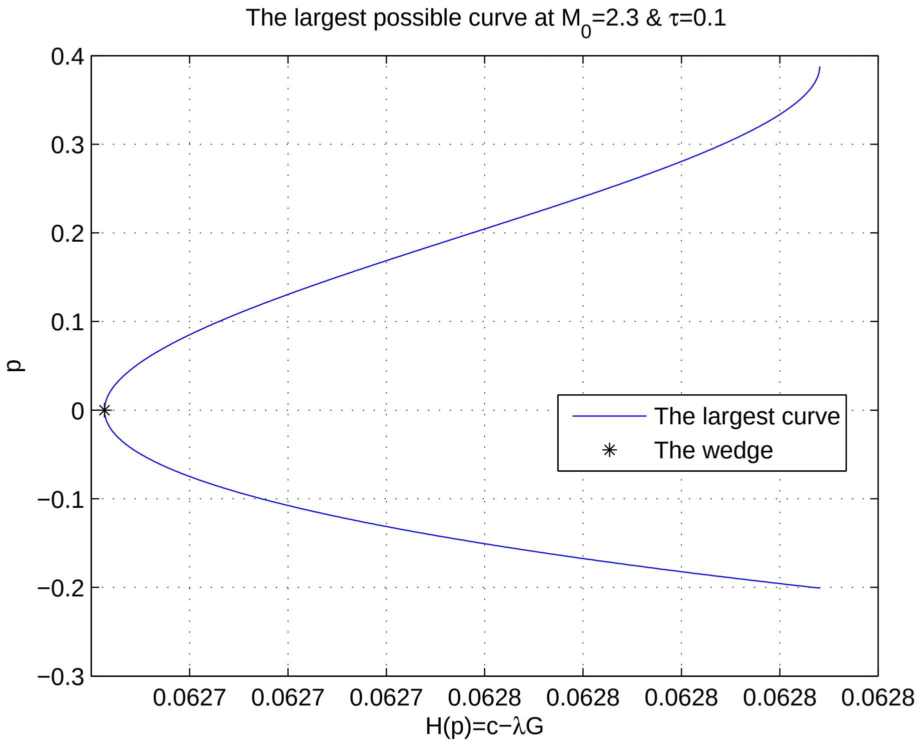

Figure 7.3: Upper plot: (H-p)-curve, Lower plot :(θ-H)-curve

7.2.2 The resulting contour function

Integration of H-p)-curve results in the unknowns c and λ. These values enable us to find the corresponding G-function by using equation (7.3). Figure 7.4 shows that the G-function of the third variant can be identified by the nose towards down. The negative values of G can be explained by the minus sign in equation (7.3). And knowing $y = \tau(x + G)$ we are now able to define the third variant contour as shown in figure 7.5. And the influence of constant c that can be chosen on the H-p-curve on the volume of the third variant contours is illustrated in figure 7.6. We can notice from this figure if point c is chosen far from the wedge point (when the H_c-value is larger), then the corresponding curve line becomes larger and this again results in a contour with a smaller volume.

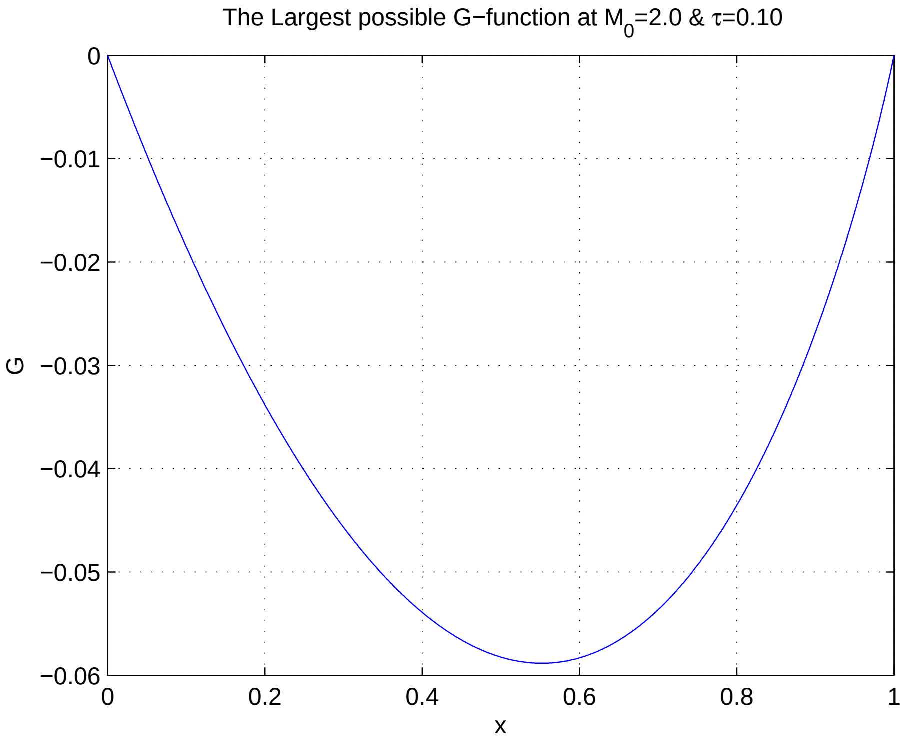

Figure 7.4: The corresponding G-function to the largest curve

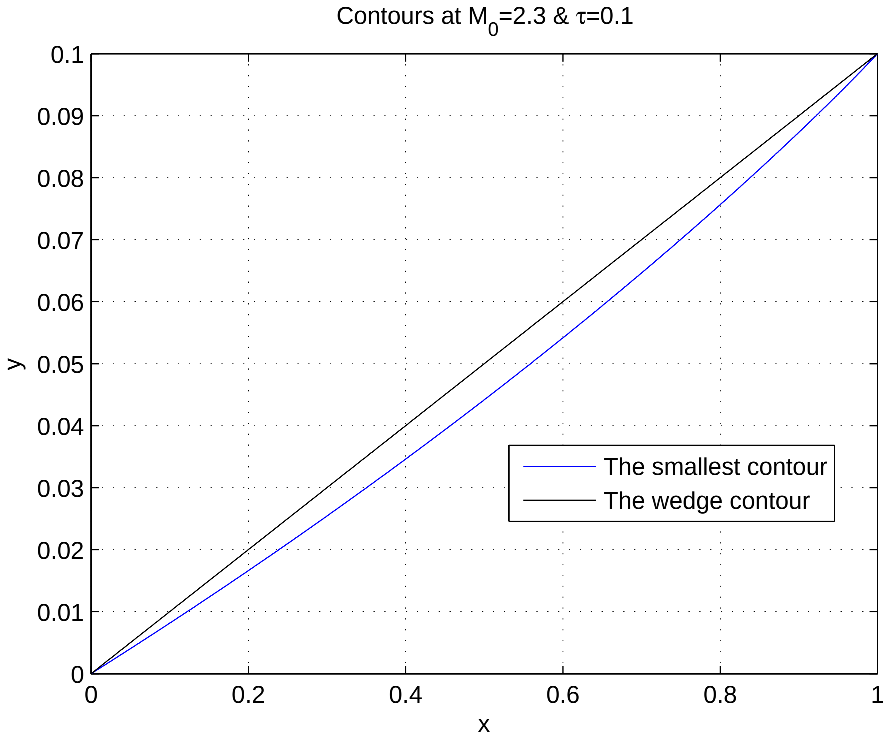

Figure 7.5: The possible contours, third variant

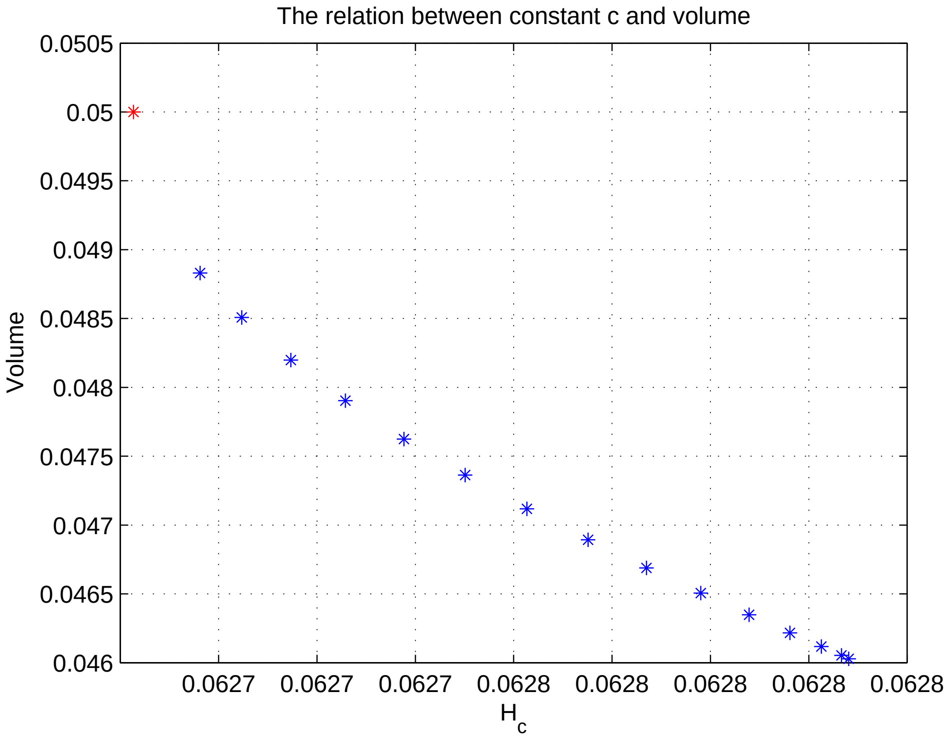

Figure 7.6: The influence of constant *c* on contour volumes, third variant

7.3 Asymptotic shock strength for the third variant

Based on the (H-p)-curve shown in figure 7.3 we are able to obtain many contours with different geometries with a volume less than 0.5τ. Each of these contours causes a certain amount of the asymptotic shock. In order to determine the shock strength we need to use the integral (3.36). Figure 7.7 represents the relation between the asymptotic shock strength and volumes for the optimized contours with τ=0.10 at M_0=2.3. The blue point represents the contour with the smallest volume. This contour is the result of the integrated green curve from figure 7.3. It seems that the wedge contour with the largest volume causes the largest amount of the shock. From this figure it is obvious that the shocks caused by these contours seem to be equal. This is because at this Mach number the achieved contours with τ=0.10 have almost the same volume. In order to confirm this reason we bring the result of the asymptotic shock strength for contours with τ=0.10 at M_0=2.6, see figure 7.8. This figure shows in fact that for this Mach number between the smallest and wedge contour we can have more contours with a larger volume. Both figures 7.7 and 7.8 show that there is a proportional relation between the asymptotic shock strength and volume of the third variant contours.

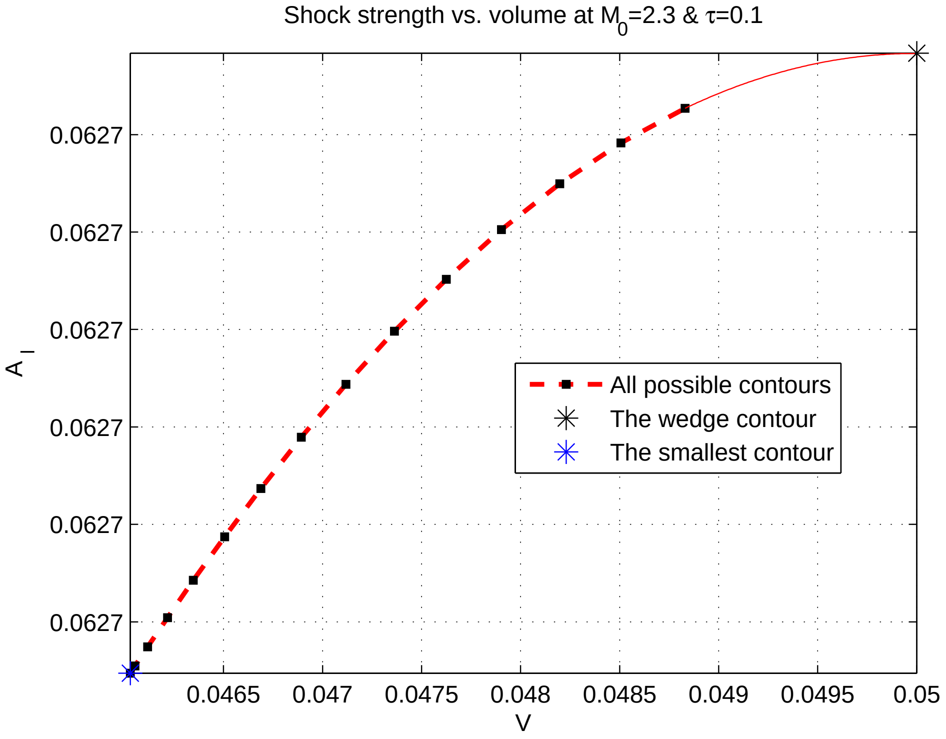

Figure 7.7: The shock strength vs. volume, third variant

Another interesting point is to see all possible contours at different Mach numbers with the same τ. Figure 7.9 shows the possible contours with the corresponding asymptotic shock strength for the Mach number domain of $2.3 \leq M_0 \leq 3.0$ with a step size of 0.1. The shortest line in this figure represents the optimum contours with τ=0.10 at M_0=2.3 and the longest line indicates the contours with the same τ at M_0=3.0. It is easy to

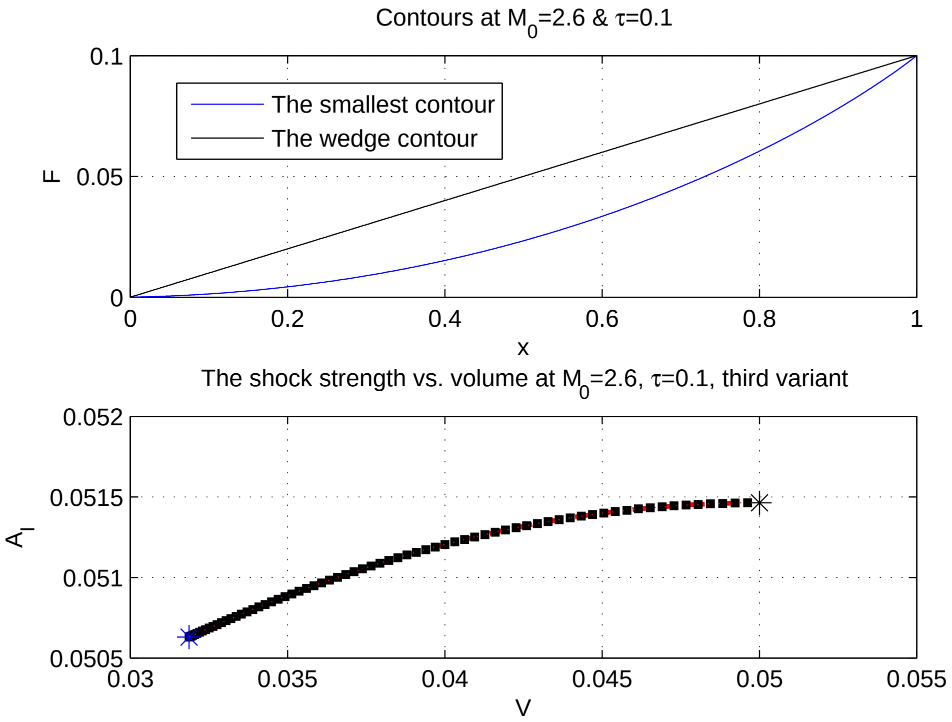

Figure 7.8: The shock strength vs. volume, third variant

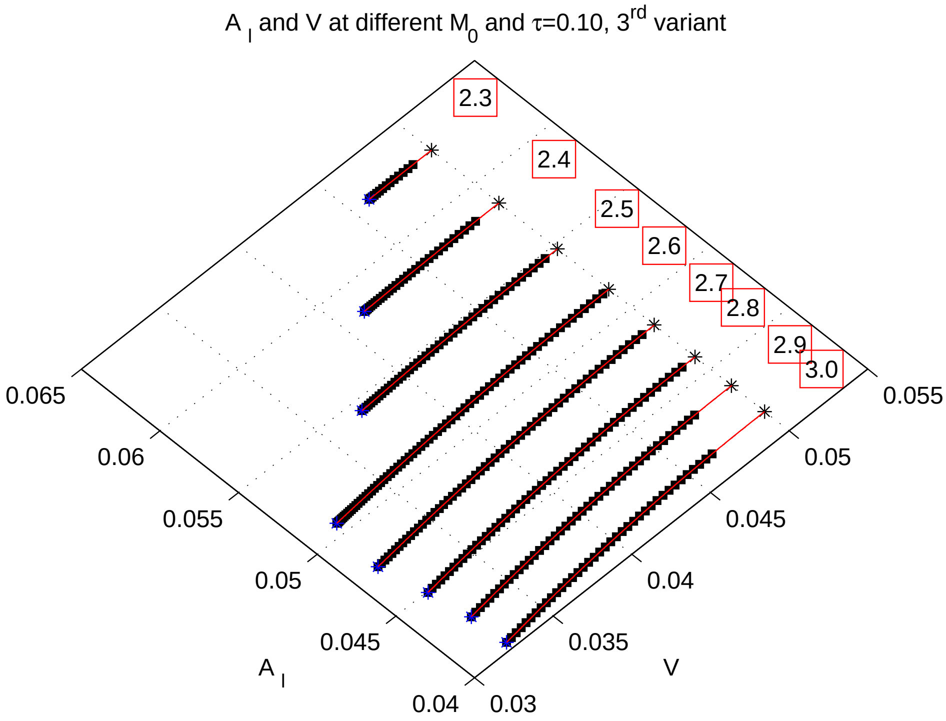

Figure 7.9: The shock strength vs. volume, all possible third variant contours

observe from this figure that increasing the Mach number leads to the contours with a larger volume which cause a larger amount of the asymptotic shock strength.

7.4 Validation for the third variant

The validation of results for the third variant contours can be proved by comparing these results to the analytical results of the non-optimized contours with the same volume. Figure 7.10 represents a non-optimized contour which is created from a wedge body for which the surface is changed by a kink inwardly. This configuration in a supersonic flow will lead to a shock-shock-expansion situation. In the same way as the first variant, the Γ^+ characteristics are projected on the u-axis to determine the θ distribution along the projected line. In the ($\cos\,\theta$)-graph due to the shock wave at the leading edge a, there appears a discontinuous jump from $\cos\,\theta_0$ to $\cos\,\theta_1$. At point d, there occurs another shock wave which has a jump from $\cos\,\theta_1$ to $\cos\,\theta_2$ as a consequence. The slope of this

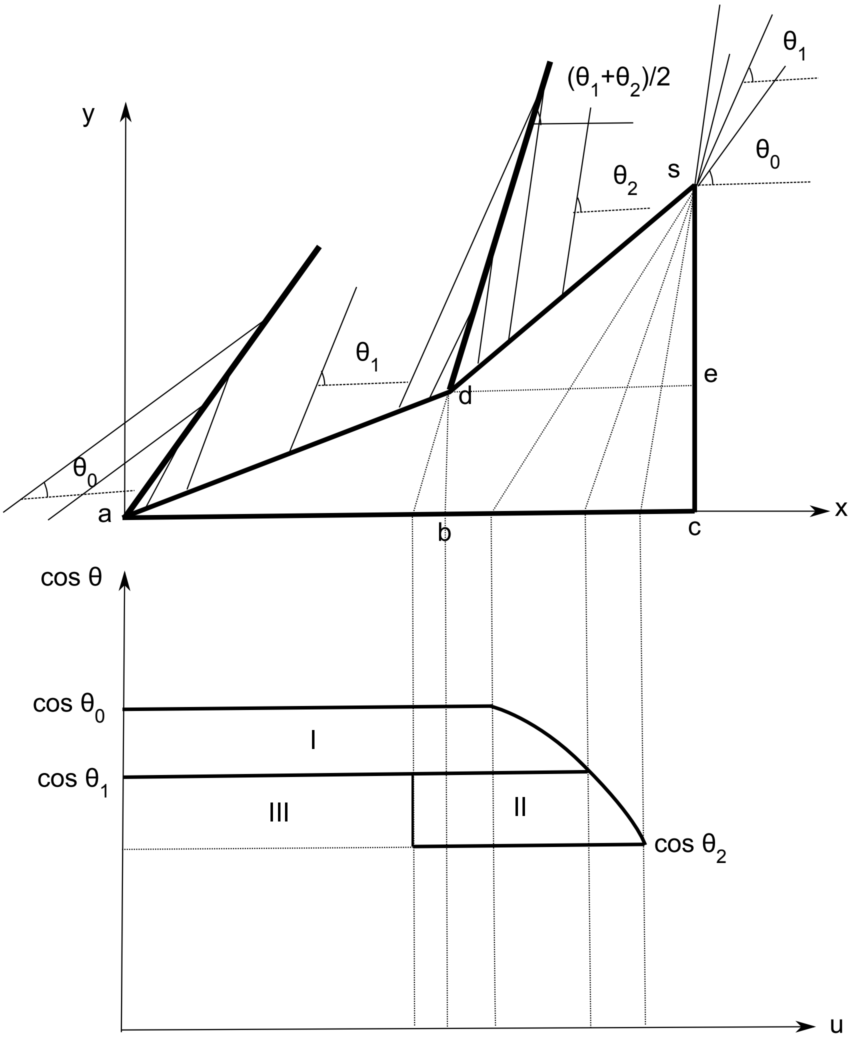

Figure 7.10: A wedge contour with a kink in steady supersonic flow

shock wave is according to the jump equation (3.2) is the average of θ_1 and θ_2. The centered expansion wave at the shoulder point results also in a curved path first from cos θ_2 to cos θ_1 and then to the free stream level cos θ_0. The sum of the areas I and II in ($cos\theta$)-plot is the measure of the asymptotic shock strength for this configuration. In order to have the area I we follow the same process which was needed to determine equation (6.24):

$$\begin{aligned} A_I &= (cos\theta_0 - cos\theta_1)(1 - \tau/tan\theta_0) \\ &\quad +\tau(1/sin\theta_0 - 1/sin\theta_1) \\ &\quad -cos\theta_1(tau/tan\theta_0 - tau/tan\theta_1) \end{aligned} \tag{7.4}$$

The area's II and III also can be obtained in the same way as explained above;

$$\begin{aligned} A_{II} + A_{III} &= (cos\theta_1 - cos\theta_2)(1 - \tau/tan\theta_1) \\ &\quad +\tau(1/sin\theta_1 - 1/sin\theta_2) \\ &\quad -cos\theta_2(tau/tan\theta_1 - tau/tan\theta_2) \end{aligned} \tag{7.5}$$

The area III separately from area I is calculated as follows:

$$A_{III} = (cos\theta_1 - cos\theta_2)\left(l_{ab} - \frac{\tau l_{ce}}{tan\frac{(\theta_1+\theta_2)}{2}}\right) \tag{7.6}$$

Now the total area's of I and II can be calculated as follows:

$$\begin{aligned} A_I + A_{II} + A_{III} - A_{III} &= (cos\theta_0 - cos\theta_1)(1 - \tau/tan\theta_0) \\ &\quad +\tau(1/sin\theta_0 - 1/sin\theta_1) \\ &\quad -cos\theta_1(tau/tan\theta_0 - tau/tan\theta_1) \\ &\quad +(cos\theta_1 - cos\theta_2)(1 - \tau/tan\theta_1) \\ &\quad +\tau(1/sin\theta_1 - 1/sin\theta_2) \\ &\quad -cos\theta_2(tau/tan\theta_1 - tau/tan\theta_2) \\ &\quad -(cos\theta_1 - cos\theta_2)\left(l_{ab} - \frac{\tau l_{ce}}{tan\frac{(\theta_1+\theta_2)}{2}}\right) \end{aligned} \tag{7.7}$$

7.4.1 Comparison between the optimized and non-optimized contour, 3^{rd} variant

Figure 7.11 represents the different geometries of an optimized and a non-optimized third variant contour. The non-optimized contour is obtained by a kink in its upper surface of a wedge contour. Both contours must have equal volume and being exposed to the uniform supersonic flow which in this case M_0=2.6 has been chosen. Figure 7.12 shows the corresponding A_l with the volume V for both optimized- and non-optimized contours with a thickness τ=0.10 at M_0=2.6. From this figure it is obvious to see that third variant contours are not optimized.

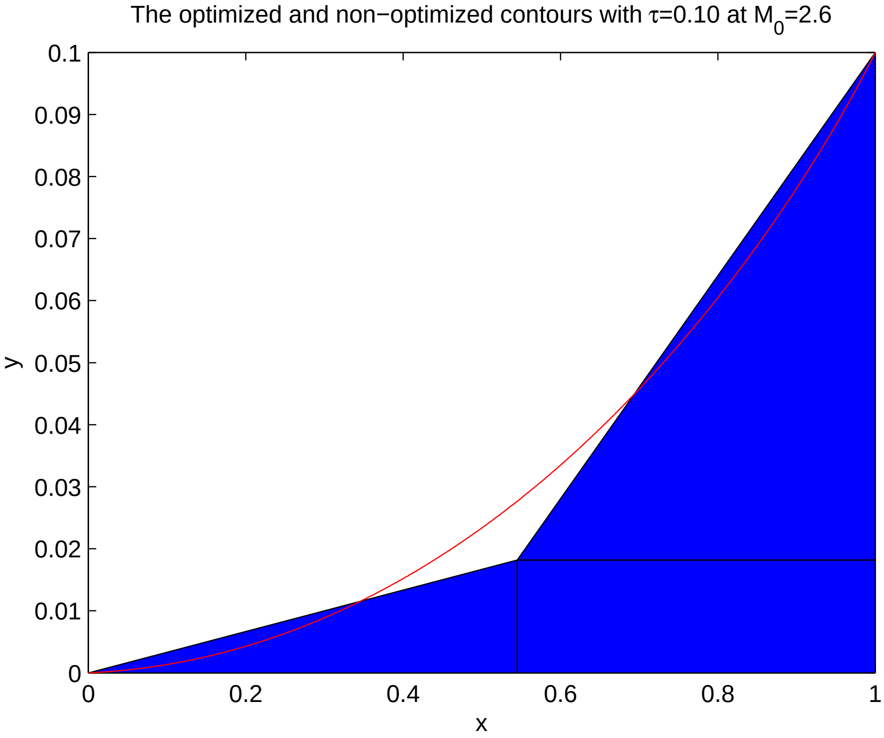

Figure 7.11: The optimized and non-optimized bodies

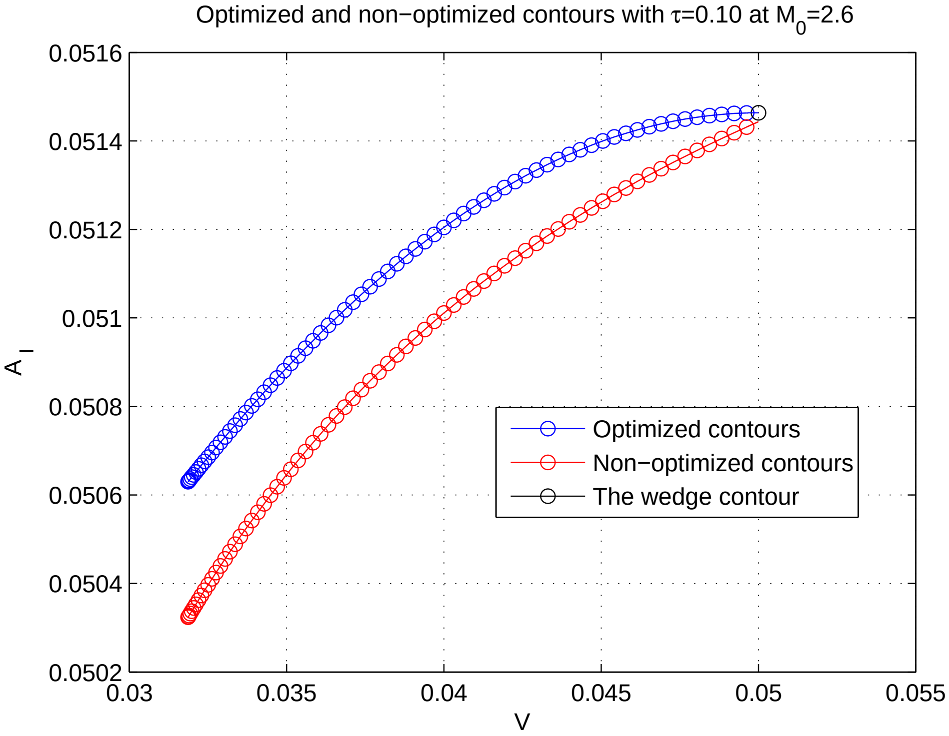

Figure 7.12: Comparison between optimized and non-optimized contours with τ=0.10 at $\mathrm{M}_0 = 2.6$

Figure 7.13 illustrates different contour's geometry with the corresponding difference rate η in A_l. The difference rate η is defined in section 6.5.3 by (6.32). From positive sign for η-values we can see that the optimized third variant contours cause higher asymptotic shock strength than non-optimized contours with the same volume. In addition it is also to observe from figure 7.13 that moving the kink towards right on the horizontal line results in contours with a smaller volume while they have a larger difference rate η in shock strength. So, we can conclude from this that the third variant contours are not optimized.

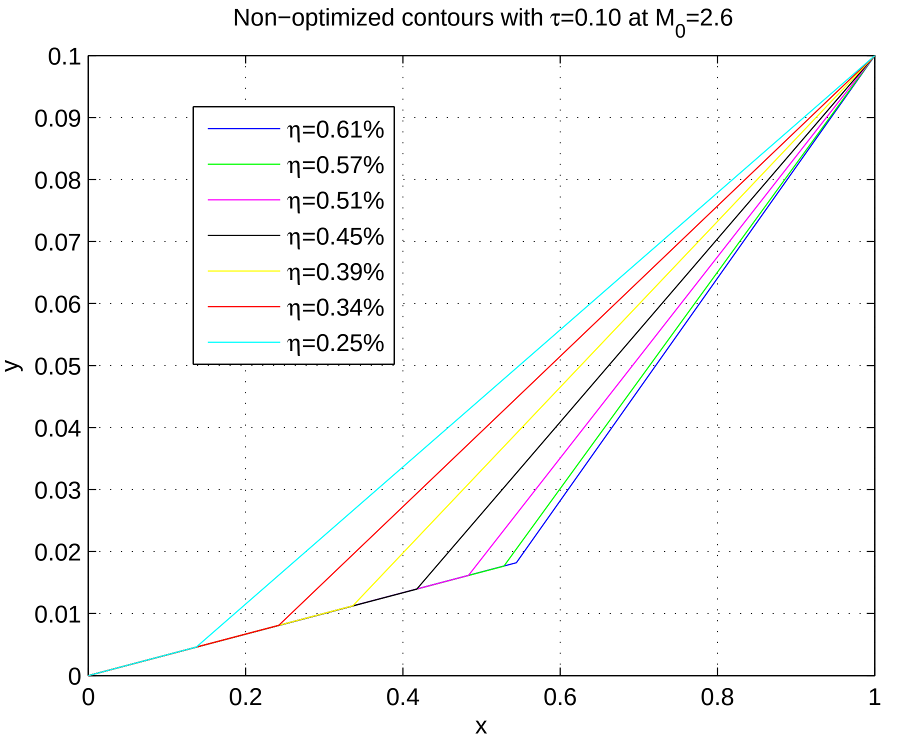

Figure 7.13: The non-optimized bodies, 3^{rd} variant

7.4.2 The asymptotic shock strength area, 3^{rd} variant

In the previous chapter, we have constructed the ($\cos\theta$)-plot for a wedge and a contour with the largest possible volume for the first variant. This plot gives an indication of the shock strength and was achieved by the Γ^+ characteristics after the shock along the surface. Therefore it was called the asymptotic shock strength area. This area for a wedge contour of a third variant is supposed to have the same configuration because the slope of the surface will be the same. But the magnitude of the area will be different because of the Mach number. So, this is the reason why the ($\cos\theta$)-plot for a wedge body of a third variant will not be concerned. Figure 7.14 shows the distribution of Γ^+ characteristics for a contour with the smallest volume in a flow of M_0=2.3. The jump from $\cos\theta_0$ to the red line at u=0 indicates the shock at the leading edge. Further this line shows the distribution of Γ^+ characteristics to the shoulder point. As it is clear from this plot, this

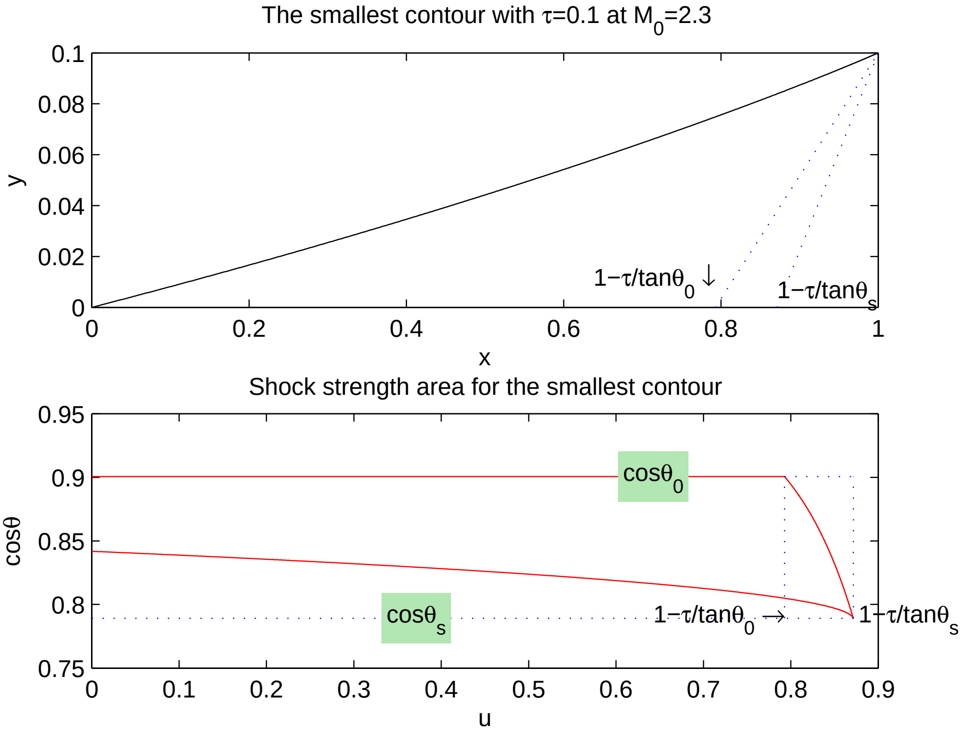

Figure 7.14: The asymptotic shock strength for the smallest contour, 3^{rd} variant

line is decreasing until the shoulder point compared to the similar line in figure 6.16. This attitude can be explained by increasing the slope at the surface of a third variant contour. At the shoulder point there occurs a centered expansion wave where the flow expands again to the free flow which is noticed from the curved path between $\cos\theta_s$ and $\cos\theta_0$.

7.5 Variation extreme values

In the previous section, we have reached an unexpected result which states that the third variant contours are not optimized. This is in contrast to the optimization results for the first variant in section 6.5. In order to investigate this unexpected outcome we need to analyze the variation problem explained in chapter 4. The expression (4.14) needed for calculating the A_l magnitude for a 2D body with a thickness τ was changed to a variation problem (4.15). This variation problem gets extreme values for A_l by finding the corresponding *G(x)*-function. But, at that moment it was not clear whether these extreme values are maximum or minimum. So, in order to determine this effect we just need to take an optimum contour with a certain volume and change its geometry with a known function. Subsequently, finding the A_l variation due to this geometry change. Since the volume of this contour must be remained constant so this function will be a *sine*-function with an amplitude of $A_{func}\tau$ where A_{func} is a given constant, see the following expression:

$$y_{sin} = A_{func}\tau sin(2\pi x) \tag{7.8}$$

The top figure 7.15 shows the influence of *sine*-function on geometry of a first variant contour with a volume of $V \approx 0.0571$. And figure 7.15 below shows the effect of this function on A_l value. From figure 7.15, we conclude that the extreme value of A_l resulting from variation problem is a minimum extreme value for the first variant contours. The same process can be applied for a third variant contour with a volume of $V \approx 0.032$ which is achieved at $M_0 = 2.6$. The result of figure 7.16 below is very interesting because it shows why the third variant contours are not optimum. This is because solving the variation problem (4.15) leads to the maximum extreme values of A_l for the third variant contours.

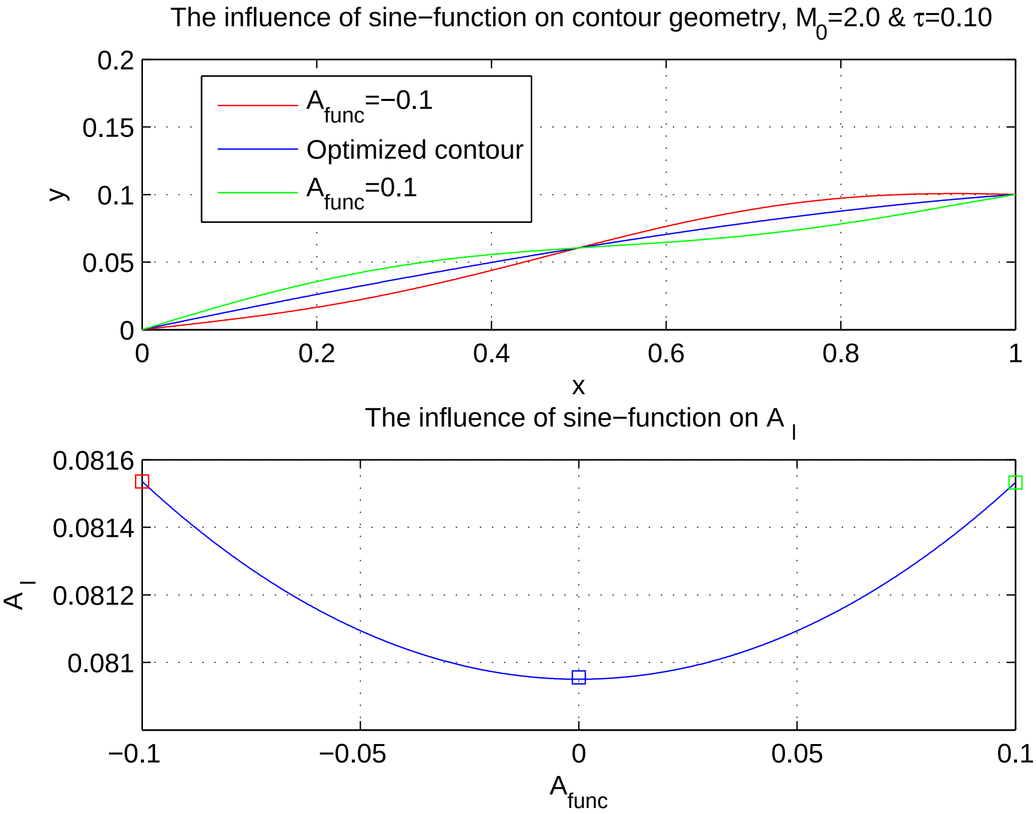

Figure 7.15: The influence of *sin*-function on contour geometry and A_l, 1^{st} variant

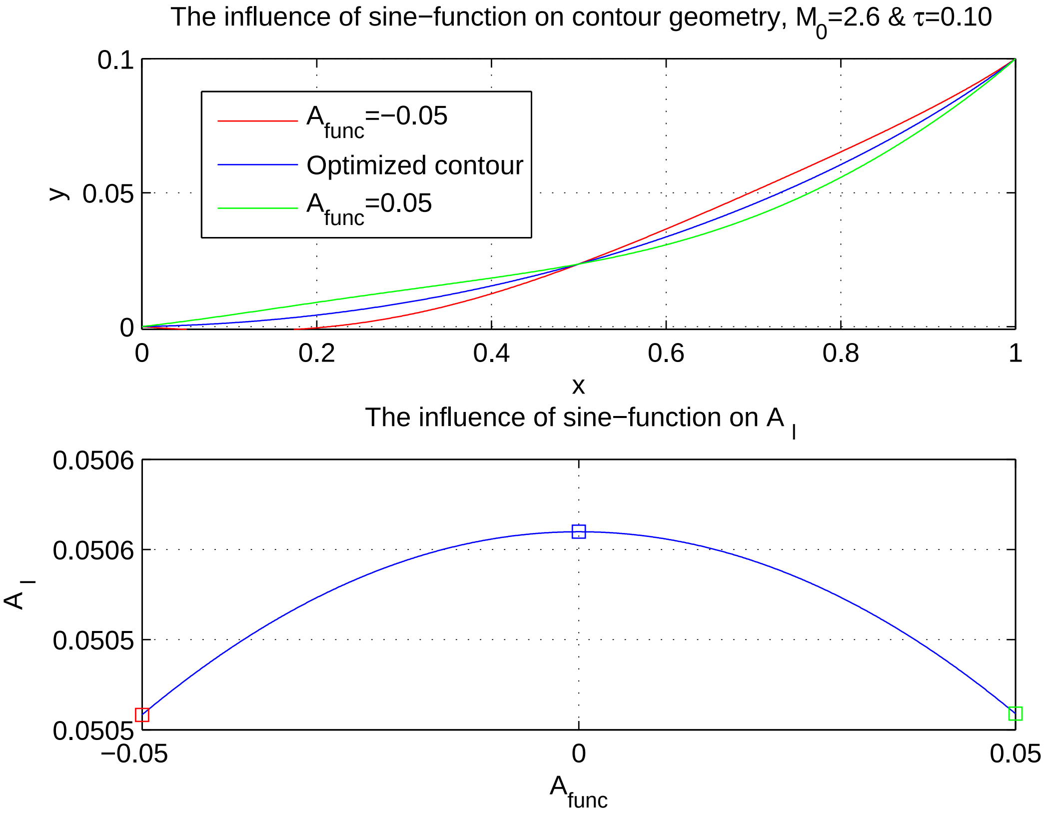

Figure 7.16: The influence of *sin*-function on contour geometry and A_l, 3^{rd} variant

7.6 Prandtl-Meyer expansion wave, 3^{rd} variant

For the first variant, it was proved that there is a proportional relation between the asymptotic shock strength and volume. This relation was to be explained by the interaction between the shock and expansion waves. And again this interaction could be followed by the contour's geometry. The conclusion of this study was that the wedge contour with the smallest volume shows a faster intersection between these two kind of waves compared to other contours. We will analyze the centered expansion wave with the same goal for the third variant contours. Figure 7.17 shows all possible third variant contours with τ=0.10 at M_0=2.3. The wedge contour is indicated by the red mark. And the red line with the red axis indicate the shock angle β_s for different contours while the blue line with blue axis represent the last characteristic angle θ_s at the shoulder point. As it is clear from this figure, the wedge contour has the maximum angle of the shock according to the invariant jump equation (3.2). In addition the smallest angle of the last characteristic at the shoulder belongs to the wedge contour. So, it means that interaction between the shock and the first characteristic of the centered expansion wave takes place for the wedge contour. Figure 7.18 shows the magnitude of the centered expansion waves for different contours. From this figure, it is known that wedge which is the largest third variant contour shows the minimum *Prandtl-Meyer* expansion fan. Combination of figures 7.17 and 7.18 gives the conclusion that the third variant wedge body has the strongest asymptotic shock and the minimum centered expansion wave.

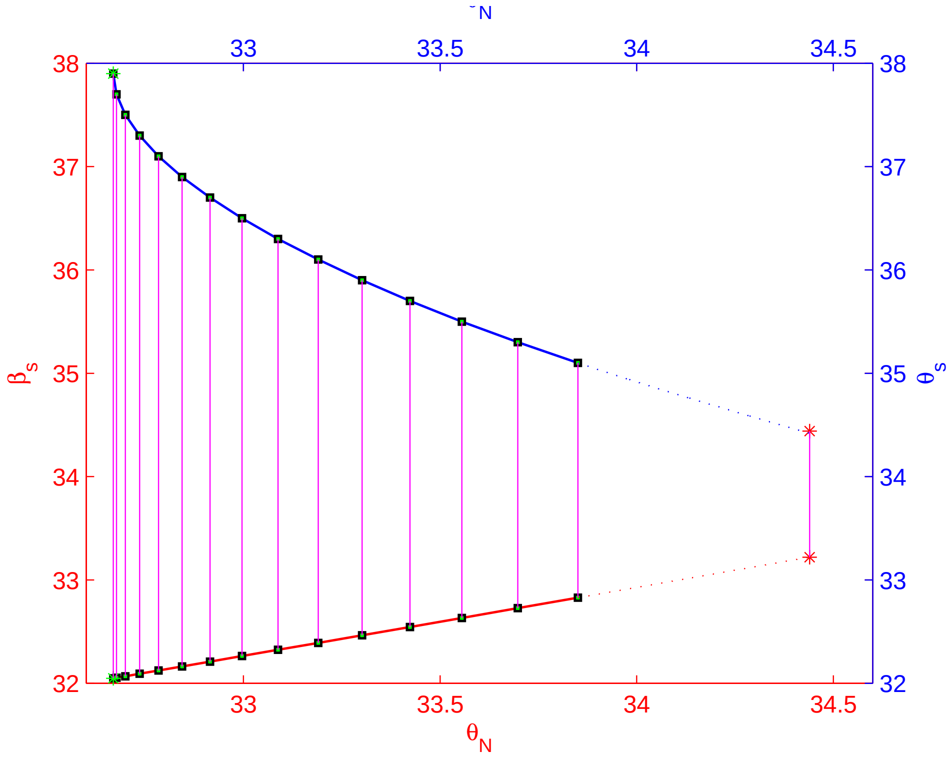

Figure 7.17: The angle of shock and first characteristic of the centered expansion

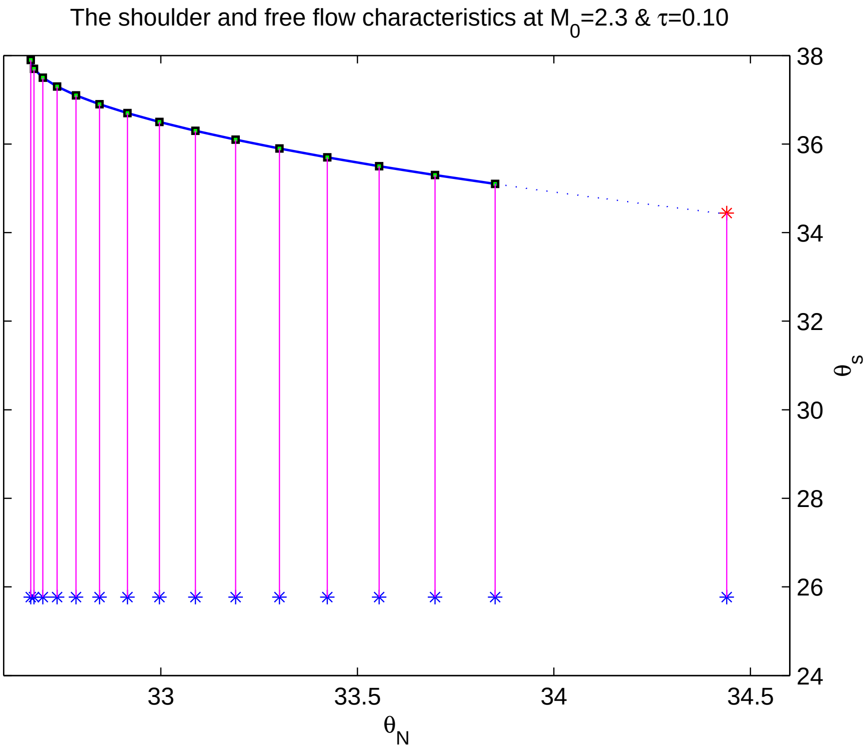

Figure 7.18: The centered expansion magnitude, 3^{rd} variant

7.7 Influence of Mach number on k_l, 3^{rd} variant

In the same way we use equation (6.34) to see the variation of the characteristics along the surface when a third variant contour is exposed to the flow with other Mach numbers. Because the angle of upper surface φ of a third variant contour is increasing so the relation (6.35) results in other values for ν. This again has influence on values for θ's. Figure 7.19 illustrates how the characteristic lines are being influenced by the Mach number for a contour which is achieved at M_0=2.6 with τ=0.10. In contrast to figure 6.20, the line which represents the Γ^+ characteristics along the surface is increasing. This is due to the increasing of upper surface slope. It is also clear from this figure, when a contour with a certain volume is put in a supersonic flow of lower Mach numbers, we expect larger area covered by the characteristics.

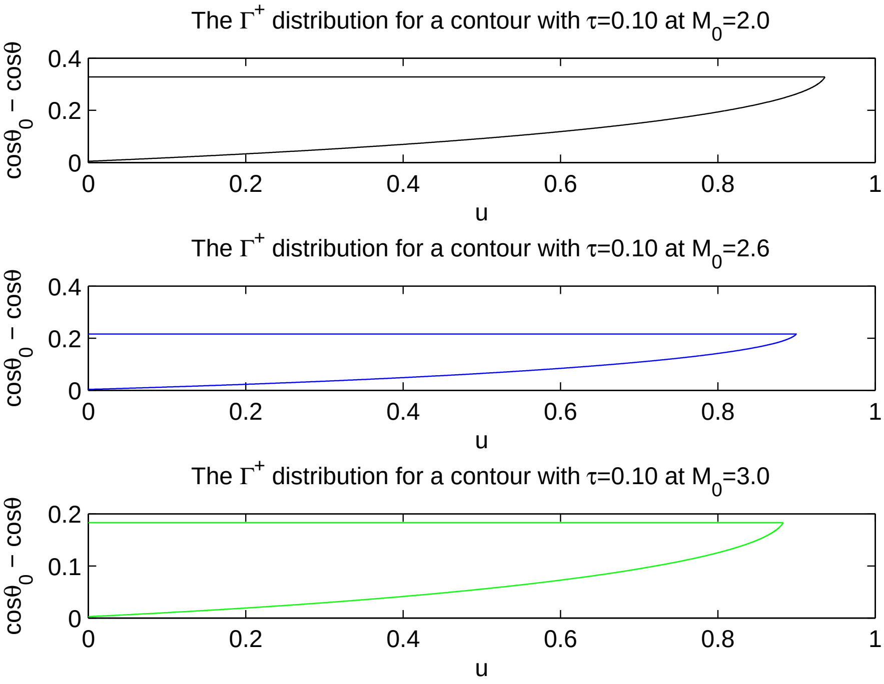

Figure 7.19: The influence of Mach number on the characteristics distribution

Figure 7.20 represents the influence of Mach number M_0 on k_l value of a contour with a volume of $V \approx 0.032$ which is obtained at M_0=2.6. The k_l bahavior for this contour at different Mach number is indicated by the red line. The blue signs represent the k_l values for a non-optimized contour with the same volume. As it can be seen in this figure, the non-optimized contour causes higher asymptotic shock strength only for the lower Mach numbers compared to the optimized contour. Furthermore we are interested in k_l-variation for two optimum contours with different volumes, so we calculate the term $k_l^{wedge} - k_l^{opt}$ for a larger range of Mach number. This term shows the k_l-variation w.r.t the Mach number for a wedge body and an optimum contour with a volume $V \approx$ 0.032. From figure 7.21, it is obvious that the wedge contour with a volume of V=0.05 shows lower

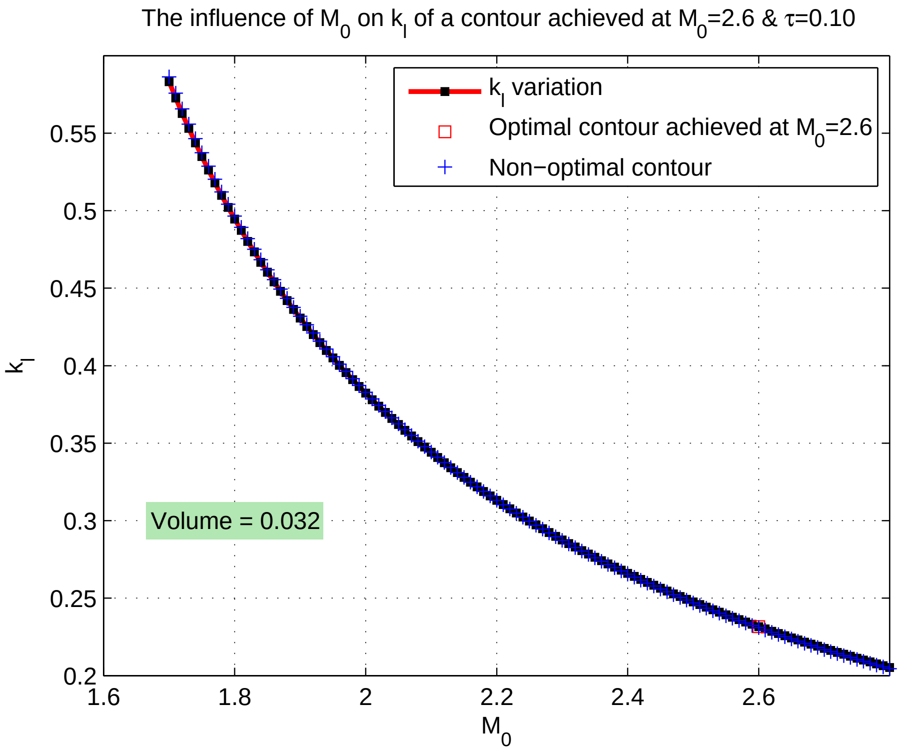

Figure 7.20: The influence of Mach number on the shock strength

values for k_l at lower Mach numbers, $1.5 \leq M_0 \leq 2.3$, compared to a smaller optimum contour with a volume $V \approx 0.032$. Subsequently, this difference indicates an asymptotic characteristic for higher Mach numbers. In other words, the optimum contour with a smaller volume shows higher values for k_l compared to a larger wedge body at lowe Mach number $M_0 \leq 2.3$.

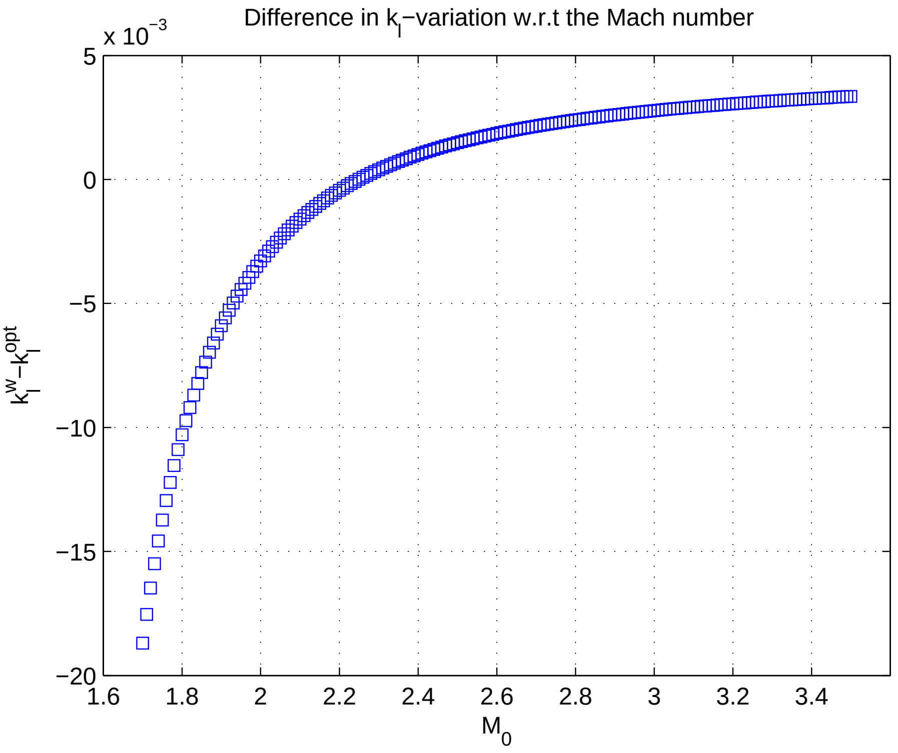

Figure 7.21: Difference in k_l-variation w.r.t Mach number, 3^{rd} variant

7.8 M_0 variation for the third variant

For the first variant, it was shown that with decreasing the Mach number there are contours to be achieved with a larger volume. In section 6.8 from previous chapter it was mentioned that this volume variation is to be explained by the (H-p)-curves from figure 5.1. We observe from the same figure 5.1 when the Mach number increases it will result in curves which are more extended with their nose towards left. And as we know for the third variant, a larger (H-p)-curve means an optimum contour with a smaller volume. Figure 7.22 represents the smallest possible contours at M_0=2.3 and M_0=3.0. From this we conclude that a larger (H-p)-curve which is a result of higher Mach number leads to the third variant contours with a smaller volume. The results of A_l for the possible contours at M_0=2.3 and M_0=3.0 have been shown in figure 7.23. Figure 7.23 shows the inverse proportional relation between A_l and M_0 for the third variant. The results of other cases for different Mach numbers can be found in appendix E.

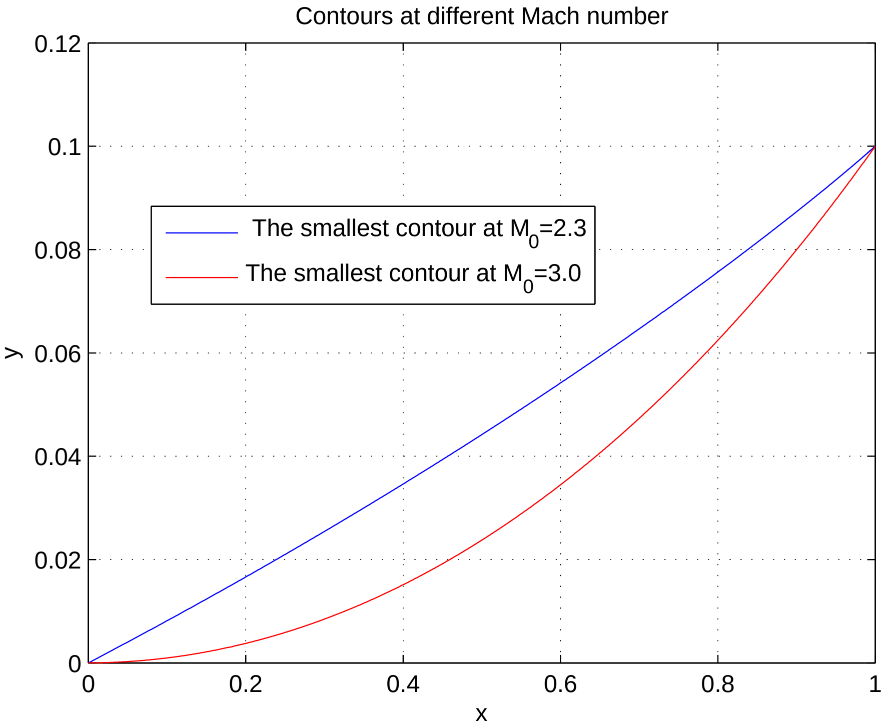

Figure 7.22: Contours at M_0=2.3 and M_0=3.0

In section 6.8 it was already proved that all contours which are obtained at different Mach numbers show similar asymptotic shock strength behavior at other Mach numbers. Figure 7.24 shows the same characteristic for the third variant contour. The red line represents the k_l variation w.r.t the Mach numbers for an optimum contour with a volume of $V \approx 0.032$ obtained at M_0=2.6. The blue- and red sign represent respectively the asymptotic shock strength for the optimized and non-optimized contour. These points are placed very close to each other because of the small difference. But as it was proved in figure 7.12, the non-optimized contour at this Mach number causes a lower value of A_l.

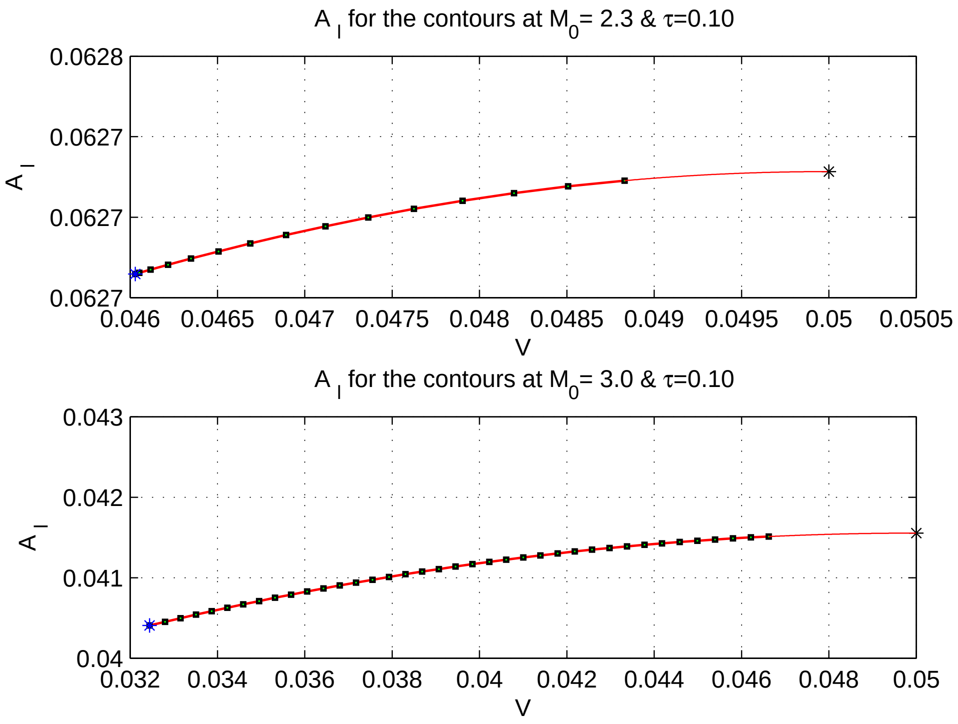

Figure 7.23: The asymptotic shock strength at M_0=2.3 and M_0=3.0

In addition, all other color marks show the achieved contours at different Mach number with the same volume, $V\approx0.032$. This is the same result as what we have obtained for the first variant.

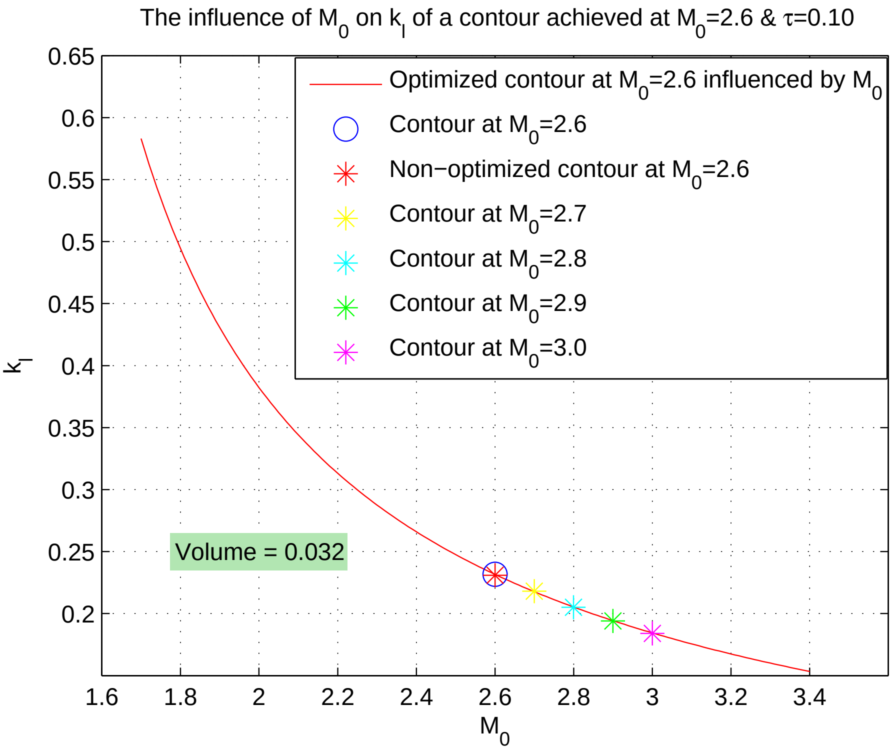

Figure 7.24: The most optimum contour in the third variant

7.8.1 Same contour at different Mach numbers, 3^{rd} variant

By using diagram 6.26 we perform the same process to investigate that the third variant contours are also independent of Mach number. The contour for which the new θ-distribution is determined at different Mach numbers can be seen with red line at M_0=2.3 in figure 7.25. Figure 7.25 confirms the results depicted in figure 7.24 and shows that A_l value for third variant contours indicates similar behavior at different Mach numbers.

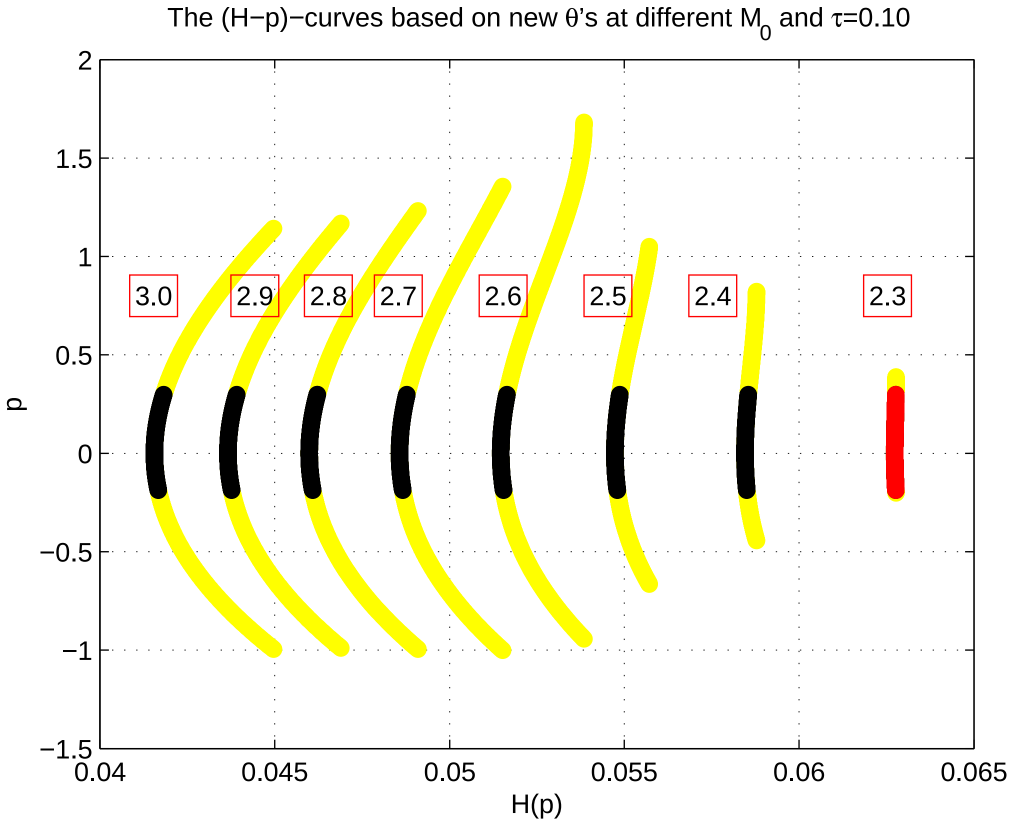

Figure 7.25: Coincidence of (H-p)-curves, 3^{rd} variant

7.9 Thickness variation for the third variant

Figure 5.6 in chapter 5 represents different (H-p)-curves at constant M_0=2.6 corresponding to different τ. Until now we have developed third variant contours which have a volume less than 0.5τ. On the other hand it is known that wedge contour with a volume of $0.5tau$ is the largest possible third variant contour. So, in order to achieve third variant contours with a larger volume than the wedge contour it is necessary to increase the thickness τ. Figure 7.26 shows the possible third variant contours for different τ and the corresponding shock strength A_l. It is also to notice from this figure when τ is increased there are contours to be obtained with a larger volume which also produce higher asymptotic shock strength.

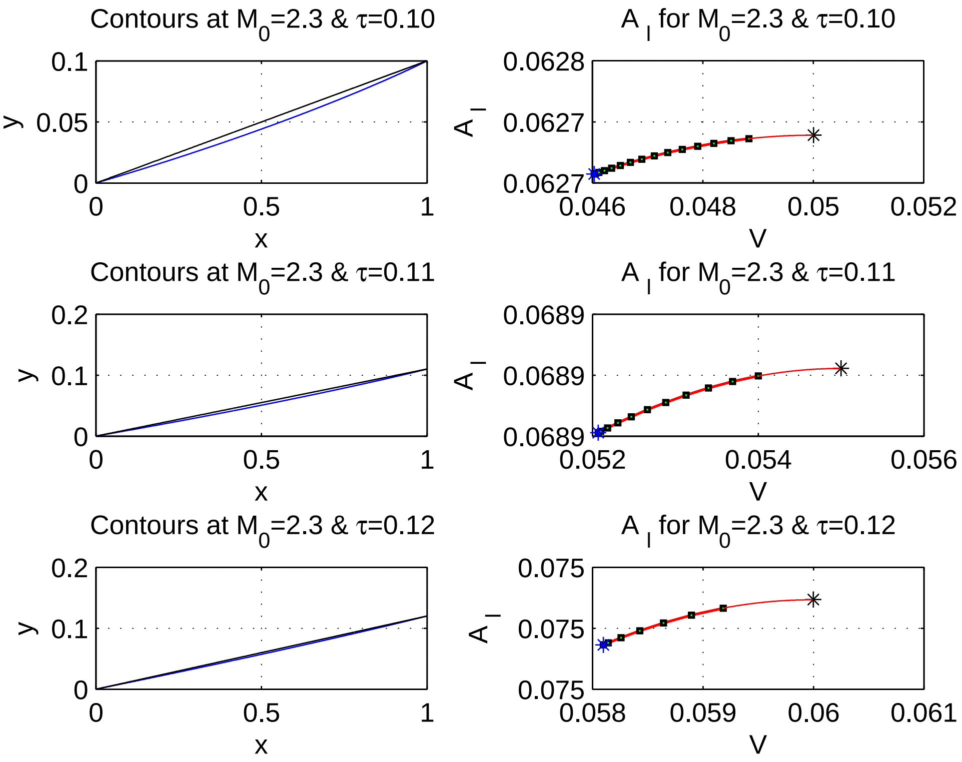

Figure 7.26: The variation of thickness for the third variant

7.9.1 Influence of thickness on k_l, 3^{rd} variant

As we have observed from section 6.9.1, the first variant contours with a smaller thickness produce lower asymptotic shock strength than those with the same volume and a larger thickness. So, it is also worthy to investigate if the third variant contours have the same characteristic. The red line in figure 7.27 represents the influence of τ on k_l-value of an optimal contour with τ=0.11 which is obtained at M_0=2.5. This contour has a volume of $V\approx$ 0.051. Furthermore, we notice from this figure that the asymptotic shock strength k_l of a contour with τ=0.12 obtained at M_0=2.5 is also located on the red line. So, we can conclude from this that the third variant contours with a certain volume and a smaller thickness produce lower asymptotic shock strength than those with the same volume but a larger thickness. Figure 7.28 represents different geometries for these two contours with the same volume and different thickness. It is also interesting to investigate the asymptotic shock strength w.r.t the different Mach numbers as result of these two contour's geometry. Figure 7.29 represents this relation from which it is clear that a third variant contour with a certain volume and a smaller thickness produces lower asymptotic shock strength than those with the same volume and a larger thickness.

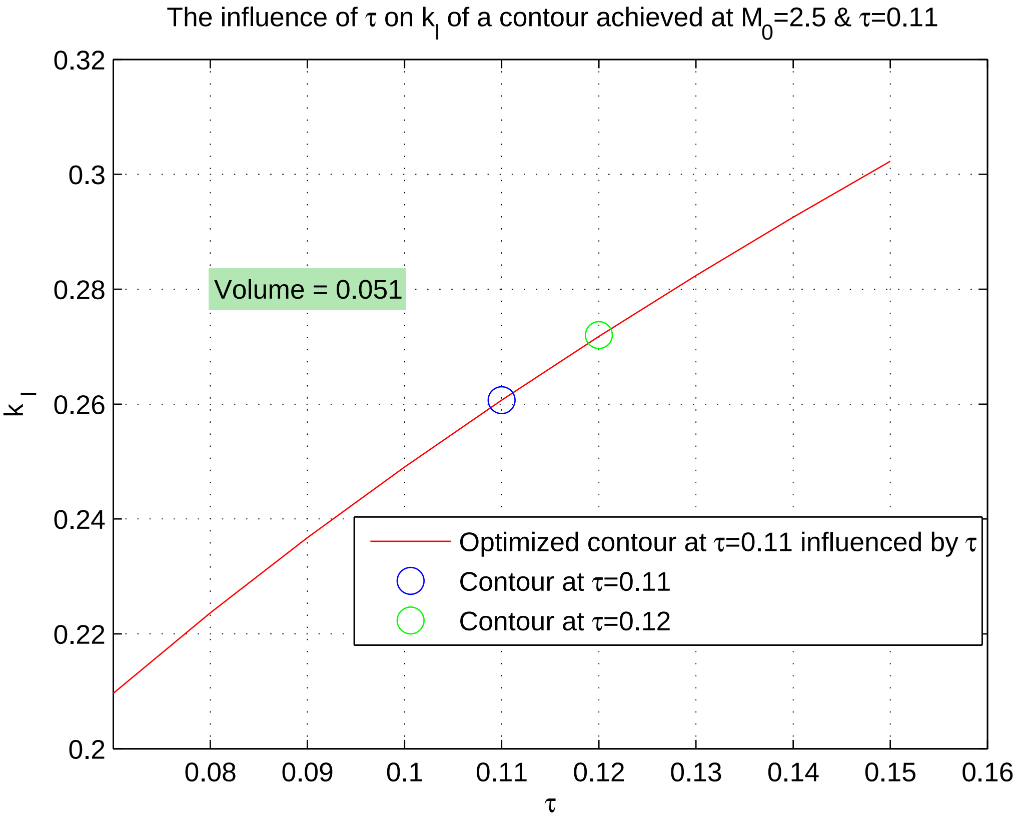

Figure 7.27: The most optimum contour in the first variant, M_0=2.5 and different τ

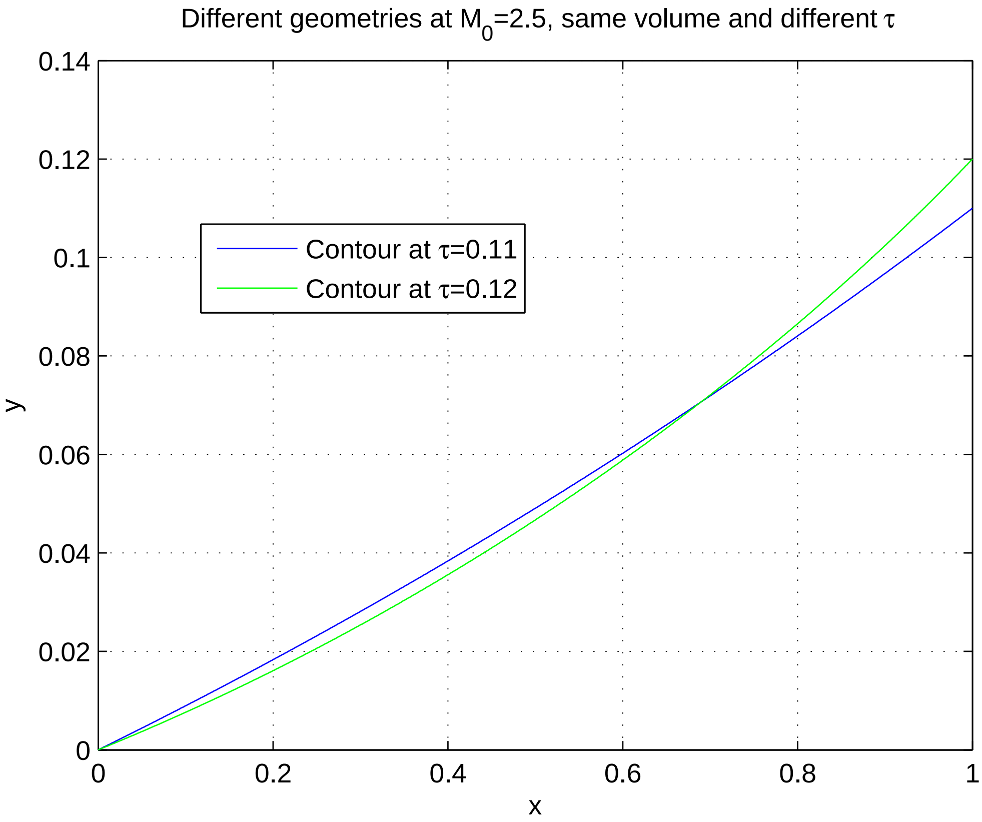

Figure 7.28: Different geometries same volume, different thickness, M_0=2.5

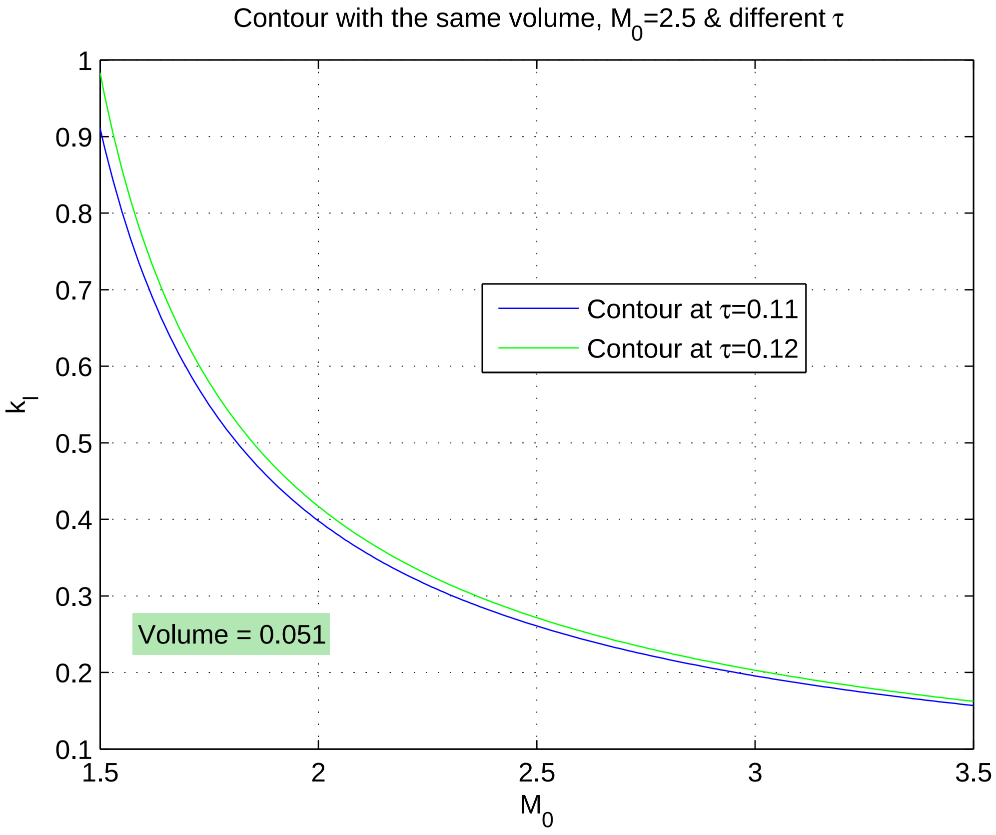

Figure 7.29: The asymptotic shock strength characteristic at different Mach numbers, different thickness

7.10 Aerodynamic properties for 3^{rd} variant

In section 6.10 from previous chapter, the aerodynamic properties of a first variant contour was studied. In the same manner we analyze these properties for a third variant contour with a volume $V \approx 0.032$. This contour is obtained with a constant τ=0.10 at M_0=2.6.

Flow velocity and pressure across the shock, 3^{rd} variant

By using equation (6.35) and the *Hall*-function we are able to find the Mach variation across the shock and subsequently along the surface. From figure 7.30 it is clear that the undisturbed flow Mach number M_0=2.6 directly after the shock decreases. Subsequently the local Mach number M_c will decrease until the shoulder point. This is the opposite result as what we have observed from figure 6.32 for a first variant contour. The reason for that is the increasing of the flow direction φ along the third variant surface. So, according to equation (6.35) an increasing of φ means smaller values for *Prandtl-Meyer* angle along the surface which again results in smaller local Mach numbers. Knowing the ambient Mach numbers along the surface and using equation (6.10) enable us to find the static pressure change $\frac{p_c}{p_0}$ across the leading shock. In contrast with the first variant contour, the static pressure increases until the shoulder point, see figure 7.31. It is also worthy to investigate the difference between the linearized supersonic pressure coefficient and the real pressure coefficient for a third variant contour. The linearized supersonic pressure coefficient can be determined by equation (6.40). This figure represents an increase of pressure coefficient c_p along the surface for a third variant contour. This is also the

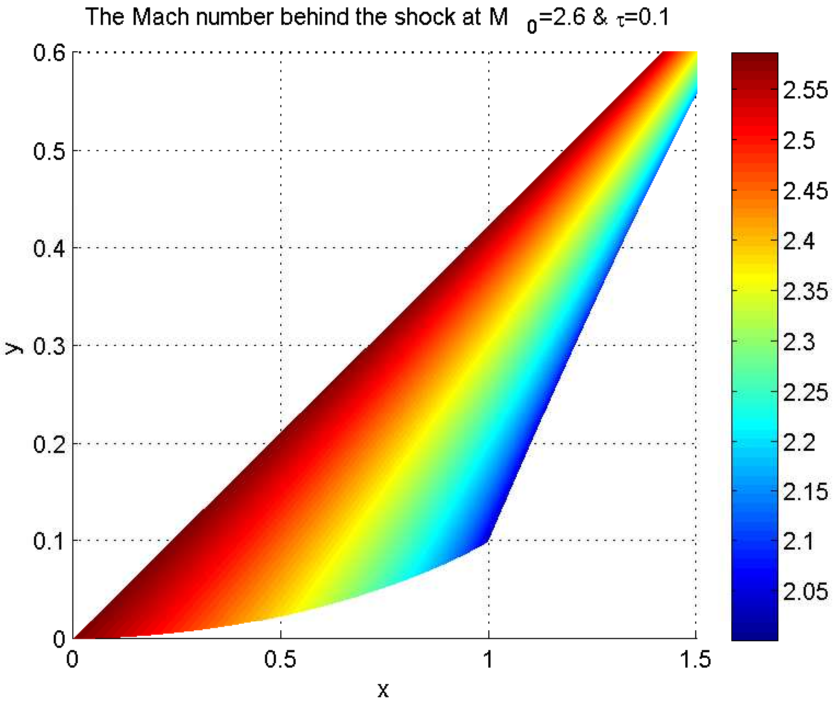

Figure 7.30: The Mach variation for a third variant contour

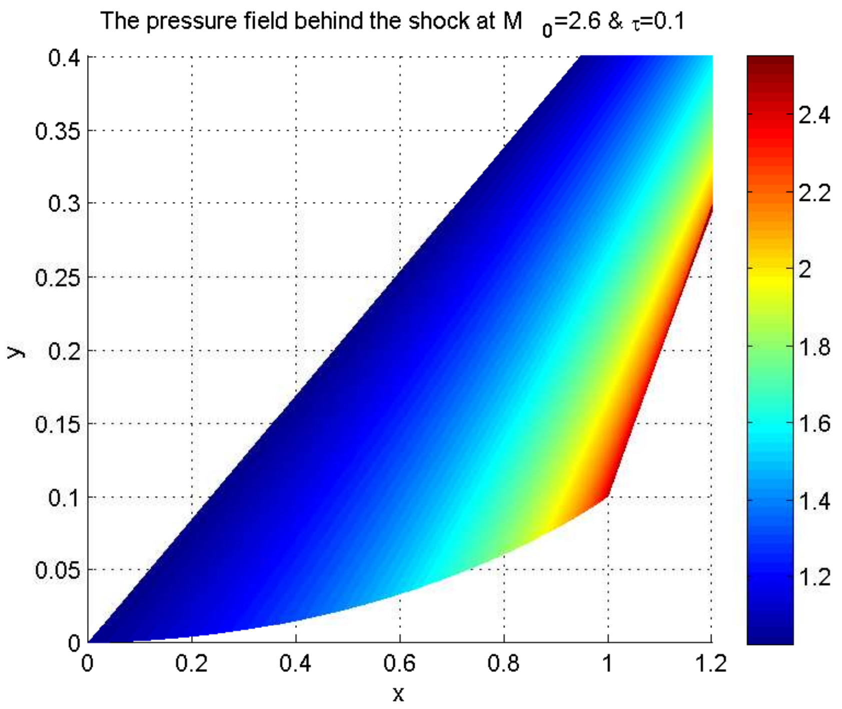

Figure 7.31: Static pressure at M_0=2.6 τ=0.10

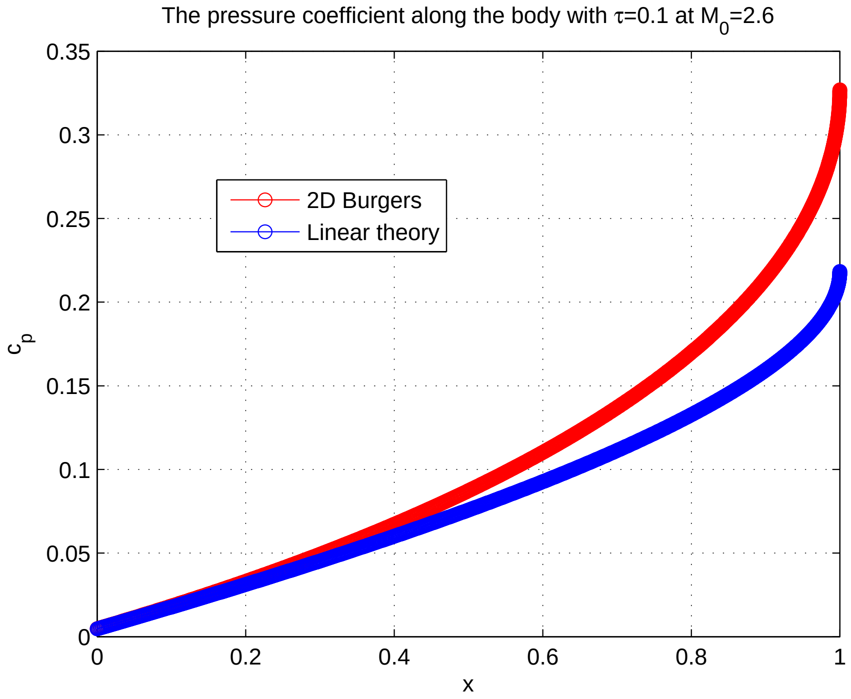

Figure 7.32: Comparison between the supersonic linear theory and 2D Burger

opposite result compared to the first variant contour because of an increase for the local pressure. In a similar way as for the first variant, the ratio of the static temperature (6.41) is needed to determine the local speed of sound a_c. Equations (6.42) can be used now to find the flow velocities u and u for the third variant contours. The flow velocity in the x-direction is decreased while in the y-direction increases, see figure 7.33. These results are in contrary to those shown in figure 6.35 for the first variant contour.

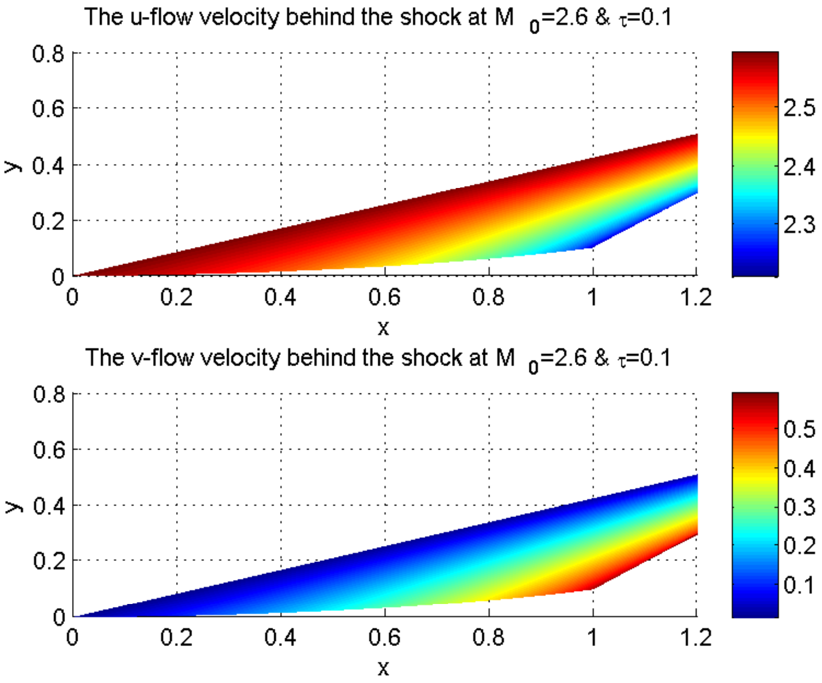

Figure 7.33: The flow velocities, 3^{rd} variant

Entropy, 3^{rd} variant

Equations (6.44) and (6.45) can be used to investigate the entropy- and the total pressure change for the third variant contours. The upper figure 7.34 represents the normal upstream Mach numbers $M_{0,n}$ for a third variant contour for which the values are reversed compared to the first variant contour. At the nose of the body it seems as $M_{0,n}$ ≈1.0 which means that the entropy change here at this point is nearly equal to zero. In order to see this condition the total pressure change $\frac{p_{t,2}}{p_{t,1}}$ which is also a function of $M_{0,n}$ is plotted in figure 7.35. This figure shows a total pressure ratio $\frac{p_{t,2}}{p_{t,1}}$ of almost 1 at the body's leading edge for which Δs approaches zero. So, from this figure we can also conclude that assuming the flow being isentropic for the third variant is allowable.

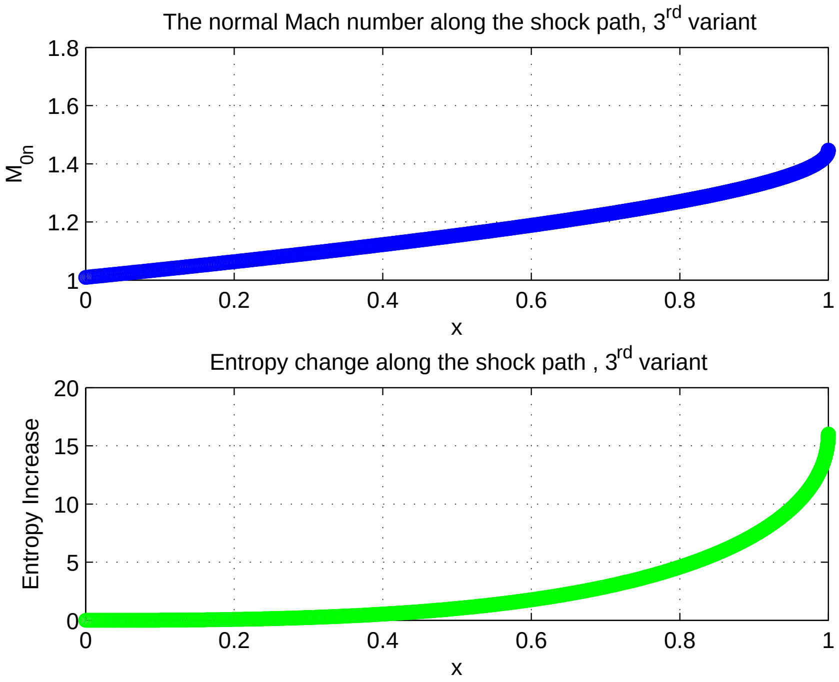

Figure 7.34: Upper plot: the normal Mach number, Lower plot: entropy change, 3^{rd} variant

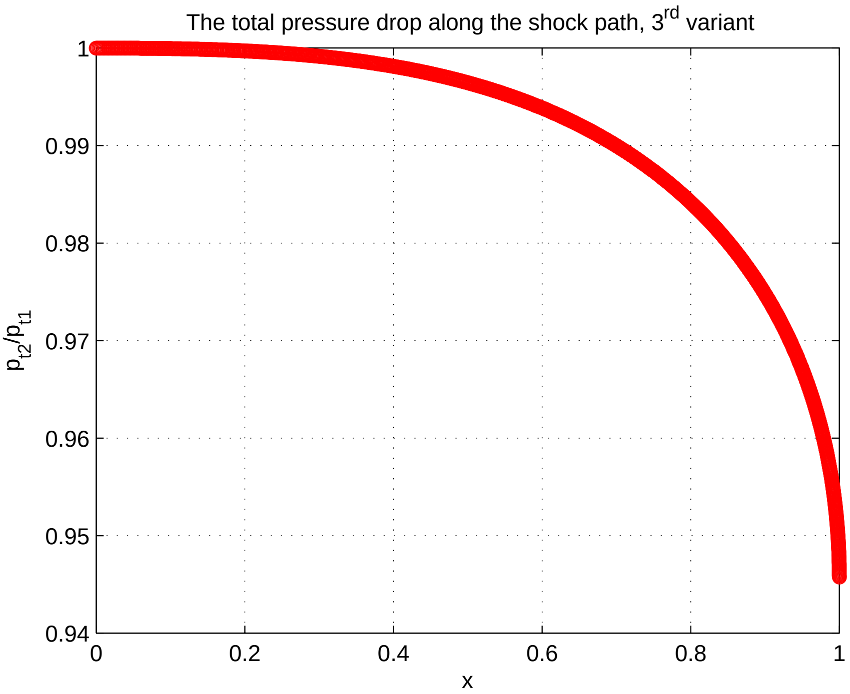

Figure 7.35: The total pressure drop along the shock path

7.11 Drag for the third variant contours

Equation (6.46) can be used to determine the drag force for the third variant contours. From this we can have the drag coefficient for these contours. Figure 7.36 shows an inverse relation between the third variant contours and drag. It means that the third variant contours with a smaller volume show a higher drag coefficient while the first variant contours with a smaller volume caused a lower drag, see figure 6.38. It is also worthy to investigate the relation between the volume of these contours and the corresponding asymptotic shock strength, see figure 7.37. From this figure there is obvious there exists an inverse linear relation between drag C_D and the asymptotic shock strength,A_l for the third variant contours. This result is in opposite of what we have observed from figure 6.39 for the first variant contour. The results for other Mach numbers $2.4_0 \leq 3.0$ have been depicted in appendix F. These results show that there exists also an inverse linear relation between C_D and A_l for higher Mach numbers. In addition figure 7.38 shows the influence of Mach number on A_l and C_D for a third variant contour. The blue mark indicates a third variant contour with a volume of $V{\approx}0.0464$ which is obtained at $M_0{=}2.3$. Further the red line represents the variation of A_l and C_D for this contour at other Mach numbers. This is exactly the same result as we have achieved for the first variant contour from figure 6.40 in which with increasing Mach number these two quantities A_l and C_D will be decreased.

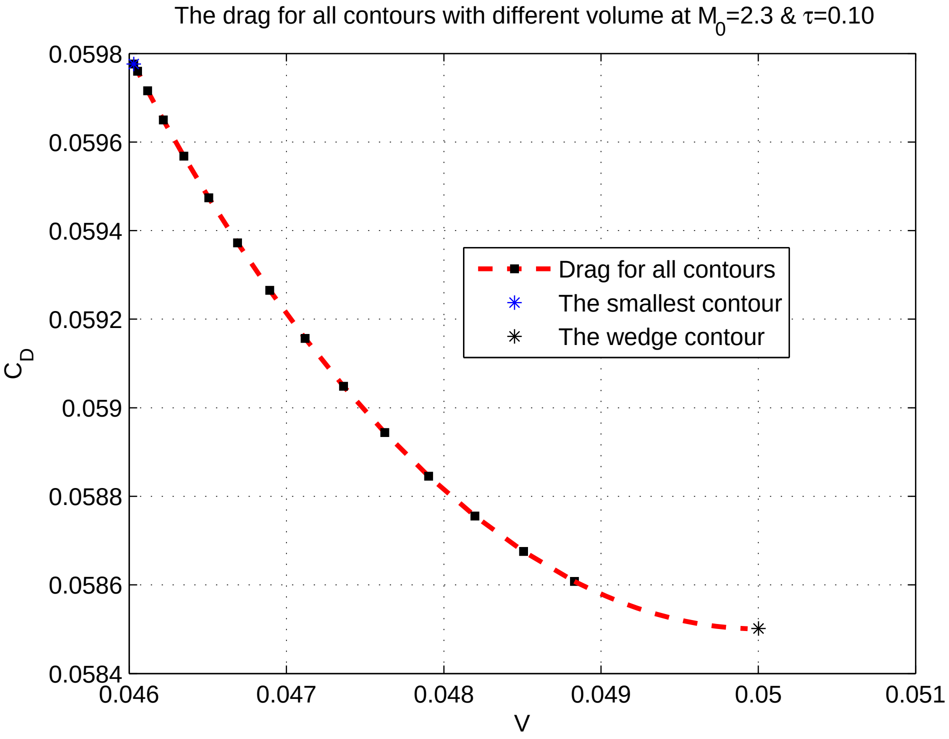

Figure 7.36: The drag coefficient for the optimal contours, 3^{rd} variant

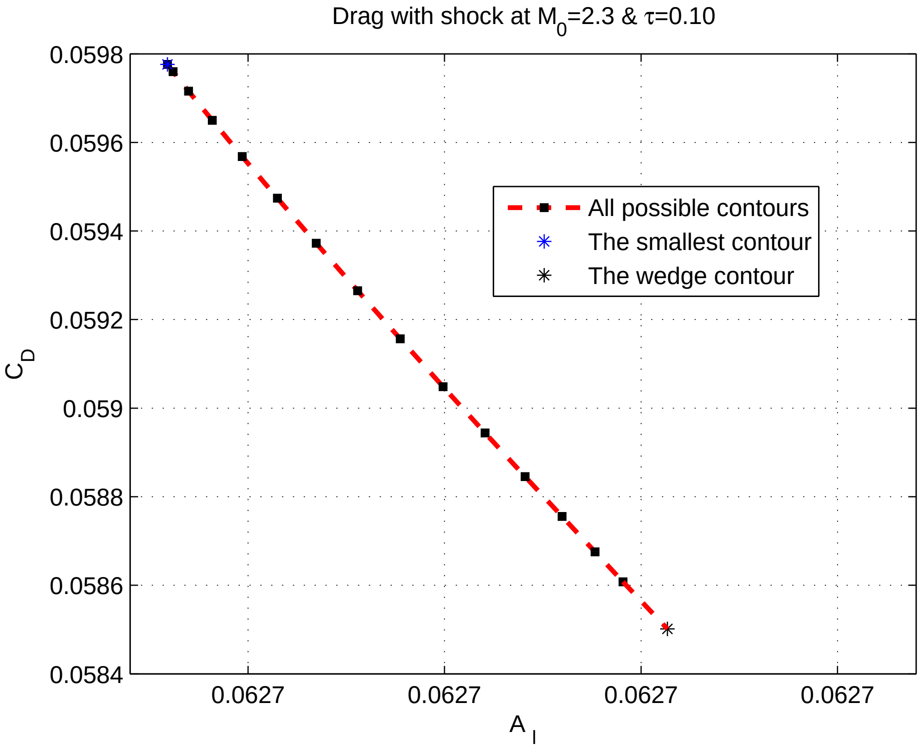

Figure 7.37: Drag with shock strength for the optimum contours, 3^{rd} variant

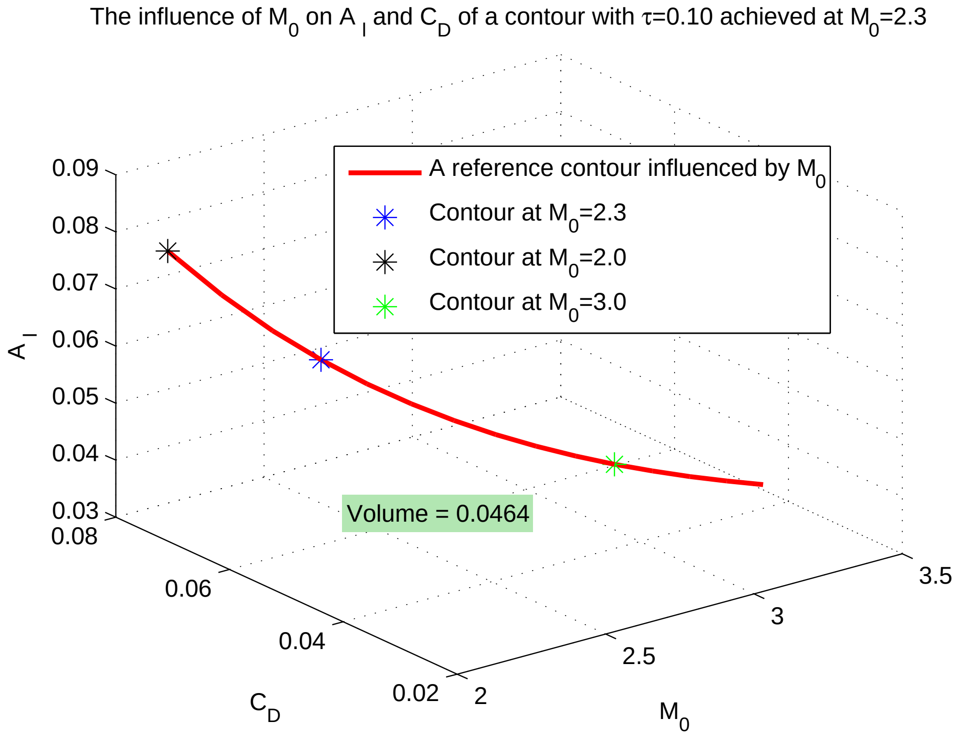

Figure 7.38: The influence of Mach number on shock strength and drag, 3^{rd} variant

CHAPTER 8

ASYMPTOTIC AND WHITHAM THEORY

Almost in all of the studies on sonic boom, the conventional expression which describes the shock strength is the overpressure Δp. In this chapter, first the asymptotic shock strength Σ which has been used throughout this thesis will be transformed to the overpressure. Subsequently, the *Whitham's theory* will be applied to the optimum contours in a 2D steady and inviscid supersonic flow.

8.1 Change the asymptotic shock strength into the overpressure

The overpressure which represents the pressure disturbance due to the shock wave can be described as follows:

$$\Delta p = p - p_0 = \left(\frac{p}{p_t} - \frac{p_0}{p_t}\right) p_t \tag{8.1}$$

From the isentropic flow relations the ratio of the static pressure to the total pressure is the following:

$$\frac{p}{p_t} = \left(1 + \frac{\gamma - 1}{2} M^2\right)^{\frac{-\gamma}{\gamma-1}} \tag{8.2}$$

This gives the ratio of the overpressure to the free flow pressure:

$$\frac{\Delta p}{p_0} = \frac{\left(1 + \frac{1}{5}M^2\right)^{\frac{-7}{2}} - \left(1 + \frac{1}{5}M_0^2\right)^{\frac{-7}{2}}}{\left(1 + \frac{1}{5}M_0^2\right)^{\frac{-7}{2}}} \tag{8.3}$$

Using $\beta = \sqrt{M^2 - 1}$ results in the following expression:

$$\frac{\Delta p}{p_0} = \left(\frac{6 + \beta_0^2}{6 + \beta^2}\right)^{\frac{7}{2}} - 1 \tag{8.4}$$

Considering equation (3.4) being equal to $k\epsilon$ and assuming when $y\rightarrow\infty$ so then $\frac{1}{\sqrt{y}}\rightarrow 0{=}\epsilon$. It means that the slope of the characteristic line behind the shock will be the following:

$$tan\theta = tan\theta_0 + k_l\epsilon + O(\epsilon^2) \tag{8.5}$$

Inserting this result into equation (3.9) gives us:

$$\beta = \sqrt{6}tan\left(\frac{\nu_0 + \frac{\pi}{2} - tan^{-1}\left(tan\theta_0 + k_l\epsilon\right)}{\sqrt{6}}\right) \tag{8.6}$$

Differentiation β w.r.t. ϵ gives us:

$$\frac{d\beta}{d\epsilon} = \frac{-cos^2\theta_0 k_l}{cos^2\widehat{\theta_0}} \tag{8.7}$$

In this equation $\widehat{\theta_0}$ is the simplified form of term $\frac{\nu_0+\frac{\pi}{2}-\theta_0}{\sqrt{6}}$. So, this enables us now to develop β in terms of ϵ as follows:

$$\beta = \beta_0 - \frac{cos^2\theta_0 k_l}{cos^2\widehat{\theta_0}} + O(\epsilon^2) \tag{8.8}$$

Inserting the new expression for β into the equation (8.4) gives us the following relation:

$$\frac{\Delta p}{p_0} = 1 + \frac{7}{2}\frac{2\beta_0 cos^2\theta_0}{(6+\beta_0)cos\widehat{\theta_0}}k_l\epsilon - 1 \tag{8.9}$$

Using equation (3.23) enables us to write this equation in an expression which depends only on free Mach number M_0, the shock strength A_l and the distance y as follows:

$$\frac{\Delta p}{p_0} = \frac{7\sqrt{M_0^2-1}\sqrt{2}}{\sqrt{M_0}(5+M_0^2)}\left(1 + tan^2\left(\frac{\nu_0+\frac{\pi}{2}-\theta_0}{\sqrt{6}}\right)\right)\sqrt{A_l}\frac{1}{\sqrt{y}} \tag{8.10}$$

8.2 Application of Whitham's theory to the optimum contours

The first step to apply the *Whitham's theory* to the optimum contours which have been obtained already in the previous chapters, is to find the corresponding *Whitham*'s F-function, see $F(\xi)$ in figure 8.1. This function represents in fact the flow disturbance caused by the body. In other words, the contour geometry is the main factor for the magnitude of the *Whitham* F-function. In reference [G.B.Whiham [1952]] the disturbed potential velocities are given as follows:

$$u = \frac{-F(\xi)}{\beta} \text{ and } v = F(\xi) \tag{8.11}$$

According to the *Whitham's theory*, every characteristic curve originating from the body surface can be determined by the variable ξ. This variable is a function of x and y which are respectively the distances along and perpendicular to the boundary wall *y=y(x)*. In 2D steady supersonic flows, $F(\xi)$ is equal to the slope of the boundary at the point where

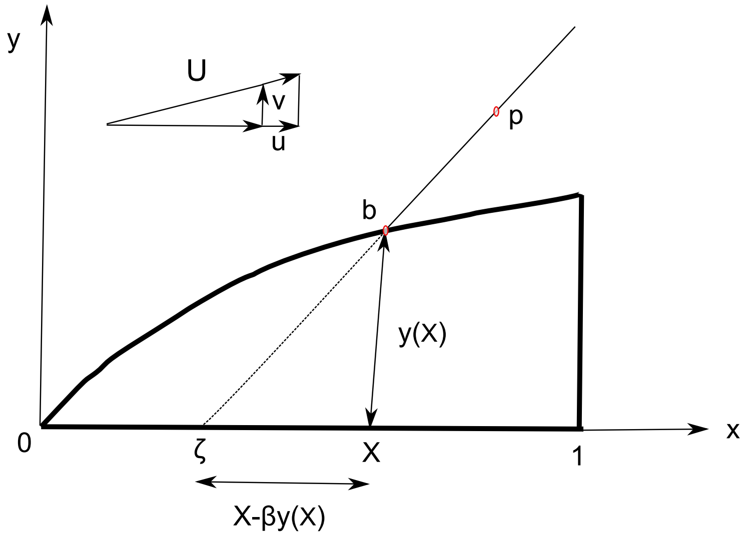

Figure 8.1: Sketch of a characteristic line, Whitham's theory

it is crossed by the characteristic line ξ, that is, $F(\xi)=y^{'}(X)$. The distance from the tip of the nose to this characteristic line $X(\xi)$ can be determined by X-$\beta y(X)=\xi$. Figure 8.1 represents a sketch of the characteristic line which is emanating from the body at point b and passing through the point p in flow field. Knowing the *Whitham*'s F-function enables us to approximate the pressure jump $\frac{\Delta p}{p_0}$ for the occurred shock wave as follows:

$$\frac{\Delta p}{p_0} = \frac{\gamma M_0^2 F(\xi)}{\beta\sqrt{r}} \tag{8.12}$$

Figure 8.2 represents the *Whitham*'s F-function with the corresponding overpressure for a first variant contour with a volume of about $V \approx 0.0571$ at $M_0=2.0$. The upper plot shows that F-function which is a result of the surface inclination decreases from the nose to the shoulder point. The lower plot 8.2 represents the values for the near-field overpressure $\frac{\Delta p}{p_0}$ by considering a distance of $r=1.0$ away from the x-axis. It is also remarkable from lower plot 8.2 that the first value for $\frac{\Delta p}{p_0}$ indicates in fact the leading shock strength for this body at $M_0=2.0$. From this, we are now able to obtain the leading shock strength by using the *Whitham's theory* for different contours.

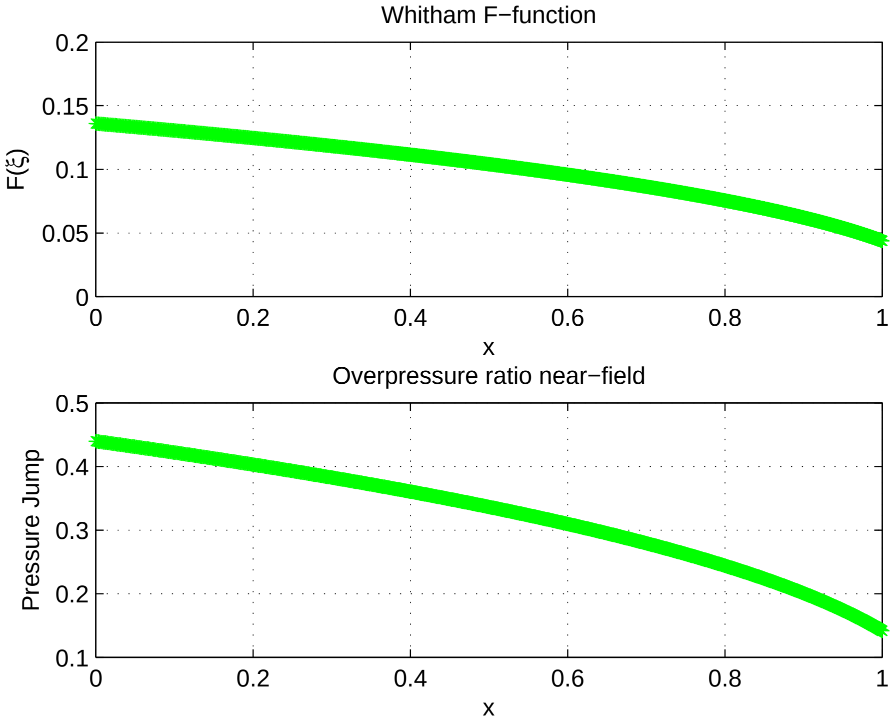

Figure 8.2: Upper plot: *F*-function, Lower plot: pressure jump $\frac{\Delta p}{p_0}$

Figure 8.3 shows the difference between the pressure jump based on the asymptotic shock strength and the pressure jump which is based on the *Whitham's theory* for the same contours at M_0=2.0. From figure 8.3 it is obvious that the values for the pressure jump based on the asymptotic shock are larger than those related to the *Whitham's theory*. The reason for that is because the pressure jump related to the asymptotic shock strength indicates the field away from the body while the results based on the *Whitham's theory* represent the near-field pressure jump. The results for the *Whitham*'s overpressure in the far-field can be achieved by adding the non-linear effects to the near-field overpressure results shown in figure 8.3.

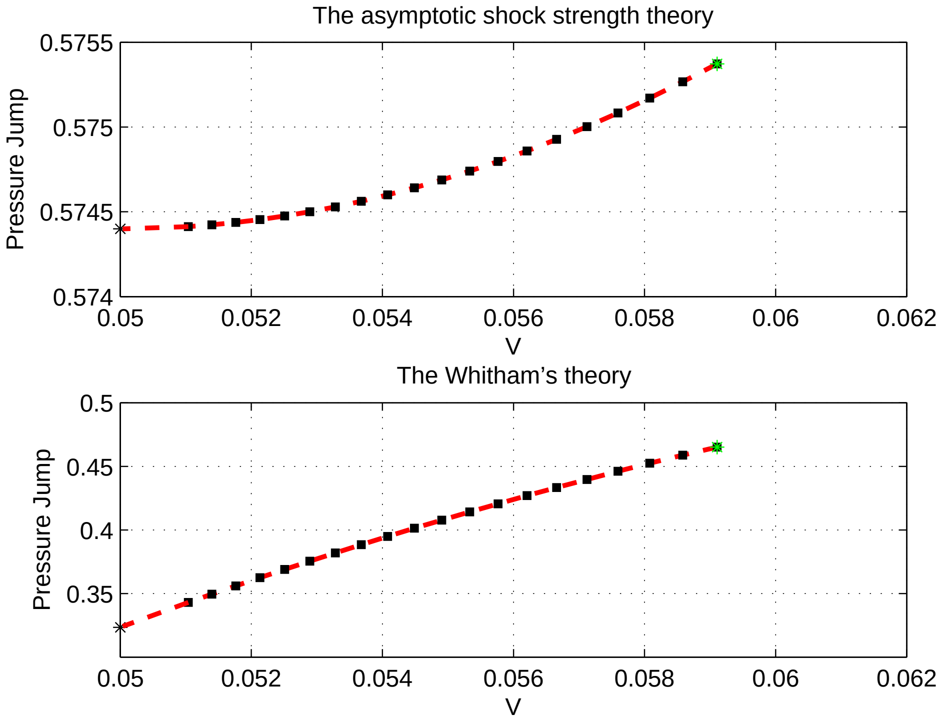

Figure 8.3: Comparing the asymptotic shock with the Whitham's theory

CHAPTER 9

CONCLUSION & RECOMMENDATIONS

The origin of the sonic boom has shown that total elimination of its influence is impossible. But the studies have enabled men to develop theories in order to reduce the strength of the sonic boom. On the basis of the method of characteristic the asymptotic behavior of the shock wave has been investigated for a 2D object with infinitesimally small thickness in a supersonic flow. And its strength can be determined by *BASS* measure:

$$A_l = \int_0^{x_0} (cos\theta_0 - cos\theta)\, dx \tag{9.1}$$

This measure can be applied to a 2D body with a certain thickness τ in a non-lift generating condition:

$$A_l = \int_0^{1-\tau/tan\theta_s} (cos\theta_0 - cos\theta) du + \tau \left(s_0 - \frac{1 - c_0 c_s}{s_s} \right) \tag{9.2}$$

This result together with a volume constraint can be viewed as a variational problem. And solving this problem leads to a complex 1^{st} order differential equation for *G(x)*, where $p{=}\frac{dG}{dx}$, which depends on two constants τ and M_0 and a given θ-range.

$$H(p) = c - \lambda G = F_0(p) - pF_0^{'}(p) + p^2 F_1(p) \tag{9.3}$$

The *H(p)*-function can be analyzed as a variable of p and has the form of a curved line. Based on M_0, the *H(p)*-function results in three curves variant from which the second type plays a transitional variant. Integration of the first and third variant curves results in two kind of optimum contours. The variational approach enables us in fact to define two kind of contours in terms of asymptotic shock strength.

First variant contours

The first variant contours are really optimized compared to the non-optimized contours with the same volume. Further, the first variant contours which are achieved at lower

Mach numbers show higher asymptotic shock strength than those obtained at higher Mach numbers.

The study on expansion wave and shock path shows that interaction between the shock and *Prandtl-Meyer* expansion waves has an inverse proportional relation with contours volume. In addition, the wedge contour with the smallest volume which causes the lowest asymptotic shock strength indicates the greatest centered expansion wave at the shoulder point.

The optimum contours which are the result of the integrated *H(p)*-function are in fact a function of M_0 and τ. So, not only M_0 has influence on contour geometry but also the variable τ. So, increasing τ results in contours with larger volume. And again these larger contours cause higher asymptotic shock strength.

The next task was investigation on the influence of M_0 on the asymptotic shock strength. For this reason an optimum contour with a certain volume which was obtained at a certain Mach number was exposed in the supersonic flows of other Mach numbers. The result of this investigation shows an inverse relation between M_0 and k_l. In addition, it was proved that contours with the same volume which are achieved at other Mach numbers show the same shock strength characteristic. So, it does not matter at which Mach number we achieve an optimum contour with corresponding asymptotic shock strength.

The same procedure was applied for when M_0 being constant while τ varies. The results show that contours with a certain volume and a smaller thickness cause lower asymptotic shock strength than those with the same volume and a larger thickness. So, it means that increasing thickness results in contour geometries which produce higher asymptotic shock strength at different Mach numbers.

The aerodynamic properties such as local Mach number, flow velocities, and pressure as results of the leading shock wave were studied for the first variant contours. And the results of entropy change along the shock wave indicates that assumption of isentropic flow where the shock occurs is acceptable.

The last point was investigation of wave drag caused by the first variant contours. Contours with a larger volume show larger wave drag and there is also a linear relation between the asymptotic shock strength and wave drag.

Third variant contours

The third variant contours are not optimized comparing to the non-optimized contours with similar volumes. The reason for it is because solving the variation problem leads to the maximum extreme values of A_l for the third variant contours. The wedge contour is the largest possible third variant contour which causes the largest amount of asymptotic shock strength. Increasing Mach number results in contours with a smaller volume which cause lower asymptotic shock strength. There is also a proportional relation between τ

and asymptotic shock strength for third variant contours.

Study on centered expansion waves at the shoulder point brings the same results for third variant contours as the first variant. The third variant wedge contour shows an earlier interaction between the shock and *Prandtl-Meyer* expansion wave. And it has the largest centered expansion wave at the shoulder point.

The influence of Mach number on asymptotic shock strength for third variant contours is studied in the same way as for the first variant. There is also an inverse relation between Mach number and the asymptotic shock strength. Furthermore, it was proved that contours with the same volume which are achieved at other Mach numbers show the same shock strength characteristic. Furthermore, when Mach number remains constant and the thickness increases, it will result in contour geometries which generate higher asymptotic shock strength for different Mach numbers.

Due to the surface inclination of third variant contours, the aerodynamic properties such as local Mach number, pressure and flow velocities show reversed results compared to the first variant contours. Furthermore, the concave geometry of the third variant contours results in an inverse relation between volume and wave drag magnitude and the third variant wedge contour with the maximum volume causes the minimum possible wave drag.

The Whitham and asymptotic shock strength theories

The body geometry has influence on the *Whitham's* F-function which subsequently determines the value of near-field overpressure ratio $\frac{\Delta p}{p_0}$. In a real 3D view, the near-field overpressure must be extrapolated to the far-field by using the geometrical acoustic ray tracing method. This method includes the atmospheric non-linear effects which results in N-wave which can be observed on the ground.

The asymptotic shock strength is an indication of sonic boom caused by the geometry of an object which can be observed in a far distance. The sonic boom is the result of shock establishing for which the strength can be determined by:

$$\Sigma = tan\theta_1 - tan\theta_0 = \upsilon_1 - \upsilon_0 \tag{9.4}$$

Where θ_1 and θ_0 are the characteristic angles behind and before the shock wave respectively. This expression can be transformed to the overpressure ratio.

Both theories, the *Whitham* and asymptotic shock strength theories, can be applied to the same optimal contours which are achieved based on the optimized *BASS* measure. The results of *Whitham's theory* seem being smaller than those based on the asymptotic shock strength. The reason for that is because the *Whitham's* results are achieved in the near-field while the asymptotic shock theory indicates the results in a very large distance.

Comparing theses theories also shows the different results between applied basic methods. The *Whitham's theory* is derived from linear supersonic flow theory while the asymptotic shock strength theory is achieved from inviscid 2D *Burgers'* equation based on non-linear method of characteristic.

Research question

The research question for this thesis which was stated in the introduction was:

What is the most optimum 2D and non-lift generating contour with a certain thickness to have the minimum asymptotic shock strength for different Mach numbers?

Optimization of the *BASS* measure for a 2D forebody by a variational approach results in two kind of optimum contours. The first variant contours which have a convex upper surface and third variant contours with a concave upper surface. This approach causes the first variant contours being optimum because the extreme value of A_l resulting from variational analyze is a minimum extreme value. Contrary to the first variant, the variational approach results in the maximum extreme values of A_l for the third variant contours. So, it means that only the first variant contours are optimized in the sense that they cause the minimum possible asymptotic shock strength. Furthermore, it was shown that both contour types have similar asymptotic shock behavior in the steady and inviscid supersonic flow of other Mach numbers.

Recommendations

The *BASS* measure used in this thesis is first order accurate because the asymptotic shock strength Σ was developed explicitly by using Taylor series expansions. And the influence of higher order terms was neglected. So, for further research, especially when the asymptotic shock strength is compared to the *Whitham's theory*, it is recommend to include also the higher order terms.

The *BASS* measure was applied to a 2D forebody in a non-lift generating condition. So, the influence of angle of attack was neglected. It is recommended to incorporate the lift requirement. And in this way, the relation between the body geometry and asymptotic shock strength can be coupled with the lift influence. And even the wave drag can be studied closely to the relation between the shock strength and lift.

Since we are dealing with asymptotic shock strength, shock establishing at a very large distance, it is not possible to compare numerical results with experimental wind tunnel data. But, the aerodynamic properties based on numerical approach can be validated by obtaining data from wind tunnel tests.

Furthermore a measure for the shock strength validation can be achieved when we compare the linear *Whitham*'s results with the wind tunnel data. And subsequently extrapolating these data to a large distance gives us an indication of the shock strength which is comparable with results from the asymptotic shock strength theory.

Another way to verify the results for asymptotic shock strength theory is applying the new CFD techniques.

REFERENCES

Curry, M. (2008, March 01). Dryden flight research center. `http://www.nasa.gov/centers/dryden/news/FactSheets/FS-016-DFRC.html`.

D.Hayes, W. (1971). Sonic boom.

Ferri, A., & Schwartz, I. R. (n.d.). Sonic boom generation propagation and minimization.

Francken, T. (2009). *The asymptotic shock strength of a 2D lift generating object, Master of Science Thesis, Delft University of Technology.*

G.B.Whiham. (1952). The flow pattern of a supersonic projectile. (Vol,v,301-348).

J.Plotkin, K. (2001, April). State of the art of sonic boom modeling. (4328.Mw,43.50.Lj[MRS]).

J.Plotkin, K., & J.Maglieri, D. (2003, June). Sonic boom research: history and future. (AIAA 2003-3575).

Kaour, K. (2004). *Secondary sonic boom.* Ph.D. Thesis, University of Oxford.

K.J.Plotkin. (1989, April). Review of sonic boom theory. (AIAA 12th aeroacoustics conference).

Nadarajah, S. (2011, Augustus 09). Automatic aerodynamic shape optimization via the continuous and discrete adjoint equations. `http://www.mcgill.ca`.

P.G.Bakker, & Leer van. (2005). *Lecture notes on Gasdynamics, Delft University of Technology.*

Seebass, R., & Argrow, B. (1998). Sonic boom minimization revisited. (AIAA-98-2956).

APPENDIX A

THE HALL FUNCTION

The *Prandtl-Meyer* function is needed to determine the local Mach number from the known local *Prandtl-Meyer* angle. This function can be approximated by using the polynomial function from *Hall* [1]:

$$M = \frac{1 + Ax + Bx^2 + Cx^3}{1 + Dx + Ex^2} \tag{A.1}$$

With $x = \left(\frac{\nu}{\nu_\infty}\right)^{\frac{2}{3}}$, $\nu_\infty = \frac{\pi}{2}(\sqrt{6} - 1)$ which is the maximum *Prandtl-Meyer* angle for γ=1.4 and the following coefficients:

$$A = 1.3604\ ,\ B = 0.0962\ ,\ C = -0.5127\ ,\ D = -0.6722\ ,\ E = -0.3278 \tag{A.2}$$

---

[1] I.M.Hall, Inversion of the prandtl-meyer relation, Aeronautical Journal

APPENDIX B

FIRST VARIANT CONTOURS FOR A CONSTANT τ AND DIFFERENT M_0

In chapter 6 it was explained how the asymptotic shock strength A_l caused by a 2D first variant contour can be calculated. In this appendix an overview of the optimal contour configurations with the corresponding shock strength is depicted for different M_0 separately. The Mach range is defined within $1.5 \leq M_0 \leq 2.0$. In all these cases the (thickness/chord)-ratio is assumed to be constant τ=0.10.

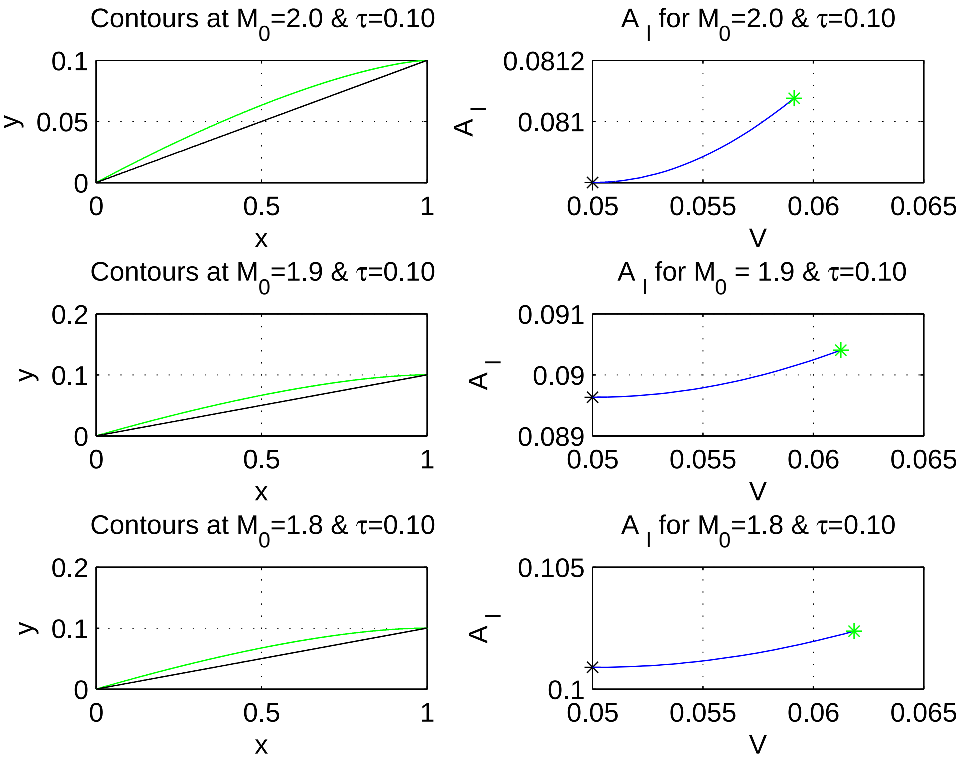

Figure B.1: Different cases for τ=0.10 and $M_0 = 2, 1.9, 1.8$

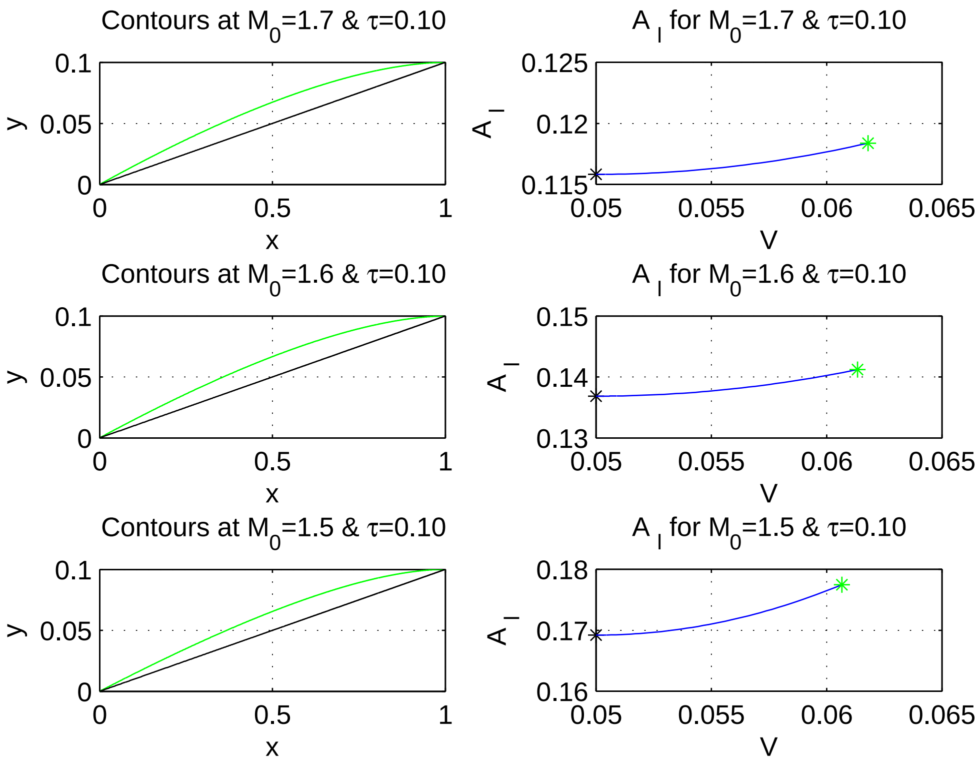

Figure B.2: Different cases for τ=0.10 and $\mathrm{M}_0 = 1.7, 1.6, 1.5$

APPENDIX C

FIRST VARIANT CONTOURS FOR A CONSTANT M_0 AND DIFFERENT τ

In chapter 6 it was explained how the asymptotic shock strength of a 2D first variant body can be calculated for a constant Mach number and τ. In this appendix an overview of the optimal contour configurations with the corresponding shock strength is depicted for different τ. In all these cases the free flow Mach number M_0 is assumed to be constant, M_0=2.0

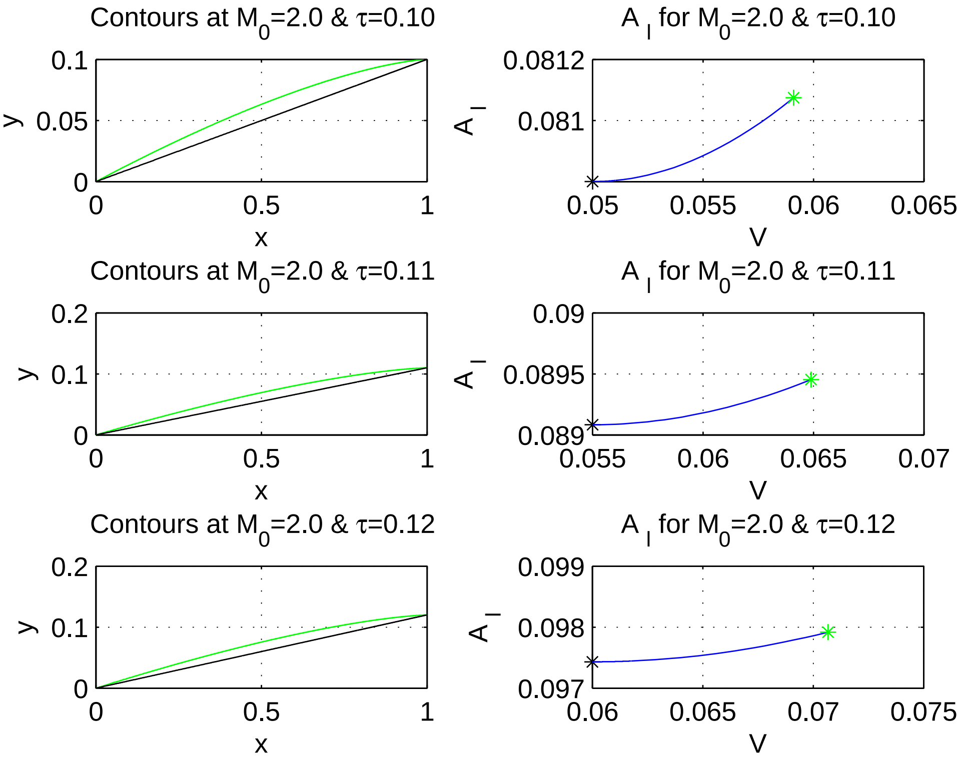

Figure C.1: Different cases for M_0=2.0 and τ=0.10, 0.11, 0.12

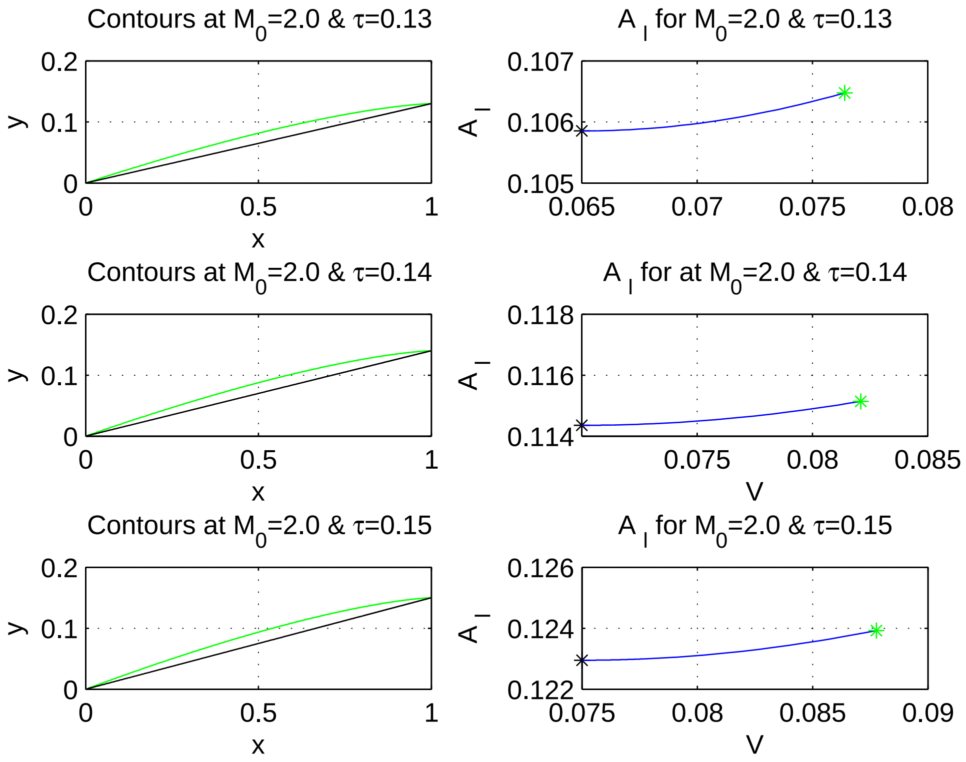

Figure C.2: Different cases for M_0=2.0 and τ=0.13, 0.14, 0.15

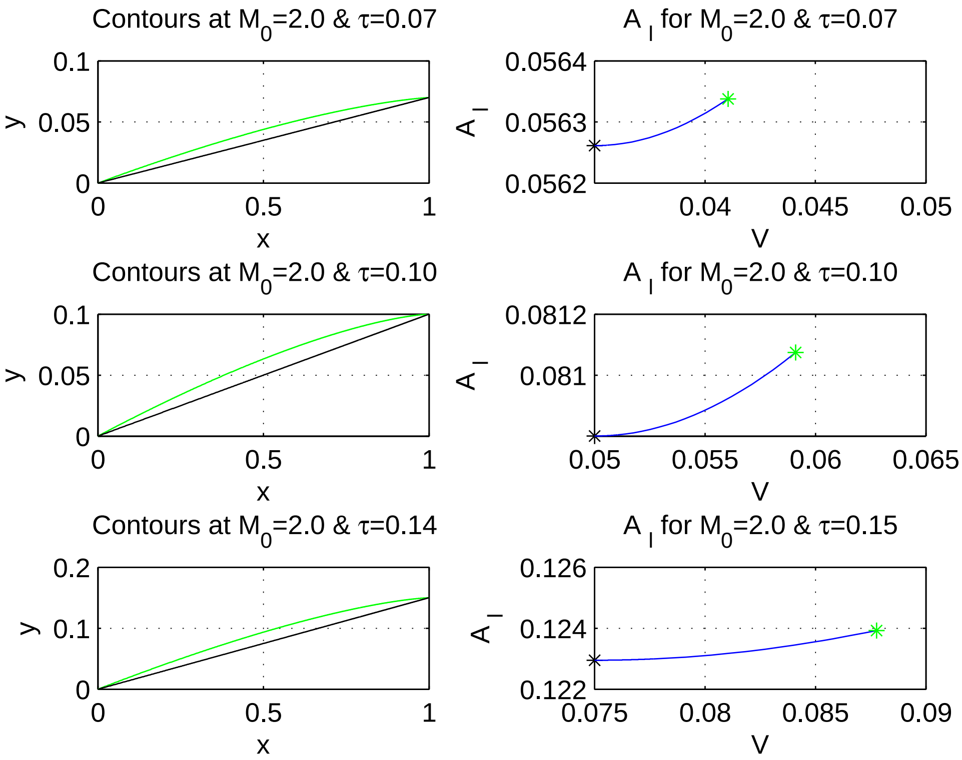

Figure C.3: Different cases for M_0=2.0 and τ=0.07, 0.10, 0.15

APPENDIX D

DRAG AND ASYMPTOTIC SHOCK STRENGTH, FIRST VARIANT

In this chapter the relation between volume and asymptotic shock strength have been depicted for the Mach range $1.5 \leq M_0 \leq 1.9$. Furthermore, the relation between drag and asymptotic shock strength have been shown for the same Mach range.

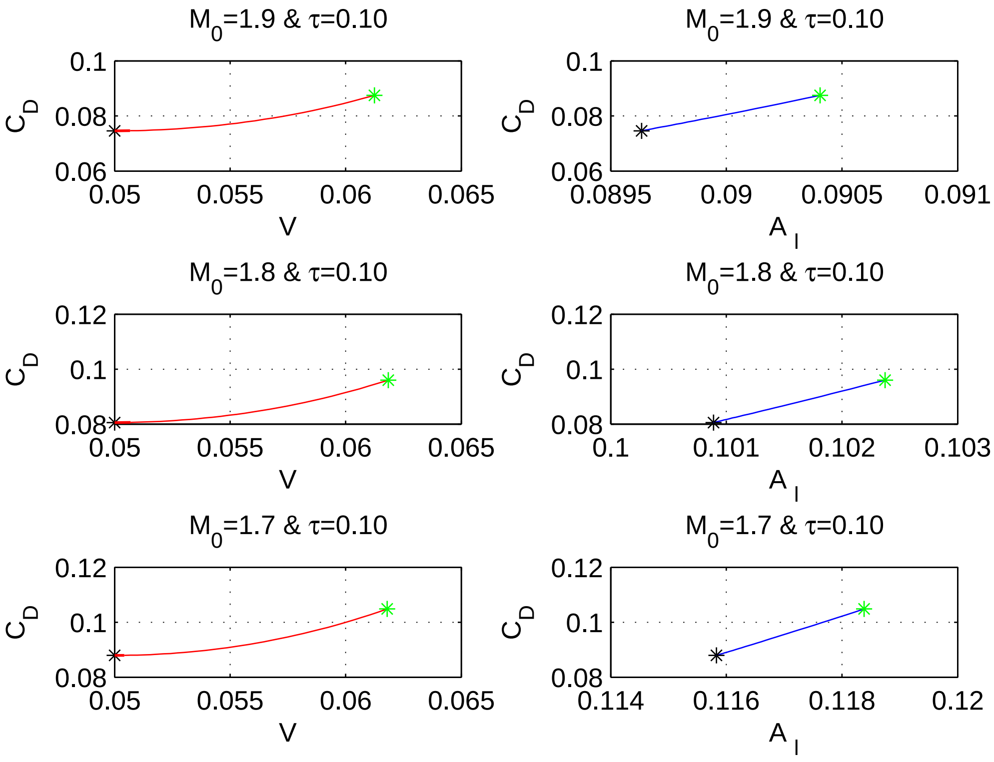

Figure D.1: Drag and shock strength for M_0=1.9, 1.8, 1.7 and τ=0.10

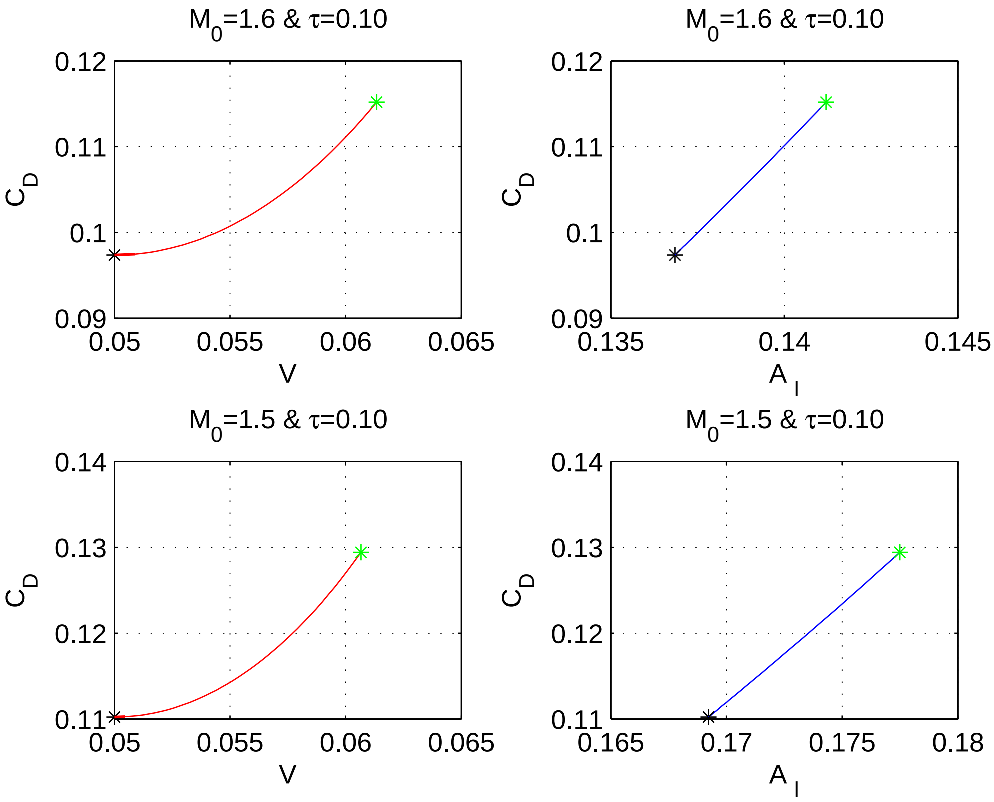

Figure D.2: Drag and shock strength for M_0=1.6, 1.5 and τ=0.10

APPENDIX E

THIRD VARIANT CONTOURS FOR A CONSTANT τ AND DIFFERENT M_0

In chapter 7 it was explained how the asymptotic shock strength caused by a 2D third variant body can be calculated. In this appendix an overview of the optimal contour configurations with the corresponding shock strength is depicted for different M_0. The Mach range is defined within $2.3 \leq M_0 \leq 3.0$. In all these cases the (thickness/chord)-ratio is assumed to be constant, τ=0.10.

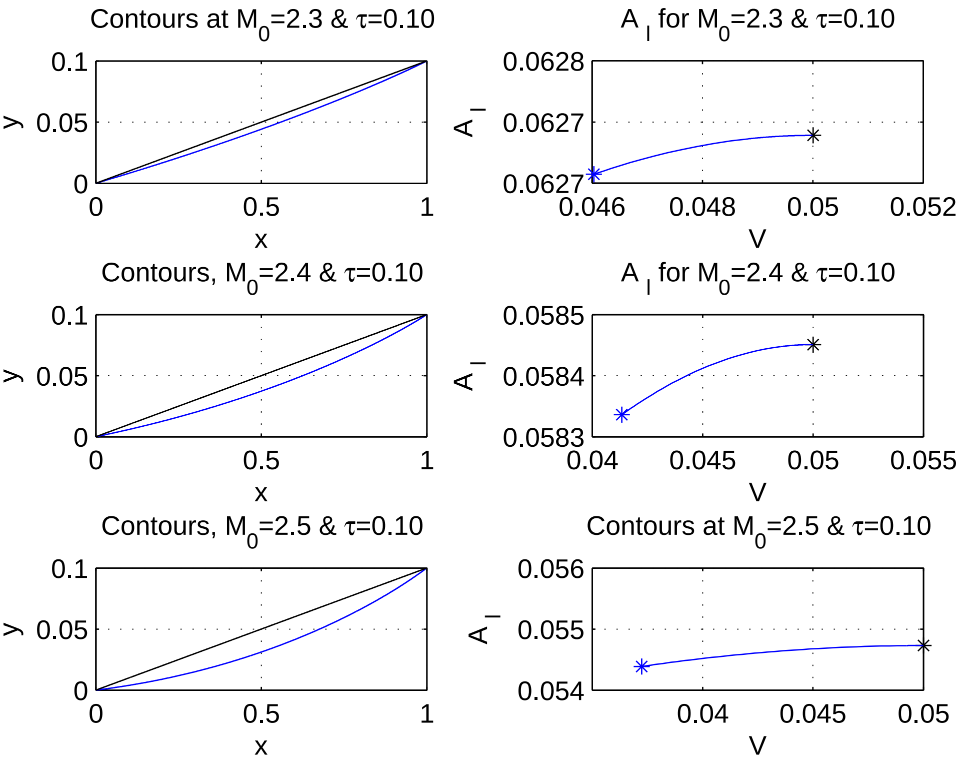

Figure E.1: Different cases for M_0=2.3, 2.4, 2.5

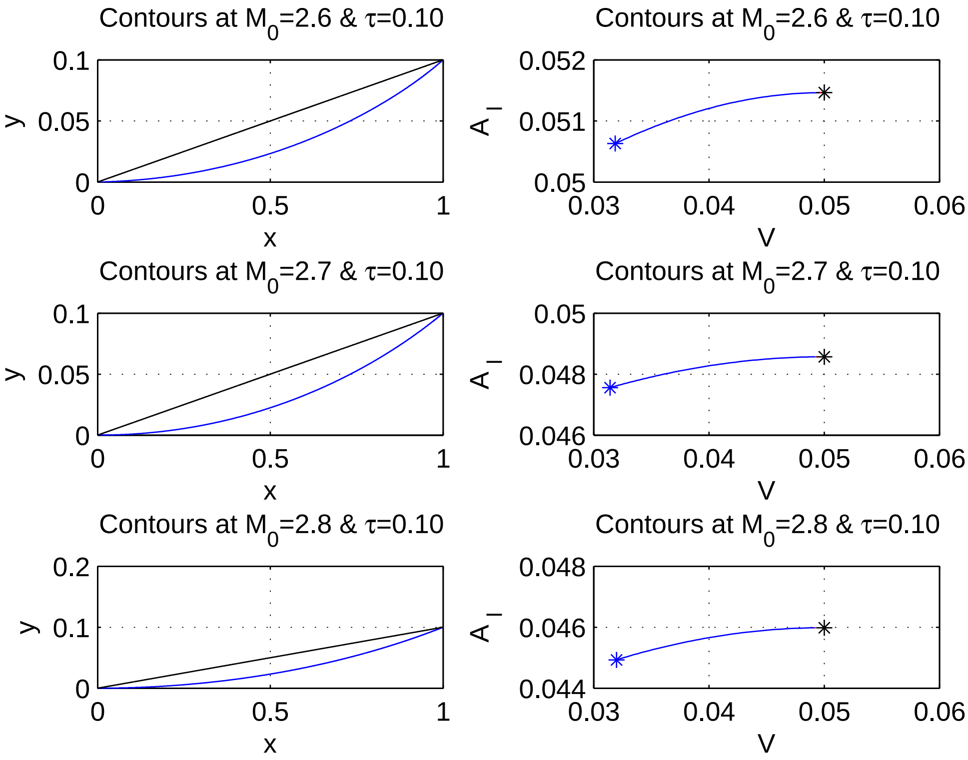

Figure E.2: Different cases for M_0=2.6, 2.7, 2.8

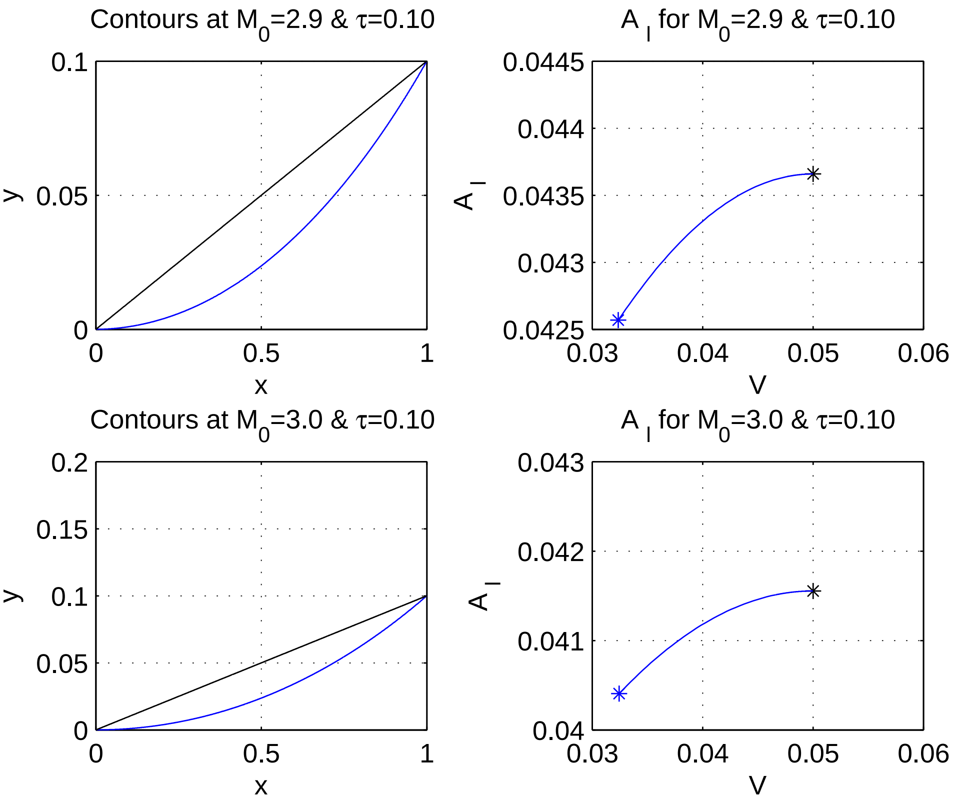

Contours at M_0=2.9 & τ=0.10

A_l for M_0=2.9 & τ=0.10

Contours at M_0=3.0 & τ=0.10

A_l for M_0=3.0 & τ=0.10

Figure E.3: Different cases for M_0=2.9, 3.0

APPENDIX F

DRAG AND ASYMPTOTIC SHOCK STRENGTH, THIRD VARIANT

In this chapter the relation between volume and asymptotic shock strength have been depicted for the Mach range $2.3 \leq M_0 \leq 3.0$. Furthermore, the relation between drag and asymptotic shock strength have been illustrated for the same Mach range.

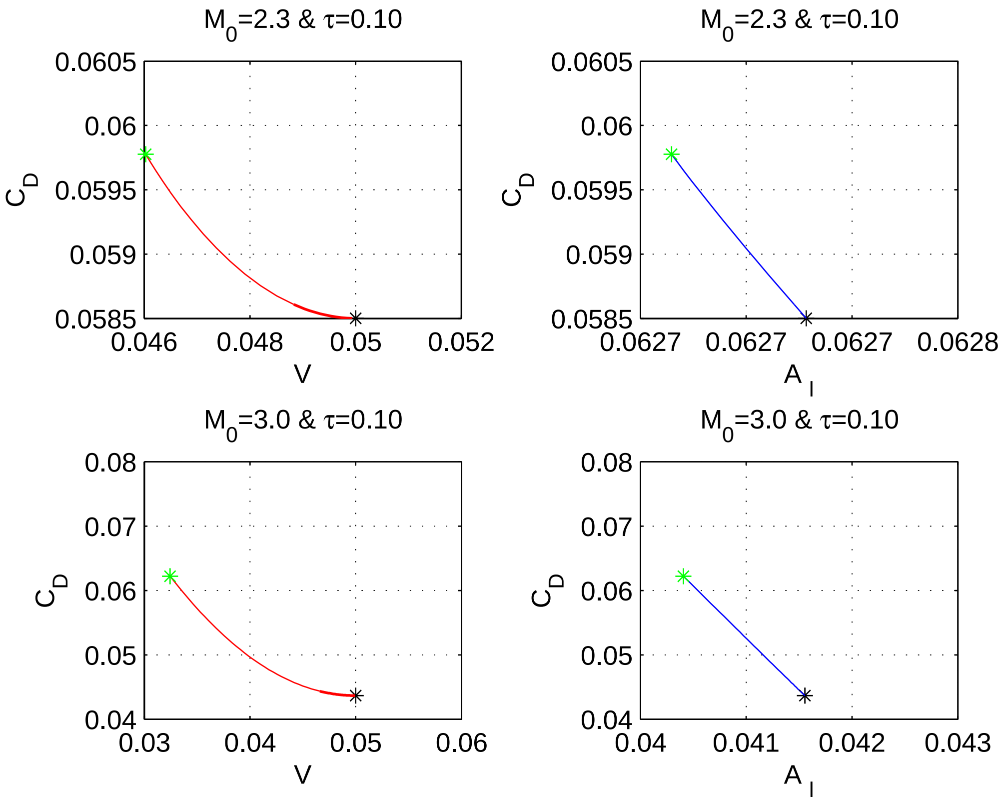

Figure F.1: Drag and shock strength for M_0=2.3, 3.0 and τ=0.10

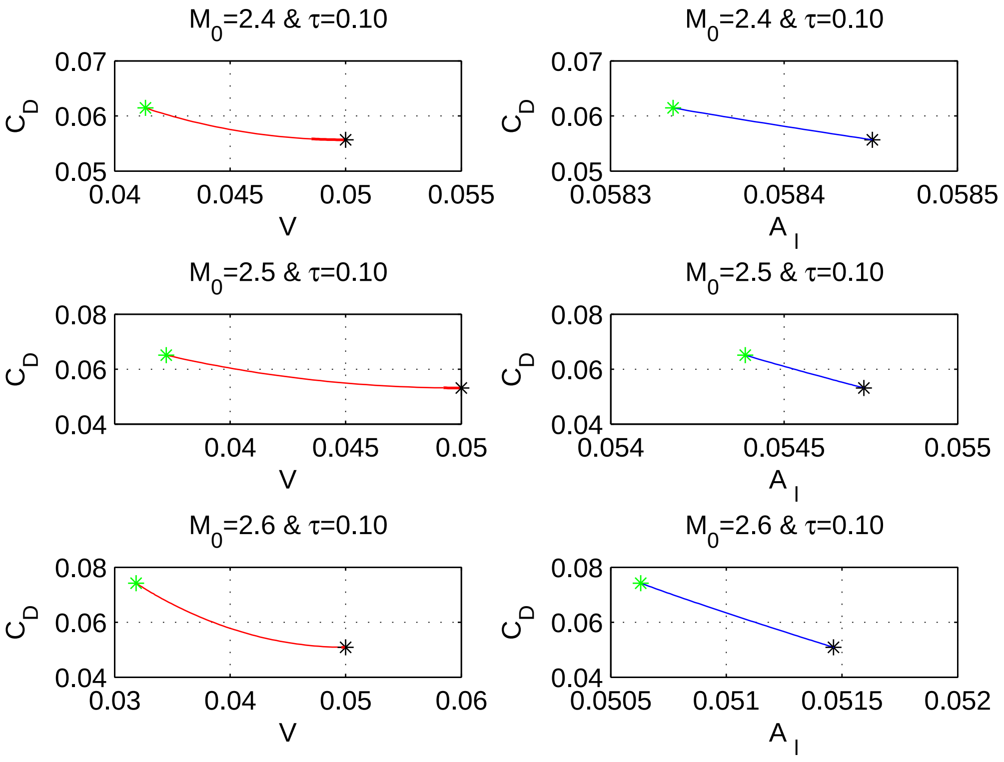

Figure F.2: Drag and shock strength for M_0=2.4, 2.5, 2.6 and τ=0.10

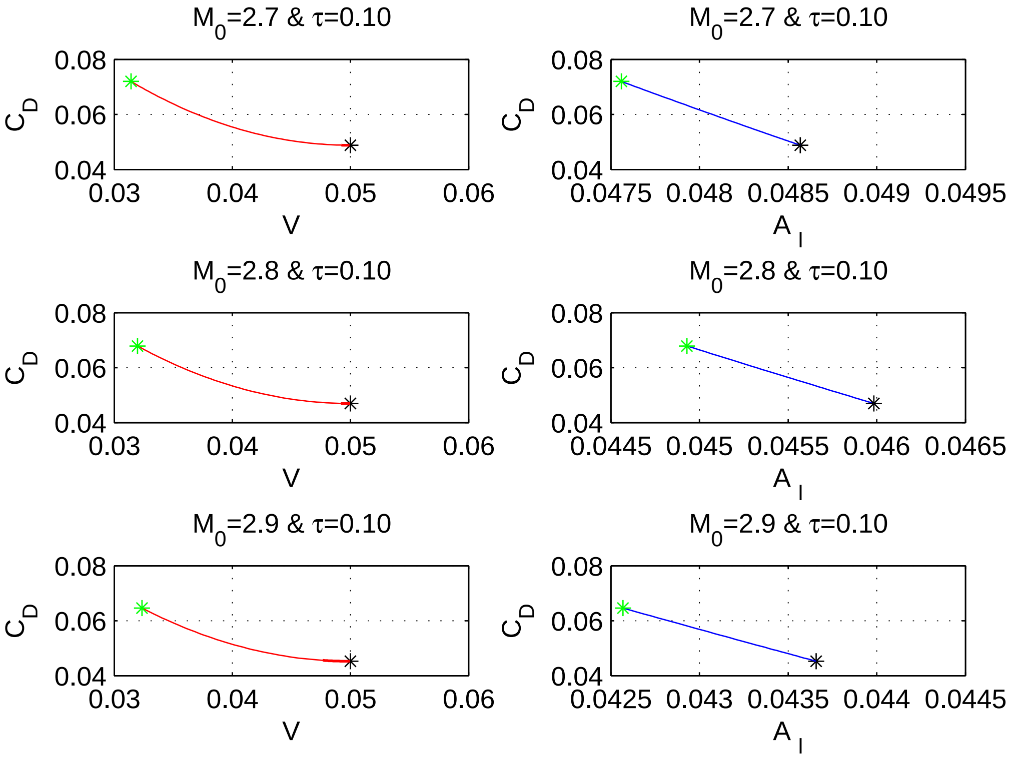

Figure F.3: Drag and shock strength for M_0=2.7, 2.8, 2.9 and τ=0.10